

AD/A-007 034

EFFECTS OF MESO-SCALE AND SMALL-SCALE INTERACTIONS  
ON GLOBAL CLIMATE. VOLUME I. OROGRAPHIC EFFECTS  
ON GLOBAL CLIMATE

John Schaibly

Systems, Science and Software

Prepared for:

Air Force Office of Scientific Research  
Advanced Research Projects Agency

28 February 1975

DISTRIBUTED BY:

**NTIS**

National Technical Information Service  
U. S. DEPARTMENT OF COMMERCE

AD A007034



DEFENSE OFFICE OF SCIENTIFIC RESEARCH (AFSC)  
NOTICE OF TECHNICAL TO DOG  
This technical report is the property of the AFSC and is  
loaned to you for your use only. It is not to be distributed  
outside your organization.  
D. V. GIBSON  
Technical Information Officer

090119

**SYSTEMS, SCIENCE AND SOFTWARE**

AFOSR - TR - 75 - 0397

EFFECTS OF  
MESO-SCALE AND SMALL-SCALE INTERACTIONS  
ON GLOBAL CLIMATE  
VOLUME I  
OROGRAPHIC EFFECTS ON GLOBAL CLIMATE

Final Technical Report  
for Period  
1 November 1973 through 31 December 1974

Sponsored by:  
Defense Advanced Research Projects Agency

DARPA Order No. 2609  
Program Code 4P10

Contract No.: F44620-74-C-0035  
Effective Date of Contract: 1 November 1973  
Contract Expiration Date: 31 December 1974  
Amount of Contract: \$73,271  
Principal Investigator: Hans Giroux

28 February 1975



UNCLASSIFIED

SECURITY CLASSIFICATION OF THIS PAGE (When Data Entered)

REPORT DOCUMENTATION PAGE		READ INSTRUCTIONS BEFORE COMPLETING FORM
1. REPORT NUMBER <b>AFOSR - TR - 75 - 0397</b>	2. GOVT ACCESSION NO.	3. RECIPIENT'S CATALOG NUMBER <b>AD/A-007 034</b>
4. TITLE (and Subtitle) <b>Meso-Scale and Small-Scale Interactions on Global Climate  Vol. I - Orographic Effects on Global Climate</b>		5. TYPE OF REPORT & PERIOD COVERED <b>Final Report 1 Nov 1973 - 31 Dec 1974</b>
		6. PERFORMING ORG. REPORT NUMBER <b>SSS-R-75-2556</b>
7. AUTHOR(s) <b>John Schaibly</b>		8. CONTRACT OR GRANT NUMBER(s) <b>F44620-74-C-0035</b>
9. PERFORMING ORGANIZATION NAME AND ADDRESS <b>Systems, Science and Software P.O. Box 1620 La Jolla, CA 92038</b>		10. PROGRAM ELEMENT, PROJECT, TASK AREA & WORK UNIT NUMBERS <b>ARPA Order No. 2609 Program Code 4P10</b>
11. CONTROLLING OFFICE NAME AND ADDRESS <b>Advanced Research Projects Agency/NMR 1400 Wilson Boulevard Arlington, VA 22209</b>		12. REPORT DATE <b>28 Feb 1975</b>
14. MONITORING AGENCY NAME & ADDRESS (if different from Controlling Office) <b>Air Force Office of Scientific Research/NP 1400 Wilson Boulevard Arlington, VA 22209</b>		13. NUMBER OF PAGES <b>360</b>
		15. SECURITY CLASS. (of this report) <b>Unclassified</b>
16. DISTRIBUTION STATEMENT (of this Report)  <b>Approved for public release; distribution unlimited.</b>		15a. DECLASSIFICATION/DOWNGRADING SCHEDULE
17. DISTRIBUTION STATEMENT (of the abstract entered in Block 20, if different from Report)		
18. SUPPLEMENTARY NOTES		
19. KEY WORDS (Continue on reverse side if necessary and identify by block number)  <b>Radiation Transport Atmospheric Scattering</b>		
20. ABSTRACT (Continue on reverse side if necessary and identify by block number)  <b>This report summarizes the three-year research program at Systems, Science and Software to investigate the effects of meso-scale and small-scale interactions on global climate. The research concentrated on two areas, orographic effects on the wind patterns and effects of radiation transport on the climate. Volume I describes the orographic research and includes the theory of momentum transport due to mountain ranges, the formulation of several computer codes to calculate the effects for realistic topography and wind profiles, and the</b>		

application of these codes to various problems and comparison with other calculations as well as experimental results. Volume II describes the radiation transport research which produced a benchmark code against which more simplified models can be compared. This code, ATRAD, is characterized by high angular and frequency resolution and by the ability to calculate radiative atmospheric heating rates taking into account molecular absorption and scattering from arbitrary distributions of aerosols and particulates.

## TABLE OF CONTENTS

	<u>Page</u>
ABSTRACT. . . . .	xiv
1. INTRODUCTION. . . . .	.1-1
1.1 Orographic Effects on Global Climate . . . . .	.1-3
2. The BASIC HAIFA Code. . . . .	.2-1
2.1 The BASIC HAIFA Equations. . . . .	.2-1
2.2 Numerical Approximation of HAIFA Equations . . . . .	.2-5
2.2.1 Finite Difference Scheme. . . . .	.2-5
2.2.2 The Advection Scheme. . . . .	.2-8
2.2.3 Update of Other Terms in the Vorticity and Energy Equations. . . . .	.2-10
2.2.4 Solution of the Poisson Difference Equa- tion by Finite Fourier Transform. . . . .	.2-11
2.2.5 The FFT Solution of the Poisson Equation Having Non-Rectangular Boundaries . . . . .	.2-16
2.2.6 Description of Poisson Solver Routines. . . . .	.2-16
2.3 Stability Analysis . . . . .	.2-19
2.4 Boundary Conditions. . . . .	.2-21
2.5 HAIFA Code Description . . . . .	.2-24
2.5.1 Initiating a Calculation. . . . .	.2-26
2.5.2 Major Subroutines in the Main HAIFA Calculational Loop. . . . .	.2-27

	<u>Page</u>
3. MODIFICATIONS TO THE HAIFA CODE . . . . .	3-1
3.1 Compressibility. . . . .	3-1
3.1.1 Derivation of the Differential Equations.	3-1
3.1.2 Method of Numerical Solution. . . . .	3-4
3.1.2.1 Computational Logic. . . . .	3-4
3.1.2.2 Finite Difference Scheme . . . . .	3-4
3.1.3 Initial Conditions. . . . .	3-7
3.1.4 Modification of Advection Scheme. . . . .	3-8
3.1.5 Timing Comparison . . . . .	3-8
3.1.6 Test Problem. . . . .	3-9
3.1.6.1 Wave Drag Results. . . . .	3-12
3.1.6.2 Numerical Stability. . . . .	3-17
3.2 Moisture Effects . . . . .	3-18
3.2.1 Integration of the Finite Difference Equations . . . . .	3-26
3.2.1.1 The Advection Scheme . . . . .	3-26
3.2.1.2 Changes in Vorticity and Water Content Due to Other Terms in the Conservation Equations . . . . .	3-29
3.2.2 Moisture Equation Source Terms. . . . .	3-29
3.2.2.1 Terminal Velocity. . . . .	3-29
3.2.2.2 Saturation Vapor Pressure. . . . .	3-29
3.2.2.3 Water Production Term. . . . .	3-30
3.2.2.4 Density of Air Containing Water Vapor. . . . .	3-30
3.2.3 Test Problem. . . . .	3-31
3.3 Zoning Modifications in the HAIFA Code in Verti- cal Direction. . . . .	3-38
3.3.1 Variable Zoning in the Vertical Direc- tion. . . . .	3-38
3.3.1.1 The Poisson Solver . . . . .	3-38
3.3.1.2 Vertical Advection . . . . .	3-42
3.3.1.3 Test Calculations for Variable Vertical Zoning. . . . .	3-44

	<u>Page</u>
3.3.2 Numerical Checks of Crowley's Advection Scheme. . . . .	3-48
3.3.3 Triangular Zones in HAIFA . . . . .	3-52
3.4 Coriolis Terms in HAIFA. . . . .	3-59
3.4.1 Formulation . . . . .	3-59
3.4.2 Difference Equations. . . . .	3-63
3.4.3 Initial Conditions. . . . .	3-65
3.4.4 Test Problem. . . . .	3-67
3.5 Heuristic Numerical Model of Turbulence. . . . .	3-68
3.5.1 Formulation . . . . .	3-70
3.5.2 Numerics. . . . .	3-79
4. BASIC HAIFA WAVE DRAG CALCULATIONS. . . . .	4-1
4.1 Single Wave Problem. . . . .	4-1
4.2 Two Wave Problem . . . . .	4-14
4.2.1 Wave Drag Results . . . . .	4-17
4.3 Uniform Velocity . . . . .	4-21
4.4 Inversion Layer I. . . . .	4-30
4.5 Tropopause Problem . . . . .	4-36
4.6 Sierra Nevada Lee Wave Study . . . . .	4-36
5. LINEAR STEADY STATE CALCULATION OF WAVE DRAG. . . . .	5-1
5.1 A Derivation of Reynolds Stress for Linear-Steady State Formulations. . . . .	5-3
5.1.1 Linear Steady State Equations . . . . .	5-4
5.1.2 Boundary Condition. . . . .	5-7
5.2 LSS:A 3-D Steady State Wave Drag Calculation . . . . .	5-17
5.2.1 Atmospheric Response Function, $F(k,l)$ . . . . .	5-17
5.2.1.1 Choice of Vertical Velocity at Upper Boundary . . . . .	5-18
5.2.2 The Topography Spectrum Function Code . . . . .	5-22
5.2.2.1 The Equations. . . . .	5-22

	<u>Page</u>
5.2.2.2	Numerical Method . . . . . 5-22
5.2.2.3	Spectrum Function Calculations .5-27
5.2.3	Computer Code for Calculation of Reynold's Stress . . . . . 5-34
5.2.3.1	Reduction of Domain of Integra- tion . . . . . 5-34
5.2.3.2	The Equations. . . . . 5-36
5.2.3.3	Numerical Method . . . . . 5-36
5.2.4	Topography. . . . . 5-42
5.2.5	Test Calculations . . . . . 5-43
5.2.5.1	Comparison of Transient and Steady-State Wave Drag . . . . 5-43
5.2.6	Test Calculations to Parameterize the Wavedrag. . . . . 5-48
5.2.6.1	The Topography Spectrum Func- tion . . . . . 5-62
5.2.6.2	The Atmospheric Response Func- tion . . . . . 5-64
5.2.6.3	Parameterization of the Stress Integral . . . . . 5-73
5.2.6.4	Summary of Parameterization At- tempts . . . . . 5-87
5.3	DRAG - A Subroutine for a Two-Level Global Circulation Model. . . . . 5-87
5.3.1	Wave Drag Contribution to the Atmos- pheric Momentum Equations . . . . . 5-89
5.3.2	Summary of the Bretherton Model . . . . 5-91
5.3.2.1	Reduction to a Fourier Integral.5-91
5.3.2.2	Topography Function, $A(k,1)$ . 5-94
5.3.2.3	Atmospheric Response Function. 5-95
5.3.2.4	Effect of a Critical Level . . 5-102
5.3.3	The DRAG Subroutines. . . . . 5-103
5.3.4	Representative Calculations . . . . . 5-104

	<u>Page</u>
6. A THREE-DIMENSIONAL BOUSSINESQ CODE 'STUFF' . . . . .	.6-1
6.1 Derivation of Equations. . . . .	.6-2
6.1.1 The Numerical Scheme. . . . .	.6-11
6.1.2 Boundary Conditions . . . . .	.6-13
6.1.3 Initial Conditions. . . . .	.6-14
6.1.4 The Buffering Scheme. . . . .	.6-15
6.1.5 The Macro-Scale Calculation . . . . .	.6-17
6.1.6 Numerical Method. . . . .	.6-18
6.1.6.1 Initialization . . . . .	.6-27
6.1.6.2 The Grid . . . . .	.6-28
6.1.6.3 Procedure in Updating Particle Arrays Due to Source and Diffu- sion Terms . . . . .	.6-30
6.1.7 Sample Calculations . . . . .	.6-37
6.1.7.1 Treatment of Advection - Viscous Wave Calculations. . . . .	.6-41
 REFERENCES. . . . .	 .R-1
 APPENDIX A - DERIVATION OF BOUSSINESQ EQUATIONS . . . . .	 .A-1
 APPENDIX B - LISTING OF THE DRAG PROGRAM. . . . .	 .B-1

## LIST OF FIGURES

	<u>Page</u>
2.1 HAIFA Scheme Used in Numerical Integration of Eqs. (2.7), (2.8), and (2.10). . . . .	2-6
2.2 HAIFA Finite Difference Grid. . . . .	2-7
2.3 Schematic of HAIFA Boundary Conditions. . . . .	2-22
2.4 Flow Diagram of HAIFA Code. . . . .	2-25
3.1 Streamlines and Vertical Velocity Profiles for the Compressible Problem. (time = 1484 seconds). . .	3-10
3.2 Streamlines and Vertical Velocity Profiles for the BASIC HAIFA Problem. (time = 1565 seconds) . . .	3-11
3.3 Vertical Transport of Horizontal Momentum Above the Obstacle. . . . .	3-13
3.4 Momentum Flux as a Function of Vertical Height Centered Over the Obstacle. (time ~ 1000 sec). . .	3-14
3.5 Momentum Flux as a Function of Vertical Height Centered Over the Obstacle. (time ~ 1500 sec). . .	3-15
3.6 Momentum Flux as a Function of Vertical Height Centered Over the Obstacle. (time ~ 2000 sec). . .	3-16
3.7 Flowchart for Routine UPDATE. . . . .	3-25
3.8 HAIFA*MOISTURE Calculation Sequence Used in Numerical Integration of Eqs. (3.27) through (3.31) . . .	3-27
3.9 Finite Difference Grid - HAIFA*MOISTURE . . . . .	3-28
3.10 Streamline Pattern - Two Wave Problem with Moisture Effects . . . . .	3-32
3.11 Vertical Velocity Contours - Two Wave Problem with Moisture Effects. . . . .	3-33

	<u>Page</u>
3.12 Cloud Formation - Two Wave Problem with Moisture Effects . . . . .	.3-34
3.13 Rain Water Contours - Two Wave Problem with Moisture Effects. . . . .	.3-35
3.14 Computer Plots of Vertical Velocity Contours - Two Wave Problem with Moisture Effects. . . . .	.3-36
3.15 Computer Plot of Vertical Velocity Contours - Two Wave Problem. . . . .	.3-37
3.16 Comparison of Two Wave Problem with and without Moisture Momentum Transfer Above Obstacle . . . .	.3-39
3.17 Comparison of Variable $\Delta z$ and Constant $\Delta z$ HAIFA - Temperature Deviations. . . . .	.3-45
3.18a Comparison of Variable $\Delta z$ and Constant $\Delta z$ HAIFA - Vorticity . . . . .	.3-46
3.18b Comparison of Variable $\Delta z$ and Constant $\Delta z$ HAIFA - Vorticity . . . . .	.3-47
3.19 Comparison of Variable $\Delta z$ and Constant $\Delta z$ HAIFA Codes - Momentum Flux Edits at 781 Meters .	.3-49
3.20 Determination of Node-Centered Vorticity. . . . .	.3-57
3.21 Flow Logic for Subroutine TURB. . . . .	.3-80
4.1 Initial Temperature Profiles Used in Test Problems.	4-4
4.2 Single Wave Velocity Profile. . . . .	.4-5
4.3 Streamlines from Single Wave Problem. . . . .	.4-6
4.4 Streamlines from Single Wave Problem (page 2) . .	.4-7
4.5 Vertical Velocity Field from Single Wave Problem.	.4-8
4.6 Vertical Velocity Field from Single Wave Problem (page 2). . . . .	.4-9
4.7 Single Wave Problem Momentum Flux Edits . . . . .	.4-10
4.8 Single Wave Problem Momentum Flux Edits (page 2).	.4-11
4.9 Momentum Flux as a Function of Vertical Height. .	.4-13
4.10 Initial Velocity Profile - Two Wave Problem . . .	.4-15
4.11 Streamlines and Vertical Velocity Profiles for the Two-Wave Problem. (time = 4691 seconds). . . . .	.4-16
4.12 Two-Wave Problem - Vertical Transport of Horizontal Momentum Above the Obstacle . . . . .	.4-19

	<u>Page</u>
4.13 Momentum Flux as a Function of Height for Two-Wave Problem . . . . .	4-20
4.14 Streamlines from Uniform Velocity Problem . . . . .	4-22
4.15 Streamlines from Uniform Velocity Problem (page 2).	4-23
4.16 Vertical Velocity Field from Uniform Velocity Problem . . . . .	4-24
4.17 Vertical Velocity Field from Uniform Velocity Problem (page 2). . . . .	4-25
4.18 Computed Streamlines from Foldvik and Wurtele at Successive Times for Uniform Velocity Problem . . .	4-26
4.19 Computed Streamlines from Foldvik and Wurtele at Successive Times for Uniform Velocity Problem (page 2). . . . .	4-27
4.20 Field of Vertical Motion Computed Under Upwind Conditions for Successive Times from Uniform Velocity Problem. . . . .	4-28
4.21 Streamlines from the Linear Theory (after Lyra) . . .	4-29
4.22 Field of Vertical Velocity when $U = \text{Constant}$ with Height (after Lyra). Isopleths for $w > 0$ only. . .	4-29
4.23 Temperature Distribution used in Inversion Layer Problem . . . . .	4-31
4.24 Streamlines from Inversion Layer Problem. . . . .	4-32
4.25 Streamlines from Inversion Layer Problem (page 2) . . .	4-33
4.26 Vertical Velocity Field from Inversion Layer Problem . . . . .	4-34
4.27 Vertical Velocity Field from Inversion Layer Problem (page 2). . . . .	4-35
4.28 Streamlines from Tropopause Problem . . . . .	4-37
4.29 Streamlines from Tropopause Problem (page 2). . . . .	4-38
4.30 Vertical Velocity Field from Tropopause Problem . . .	4-39
4.31 Vertical Velocity Field from Tropopause Problem (page 2). . . . .	4-40
4.32 Meteorological Conditions for February 16, 1952, in the Owens Valley Area . . . . .	4-41
4.33 Observed Flow for February 16, 1952, Over Owen's Valley. . . . .	4-42

	<u>Page</u>
4.35 Sierra Nevada Cross-Section with HAIFA Approximation. . . . .	.4-44
4.34 Typical Cross-Section of Sierra Nevada at Owen's Valley. . . . .	.4-45
4.36a Velocity Profile, Set 1 . . . . .	.4-47
4.36b Moisture Profile, Set 1 . . . . .	.4-48
4.36c Temperature Profile, Set 1. . . . .	.4-49
4.37 Streamlines Set 1, Dry Run, Grid Base at Sea Level, t = 2000 sec. . . . .	.4-51
4.38 Streamlines Set 1, Wet Run, Grid Base at Sea Level, t = 2000 sec. . . . .	.4-51
4.39 Cloud Water Distribution, Set 1, Grid Base at Sea Level, Contours 1, 5, 10 ( $\times 10^4$ Kg/Kg), t = 2000 sec . . . . .	.4-53
4.40a Velocity Profile, Set 2 . . . . .	.4-54
4.40b Moisture Profile, Set 2 . . . . .	.4-55
4.40c Temperature Profile, Set 2. . . . .	.4-56
4.41 Streamlines Set 2, Dry Run, Grid Base at 1.5 km, t = 2000 sec. . . . .	.4-58
4.42 Streamlines Set 2, Wet Run, Grid Base at 1.5 km, t = 2000 sec. . . . .	.4-58
4.43 Cloud Water Distribution, Set 2, Grid Base at 1.5 km, Contours 1, 5, 10 ( $\times 10^4$ Kg/Kg), t = 2000 sec .4-60	.4-60
4.44 Horizontal Momentum Flux Dry Run of Set 2, Grid Base at 1.5 km. . . . .	.4-61
4.45 Horizontal Momentum Flux Wet Run of Set 2, Grid Base at 1.5 km. . . . .	.4-62
5.1 A Hypothetical Topographical Grid Extending 25'x 20'. The Numbers Represent Mean Values for the Cell. Grid Resolution is 5 Minutes . . . . .	.5-24
5.2 San Joaquin-Sierra Nevada Topography Contour Map Derived from 5' Resolution Data . . . . .	.5-29
5.3 Spectrum Function Distribution Using Topography Data from Figure 5.2. . . . .	.5-30
5.4 San Joaquin-Sierra Nevada Topography Contour Map Derived from 10' Resolution Data. . . . .	.5-31

	<u>Page</u>
5.5 Spectrum Function Distribution Using Topography Data from Figure 5.4. . . . .	.5-32
5.6 General Flow Diagram of Drag Code . . . . .	.5-37
5.7 Typical Dependence on Wavenumber of the Solution of the Scorer Equation at $z=0$ , $w_R(0)$ vs. $\kappa$ . . . . .	.5-40
5.8 Contour Map of the Sierra Nevada-Owen's Valley Region Showing Contours at 1 km Intervals. Data are Obtained from Defense Mapping Agency 5'x5' Topography Tables . . . . .	.5-45
5.9 2-D Cross-Sections of Sierra Topography from 120°W through 116°50'W Longitude. . . . .	.5-46
5.10 Vertical Flux of Horizontal Mementum from HAIFA Calculation, Compared with Steady-State Calcula- tions . . . . .	.5-47
5.11 Seasonally Averaged Zonal Mean Wind at 110°W 45°N from U.S. Department of Commerce Technical Paper 41. . . . .	.5-52
5.12 Seasonally Averaged Meridional Mean Wind for 110°W 45°N from U.S. Dept. of Commerce Technical Paper 41. . . . .	.5-53
5.13a Wind Speed Data from NCAR for March 12, 1973. . . . .	.5-54
5.13b Wind Direction Data from NCAR for March 12, 1973. . . . .	.5-55
5.14 The Zonal Wind Profile for West Virginia from the National Weather Service Tapes. . . . .	.5-56
5.15 The Meridional Wind Profile for West Virginia from the National Weather Service Tapes. . . . .	.5-57
5.16 The Temperature Profile for the West Virginia Data Taken from the National Weather Service Tapes . . . . .	.5-58
5.17 The Pressure Profile for West Virginia from the National Weather Service Tapes. . . . .	.5-60
5.18 Location of Critical Levels for the Sample Atmos- phere . . . . .	.5-67
5.19 The Real and Imaginary Parts of the Ground Level Wave Amplitude for $\phi = 0$ . . . . .	.5-68
5.20 Wavenumber Dependence of the Atmospheric Response Function for Fixed Angles of the Wavevector . . . . .	.5-69
5.21 Wavenumber Dependence of the Atmospheric Response Function for Fixed Angles of the Wavevector . . . . .	.5-70

	<u>Page</u>
5.22 Wavenumber Dependence of the Atmospheric Response Function for Fixed Angles of the Wavevector . . . . .	.5-71
5.23 Wavenumber Dependence of the Atmospheric Response Function for Fixed Angles of the Wavevector . . . . .	.5-72
5.24 The Topography Grids Containing the Mountainous Terrain Around the World. . . . .	.5-75
5.25 The Wavedrag as a Function of the Topography Grid for Atmosphere 1. . . . .	.5-77
5.26 Schematic Diagram of Mountain Wave Configuration.	.5-90
5.27 Coordinate System in the 2-Level General Circula- tion Model. . . . .	.5-92
6.1 General Flow Diagram for STUFF. . . . .	.6-20
6.2 Cross-Section of STUFF3 Grid with Interior and Boundary Obstacle Cells . . . . .	.6-29
6.3 The Distribution of Particles within a Given Cell	.6-31
6.4 Notation Utilized by STUFF. . . . .	.6-32
6.5 A Cross-Section of Eulerian Cells Containing a Particle "Cube" . . . . .	.6-35
6.6 Lateral Velocities for Lowest Horizontal Layer of Cells . . . . .	.6-38
6.7 Lateral Velocities in a Vertical Slice Taken through the Obstacle Centerline . . . . .	.6-39
6.8 Axial Velocities in a Vertical Slice Taken through the Obstacle Centerline . . . . .	.6-40
6.9 Initial Conditions for Laminar Internal Wave Test Problem . . . . .	.6-42
6.10 Evolution of the Density Field with Time. . . . .	.6-44
6.11 Vertical Distribution of Density at $t=25$ , $x=0$ for Internal Wave Problem . . . . .	.6-46
6.12 Internal Wave Problem - Height vs Time of Interface at $x=0$ . . . . .	.6-47

## LIST OF TABLES

	<u>Page</u>
3.1 Test Advection Schemes - Crowley Second-Order . . .	.3-51
4.1 Summary of Initial Conditions Used for Each Problem . . . . .	.4-2
4.2 Two Wave Problem. . . . .	.4-14
4.3 HAIFA Input Profiles for Set 1. . . . .	.4-50
4.4 HAIFA Input Profiles for Set 2. . . . .	.4-57
5.1 Topographies Investigated . . . . .	.5-62
5.2 Atmospheres Studied . . . . .	.5-63
5.3 The Results of the Stress Parameterization. . . . .	.5-78
5.4 The Magnitude of $U_n^2 F$ for the Wavevectors which Dominate the Stress <sup>n</sup> Integral . . . . .	.5-82
5.5 Analysis of Treating $U_n^2 F$ to be a Constant Value . . . . .	.5-85
5.6 Vertical Distribution of the Momentum Flux. . . . .	.5-98
5.7 Temperature Dependence on Pressure for the Test Problems. . . . .	.5-104
5.8 Calculated Wavedrag for Four Wind Conditions Over the Sierra Nevada and Himalayan Mountains Using the DRAG Subroutines. . . . .	.5-105

## ABSTRACT

This report summarizes the three-year research program at Systems, Science and Software to investigate the effects of meso-scale and small-scale interactions on global climate. The research concentrated on two areas, orographic effects on the wind patterns and effects of radiation transport on the climate. Volume I describes the orographic research and includes the theory of momentum transport due to mountain ranges, the formulation of several computer codes to calculate the effects for realistic topography and wind profiles, and the application of these codes to various problems and comparison with other calculations as well as experimental results.

Volume II describes the radiation transport research which produced a benchmark code against which more simplified models can be compared. This code, ATRAD, is characterized by high angular and frequency resolution and by the ability to calculate radiative atmospheric heating rates taking into account molecular absorption and scattering from arbitrary distributions of aerosols and particulates.

## 1. INTRODUCTION

The numerical prediction of the general circulation of the atmosphere predates most of the other applications of high speed computers to physical problems. The codes which exist at several major research centers have reached levels of considerable sophistication. These codes are used to solve time-dependent equations describing atmospheric motion in a three-dimensional representation. Parametric descriptions are included to take into account the effects of insolation, turbulent transport, and moisture.

There are two aspects of current computational capabilities, however, which have been treated rather crudely in the past, and which have been the subject of the present research program at Systems, Science and Software (S<sup>3</sup>): orographic effects and effects of radiative transfer on the climatology. Orographic (mountainous) effects are mesoscale phenomena, i.e., occurring on a distance scale of a few kilometers which is smaller than the typical grid size in the Global Circulation Models (GCM). Qualitatively, the effect of mountains is to transport horizontal momentum to high altitudes over the mountains and long distances down wind. This perturbation in the flow field can cause moisture to be advected to high altitudes and cloud formation is common. The clouds and moisture, on the other hand, can alter the climatic conditions over areas large compared to the mountainous source.

For the application to short period forecasts, covering the time interval shorter than a few days, the details of the atmospheric heating by solar insolation are probably not

necessary. Over longer periods of time, however, the processes which transform the solar energy into motion of the atmosphere are much more important, and more accurate models are necessary.

The research effort described in this report has led to the development of computer codes capable of calculating the orographic effects and radiative effects in considerable detail. S<sup>3</sup> has used its extensive hydrodynamics and radiation modeling capabilities to produce codes that include descriptions of most of the physical processes which are relevant. Through test calculations the accuracy of various physical and mathematical approximations was determined, allowing simplification in the models. Finally, parameterized models have been developed for the RAND Mintz-Arakawa two-level Global Circulation Model (GCM) which provide increased accuracy in the momentum transport and radiative heating calculations at a nominal increase in computation time.

The present report is a comprehensive summary of nearly four years of research. The editors have attempted to discard the many blind alleys encountered and reported in the various semi-annual reports, and to condense the material as much as possible, but the sheer volume of useful results has required publication in two volumes. Volume I describes the work on orographic modeling, and the radiation transport work is described in Volume II.

## 1.1 OROGRAPHIC EFFECTS ON GLOBAL CLIMATE

Phenomena taking place on a scale smaller than the resolution of global circulation codes can cause changes in climate. The tropospheric transport coefficients that are required in the global atmospheric model may arise from atmospheric motions that occur in quite small regions (e.g., mountain lee waves). Transport is also effected by convective eddies such as cumulus and cumulo-nimbus convective cells. These may be influenced by small geographic features such as islands and by upper atmospheric phenomena such as jet streams and waves.

The simplest method of accounting for meso-scale phenomena is to calculate parameters (such as eddy diffusivities) according to some fit of experimental data, risking large inaccuracies due to incomplete and inappropriate data. A technique which can give more accuracy is to compute these parameters by means of several meso-scale calculations performed separately, or concurrently with the large scale calculation. This permits a more complete description of relevant physical processes to be built into the global model.

Models having various degrees of sophistication have been developed under the present program. The basic code is a two-dimensional time-dependent code which makes use of the Boussinesq approximation. This code is described in Section 2. Several test calculations have been completed which show the transient effects on the air flow over mountain ranges under various atmospheric conditions. These results are presented in Section 4.

Modifications to the code, reported in Section 3, include full compressibility and moisture effects. Test calculations which evaluate the importance of these modifications are also presented. Modifications of the zoning capabilities are also discussed.

A full time-dependent calculation of the wind wave phenomena is, of course, too time consuming and unnecessarily sophisticated for a large scale GCM calculation. A three-dimensional Linear Steady-State (LSS) code was, therefore, developed to provide the correct time-average of the wave momentum transport. This code is described in Section 5. This model was further simplified for the Mintz-Arakawa two-level code in the subroutine DRAG which is described in Section 5.3.

A final code, STUFF3, was developed during this research, and is described in Section 6. This is a fully three-dimensional Boussinesq code, including effects of turbulent diffusion. The numerical treatment includes a mixed mode, Eulerian-Lagrangian grid specification which is a distinct improvement over other codes of its type.

## NOMENCLATURE FOR SECTIONS 2 AND 3

- $\alpha = \frac{u\Delta t}{\Delta x}$  = numerical stability parameter  
 $C_p$  = specific heat at constant pressure  
 $D$  = drag force on the obstacle  
 $\frac{d}{dt} = \frac{\partial}{\partial t} + \vec{V} \cdot \nabla$  = total derivative  
 $\eta =$  fluid vorticity =  $\frac{\partial u}{\partial z} - \frac{\partial v}{\partial x}$   
 $F$  = advective flux across a boundary  
 $g$  = acceleration of gravity  
 $\Gamma =$  dry adiabatic lapse rate =  $g/C_p$   
 $h$  = enthalpy  
 $I$  = maximum value of the grid index  $i$   
 $J$  = maximum value of the grid index  $j$   
 $i, j$  = numerical grid indices  
 $k_t$  = temperature diffusion constant  
 $k_v$  = viscous diffusion constant  
 $L$  = latent heat of vaporization for water  
 $l_c$  = cloud water content  
 $l_r$  = rain water content  
 $P_r$  = water production terms  
 $p$  = pressure  
 $\phi =$  compressibility stream function defined in Eq. (3.6)  
 $\psi =$  stream function

- Q = total water content  
 q = water contained as cloud moisture and vapor  
 R = gas constant for air  
 r = relative humidity  
 $\rho$  = density  
 S = static stability  
 s = entropy  
 T = temperature  
 t = time  
 $V_t$  = terminal velocity of water droplet in atmosphere  
 $\vec{V}$  =  $i_u + k_w$  = total velocity  
 u = total horizontal velocity  
 w = vertical velocity  
 x = horizontal Cartesian coordinate  
 z = vertical Cartesian coordinate  
 $\zeta$  = compressibility vorticity function  
 $= \frac{\partial}{\partial z}(\rho u) - \frac{\partial}{\partial x}(\rho w)$

## SUBSCRIPTS

- D = diameter of water droplet  
 i, j = numerical grid indices  
 o = initial spatial distribution (sometimes used to indicate a ground level value)

## 2. THE BASIC HAIFA CODE

HAIFA (Hydrodynamics in an Almost Incompressible Flow Approximation) is a two-dimensional Eulerian time-dependent Boussinesq hydrodynamic code including effects of inertia and buoyancy. Modifications were made to BASIC HAIFA to include effects of compressibility and moisture.

### 2.1 THE BASIC HAIFA EQUATIONS

The numerical investigation of mountain waves requires that the effects of inertia and buoyancy be taken into account. The two-dimensional time-dependent Boussinesq equations, developed herein, include these effects in the HAIFA computer code. The buoyancy effects are due to adiabatic changes of temperature induced by perturbations of an initially thermally stratified atmosphere. Deviations from constancy of the density in other terms of the fluid equations, including the continuity equation, are neglected, giving a set of equations which are basically valid for an incompressible fluid. The use of the Boussinesq equations for the investigation of mountain waves, therefore, is appropriate in that the effects of buoyant stability are restricted by the incompressibility approximation. These equations, as used in HAIFA, are the vorticity equation derived from the two-dimensional equations of motion, the

energy equation, and the continuity equation for an incompressible fluid. An outline of the derivation of these equations follows. (The symbols used in the equations are defined in the Nomenclature list.)

In the Boussinesq approximation, the momentum equations in the horizontal (x) and the vertical (z) directions are:

$$\frac{du}{dt} = - \frac{1}{\rho_0} \frac{\partial p}{\partial x} + \nabla \cdot (k_v \nabla u) \quad , \quad (2.1)$$

$$\frac{dw}{dt} = - \frac{1}{\rho_0} \frac{\partial p}{\partial z} - \frac{\rho}{\rho_0} g + \nabla \cdot (k_v \nabla w) \quad . \quad (2.2)$$

For the present, we have neglected the Coriolis terms in this set of equations.

The incompressible continuity equation in two dimensions is

$$\frac{\partial u}{\partial x} + \frac{\partial w}{\partial z} = 0 \quad . \quad (2.3)$$

The vorticity equation used in the HAIFA code is derived using Eqs. (2.1), (2.2), and (2.3). Eq. (2.1) is differentiated with respect to z and Eq. (2.3) with respect to x. Consistent with the Boussinesq approximation, the variation of  $\rho_0$  with height is assumed negligible. Subtracting one from the other removes the pressure terms. If one also treats the diffusion coefficient  $k_v$  as a constant, the resulting expression is:

$$\frac{d}{dt}(\eta) = + \frac{g}{\rho_0} \frac{\partial \rho}{\partial x} + k_v \nabla^2(\eta) \quad , \quad (2.4)$$

where  $\eta$  is defined as the vorticity component perpendicular to the x-z plane. Mathematically,

$$\eta = \frac{\partial u}{\partial z} - \frac{\partial w}{\partial x} .$$

It is further possible to modify Eq. (2.4) consistent with the Boussinesq approximations. The variables  $\rho$ ,  $T$  and  $p$  may be written as functions of their static values plus a perturbation contribution as follows:

$$\begin{aligned} \rho(x,z,t) &= \rho_0(z) + \rho'(x,z,t) , \\ T(x,z,t) &= T_0(z) + T'(x,z,t) , \\ p(x,z,t) &= p_0(z) + p'(x,z,t) . \end{aligned} \tag{2.5}$$

The buoyancy term

$$\frac{1}{\rho_0} \frac{\partial \rho}{\partial x}$$

can then be written as

$$\frac{1}{\rho_0} \frac{\partial \rho'}{\partial x} .$$

However, for the Boussinesq approximation to be valid, the density variation  $\rho'$  must depend mainly on temperature, i.e., the variation of density due to the dynamical pressure is assumed negligible (see Appendix A). Therefore,

$$\rho' = \left( \frac{\partial \rho}{\partial T} \right)_p T' = - \frac{\rho_0}{T_0} T' \quad (2.6)$$

Substituting Eq. (2.6) into Eq. (2.4) and using Eq. (2.3) to allow the result to be written in conservative form, the vorticity equation is

$$\frac{\partial}{\partial t}(\eta) + \frac{\partial}{\partial x}(u\eta) + \frac{\partial}{\partial z}(w\eta) = - \frac{g}{T_0} \frac{\partial T'}{\partial x} + k_v \nabla^2 \eta \quad (2.7)$$

Eq. (2.7) is the first of three equations to be solved in the HAIFA code. The second equation results from the continuity equation and the definition of vorticity. Defining a stream function  $\psi$  such that  $u = \partial\psi/\partial z$  and  $w = -\partial\psi/\partial x$ , the continuity equation is automatically satisfied. Further, the stream function is related to the vorticity through a Poisson equation of the form

$$\nabla^2 \psi = \eta \quad (2.8)$$

The final equation necessary to complete the description of mountain waves is the energy equation. This equation expresses the first law of thermodynamics

$$\frac{dh}{dt} = + \frac{1}{\rho} \frac{dp}{dt} + k_t \nabla^2 h$$

for an adiabatic system. For a perfect gas with constant specific heat and using the hydrostatic approximation in the  $dp/dt$  term, this equation may be expressed by

$$\frac{dT}{dt} = - \frac{1}{C_p} wg + k_t \nabla^2 T \quad (2.9)$$

Defining  $T'' = T + \Gamma z$  and substituting Eq. (2.5) into Eq. (2.9), the resulting energy equation is

$$\frac{dT''}{dt} = k_T \nabla^2 (T'' - \Gamma z) \quad (2.10)$$

Eqs. (2.7), (2.8) and (2.10) constitute the fluid flow equations integrated in the HAIFA code.

## 2.2 NUMERICAL APPROXIMATION OF HAIFA EQUATIONS

Eqs. (2.7), (2.8) and (2.10) are written in finite difference form and integrated numerically. The integration is accomplished by updating the equations in time for each variable based on the values at the previous time step or an intermediate time located between two successive time steps. Each of these steps will be discussed in turn in this report. These descriptions include the definition of the grid used and the location of each variable listed in the equations, the evaluation of the advection terms in the vorticity and energy equations, the solution for the stream function from the Poisson eq. (2.8), and a discussion of the boundary conditions used in the numerical integration.

### 2.2.1 Finite Difference Scheme

The basic scheme used to numerically integrate the HAIFA equations is shown in Figure 2.1. The finite difference grid used in HAIFA is shown in Figure 2.2. The locations of the major variables with respect to the grid cells are defined in the figure.

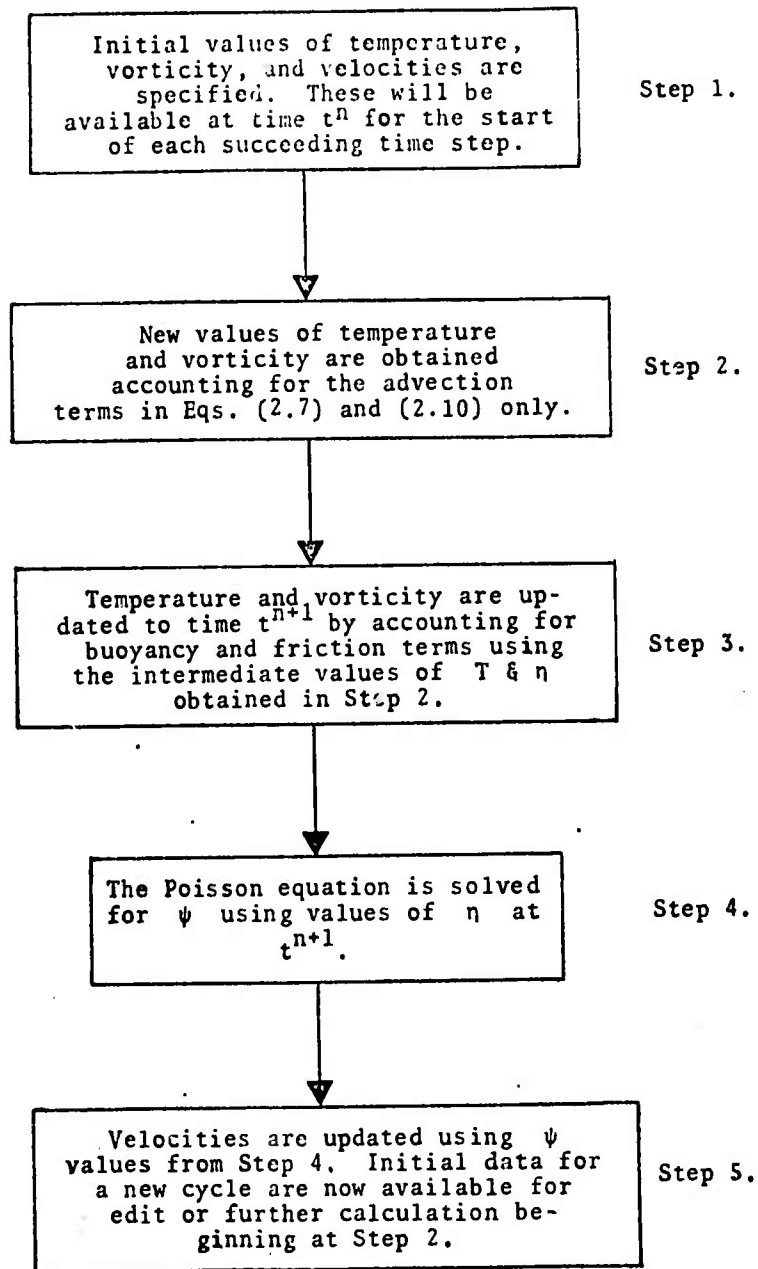


Figure 2.1 - HAIFA Scheme Used in Numerical Integration of Eqs. (2.7), (2.8), and (2.10).

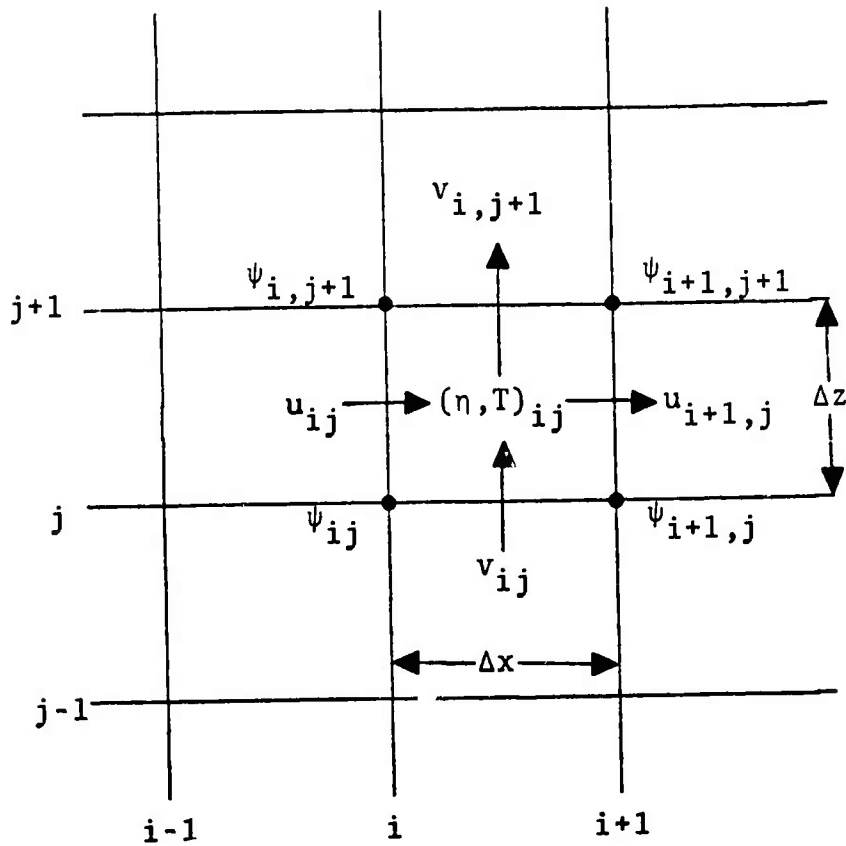


Figure 2.2 - HAIFA Finite Difference Grid.

The stream functions are located at the grid points, the vorticities and temperatures are cell centered and velocities are centered on a grid line located between stream line values. In this way, the velocities defined in finite difference form are:

$$u_{ij} \equiv \frac{\partial \psi}{\partial z} = \frac{\psi_{i,j+1} - \psi_{ij}}{\Delta z} \quad (2.11)$$

$$v_{ij} \equiv - \frac{\partial \psi}{\partial x} = - \frac{\psi_{i+1,j} - \psi_{ij}}{\Delta x} \quad (2.12)$$

### 2.2.2 The Advection Scheme

The advection of temperature and vorticity in HAIFA is calculated using either the second or fourth order scheme of Crowley.<sup>(1)</sup> The selection of the second or fourth order scheme is optional and is determined by the trade-off between accuracy and computing time. The schemes chosen are written in conservation form and are based on forward time differences and centered space differences. Test calculations performed by Crowley indicated that for the same order of accuracy, the conservation form produced more accurate solutions than the advection form.

In the conservation form, the time derivative and advection terms of the vorticity or temperature equation may be written as

$$\frac{\partial \phi}{\partial t} + \frac{\partial (u\phi)}{\partial x} + \frac{\partial (v\phi)}{\partial z} = S \quad , \quad (2.13)$$

where  $\phi$  is either  $T$  or  $\eta$  and  $S$  is the source term.

In two dimensions a splitting technique is used; the calculational scheme calls for solving a one-dimensional equation twice, i.e., the net flux of vorticity or temperature is solved for in the horizontal, the quantity solved for in the zone being updated due to this flux and the procedure is then repeated in the vertical direction using the partially updated values. The equation for the flux across the boundary  $j$  written in finite difference form (second order accurate) is

$$F_j = \frac{\Delta x}{\Delta t} \left[ \frac{\alpha_j}{2} (\phi_j + \phi_{j-1}) - \frac{\alpha_j^2}{2} (\phi_j - \phi_{j-1}) \right] \quad (2.14)$$

where  $\alpha_j = u_j \Delta t / \Delta x$  .

The net change in the variable  $\phi$  in the cell  $ij$  due to advection in the horizontal is then

$$\phi^{n+1} - \phi^n = \frac{\Delta t}{\Delta x}(F_j - F_{j+1}) \quad (2.15)$$

The corresponding fourth order scheme for the flux across the boundary  $j$  is

$$\begin{aligned} F_j = \frac{\Delta x}{\Delta t} & \left\{ \frac{\alpha_j}{16} [9(\phi_j + \phi_{j-1}) - (\phi_{j+1} + \phi_{j-2})] \right. \\ & - \frac{\alpha_j^2}{48} [37(\phi_j - \phi_{j-1}) - (\phi_{j+1} - \phi_{j-2})] \\ & - \frac{\alpha_j^3}{12} [(\phi_j + \phi_{j-1}) - (\phi_{j+1} - \phi_{j-2})] \\ & \left. + \frac{\alpha_j^4}{24} [3(\phi_j - \phi_{j-1}) - (\phi_{j+1} - \phi_{j-2})] \right\} \quad (2.16) \end{aligned}$$

The numerical stability of these equations is discussed in Section 2.3 of this report. The accuracy, as discussed by Crowley, is found by expanding the quantities in Taylor series, both in time and in space. The result gives the solution of the variable  $\phi$  at the new time accurate to order  $\Delta t^2$  in time. The time derivative of the finite difference form of the differential equation is thus accurate to order  $\Delta t^3$  in time. The second order scheme, Eq. (2.14), has a truncation of order  $\Delta x^3$  and the fourth order scheme, Eq. (2.16), is accurate to  $\Delta x^5$  in space.

### 2.2.3 Update of Other Terms in the Vorticity and Energy Equations

The vorticity equation has two additional terms besides the advective terms. In general, central differences are used in the numerical scheme. The buoyancy term

$$- \frac{g}{T_0} \frac{\partial T'}{\partial x}$$

is expressed as

$$- \frac{g}{T_{0j}} \frac{T_{i+1,j} - T_{i-1,j}}{2\Delta x} \quad (2.17)$$

The diffusion term  $k_v \nabla^2 \eta$  is expressed as

$$k_v \left\{ (n_{i,j+1} - 2n_{ij} + n_{i,j-1}) \left( \frac{\Delta}{\Delta y^2} \right) + (n_{i+1,j} - 2n_{ij} + n_{i-1,j}) \left( \frac{\Delta t}{\Delta x^2} \right) \right\} \quad (2.18)$$

#### 2.2.4 Solution of the Poisson Difference Equation by Finite Fourier Transform

The solution of the Poisson equation by means of Fourier transform results in a direct (or exact) solution of the difference equations and their boundary values. In the current version of the subroutine there are some limitations on the generality of the solution: the spatial interval  $\Delta x$  must be constant (see Section 3.3 for variable  $\Delta z$ ). The solution must be periodic in the x-direction and prescribed values of the stream function are to be maintained on the top and bottom boundaries of the rectangular region. How the boundary is modified from the rectangular shape is discussed in the following section.

A second order finite difference approximation to the Poisson equation  $\nabla^2 \psi = \eta$  is obtained by replacing the second derivative operator by a centered second difference operator.

$$\frac{\delta_x^2 \psi_{ij}}{(\Delta x)^2} + \frac{\delta_z^2 \psi_{ij}}{(\Delta z)^2} = \eta_{ij} \quad \begin{array}{l} i = 1, 2, \dots, I \\ j = 2, \dots, J-1 \end{array} \quad (2.19)$$

where

$$\delta_x^2 \psi_{ij} = \psi_{i+1,j} - 2\psi_{ij} + \psi_{i-1,j}$$

and

$$\delta_z^2 \psi_{ij} = \psi_{i,j+1} - 2\psi_{ij} + \psi_{i,j-1}$$

Boundary conditions are imposed as follows:

At the bottom of the mesh,

$$\psi_{i,1} = \alpha_i \quad , \quad i = 1, \dots, I .$$

At the top of the mesh,

$$\psi_{i,J} = \beta_i \quad , \quad i = 1, 2, \dots, I .$$

The cyclic boundary conditions in the horizontal are,

$$\psi_{0,j} = \psi_{I,j} \quad \text{and} \quad \psi_{1,j} = \psi_{I+1,j} \quad , \quad j = 2, \dots, J-1 .$$

We introduce an orthonormal base set of functions having cyclic properties on the index  $i$ :

$$w_{ik} = \sqrt{2/I} \cos \frac{2\pi ki}{I} \quad , \quad I \text{ is even}$$

$$w_{i,I-k} = \sqrt{2/I} \sin \frac{2\pi ki}{I} \quad , \quad i = 1, 2, \dots, I .$$

$$w_{i,I} = 1/\sqrt{I} \quad ,$$

$$k = 1, 2, \dots, \frac{I}{2} - 1 .$$

$$w_{i,I/2} = 1/\sqrt{I} \cos i \quad ,$$

These are the finite Fourier functions which have the properties,

$$\sum_{i=1}^I w_{ik} w_{il} = \delta_{kl}$$

and the analogous cyclic boundary conditions are valid in the horizontal. They also have the property that they are eigenfunctions of the central second difference operator

$$\delta_x^2 w_{ik} = -\lambda_k^2 w_{ik}$$

where  $\lambda_k = 2 \sin \pi k/I$ . These functions are complete functions on the interval  $i = 1, 2, \dots, I$ . Consequently, an arbitrary function  $f_i$  on this space can be represented

$$f_i = \sum_{k=1}^I a_k w_{ik}$$

where

$$a_k = \sum_{i=1}^I f_i w_{ik} .$$

We are now ready to consider Eq. (2.19) from the point of view of Fourier transformation. The vorticity and stream function are represented as Fourier series as follows:

$$\eta_{ij} = \sum_{k=1}^I b_{kj} w_{ik} , \quad \text{where } b_{kj} = \sum_{i=1}^I \eta_{ij} w_{ik} ,$$

and

$$\psi_{ij} = \sum_{k=1}^I a_{kj} w_{ik} , \quad \text{where } a_{kj} = \sum_{i=1}^I \psi_{ij} w_{ik} .$$

(2.20)

Substituting into Eq. (2.19) we obtain

$$\sum_{k=1}^I w_{ik} \left[ \left( -\frac{\lambda_k^2}{(\Delta x)^2} + \frac{\delta_z^2}{(\Delta z)^2} \right) a_{ik} - b_{jk} \right] = 0 \quad .$$

Multiplying by  $w_{i\ell}$  and summing over  $i$  gives

$$\left( -\frac{\lambda_\ell^2}{(\Delta x)^2} + \frac{\delta_z^2}{(\Delta z)^2} \right) a_{j\ell} = b_{j\ell} \quad , \quad \begin{array}{l} j = 2, \dots, J-1, \\ i = 1, 2, \dots, I. \end{array} \quad (2.21)$$

The values of  $a_{1,\ell}$  and  $a_{J,\ell}$  required by Eq. (2.21) are obtained from the boundary values

$$\begin{aligned} a_{1,\ell} &= \sum_{i=1}^I \alpha_i w_{i\ell} \quad \text{and} \\ a_{J,\ell} &= \sum_{i=1}^I \beta_i w_{i\ell} \quad . \end{aligned} \quad (2.22)$$

In Eq. (2.21) the value of the wave number,  $\ell$ , appears only parametrically. For each value of  $\ell$  there is a tri-diagonal equation having fixed values at the end points of the  $j$ -interval.

We summarize the procedure for obtaining the direct solution of the Poisson equation, Eq. (2.19), by Fourier transform:

(1) The vorticity and the top and bottom boundary values of the stream function are subjected to Fourier transformation to obtain

$$b_{j\ell} = \sum_{i=1}^I \eta_{ij} w_{i\ell} ,$$

$$a_{1,\ell} = \sum_{i=1}^I \alpha_i w_{i\ell} , \text{ and}$$

$$a_{J,\ell} = \sum_{i=1}^I \beta_i w_{i\ell}$$

(2) The Fourier components of the stream function are obtained by solving the tridiagonal system of equations, Eq. (2.21), for  $a_{j\ell}$ .

(3) The stream function itself is obtained by Fourier synthesis

$$\psi_{ij} = \sum_{\ell=1}^I a_{j\ell} w_{i\ell} .$$

The quantity  $I$  must be even. In order to take maximum advantage of the efficiency of the Fast Fourier Transform, the quantity  $I$  should also be a power of 2.

### 2.2.5 The FFT Solution of the Poisson Equation Having Non-Rectangular Boundaries

In order to represent a mountain within the computational grid it is necessary to depart from rectangular boundaries. A modification of the solution algorithm using the FFT is necessary to take account of the specified values of  $\psi$  on the mountain contour. The procedure for carrying out this modification of the direct solution of Poisson's equation on an irregular region has been described by Buzbee, et.al.<sup>(2)</sup>

We consider the case in which there are  $p$  internal grid points on which the potential is to be specified. These points constitute the adjacent mesh points lying along the boundary of the mountain which will be assigned the same value of potential (usually zero) as the lower boundary. The first step is to precalculate the stream function contribution at each of the  $p$  points of unit vorticity located at each of the points. The solution is then obtained by solving Poisson's equation twice for each cycle. First, Poisson's equation is solved with arbitrary vorticity on the boundary points. The difference between the obtained and desired values of the stream function at each of the  $p$  points is used to obtain the corresponding vorticity increments through application of the precalculated matrix. A second solution of Poisson's equation using the incremented vorticity field gives the final value of the stream function within the calculational region.

### 2.2.6 Description of Poisson Solver Routines

This section describes the subroutines currently used in the HAIFA code to solve the Poisson equation in x-z geometry. The method of solution employs a Fourier transform in the x-direction, solving the resultant set of one-dimensional difference equations (one for each wave number) by Gaussian

elimination in the z-direction and performing the inverse x-direction Fourier transform to obtain the solution. The Cooley-Tukey Fast Fourier Transform (FFT) technique<sup>(3)</sup> is employed (subroutine COOTUK) with some pre- and post-processing of the data for efficient utilization of the algorithm. In the current version the dependent variable (the stream function  $\psi$  in the HAIFA context) is assumed to have cyclic boundary conditions in the x-direction and fixed values at the top and bottom of the grid.

At the beginning of each new calculation, there are references to subroutines which are used only once in each problem. These are called SETUP and OBSET.

SETUP -- This entry references an internal subroutine SET, whose function is to define certain index parameters and required data arrays that are used throughout the calculation by the Poisson solver.

OBSET -- This subroutine is called only when internal boundary conditions are to be applied. Suppose there are  $p$  internal points required to have stream function values  $\psi_1^0, \psi_2^0, \dots, \psi_p^0$ . This subroutine computes a  $p \times p$  matrix  $C$  which has the following property:

a unit vorticity is placed in the position of internal boundary point  $j$ . The value of the independent variable (vorticity) is assumed to be zero at every other point. The Poisson equation solver XYPOIS (see discussion below) is called and returns the influence of that particular unit vorticity on all the other internal boundary points. These influences are put into row  $j$  of matrix  $C$ .

This procedure is continued until all  $p$  internal boundary influences have been computed. Finally, subroutine OBSET forms and stores the inverse matrix  $C^{-1}$ .

The controlling subroutine for the Poisson equation solution is named LAPLAC (for the Laplacian symbol  $\nabla^2$ ). This routine is responsible for the solution to both standard boundary condition cases and problems which include internal boundaries.

Each cycle, subroutine LAPLAC averages the cell-centered HAIFA vorticities to provide node-centered vorticities. Then the Poisson equation solver XYPOIS is called to provide the updated values of the stream function. In the case of internal boundaries, one more step is performed in subroutine LAPLAC. Upon the first return from solving the Poisson equation, each internal boundary has a value  $\psi_i^*$ ,  $i=1, \dots, p$  which in general is not the required value  $\psi_i^0$ . A vector  $\Delta\psi$  of the differences  $\psi_i^0 - \psi_i^*$  is formed. Then, using the inverse matrix  $C^{-1}$  formed in subroutine OBSET, one may compute the required modifications  $\Delta q_i$  to the values of the independent variable at each of the  $p$  internal boundary points from

$$C^{-1} \begin{pmatrix} \Delta\psi_1 \\ \vdots \\ \Delta\psi_p \end{pmatrix} = \begin{pmatrix} \Delta q_1 \\ \vdots \\ \Delta q_p \end{pmatrix}$$

The independent variable is so modified, and the XYPOIS package is called once again. The solution returned now contains the correct values for the internal boundary points as well as the other grid points. It remains to discuss the subroutine XYPOIS.

XYPOIS -- This entry is used every calculational cycle to carry out the solution of Poisson's equation. It contains as an argument the values of the inhomogeneous term (here, vorticity) in the interior (nodal) points of the grid, and the fixed values of the dependent variable (here, the stream function) at the top and bottom of the grid. XYPOIS references four internal subroutines:

(1) FFANL (fast Fourier analyzer), which is responsible for carrying out the x-direction transform of vorticity into Fourier components. It processes two rows at a time, so an uncoupling of the row components is required upon return from the FFT routine COOTUK;

(2) GAUSS, which is responsible for solving the resulting z-direction tridiagonal equations for the transform of the dependent variable (see Section 3.3.1.1);

(3) FFSYN (fast Fourier synthesizer), which is the inverse of FFANL, is responsible for restoring the Fourier components to the new values of the independent variable by another call to subroutine COOTUK. These values, representing the solution to the Poisson equation, are returned to the calling routine (subroutine LAPLAC) in the array containing the original argument list; and

(4) COOTUK, which carries out the Cooley-Tukey fast Fourier transform.

### 2.3 STABILITY ANALYSIS

A numerical stability analysis of the advection terms in the vorticity and temperature equations has been completed by other researchers. Among them, Crowley<sup>(1,4)</sup> did a complete analysis for the scheme presently being used in the HAIFA code. The results obtained by Crowley indicate that both his

second and fourth order scheme are stable for all wave numbers if

$$\left| \frac{u\Delta t}{\Delta x} \right| < 1 .$$

Further, the fourth order conservation scheme being used in HAIFA is stable for  $(u\Delta t/\Delta x) < 1.5$ .

As indicated by Crowley, the schemes both result in amplitude damping and phase lag. For long wavelength disturbances the damping and phase errors are appreciably smaller for the fourth order scheme than for the second order. Comparison tests with a typical mountain wave problem indicated, however, that the differences between fourth and second order solutions are not large. Most of our calculations have been performed with the second order scheme. The criterion built into the HAIFA code is more stringent than any of those noted above, i.e.,

$$\left| \frac{u\Delta t}{\Delta x} \right| < 0.8 .$$

A stability criterion also has been established for the diffusion terms, however, in all problems calculated for this research, the diffusion coefficients are set to zero and thus these terms play no part in the solution.

One unstable region was found using the above criteria in computing the uniform velocity problem discussed in Section 4.3. The details of the instability and the new criteria developed for that problem are also given in that section.

## 2.4 BOUNDARY CONDITIONS

The initial value problem solved using the HAIFA code requires initial temperature, vorticity and stream function distributions. This is accomplished by prescribing a value of the stream function which is constant in the horizontal direction and which gives the desired horizontal velocity distribution as a function of the vertical coordinate. The vertical velocity component is set to zero. The vorticity at each point in the grid is calculated analytically using the definition

$$\eta = \frac{\partial u}{\partial z}, \text{ since } \frac{\partial v}{\partial x} \text{ is everywhere zero.}$$

The temperature distribution is specified as being horizontally stratified with a lapse rate which may vary with altitude. It is also possible to simulate inversions.

At the beginning of the calculation, with the flow already established, an obstacle is placed in the stream by setting the lower surface streamline to coincide with the mountain surface. A rigid lid (constant streamline) is imposed on the upper boundary of the problem. Figure 2.3 indicates these boundary conditions in graphical form.

The boundary condition imposed at the sides of the grid assumes the flow to be cyclic, i.e., the stream function at each vertical grid line  $j$  on the left side of the grid is set equal to the corresponding stream function at the right side of the grid. Mathematically, this can be expressed as  $\psi_{1j} = \psi_{n+1,j}$ . A graphical explanation of this boundary condition is also given in Figure 2.3.

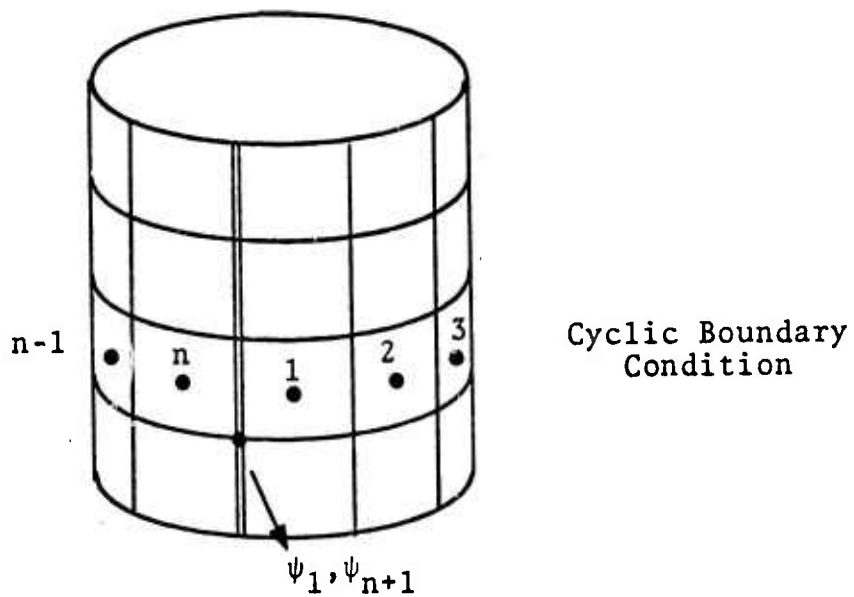
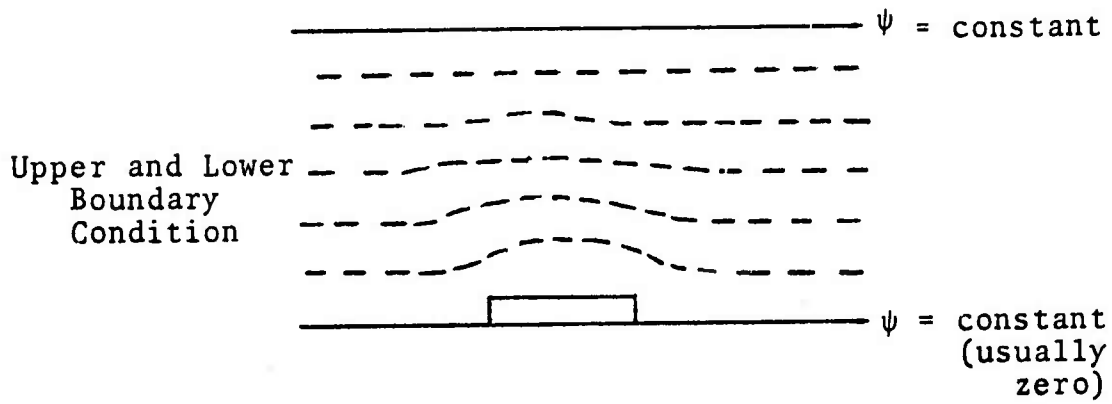


Figure 2.3 - Schematic of HAIFA Boundary Conditions.

One further boundary condition is necessary to obtain the transient solution. The vorticity equation requires that the temperature gradient in the x-direction be specified at the cell center bounded by the obstacle. This requires a value for the temperature perturbation on the obstacle boundary. The assumption is made that the air immediately next to the mountain has risen from the bottom of the grid. The temperature of the air alongside the mountain is thus given by

$$T_m = T_0 - \Gamma \cdot z$$

where

$T_m$  = the temperature along the vertical mountain boundaries

$T_0$  = the temperature at ground level

$\Gamma$  = the dry adiabatic lapse rate

$z$  = the distance above ground level.

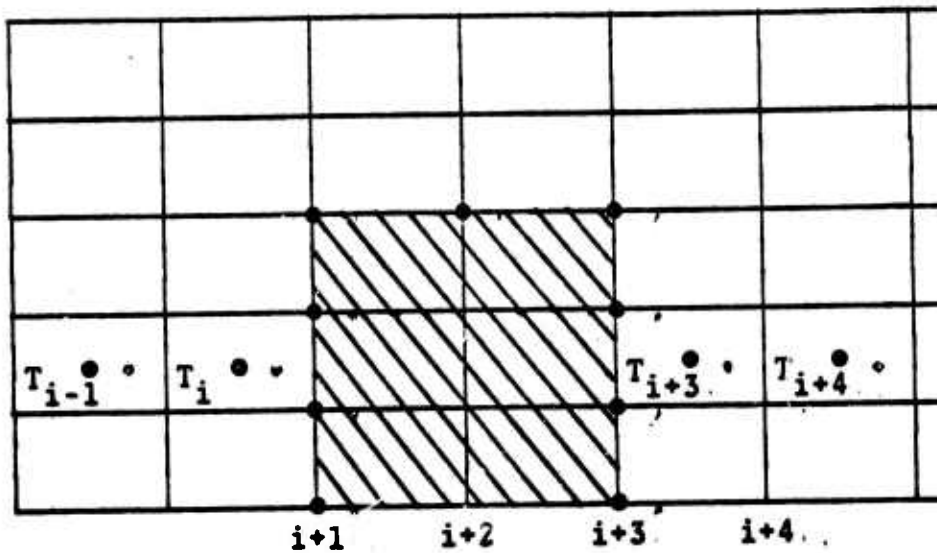
Since the initial temperature profile ( $T_i$ ) is given as an analytic function of  $z$ , the temperature perturbation along the mountain is

$$T'_m = T_0 - \Gamma \cdot z - T_i$$

Referring to the example of a two-cell thick mountain in the figure below,  $\partial T' / \partial x$  at the cell centers adjacent to the obstacle are calculated as

$$\frac{\partial T'_i}{\partial x} = \frac{T'_m - \frac{T'_i + T'_{i-1}}{2}}{\Delta x}$$

$$\frac{\partial T'_{i+3}}{\partial x} = \frac{\frac{T'_{i+3} + T'_{i+4}}{2} - T_m}{\Delta x}$$



At cycle zero (time equal to zero), these boundary conditions are then used to determine the new distribution of streamlines within the calculational grid. This completes the required information to start the computation.

## 2.5 HAIFA CODE DESCRIPTION

A flow chart giving the calculational sequence of the HAIFA code is displayed in Figure 2.4. A description of how problems are generated and the major subroutines within the code is presented below.

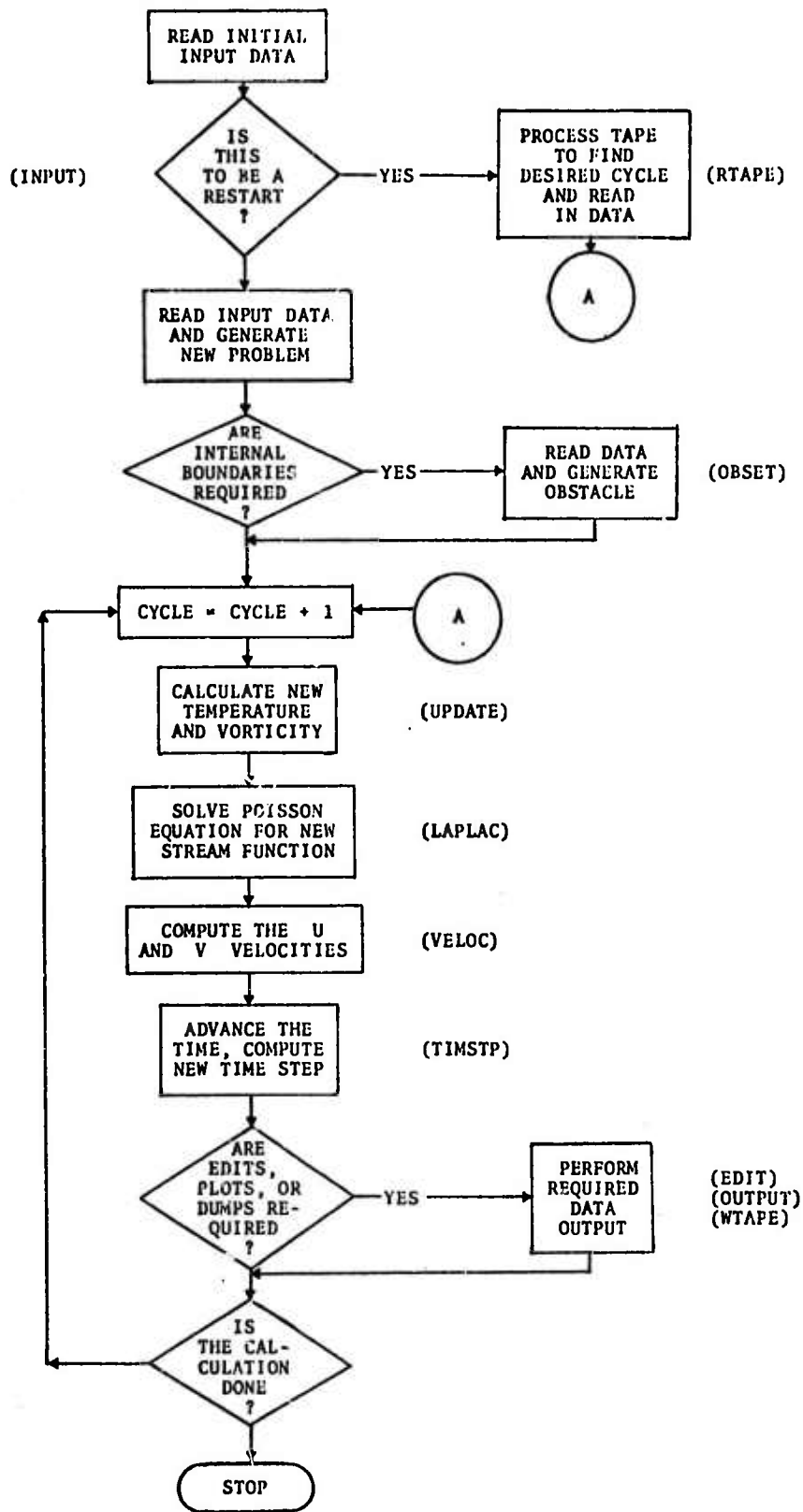


Figure 2.4 - Flow Diagram of HAIFA Code.

### 2.5.1 Initiating A Calculation

There are two methods for initiating a calculation: generating a new problem, and restarting a partially completed calculation from a data tape. These are controlled by subroutine INPUT.

Generating a New Problem - Subroutine INPUT reads all input data and sets up several constants which will be used in the calculation. The initial streamline distribution is computed from a series of input parameters, MT , DT1 , DT2 , DT3 , DT4 , and ZETA such that

$$\psi(z) = DT1 + DT2 \cdot z^{MT} + DT3 \cdot z^{(MT+1)} + DT4 \cdot \exp(-ZETA \cdot z) .$$

These parameters define the horizontal velocity distribution

$$u(z) = \frac{\partial \psi}{\partial z} = MT \cdot DT2 \cdot z^{(MT-1)} + (MT+1) \cdot DT3 \cdot z^{MT} - DT4 \cdot ZETA \cdot \exp(-ZETA \cdot z) .$$

The initial vorticities are found from differentiating the above expression with respect to  $z$ , i.e.,  $\eta = \partial u / \partial z$  since  $\partial v / \partial x$  is everywhere zero at time equal zero.

The initial temperature distribution is set in a similar fashion using the input parameters KT , AT1 , AT2 , AT3 , AT4 , and ALPHA.

$$T(z) = AT1 + AT2 \cdot z^{KT} + AT3 \cdot z^{(KT+1)} + AT4 \cdot \exp(-ALPHA \cdot z) .$$

Internal Boundaries -- The input variable NOBS defines the number of internal points which are to have fixed streamfunction values. A series of data cards specifying the grid points and the associated  $\psi$  values are read if NOBS > 0 .

Such internal boundary points are used to define grid obstacles, which are outlined by a series of connected points. Typically, the fixed value of  $\psi$  assigned to the obstacle points is the lower boundary streamfunction value. The requested initialization of the streamfunction, vorticities, and velocities in the case of internal boundaries is handled by subroutine OBSET.

Restarting A Calculation -- The option to restart a calculation is keyed by the input parameter RESTRT. If it is non-zero in value, the data tape is scanned in subroutine RTAPE until the cycle requested by input parameter ISTART is found. The values of the necessary calculational variables of the requested cycle are then read, and the computation is continued.

#### 2.5.2 Major Subroutines in the Main HAIFA Calculational Loop

UPDATE -- UPDATE is used to solve the conservative equations for vorticity and temperature. Crowley's second order or fourth order scheme is called from this subroutine to calculate the advection terms. This scheme is described in Section 2.2.2 of this report.

LAPLAC -- The Poisson equation relating the stream function and the vorticity is solved using this subroutine as the controlling program. The details of the Poisson solver are given in Section 2.2.4.

VELOC -- The updated stream function values are differenced in z-space to provide the horizontal velocity field  $u$ , and in x-space to provide the vertical velocity field  $v$ .

PRTTST -- This subroutine defines the type of output required in each cycle, viz, plots, large edits, and/or data dumps on tape are available options with this program.

TIMSTP -- The TIMSTP subroutine calculates a time step to be used in the calculation limited by the numerical stability criterion. The stability criterion is outlined in Section 2.3.

### 3. MODIFICATIONS TO THE HAIFA CODE

The BASIC HAIFA equations described in the preceding sections are limited in that the formulation has been simplified both from the mathematical and physical points of view. In Section 3 we discuss five investigations to generalize both the mathematical and physical aspects of the code. These modifications include the effects of (1) compressibility, (2) moisture, (3) improved zoning, (4) Coriolis terms, and (5) turbulence.

#### 3.1 COMPRESSIBILITY

##### 3.1.1 Derivation of the Differential Equations

The use of HAIFA for the investigation of mountain waves is appropriate in that the effects of buoyant stability and dynamics are taken into account, but its applicability is restricted by the incompressibility of the flow. In particular, if the height of the mountain range is comparable with the atmospheric scale height there will be effects induced by the expansion experienced by an air packet in being lifted over the mountain.

The effects of compressibility are to be determined through the use of a new code developed with which problems including this effect may be run and the results compared with BASIC HAIFA calculations. Several objectives were sought in arriving at a method of accomplishing this task. They are discussed below.

(1) Sound waves should be excluded from the numerical solutions in order to permit efficient calculations having time intervals comparable with material displacement through a space interval.

(2) Compressibility effects should be retained.

(3) The scheme should be formulated in physical variables to facilitate addition of new physical effects (such as Coriolis force or water vapor).

(4) Conservative difference equations should be sought.

(5) The scheme should retain a mathematical form similar to BASIC HAIFA to make programming and check-out as speedy as possible.

The "anelastic" equations of Ogura<sup>(5)</sup> meet some of the above criteria and will be compared further below. However, the anelastic equations do not allow an arbitrary atmospheric stratification, do not include the change in density due to temperature perturbations and are formulated in problem-dependent variables. These limitations can be avoided, as indicated below.

The compressibility equations used here are derived in more detail in references [6,7]

$$\frac{\partial \rho u}{\partial t} + \frac{\partial \rho u^2}{\partial x} + \frac{\partial \rho u w}{\partial z} + \frac{\partial p}{\partial x} = 0 \quad (3.1)$$

$$\frac{\partial \rho w}{\partial t} + \frac{\partial \rho u w}{\partial x} + \frac{\partial \rho w^2}{\partial z} + \frac{\partial p}{\partial z} = -g\rho \quad (3.2)$$

$$\frac{\partial \rho u}{\partial x} + \frac{\partial \rho w}{\partial z} = 0 \quad (3.3)$$

$$\frac{\partial \rho T'}{\partial t} + \frac{\partial \rho T' u}{\partial x} + \frac{\partial \rho T' w}{\partial z} = -w \left[ \rho \frac{\partial T_0}{\partial z} + \rho_0 \Gamma \right] \quad (3.4)$$

Here we recall the assumption that the density at every position can be determined from the perfect gas equation of state, in which the pressure takes the value associated with the static atmosphere,  $p_0$ , through the relation

$$\rho = \frac{p_0}{RT} \quad (3.5)$$

A stream-function-like quantity  $\phi$  can be introduced, such that Eq. (3.3) is satisfied and

$$\rho u = \frac{\partial \phi}{\partial z}, \quad \rho w = -\frac{\partial \phi}{\partial x} \quad (3.6)$$

If a vorticity-like function  $\zeta$  is defined,

$$\zeta = \frac{\partial \rho u}{\partial z} - \frac{\partial \rho w}{\partial x} \quad (3.7)$$

then the same prognostic equation as for the Boussinesq approximation results,

$$\zeta = \frac{\partial^2 \phi}{\partial x^2} + \frac{\partial^2 \phi}{\partial z^2} \quad (3.8)$$

The prognostic equation for  $\zeta$  is obtained by cross differentiating Eqs. (3.1) and (3.2) and subtracting,

$$\begin{aligned} \frac{\partial \zeta}{\partial t} + \frac{\partial}{\partial x}(u\zeta) + \frac{\partial}{\partial z}(w\zeta) + \frac{\partial}{\partial x} \left( \frac{\partial \phi}{\partial x} \frac{\partial u}{\partial x} + \frac{\partial \phi}{\partial z} \frac{\partial u}{\partial z} \right) \\ + \frac{\partial}{\partial z} \left( \frac{\partial \phi}{\partial x} \frac{\partial w}{\partial x} + \frac{\partial \phi}{\partial z} \frac{\partial w}{\partial z} \right) = g \frac{\partial \rho}{\partial x} = -\frac{g\rho}{T_0 + T'} \frac{\partial T'}{\partial x} \quad (3.9) \end{aligned}$$

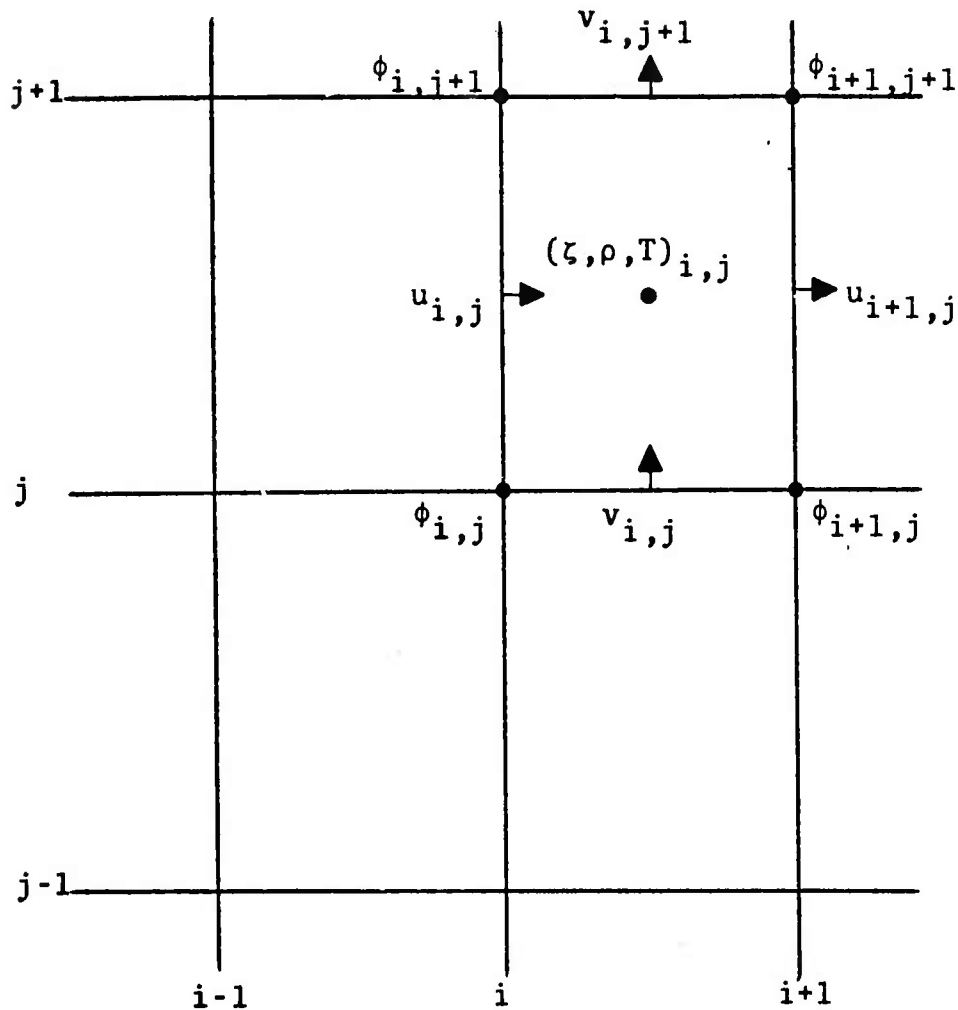
Eq. (3.9) replaces the vorticity equation of the Boussinesq system of equations, differing principally in having the additional terms containing the derivatives of  $\phi$ ,  $u$ , and  $w$ . These additional terms, which for convenience we call the "chi terms," will be discussed in detail in Section 3.1.1.2.

### 3.1.2 Method of Numerical Solution

3.1.2.1 Computational Logic - The sequence of calculations for one cycle of the compressible code is:

SUBROUTINE	FUNCTION
UPDATE	<p>(1) Eq. (3.4) is solved for new values of <math>(\rho T')</math></p> <p>(2) Eq. (3.9) is solved for <math>\zeta</math></p> <p>(3) As adjuncts, <math>\rho</math> is computed from</p> $\rho = \rho_0 - \frac{(\rho T')}{T_0}$ <p>and <math>T'</math> follows from</p> $T' = \frac{(\rho T')}{\rho}$
LAPLAC	(4) Eq. (3.8) is solved for new values of $\phi$
VELOC	<p>From Eq. (3.6)</p> <p>(5) <math>u</math> is derived from</p> $u = \frac{\partial \phi}{\partial z} / \rho$ <p>(6) <math>v</math> is derived from</p> $v = - \frac{\partial \phi}{\partial x} / \rho$

3.1.2.2 Finite Difference Scheme - The centering of the dependent variables in the compressible code is identical to the centering of the analogous variables in BASIC HAIFA, viz.,

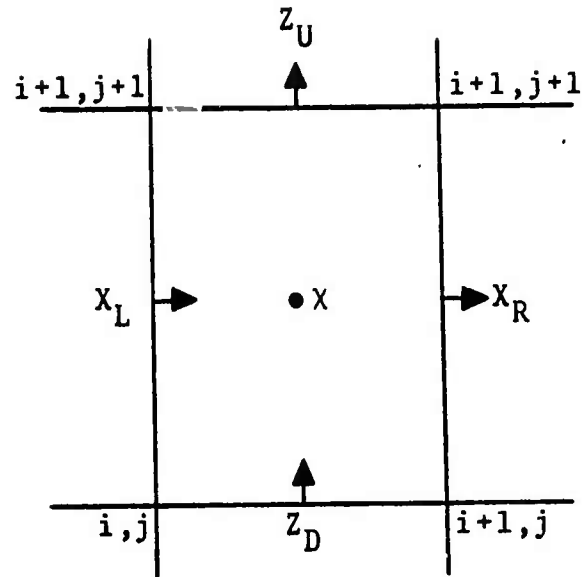


The difference scheme used in the standard HAIFA equations is applied directly to the compressible system of equations, and need not be reviewed here. The differencing of the chi term, which is unique to the compressible code, is discussed below.

To form

$$\chi = \frac{\partial}{\partial x} \left[ \frac{\partial \phi}{\partial x} \frac{\partial u}{\partial x} + \frac{\partial \phi}{\partial z} \frac{\partial u}{\partial z} \right] + \frac{\partial}{\partial z} \left[ \frac{\partial \phi}{\partial x} \frac{\partial w}{\partial x} + \frac{\partial \phi}{\partial z} \frac{\partial w}{\partial z} \right]$$

we define  $X_R$ ,  $X_L$ ,  $Z_U$ , and  $Z_D$



so that

$$X = \frac{X_R - X_L}{\Delta x} + \frac{Z_U - Z_D}{\Delta z}$$

is cell centered. Then, the difference form used is

$$\begin{aligned} X_R = & \frac{\phi_{i+2,j} + \phi_{i+2,j+1} - \phi_{i,j+1} - \phi_{i,j}}{4\Delta x} \cdot \frac{u_{i+2,j} - u_{i,j}}{2\Delta x} \\ & + \frac{\phi_{i+1,j+1} - \phi_{i+1,j}}{\Delta z} \cdot \frac{u_{i+1,j+1} - u_{i+1,j-1}}{2\Delta z} \\ Z_U = & \frac{\phi_{i+1,j+1} - \phi_{i,j+1}}{\Delta x} \cdot \frac{w_{i+1,j+1} - w_{i-1,j+1}}{2\Delta x} \\ & + \frac{\phi_{i,j+2} + \phi_{i+1,j+2} - \phi_{i,j} - \phi_{i+1,j}}{4\Delta z} \cdot \frac{w_{i,j+2} - w_{i,j}}{2\Delta z} \end{aligned} \quad (3.10)$$

Note that

$$x_L]_{i,j} \equiv x_R]_{i-1,j}$$

and

$$z_D]_{i,j} \equiv z_U]_{i,j-1}$$

### 3.1.3: Initial Conditions

As with HAIFA, the values of  $u_o(z)$  and  $T_o(z)$  are specified by input to the compressible code. In addition, the initial surface pressure  $p_o(z=0)$  must be specified. The remaining initial pressures are found using the static atmospheric equation

$$\frac{\partial p_o}{\partial z} = -g\rho_o = -\frac{gp_o}{RT_o} \quad , \quad (3.11)$$

so that

$$p_o(z) = p_o(z=0) \exp\left[-\frac{g}{R} \int_0^z \frac{dz}{T_o(z)}\right] \quad .$$

The initial density profile then follows from

$$\rho_o(z) = \frac{p_o(z)}{RT_o(z)} \quad .$$

The stream-function-like quantity  $\phi$  is formed by integrating

$$\frac{\partial \phi}{\partial z} = \rho_o(z) u_o(z) \quad ,$$

and the vorticity-like quantity  $\zeta$  is initialized from the application of Eq. (3.7) to yield

$$\zeta = \frac{\partial}{\partial z} (\rho_0(z) u_0(z)) .$$

As in BASIC HAIFA, initially there is no  $x$  dependence of any quantity.

#### 3.1.4 Modification of Advective Scheme

The quantities to be advected in the system of compressibility equations are  $\zeta$ , Eq. (3.9), and  $(\rho T')$ , Eq. (3.4). Since the equation of continuity has the form

$$\frac{\partial \rho u}{\partial x} + \frac{\partial \rho w}{\partial z} = 0 ,$$

it was necessary to modify Crowley's second-order scheme for advection in order to use  $(\rho u)$  and  $(\rho w)$  as pseudo-velocities.

#### 3.1.5 Timing Comparison

The major computational difference between the Boussinesq and compressible codes is the calculation of the chi term. Timing studies of the two code versions were performed, based on a grid of 64  $x$ -direction cells and 35  $y$ -direction cells, and incorporating an interior boundary condition (which requires two passes per cycle in the Poisson Equation Solver). The results are summarized in the table below:

	COMPRESSIBLE	BASIC HAIFA
UPDATE TOTAL	1.58 sec	0.51 sec
2 <sup>nd</sup> Order Scheme	0.33 sec	0.33 sec
Chi Term	1.02 sec	---
LAPLAC TOTAL	1.14 sec	1.14 sec
VELOC TOTAL	0.14 sec	0.11 sec
TIMSTP TOTAL	0.03 sec	0.03 sec
TOTAL/CYCLE	2.89 sec	1.79 sec

### 3.1.6 Test Problem

A two wave problem identical to that discussed in Section 4.2 was used for comparative calculations between the compressible and the Boussinesq versions of the HAIFA codes.

Comparative plots (Figures 3.1 and 3.2) of the results from the compressible code and HAIFA at a time of approximately 1500 seconds indicates a single wave (in each case) with a 10-12 km wavelength. The vertical velocity pattern indicates that only the single wave is forming in the compressible case while a second wave is appearing in the Boussinesq case. However, since the compressible calculation was run to a time of only 2000 seconds, these results are inconclusive. The first wavelength in each case agrees with the shorter of the two waves predicted by Palm and Foldvik<sup>[8]</sup> and Hesstvedt.<sup>[9]</sup>

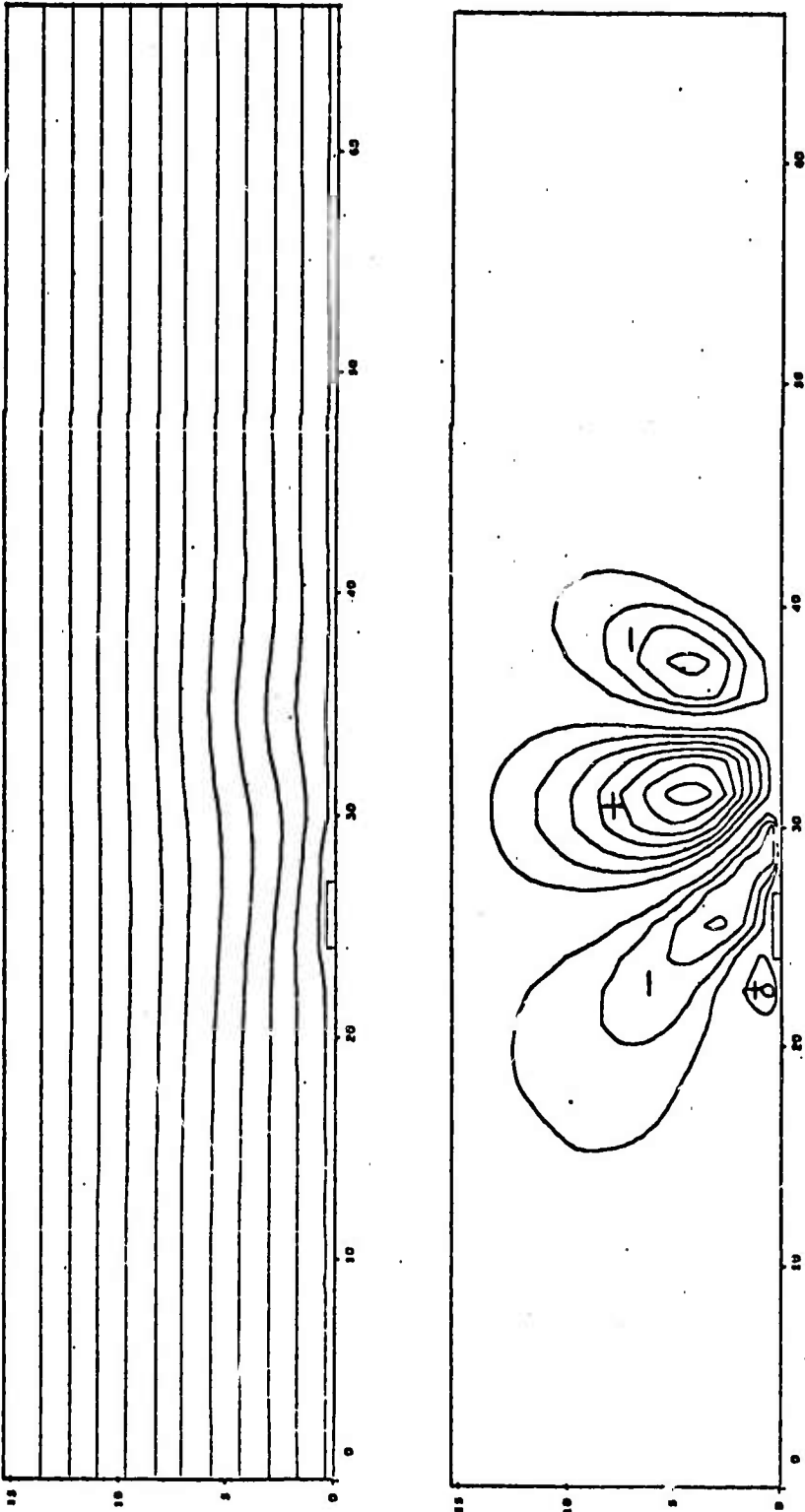


Figure 3.1. Streamlines and vertical velocity profiles for the compressible problem. (time = 1484 seconds)

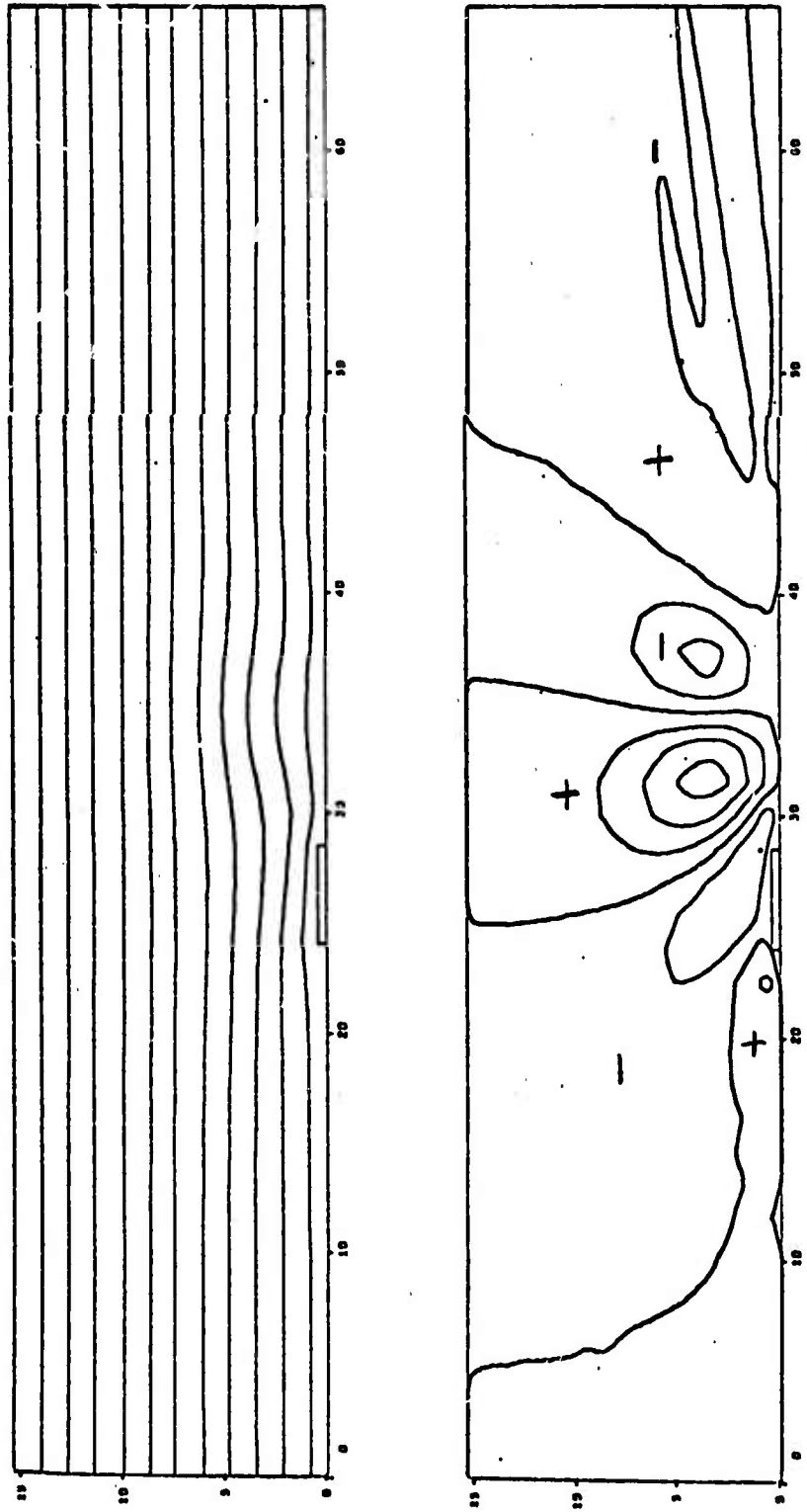


Figure 3.2. Streamlines and vertical velocity profiles for the BASIC HAIFA problem. (time = 1565 seconds)

3.1.6.1 Wave Drag Results - The momentum edits  $\overline{\rho u'w'}$ , located one cell above the mountain top, are shown as a function of time for the Boussinesq and compressible calculations in Figure 3.3. The maximum value of the drag reached during 2000 seconds of integration time was approximately equal to 5 dyne/cm<sup>2</sup> and 3.8 dyne/cm<sup>2</sup>, respectively.

Figures 3.4, 3.5 and 3.6 show the momentum edit as a function of height at a time of approximately 1000, 1500 and 2000 seconds. This sequence indicates that the solution has not yet reached a steady state value, since the drag for a steady problem will be constant with height.

The major characteristics of the momentum flux results are:

- (1) a larger value of the vertical flux of horizontal momentum just above the mountain (660 meters) is predicted by the Boussinesq code than by the compressible code; and
- (2) above a height of approximately 4.5 km, the compressible results indicate a larger flux of momentum than the Boussinesq calculations.

These results are explainable to a certain degree by the linear analysis of the equations in Section 5. The analysis shows that the vertical velocity resulting from the compressible equations increases with increasing altitude by a factor of  $(p/p_0)^{-0.36} (\rho/\rho_0)^{-1/2}$  relative to the Boussinesq equations. This velocity is reflected directly in the value of the momentum flux  $\overline{\rho u'w'}$  and the cross over of the drag results seen in the figures as a function of height is qualitatively expected.

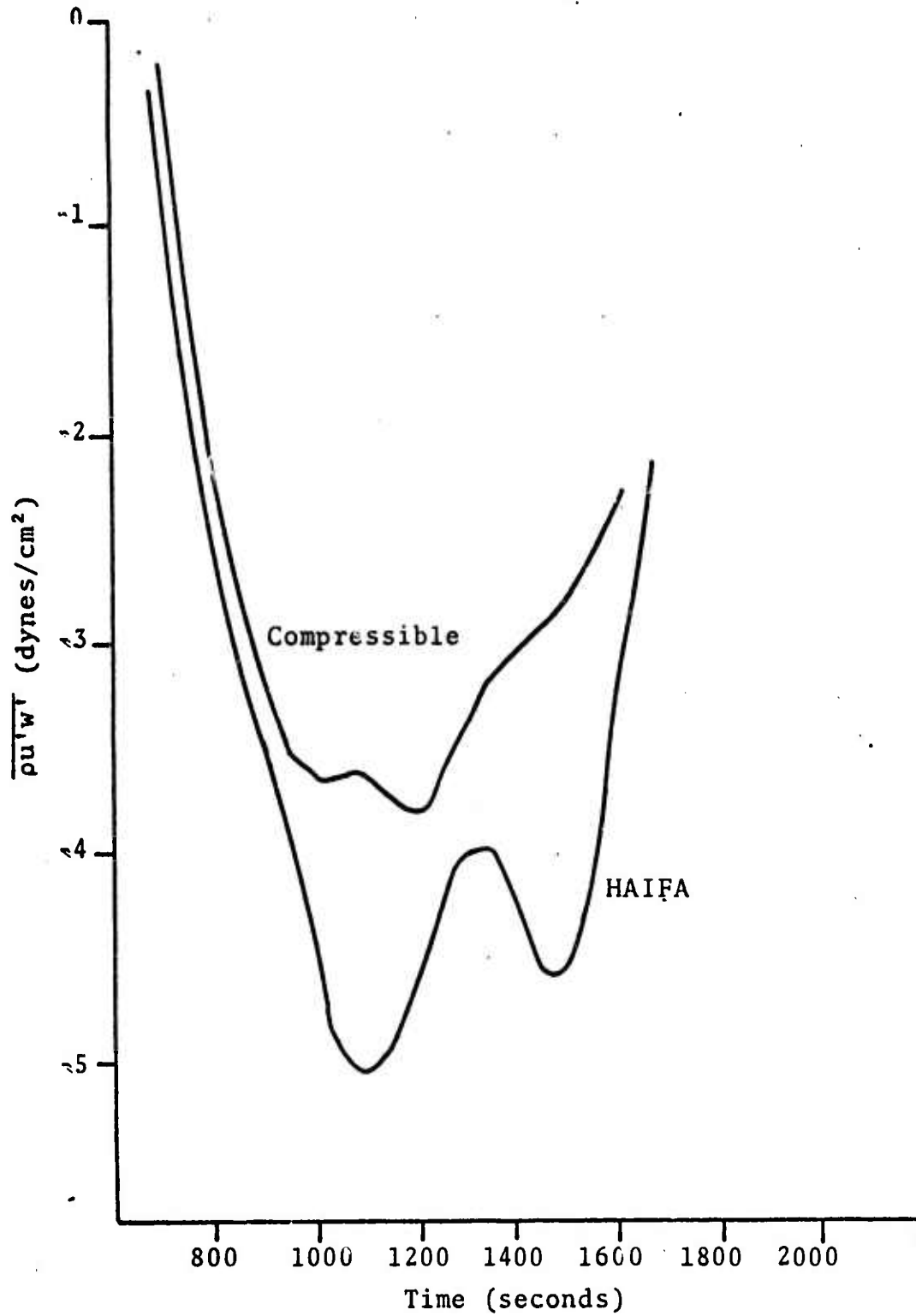


Figure 3.3. Vertical transport of horizontal momentum above the obstacle.

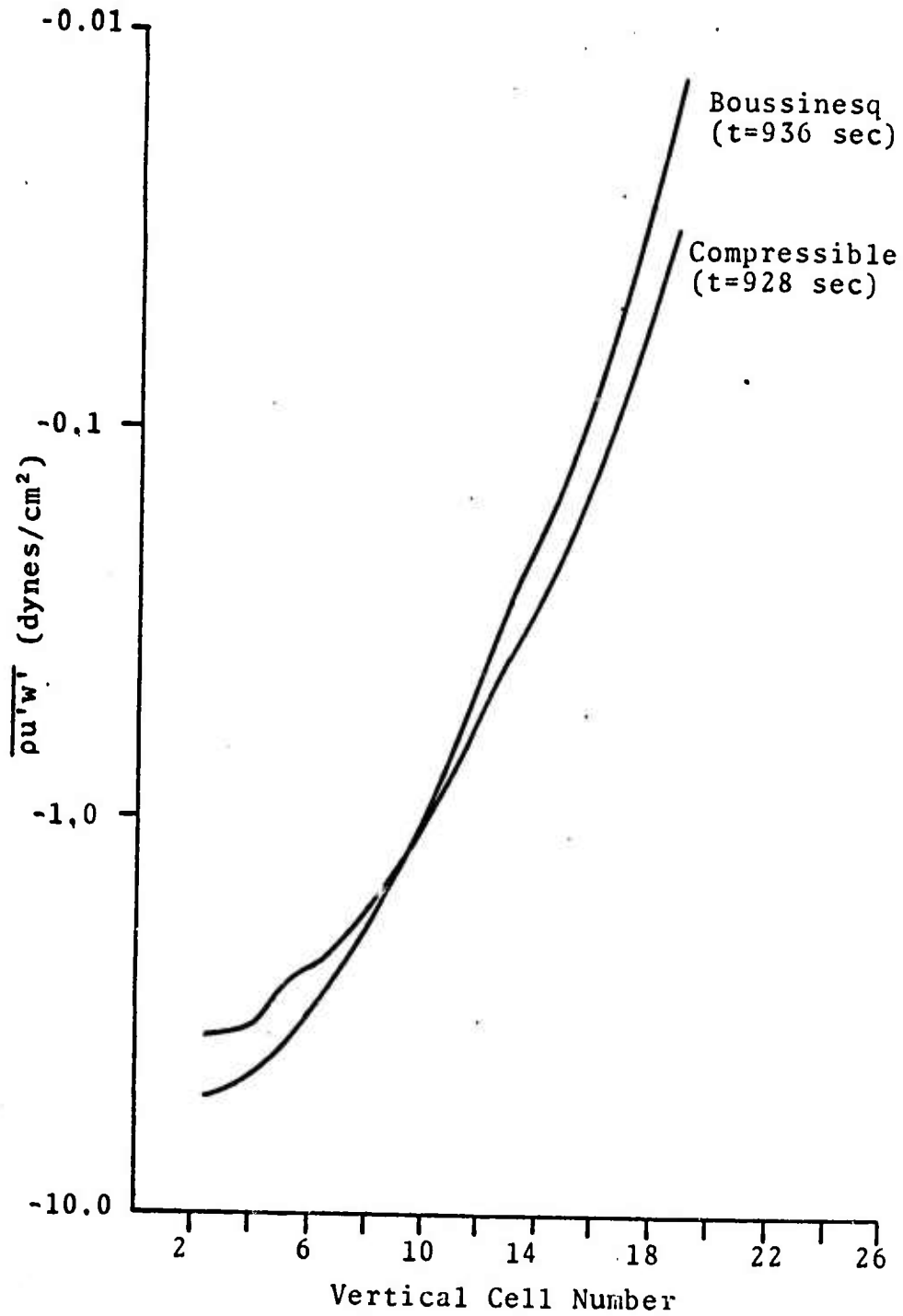


Figure 3.4. Momentum flux as a function of vertical height centered over the obstacle. (time  $\sim$  1000 sec)

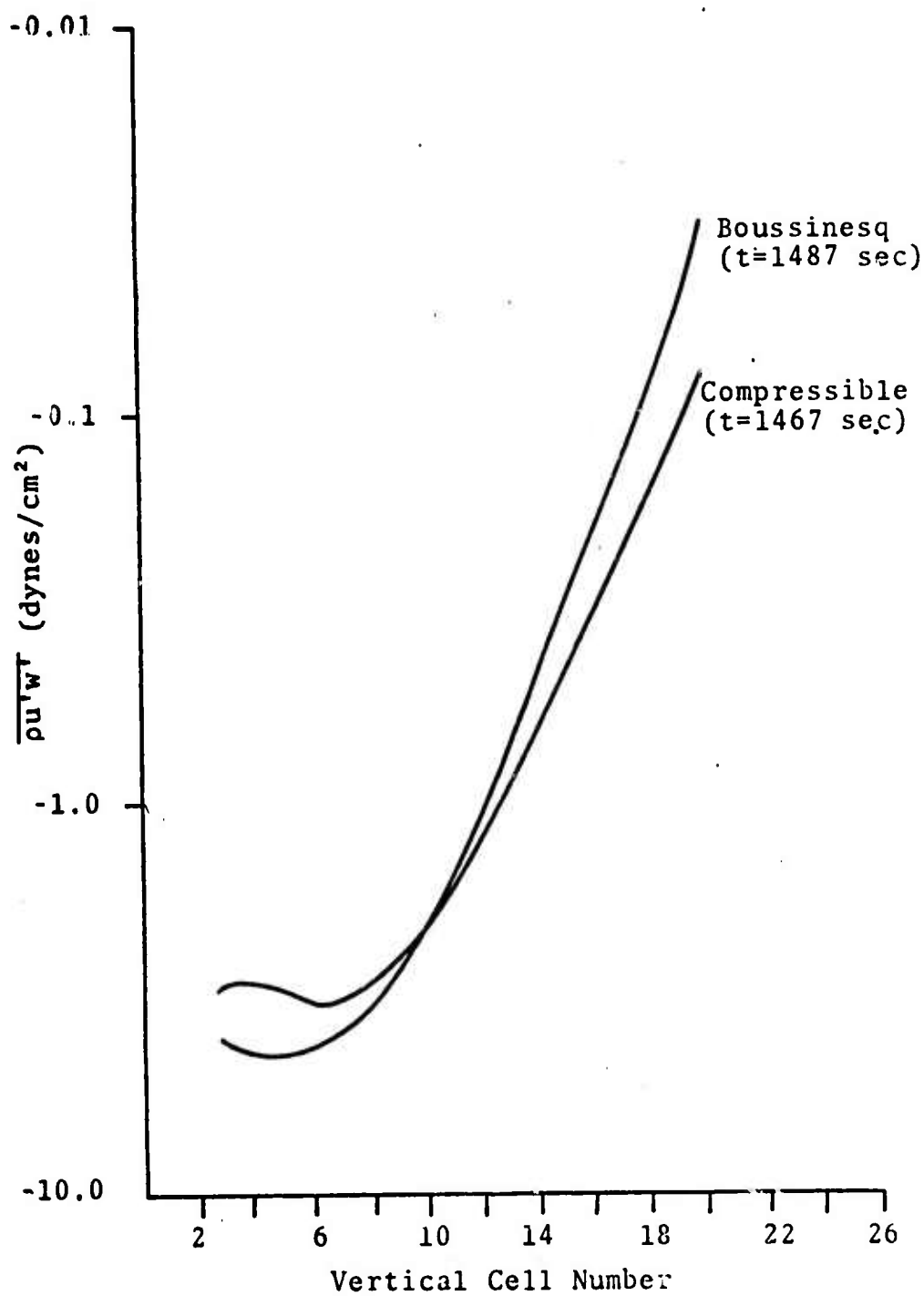


Figure 3.5. Momentum flux as a function of vertical height centered over the obstacle. (time  $\sim$  1500 sec)

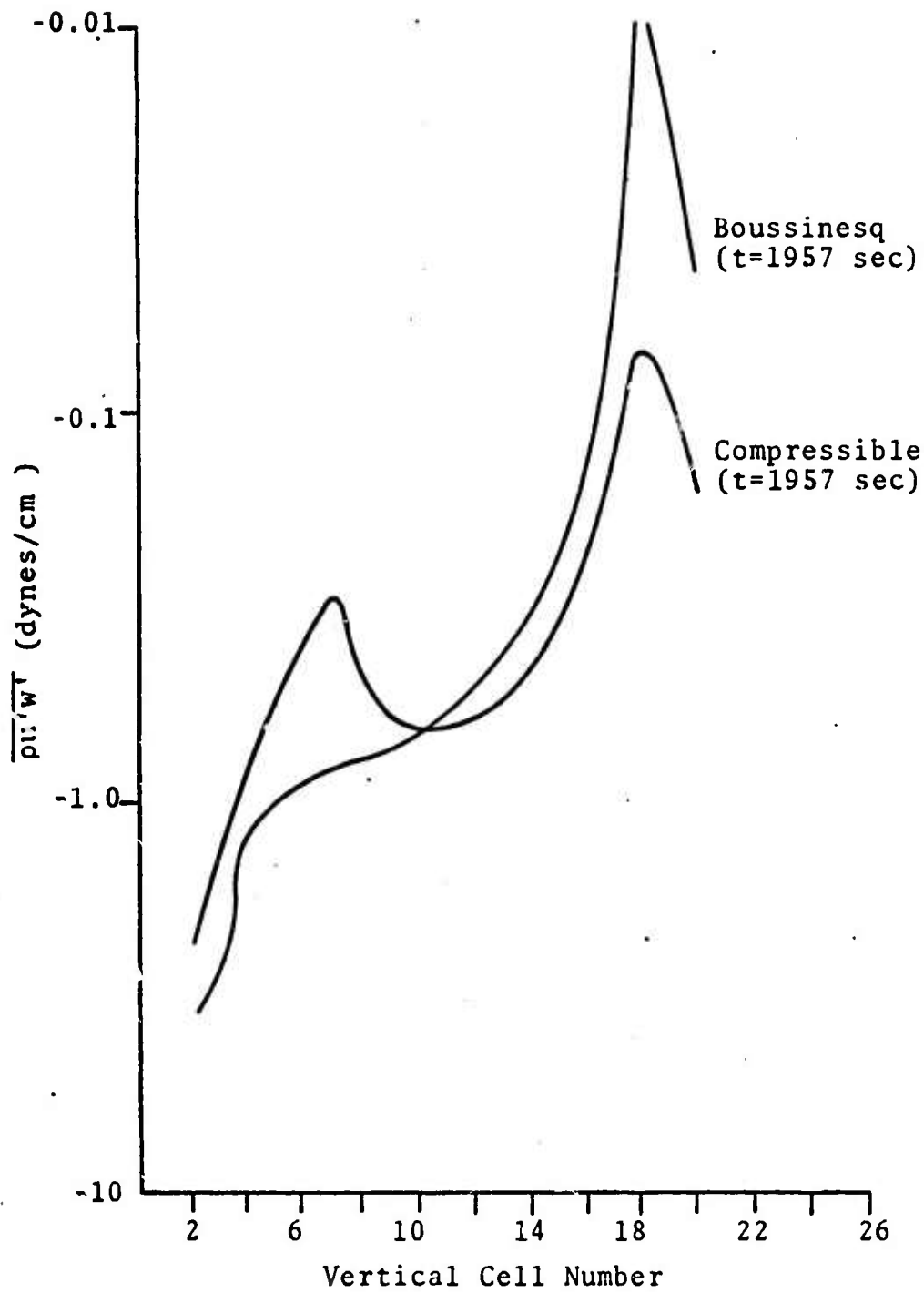


Figure 3.6. Momentum flux as a function of vertical height centered over the obstacle. (time  $\sim$  2000 sec)

3.1.6.2 Numerical Stability - The stability of the compressible finite difference equations is not well understood at this time. Originally, the time-step criterion of the Boussinesq formulation,

$$\Delta t < \min\left(\frac{\Delta x}{u_{\max}}, \frac{\Delta z}{w_{\max}}\right)$$

was also used for the compressible equations. In some instances, calculational instabilities developed. Lacking a comprehensive stability analysis upon which to base new time-step criteria, sensitivity experiments were performed in an attempt to bound the stable range for the compressible code. A quantity  $\alpha < 1.0$  defined by

$$\Delta t_{\text{compr}} = \alpha \Delta t_{\text{boussinesq}}$$

was introduced in an attempt to simplify the investigation. This approach did not yield useful results, as  $\alpha$  proved to be highly problem dependent. Indeed, values as small as  $\alpha = 0.2$  have failed to provide a stable compressible solution in some cases.

Not surprisingly, the major stability problems have been observed in the regions of highest speed flow, which typically are the uppermost portions of the calculational grid for many atmospheric test problems. This is true, for example, of the two wave test problem of this section. Further, the effects of most interest in code comparisons for the two wave problem take place near the obstacle, far removed from the upper atmosphere. This suggested another approach; the introduction of strong artificial diffusion in the upper cells of the grid, forcing the solution there to become spatially

smoothed. While the use of diffusion proved successful in this application, not enough is known yet about the stability characteristics of the compressible formulation. Further theoretical and numerical research is warranted in this area, both to improve the accuracy and economics of the compressible formulation, and to advance understanding of atmospheric meso-scale codes.

### 3.2 MOISTURE EFFECTS

Atmospheric water in the form of water vapor, cloud water, and precipitation may have important effects on the characteristics of gravity waves caused by mountains. Lee waves are frequently accompanied by clouds which can be expected to modify the stability of the air through the presence of the latent heat of condensation which the cloud water adds to the air. Consequently, the terms resulting in changes of stability of the air in which clouds are forming are of primary interest.

A code has been developed to determine the effects of moisture on the equations for a Boussinesq fluid. The HAIFA equations have been modified to incorporate the following changes:

- (1) the momentum equation incorporates the effects of moisture in the buoyancy term,
- (2) the equation of state for air takes account of a water vapor component,

- (3) the energy equation includes energy changes equivalent to the latent heat of water being given to or taken from the air,
- (4) an equation is added to account for the conservation of all moisture except rain water, and
- (5) a conservation equation is added which governs the rain water content in the atmosphere including sources and sinks at the boundaries.

The differential equations are outlined below. This set most closely matches that of Liu and Orville<sup>[10]</sup> and is similar to Arnason.<sup>[11]</sup>

$$\frac{du}{dt} = - \frac{1}{\rho_0} \frac{\partial p}{\partial x} + F_x \quad , \quad (3.12)$$

$$\frac{dw}{dt} = - \frac{1}{\rho_0} \frac{\partial p}{\partial z} - g(1 + l) + F_z \quad , \quad (3.13)$$

and

$$p = \rho RT(1 + Er) \quad , \quad (3.14)$$

where

- $l$  =  $l_c + l_r$  total liquid water content (kg H<sub>2</sub>O/kg air),
- $l_c$  = cloud water content (kg H<sub>2</sub>O/kg air),
- $l_r$  = rain water content (kg H<sub>2</sub>O/kg air),
- $r$  = specific humidity (kg H<sub>2</sub>O/kg air),
- $\rho$  = density of humid air,
- $T$  = air temperature,
- $F_x, F_y$  = friction terms,

and

$$E = \left( \frac{\text{molecular weight of air}}{\text{molecular weight of H}_2\text{O}} - 1 \right)$$

These equations can be combined to yield a vorticity equation of the form:

$$\frac{d\eta}{dt} = - \frac{g}{T_0} \frac{\partial T}{\partial x} + g \frac{\partial \lambda}{\partial x} + k_m \nabla^2 \eta \quad (3.15)$$

where the Boussinesq approximation and the further restriction that  $T_0/T = 1$  have been utilized.

The energy equation for the moist system has been rewritten to include the  $w\Gamma$  term in the definition of  $T''$ :

$$T'' = T - T_0 + \frac{Lr}{C_p} + \Gamma z \quad (3.16)$$

This allows the energy equation to be written as

$$\frac{d}{dt} T'' = k_T \nabla^2 (T'' - \Gamma z) \quad (3.17)$$

In addition to the vorticity and energy equations, the conservation of total water or moisture must be expressed. The atmospheric moisture can be divided into three distinct categories - moisture existing as water vapor, moisture existing as cloud water, and moisture existing as rain water. With this decomposition one may write the equation for total moisture conservation as follows:

$$\begin{aligned} \frac{\partial}{\partial t} (\rho Q) = & - \nabla \cdot (\rho r \vec{V}) - \nabla \cdot (\rho \lambda_c \vec{V}) \\ & - \nabla \cdot \left[ \rho \int_D (\vec{V} - \vec{V}_D) \lambda_r^D dD \right] + k_Q \nabla^2 \rho (r + \lambda_c) \end{aligned} \quad (3.18)$$

where

$Q$  = total moisture content,

$\rho$  = density of dry air,

$\vec{V}_D$  = terminal velocity of rain drops of diameter  $D$ ,

$\vec{V}$  = wind velocity,

and

$k_Q$  = diffusivity for cloud water and water vapor.

The terms on the right express water vapor convergence, cloud water convergence, rain water convergence, and diffusion of vapor and cloud water.

Again, from conservation considerations, one may obtain another equation expressing rain water content.

$$\frac{\partial}{\partial t} (\rho l_r) = -\nabla \cdot [\rho \int_D (\vec{V} - \vec{V}_D) l_r^D dD] + \rho P_r \quad , \quad (3.19)$$

where  $P_r$  is a rain water production term described in Equation (3.33). These two conservation equations may be subtracted to yield yet another, describing cloud water plus water vapor conservation.

$$\frac{d}{dt} q = k_Q \nabla^2 q - P_r \quad , \quad \text{where } q = r + l_c \quad . \quad (3.20)$$

Equations (3.19) and (3.20) comprise the moisture set solved in HAIFA. At this point, however, (3.19) is in rather awkward form. The rain water convergence term may be decomposed as follows:

$$\begin{aligned}
 -\nabla \cdot \rho \int_D (\vec{V} - \vec{V}_D) \ell_r^D dD &= -\nabla \cdot \rho \vec{V} \int_D \ell_r^D dD \\
 &\quad - \nabla \cdot \rho \int_D \vec{V}_D \ell_r^D dD
 \end{aligned}
 \tag{3.21}$$

but

$$\int_D \ell_r^D dD = \ell_r \tag{3.22}$$

Defining an average terminal velocity of the rain drops by

$$\vec{V}_T = \int_D \vec{V}_D \ell_r^D dD / \int_D \ell_r^D dD \tag{3.23}$$

Equation (4.23) becomes:

$$-\nabla \cdot \rho \int_D (\vec{V} - \vec{V}_D) \ell_r^D dD = -\nabla \cdot (\rho \ell_r \vec{V}) - \nabla \cdot (\rho \ell_r \vec{V}_T) \tag{3.24}$$

Substituting this result into the conservation Equation (3.19) we have:

$$\frac{\partial}{\partial t} (\rho \ell_r) = -\nabla \cdot (\rho \ell_r \vec{V}) - \nabla \cdot (\rho \ell_r \vec{V}_T) + \rho P_r \tag{3.25}$$

Expanding the right side with the realization that  $\vec{V}_T$  only operates in the vertical, we obtain the expression:

$$\frac{d}{dt} \ell_r = V_T \frac{\partial \ell_r}{\partial z} + V_T \frac{\ell_r}{\rho} \frac{\partial \rho}{\partial z} + \ell_r \frac{\partial V_T}{\partial z} + P_r \tag{3.26}$$

where use of the continuity condition  $\frac{d}{dt} \rho = 0$  has been made.

With this result, the equation set solved in the moisture version of HAIFA is complete. It is summarized below:

$$\frac{d}{dt}\eta = + g\left(\frac{\partial \ell_r}{\partial x} + \frac{\partial \ell_c}{\partial x}\right) - \frac{g}{T_0} \frac{\partial T}{\partial x} + k_m \nabla^2 \eta, \quad (3.27)$$

$$\nabla^2 \psi = \eta, \quad (3.28)$$

$$\frac{d}{dt}T'' = k_T \nabla^2 (T'' - \Gamma z), \quad (3.29)$$

$$\frac{d}{dt}\ell_r = v_T \frac{\partial \ell_r}{\partial z} + v_T \frac{\ell_r}{\rho} \frac{\partial \rho}{\partial z} + \ell_r \frac{\partial v_T}{\partial z} + P_r', \quad (3.30)$$

$$\frac{d}{dt}q = k_Q \nabla^2 q - P_r. \quad (3.31)$$

$$v_t = 5.32 (\ell_r)^{1/5} \quad (3.32)$$

$$P_r = \beta(r - r_s) + \alpha(\ell_c - \ell_{c_r}) + 4.6 \times 10^{-3} \ell_c (\ell_r)^{0.95} \quad (3.33)$$

and

$$\beta = 3.607 \times 10^{-8} (\rho \ell_r)^{0.65} \quad (3.34)$$

For a more detailed description of the assumptions in these equations, see Section 3.2.1 and 3.2.2.

It should be noticed that once one has progressed beyond  $t = 0$ , there is no explicit method of extracting the air temperature from the energy equation. The magnitude of the air temperature increase experienced by a parcel upon condensation of water vapor is related to the local saturation mixing ratio in that all moisture above this value condenses. The value of  $r_s$  is no longer known, however, since it is a function of the air temperature and the air temperature itself

has changed an unknown amount. As a result of this elliptic relation, an iterative procedure is required to obtain  $T$ . This is accomplished in HAIFA via the addition of a new subroutine NEWTON which utilizes a Newton-Raphson iterative scheme to achieve rapid convergence to a self-consistent value of  $T$  in the relations below:

$$T = T'' - \frac{L}{C_p} r_s - \Gamma z + T_0 ,$$

$$r_s = \frac{3.8}{p} \exp \left\{ 17.27 \left( \frac{(T-273.16)}{(T-35.86)} \right) \right\} . \quad (3.35)$$

For the case where the moisture content of the parcel is less than the saturated value, there is no latent heat change and the temperature changes as in the dry equations.

The flowchart presented in Figure 3.7 depicts the logic used in the routine UPDATE to solve the vorticity, energy, moisture, and rain water equations.

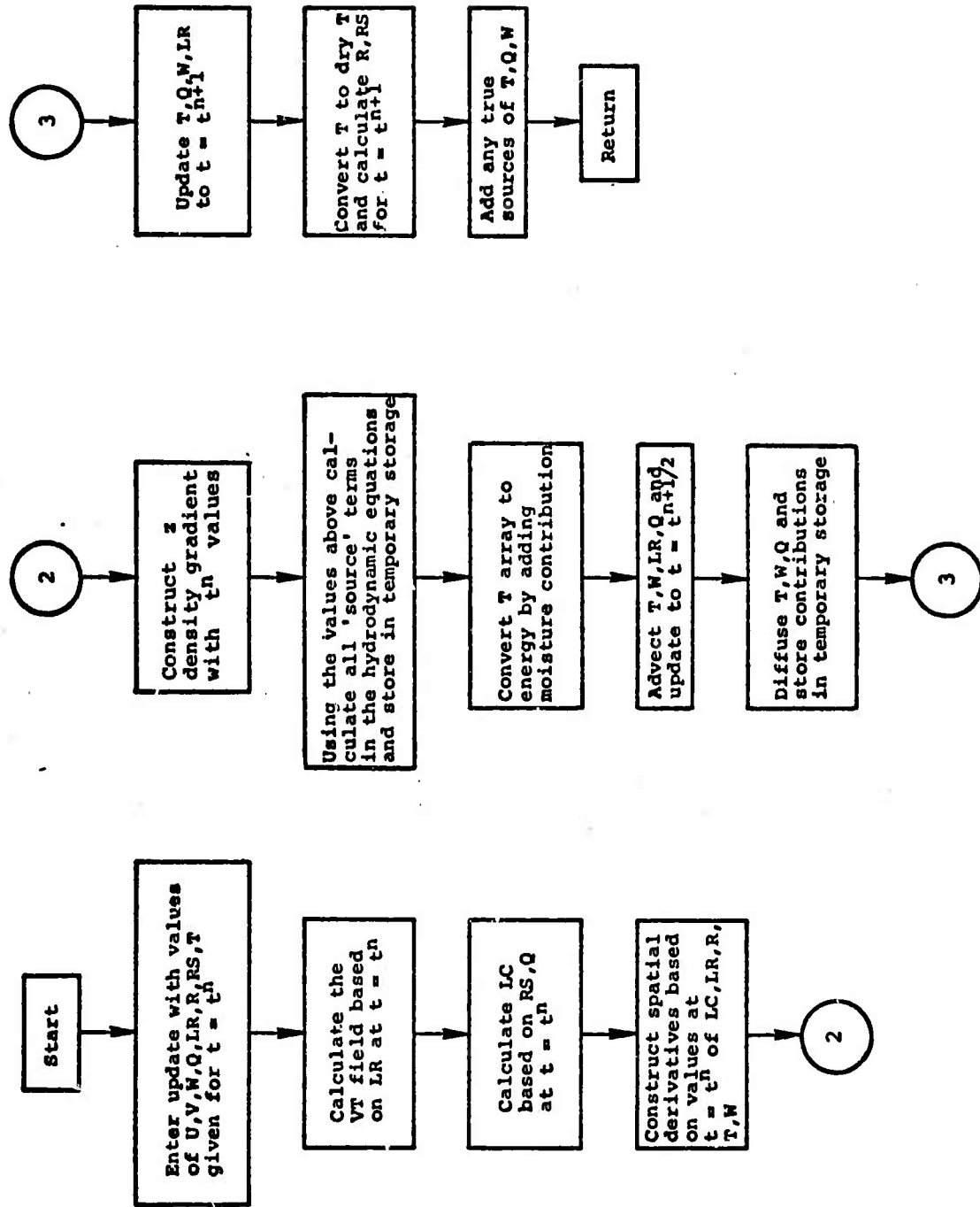


Figure 3.7 Flowchart for routine UPDATE.

### 3.2.1 Integration of the Finite Difference Equations

The Eqs. (3.27) through (3.31) are written in finite difference form and integrated numerically in a similar manner to the BASIC HAIFA equations.

The basic scheme used in the integration is shown in Figure 3.8. The locations of the major variables with respect to the grid cells are shown in Figure 3.9.

3.2.1.1 The Advection Scheme - The advection terms for vorticity, water vapor content and rain water are calculated using the second order scheme of Crowley. The scheme is written in conservation form and is based on a forward time difference and centered space differences. Test calculations performed by Crowley indicated that for the same order of accuracy, the conservation form produced more accurate solutions than the advection form.

In the conservation form, the time derivative and advection terms of the vorticity, temperature, or moisture equations may be written as

$$\frac{\partial \alpha}{\partial t} + \frac{\partial (u\alpha)}{\partial x} + \frac{\partial (v\alpha)}{\partial z} = S \quad , \quad (3.36)$$

where  $\alpha$  represents  $T$ ,  $\eta$ ,  $q$ , or  $\ell_r$  and  $S$  is the source term.

In two dimensions a splitting technique is used; the calculational scheme calls for solving two one-dimensional equations sequentially. First, the net flux of vorticity or temperature is solved for in the horizontal, the quantity solved for in the zone being updated due to this flux. The procedure is then repeated in the vertical direction using the partially updated values from the horizontal calculation.

- 
- STEP 1 Initial values of temperature; vorticity, velocities and water content are specified.
- STEP 2 Set water vapor content calculated and initial water content values are redistributed as rain water, clouds and vapor.
- STEP 3 New values of temperature, rain water, water content other than rain water, and vorticity are obtained accounting for the advection terms only.
- STEP 4 Vorticity, water content and rain water are updated to time  $t^{n+1}$  by evaluating source terms with the quantities obtained in Step 3.
- STEP 5 The Poisson equation is solved for  $\psi$  using values of  $\eta$  at  $t^{n+1}$ .
- STEP 6 Velocities are updated using  $\psi$  values from Step 4. Initial data for a new cycle are now available for edit or continuation of the calculation beginning at Step 2.
- 

Figure 3.8 HAIFA\*MOISTURE calculation sequence used in numerical integration of Eqs. (3.27) through (3.31).

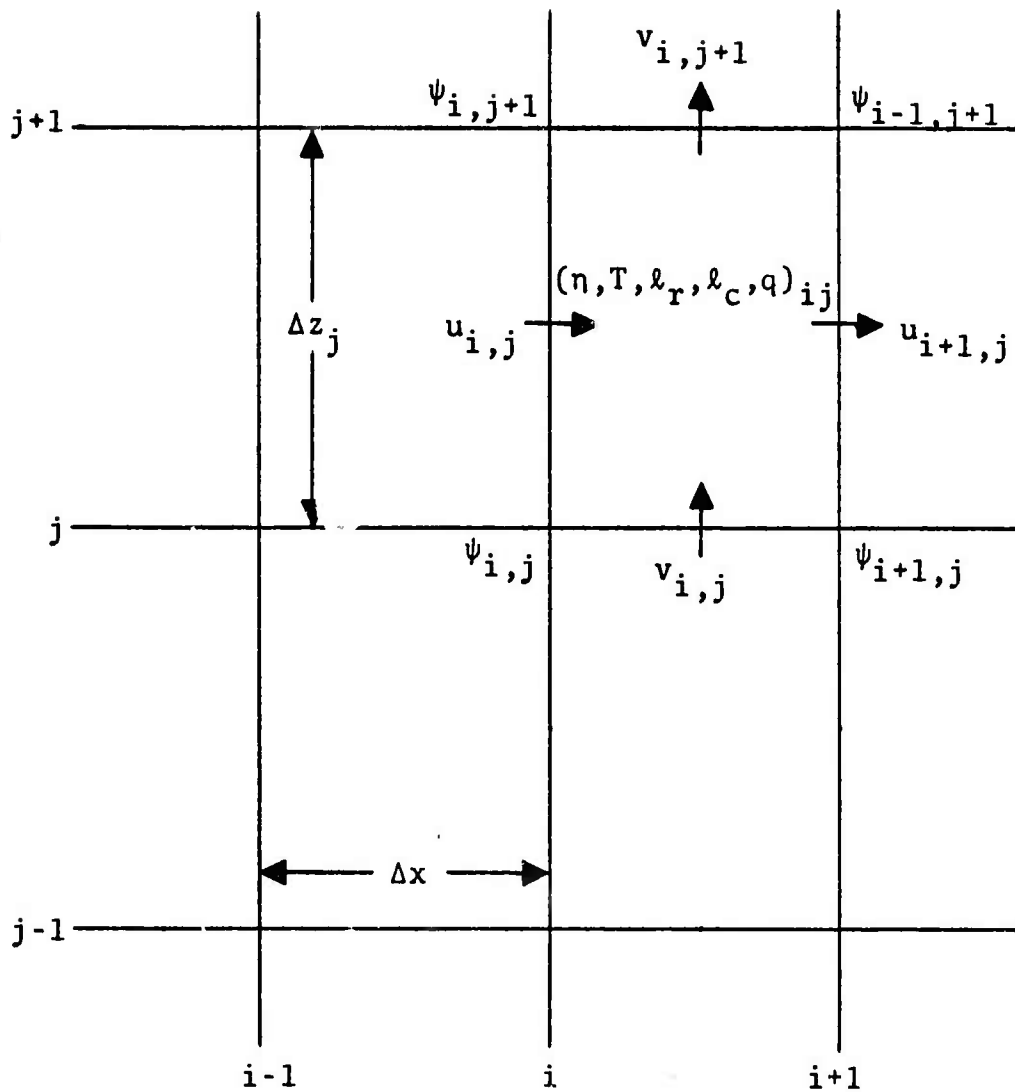


Figure 3.9 Finite difference grid - HAIFA\*MOISTURE.

3.2.1.2 Changes in Vorticity and Water Content Due to Other Terms in the Conservation Equations - All source terms in Eqs. (3.27) through (3.31) are evaluated as zone centered quantities containing centered space differences. Update takes place after the effects of advection have been calculated.

### 3.2.2 Moisture Equation Source Terms

The source terms in the conservation equations (3.12) through (3.16) depend on complicated physical processes which have been parameterized from experimental measurement data. These include the terminal velocity of rain drops, the equilibrium vapor pressure of water, and several constants dealing with the water production term. Parametric representations of these terms are given below; we have attempted to obtain the most comprehensive results available.

3.2.2.1 Terminal Velocity - The terminal velocity of rain drops is given by

$$V_t = 5.32(\lambda_r)^{1/5}$$

where  $V_t$  is in m/sec and  $\lambda_r$  in gm/Kgm .

This expression, derived by Liu and Orville<sup>[10]</sup> has been compared to data from the Smithsonian Meteorological Tables<sup>[12]</sup> and an expression developed by Srivastava.<sup>[13]</sup>

3.2.2.2 Saturation Vapor Pressure - The saturation vapor pressure is defined as

$$e_s = 6.11 \times 10^{7.5(\tilde{T}_0 - 2.73)/(\tilde{T}_0 - 36)} \text{ millibars}$$

where  $\tilde{T}_0 = T_0 - gz/C_p$  and  $r_s$ , the saturated water vapor mixing ratio in gm/Kg, is given by

$$r_s = \frac{R e_s(T_0)}{R_v p_0(z)} \exp \frac{L(T'' - L_r/C_p)}{R_v T_0^2} .$$

Both expressions are obtained from the work of Liu and Orville, [10] Orville, [14] Ogura, [15] and Ogura and Phillips. [5]

3.2.2.3 Water Production Term - The water production consists of three physical phenomena which can add to, subtract from, or change the state of the water in the atmosphere. This includes (1) the evaporation of rain water outside the clouds, (2) the conversion of cloud water to rain water, and (3) the growth of rain through coalescence. These terms were originally expressed in Orville's work as

$$p_r = \beta(r-r_s) + \alpha(l_c - l_{c_r}) + 4.6 \times 10^{-3} l_c(l_r)^{0.95} .$$

During our initial test calculations, it was discovered that treating  $\beta$ , the evaporation parameter, as a constant led to computational difficulties. This term was modified to agree with that used in Kessler's work [16] which expressed  $\beta$  as

$$\beta = 3.807 \times 10^{-8} (\rho l_r)^{0.65} .$$

3.2.2.4 Density of Air Containing Water Vapor - The equation of state utilized is that of a perfect gas consisting of air and water vapor. The expression is

$$p = \rho RT \left\{ \frac{1 + r/m}{1 + r} \right\}$$

where  $m$  is the ratio of the molecular weight of water and dry air. The pressure  $p$  is treated as  $p_0(z)$ , the initial atmospheric distribution, while  $T$  and  $r$  are allowed to vary in both the horizontal and vertical directions.

### 3.2.3 Test Problem

The test problem selected for the moisture code was chosen such that the initial water vapor content input into the atmosphere was an amount equal to the saturated value calculated by the prescription described in Section 3.2.2. The configuration of the problem was identical to the two wave problems described in Section 4.2, i.e., an obstacle height of 625 meters and a cell height of 312.5 meters.

The results of the calculation, run to a time of 1672 seconds, are shown in Figures 3.10 through 3.13. These include streamlines, vertical velocity contours, cloud water contours and rain water contours. The formation of the clouds and their movement downwind of the obstacle as a function of time is realistic physically.

Figures 3.14 and 3.15 show vertical velocity contour plots from the computer printouts at times of 1673 and 1669 seconds for the moisture and dry calculations, respectively. The numbers on the figures indicate the relative velocity in each region, i.e., the larger numbers represent positive velocities while the lower numbers represent the negative velocities.

As the computer results were compared at various times, the buoyancy forces caused by the condensation or evaporation of water as air rises or falls over the obstacle became apparent. As the air rose at the forward position of the mountain, water vapor condensed out creating a positive buoyancy force and an increase in vertical air velocity due to its rise in temperature. As the cloud water falls in the lee of the obstacle, energy is removed from the air, dropping

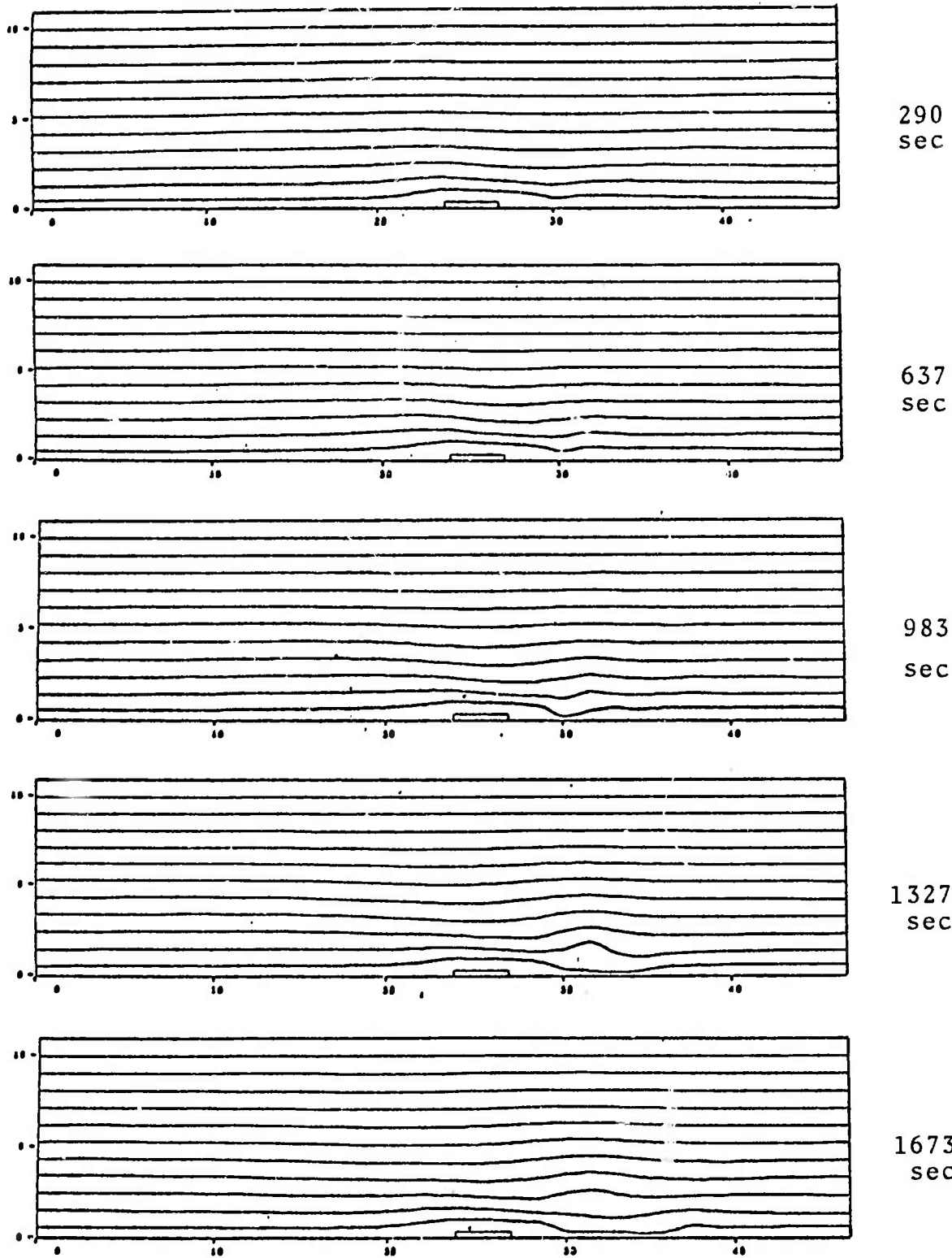


Figure 3.10. Streamline pattern - Two wave problem with moisture effects.

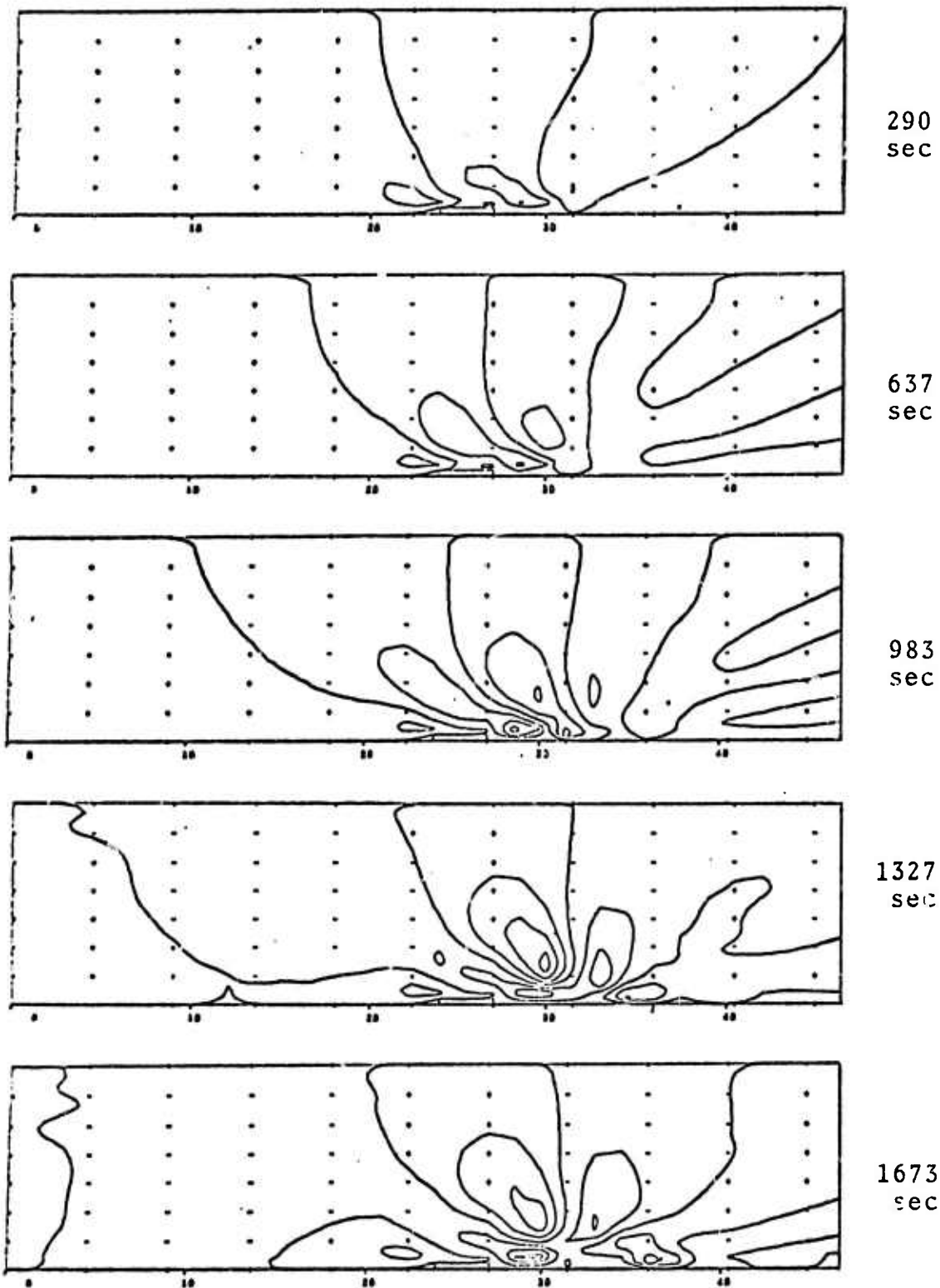
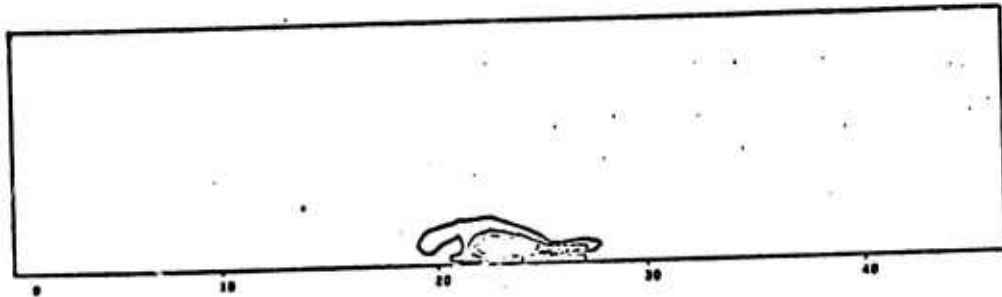
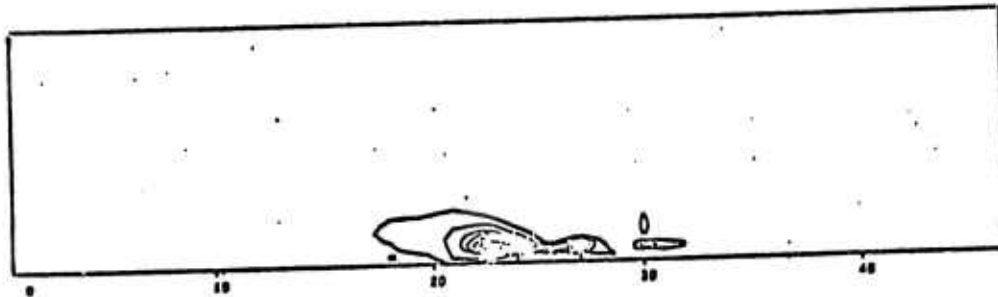


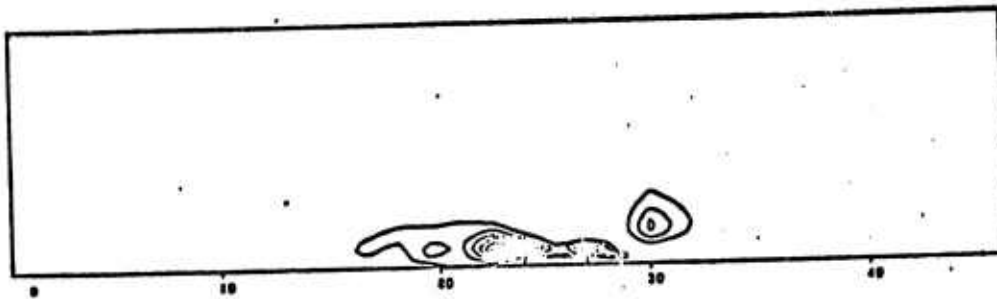
Figure 3.11. Vertical velocity contours - Two wave problem with moisture effects.



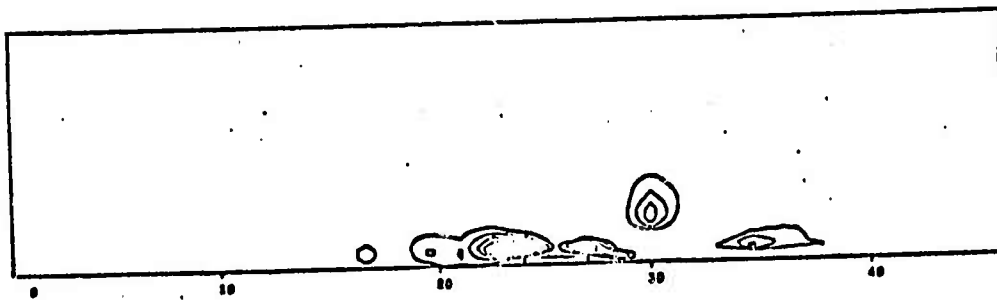
290 sec



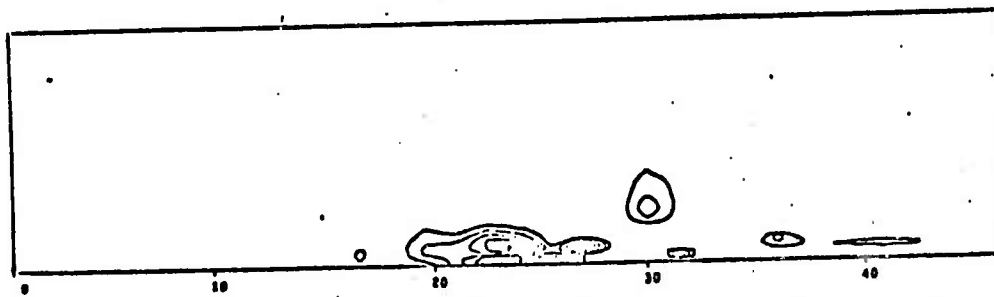
657 sec



938 sec



1327 sec



1673 sec

Figure 3.12. Cloud formation - Two wave problem with moisture effects.

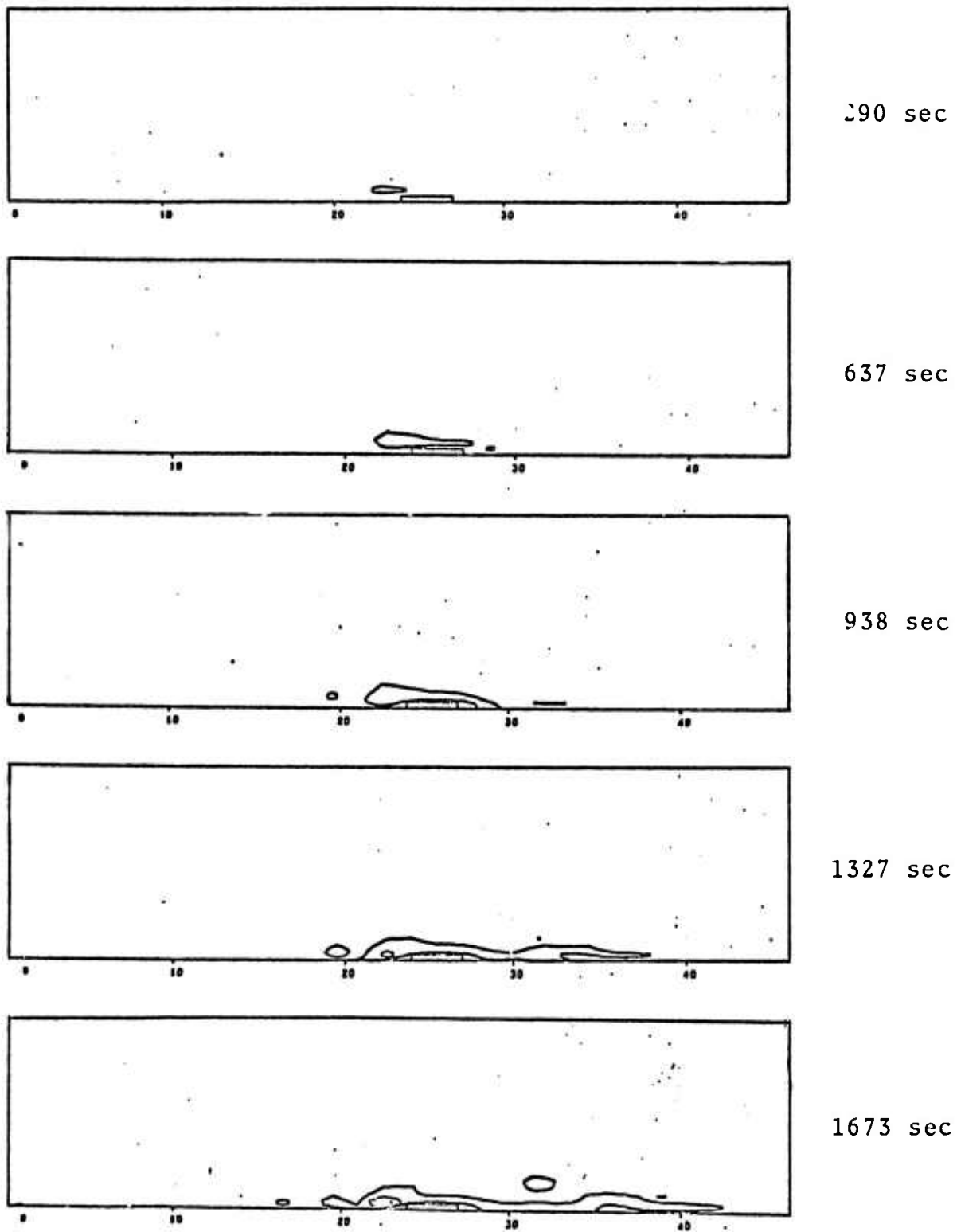


Figure 3.13. Rain water contours - Two wave problem with moisture effects.



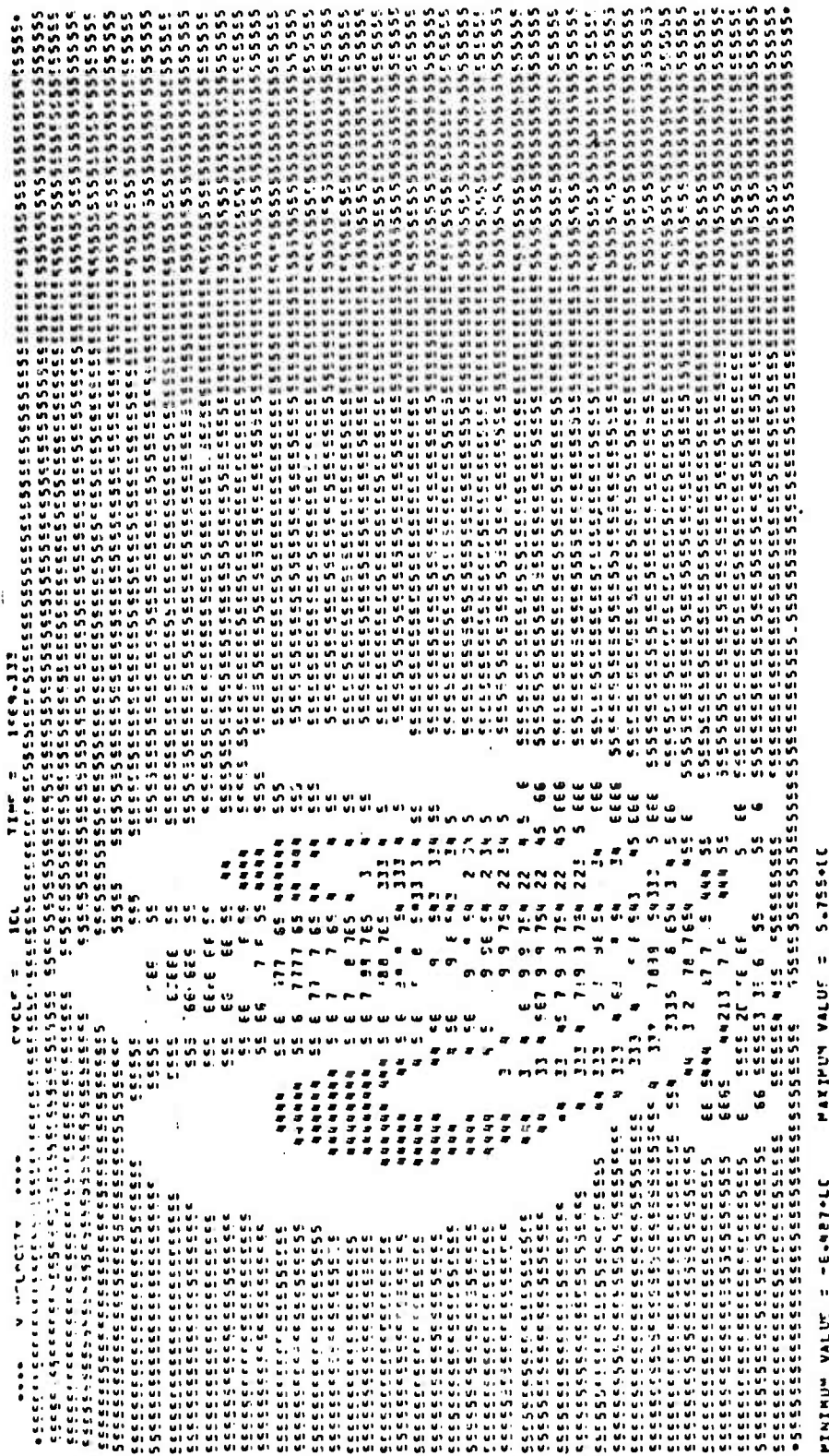


Figure 3.15. Computer plot of vertical velocity contours - Two wave problem.

its temperature and a stronger downdrift is created. These phenomena effect the velocity profiles in different ways at various times.

The momentum flux results shown in Figure 3.16 indicates only minor differences in drag between the moist and dry cases. However, since the problem has only been run a short time, the results do not necessarily reflect those expected near steady state.

### 3.3 ZONING MODIFICATIONS IN THE HAIFA CODE IN VERTICAL DIRECTION

#### 3.3.1 Variable Zoning in the Vertical Direction

The modifications to the basic HAIFA code that will enable it to operate with a mesh of variable spacing in the vertical direction are examined in this section. This modification affords the ability to resolve more finely certain areas without excessively slowing the computation by requiring fine zoning throughout the grid. Modifications to two routines of the code are necessary. They are the Poisson equation solver, and the vertical advection subroutine. Each modification is discussed below.

##### 3.3.1.1 The Poisson Solver

The use of the Fast Fourier Transform in the horizontal x-direction imposes the limitation that the spatial interval,  $\Delta x$ , be constant. In the vertical direction, however, the solution of the Poisson equation is obtained by Gaussian elimination and is not limited to a constant spatial interval.

The Gaussian elimination subroutine of POISPK solves a system of difference equations approximating

$$\frac{\partial^2 \psi}{\partial z^2} - \alpha \psi = Q \quad . \quad (3.37)$$

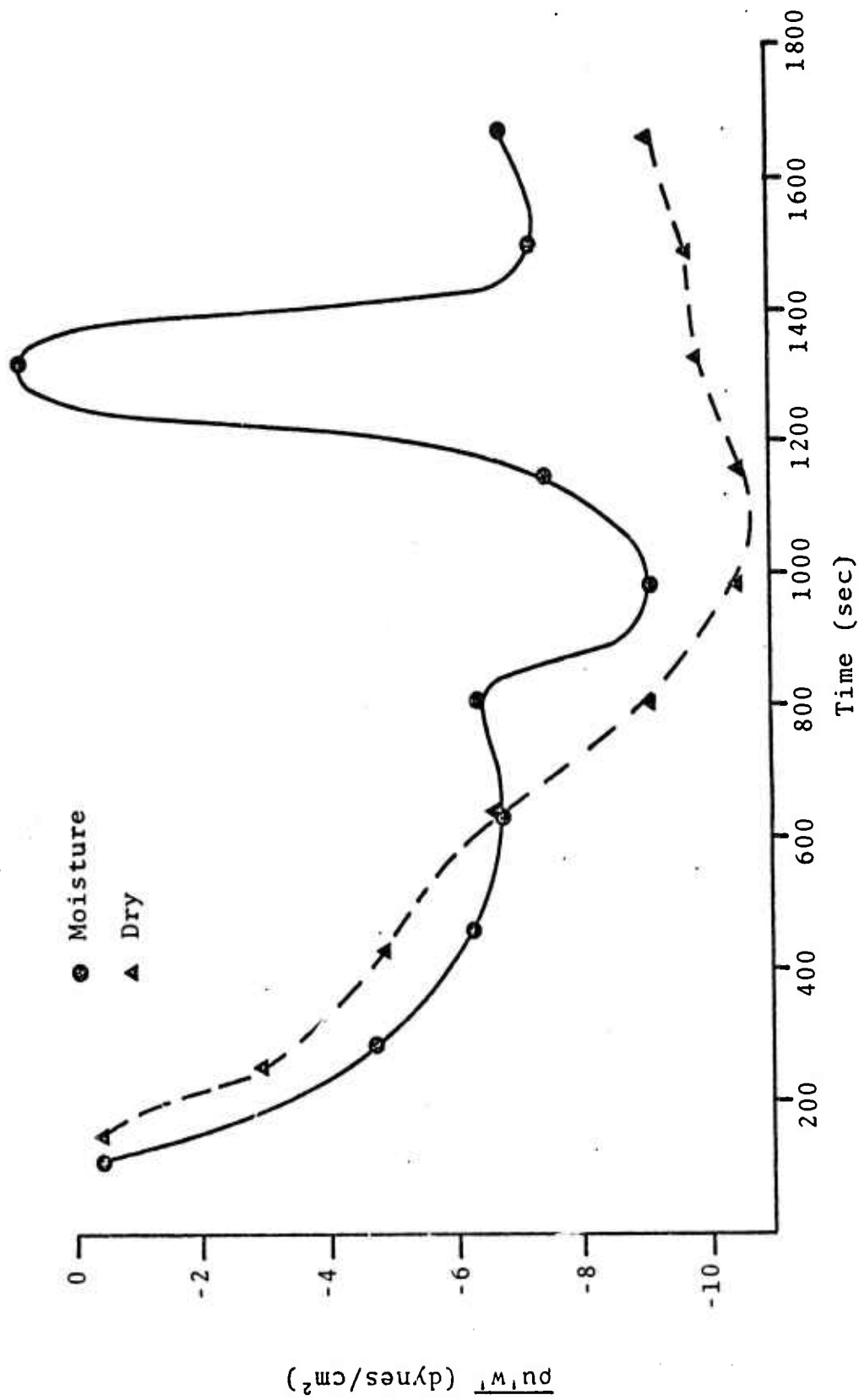


Figure 3.16. Comparison of two wave problem with and without moisture momentum transfer above obstacle.

The solution of these equations is briefly outlined below:

The finite difference form of Eq. (3.37) may be written as a tridiagonal system

$$A_i \psi_{i+1} + B_i \psi_i + C_i \psi_{i-1} = D_i \quad (3.38)$$

Letting

$$\psi_i = E_i \psi_{i+1} + G_i \quad (3.39)$$

which implies

$$\psi_{i-1} = E_{i-1} \psi_i + G_{i-1} \quad (3.40)$$

and substituting into the tridiagonal system, the coefficients  $E_i$  and  $G_i$  may be expressed as

$$E_i = - \frac{A_i}{B_i + C_i E_{i-1}} \quad (3.41)$$

$$G_i = \frac{D_i - C_i G_{i-1}}{B_i + C_i E_{i-1}} \quad (3.42)$$

The finite difference form of Eq. (3.37) for constant vertical zoning is

$$\frac{\psi_{i+1} - [2 + \alpha(\Delta z)^2] \psi_i + \psi_{i-1}}{(\Delta z)^2} = Q_i \quad (3.43)$$

and the coefficients  $A_i$ ,  $B_i$ ,  $C_i$ , and  $D_i$  are thus equivalent to

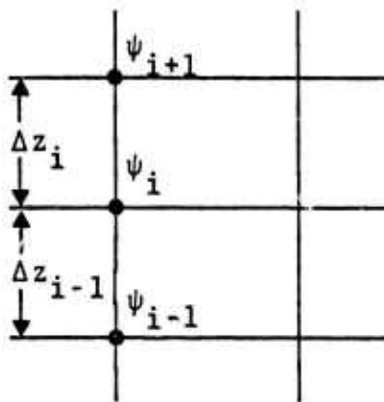
$$\begin{aligned} A_i &= 1/(\Delta z)^2, \\ B_i &= -\alpha - 2/(\Delta z)^2, \\ C_i &= 1/(\Delta z)^2, \\ D_i &= Q_i. \end{aligned} \tag{3.44}$$

Using these coefficients,  $E_i$  and  $G_i$  can be calculated and thus the  $\psi_i$  may be solved for recursively.

With variable zoning the finite difference form of Eq. (3.37) becomes

$$\frac{\frac{\psi_{i+1} - \psi_i}{\Delta z_i} - \frac{\psi_i - \psi_{i-1}}{\Delta z_{i-1}}}{\frac{\Delta z_i + \Delta z_{i-1}}{2}} - \alpha \psi_i = Q_i, \tag{3.45}$$

where the location of  $\psi$  and  $\Delta z$  are shown below,



The coefficients  $A_i$ ,  $B_i$ ,  $C_i$ , and  $D_i$  are now equivalent to

$$\begin{aligned} A_i &= 1/(\Delta z_i (\Delta z_i + \Delta z_{i-1})/2) \\ B_i &= -2/(\Delta z_i \Delta z_{i-1}) - \alpha \\ C_i &= 1/(\Delta z_{i-1} (\Delta z_i + \Delta z_{i-1})/2) \\ D_i &= Q_i \end{aligned} \quad (3.46)$$

The values of  $E_i$  and  $G_i$  are computed using the above coefficients and  $\psi_i$  is computed in the same manner as indicated above by Eq. (3.40).

### 3.3.1.2 Vertical Advection

The advection schemes discussed previously are valid for uniform zones only. The equivalent scheme for variable size zones is derived below for the Crowley second order scheme. It has been incorporated into a version of HAIFA.

The one-dimensional advection equation in conservation form may be written for flow in the z-direction as follows:

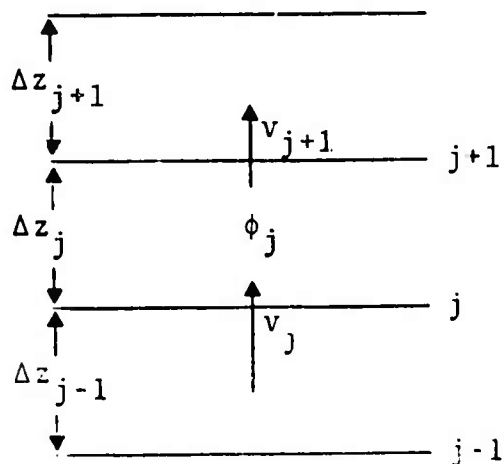
$$\frac{\partial \phi}{\partial t} + \frac{\partial}{\partial z}(v\phi) = 0 \quad , \quad (3.47)$$

where  $\phi$  is a variable representing the quantity to be advected. Only the one-dimensional equation need be considered due to the splitting technique used in HAIFA.

In finite difference form, Eq. (3.47) is

$$\phi_j^{n+1} = \phi_j^n - \frac{\Delta t}{\Delta z_j} \left[ (v\phi)_{j+1} - (v\phi)_j \right] \quad . \quad (3.48)$$

The term  $\Delta(v\phi)_j$  requires the flux across the boundary of the  $j$  cell (see figure below).



The flux at the  $j+1$  boundary may be expressed as  $v_{j+1} \phi_b$  where  $\phi_b$  represents the value of the variable  $\phi$  at that boundary. Assuming  $\phi$  to vary linearly between zone centers, this flux may be expressed as

$$v\phi)_{\text{boundary}} = \frac{1}{\Delta t} \int_{t^n}^{t^{n+1}} v\phi \, dt = \frac{1}{\Delta t} \int_{z-vt}^z \phi \, dz \quad (3.49)$$

Assuming  $\phi = a + bz$ , and integrating,

$$v\phi)_{\text{boundary}} = F_{j+1} = v_{j+1} \left[ \phi_j + \frac{(\phi_{j+1} - \phi_j) \Delta z_j}{\Delta z_{j+1} + \Delta z_j} \right] - v_{j+1}^2 \Delta t \frac{\phi_{j+1} - \phi_j}{\Delta z_{j+1} + \Delta z_j} \quad (3.50)$$

The new value of  $\phi_j^{n+1}$  can then be expressed using Eq. (3.50) as

$$\phi_j^{n+1} = \phi_j^n + \frac{\Delta t}{\Delta z_j} (F_j - F_{j+1}) \quad (3.51)$$

### 3.3.1.3 Test Calculations for Variable Vertical Zoning

Three test problems were performed using a 625 meter high mountain similar to the single wave problem described in Section 4.1. The initial input to this problem was (1) a temperature lapse rate equal to one-half the dry adiabatic, (2) an obstacle measuring 625 meters high by 4500 meters long, and (3) an exponential horizontal velocity profile described by the equation

$$u = 9.94 \exp (1.795 \times 10^{-4} z) .$$

Two of the test problems used constant vertical grid heights and the BASIC HAIFA code. The grid heights were 312.5 meters and 208.5 meters. The results were compared with a third problem run using a variable vertical grid size. This grid varied from 125 meters near the lower boundary to 738 meters at the upper boundary. The total number of vertical zones in all three calculations was the same.

Figures 3.17 and 3.18 contain the detailed comparison for the  $\Delta z = 312.5$  meter problem and the variable  $\Delta z$  problem of the temperature and vorticity at times of approximately 1500 seconds. Quantities are shown as a function of  $z$  for three locations; just upstream of the obstacle ( $I=16$ ), just downstream of the obstacle ( $I=24$ ), and far downstream of the obstacle ( $I=36$ ).

It can be noted that the trends in the results are the same for both problems. However, some differences in the computed values, particularly at small heights, are large. Part of this discrepancy was thought to be due to the smaller grid near the lower boundary. As a result, the problem was re-run using constant  $\Delta z$  equal to 208.3 meters. The results were closer to the variable  $\Delta z$  case indicating that the grid size was playing an important role in the detailed results.

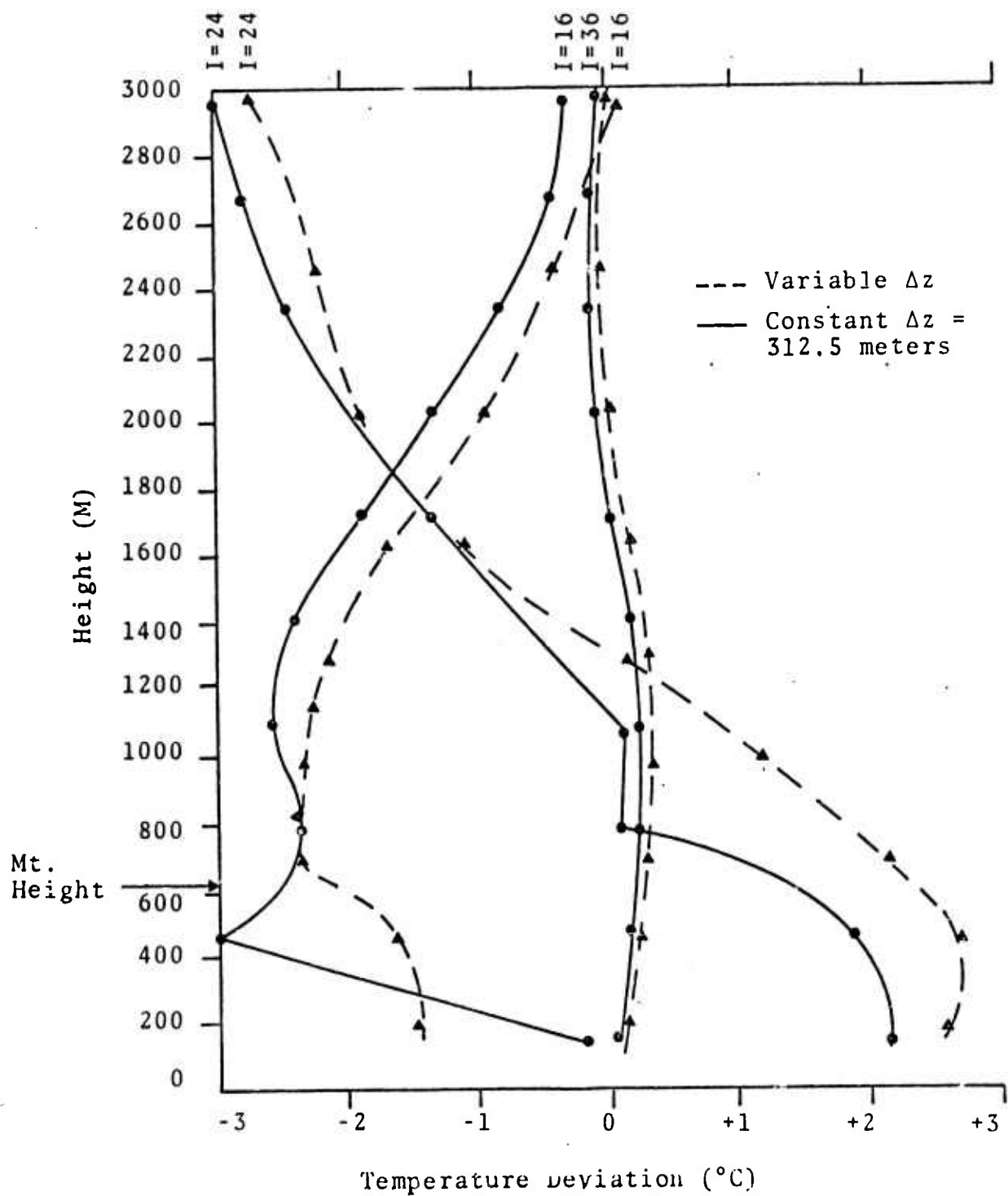


Figure 3.17. Comparison of variable  $\Delta z$  and constant  $\Delta z$  HAIFA - temperature deviations.

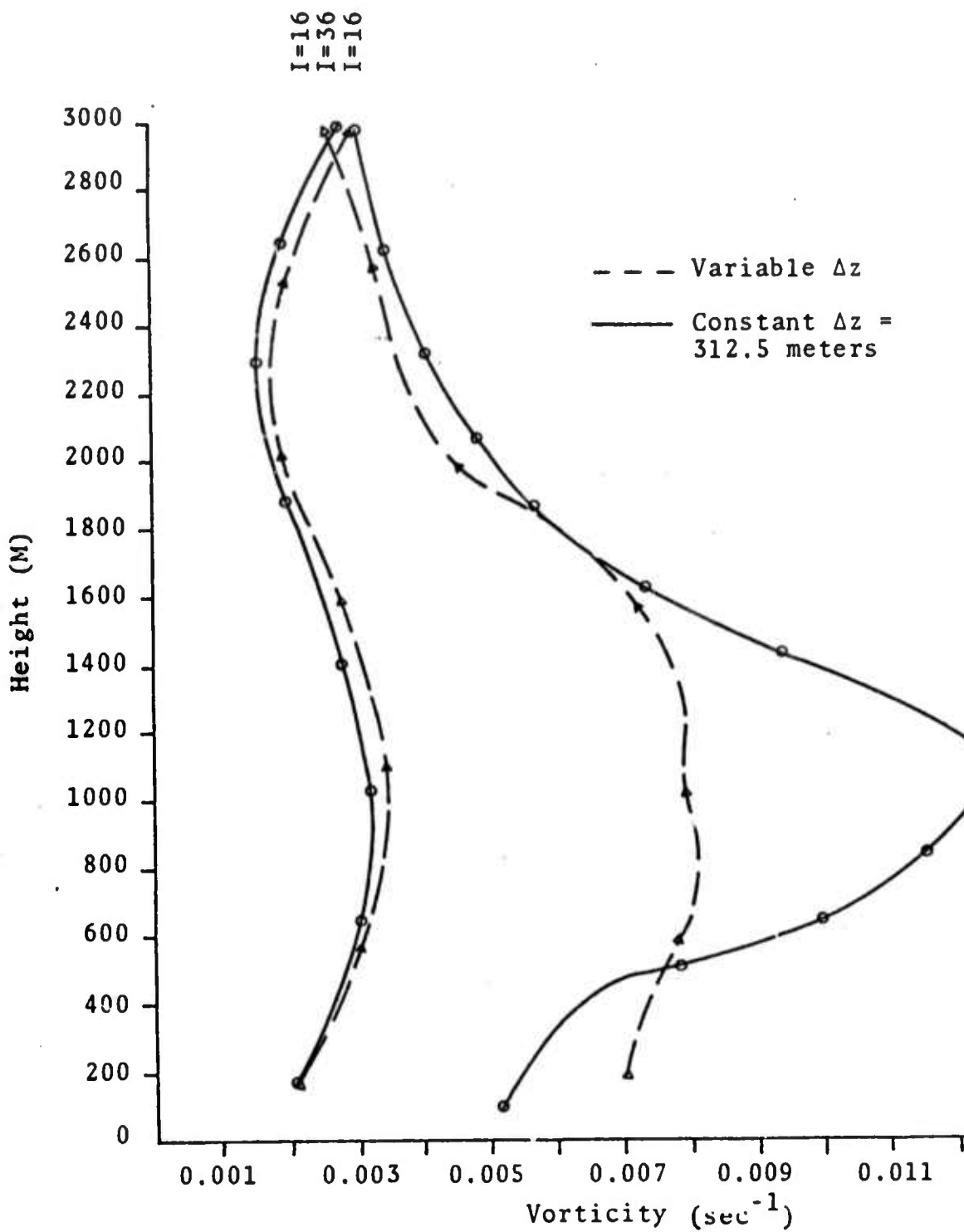


Figure 3.18a. Comparison of variable  $\Delta z$  and constant  $\Delta z$  HAIFA - vorticity.

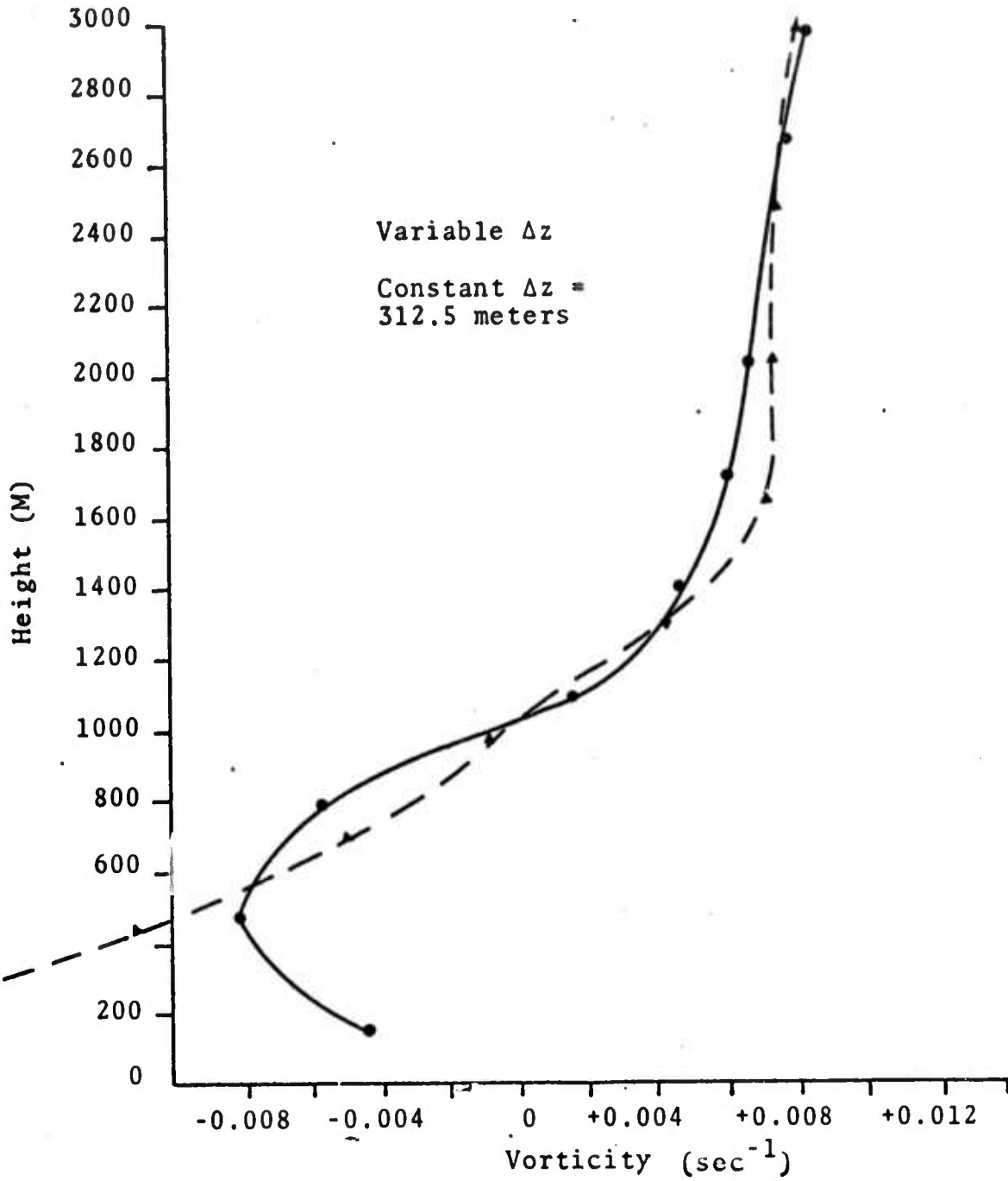


Figure 3.18b. Comparison of variable  $\Delta z$  and constant  $\Delta z$  HAIFA - vorticity.

Figure 7.19 shows the momentum flux at a height of 781 meters for the three problems as a function of time. The good agreement between the small constant  $\Delta z$  case and the variable  $\Delta z$  problem should be noted. In particular, the cyclic behavior of the drag values is not as pronounced as in the larger zoned case.

### 3.3.1 Numerical Checks of Crowley's Advection Scheme

The integration of the advection terms in the present HAIFA codes is done using Crowley's second-order finite difference method. This section describes investigations of the accuracy of this scheme, and modifications of the original scheme to improve accuracy.

The BASIC HAIFA code was used as a test bed to check the accuracy of Crowley's advection scheme. Setting the derivatives of the temperature profile to the adiabatic lapse rate reduces the HAIFA equations to:

$$\nabla^2 \psi = \eta \quad ,$$

$$\frac{\partial \eta}{\partial t} + \nabla(\vec{u}\eta) = 0 \quad ,$$

$$\frac{\partial T}{\partial t} + \nabla(\vec{u}T) = 0 \quad .$$

A wind profile of  $u = 10 + 0.01z$  m/sec was used which gives an initial vorticity field of  $\eta = 0.01 \text{ sec}^{-1}$  .

Zoning for a calculation reported in Section 4.1 was used ( $\Delta x = 1500\text{m}$ ,  $\Delta z = 312.5$ ) with an obstacle 625 meters high and 4500 meters long. The problem was run for 30 cycles with an

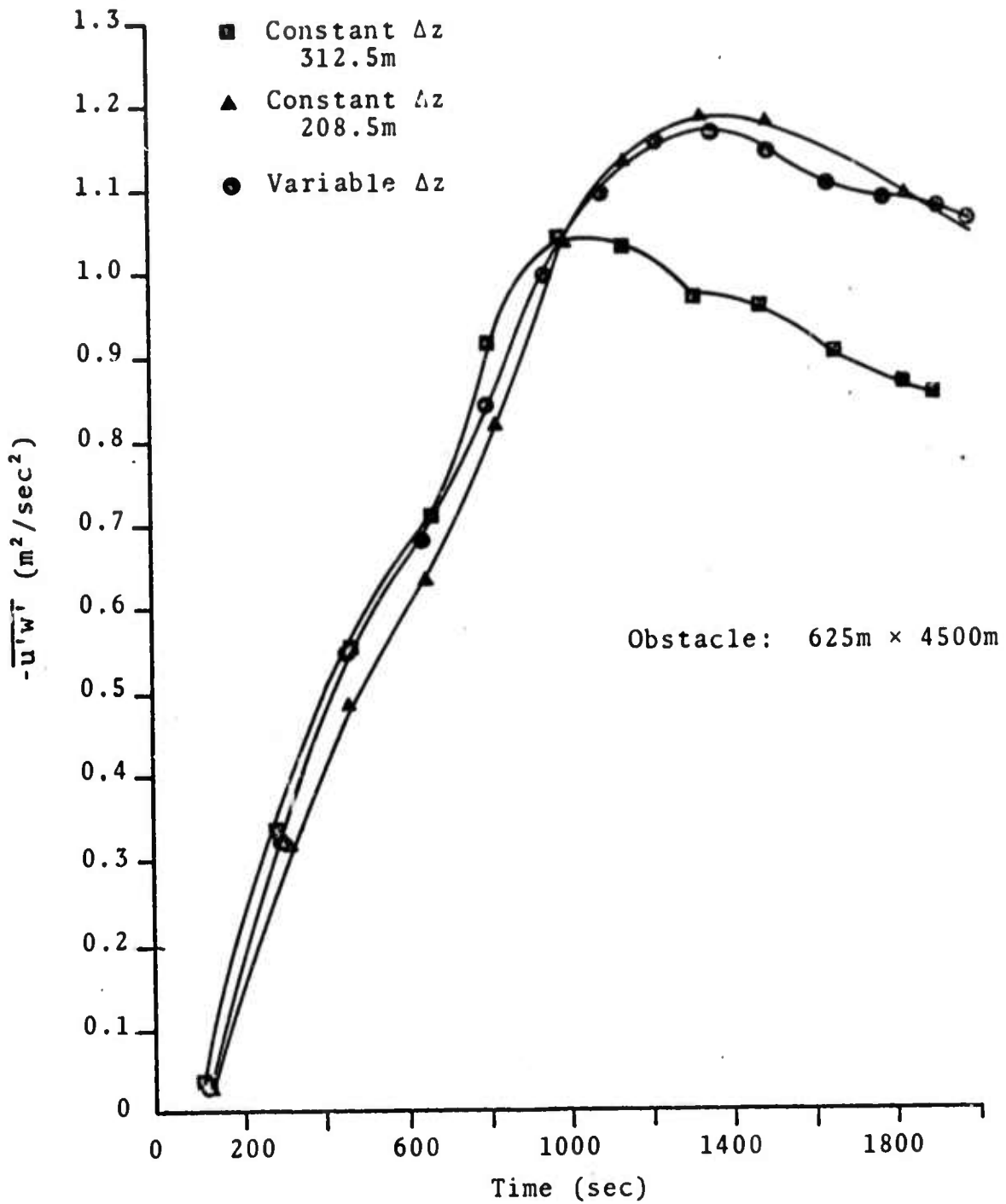


Figure 3.19. Comparison of variable  $\Delta z$  and constant  $\Delta z$  HAIFA codes - momentum flux edits at 781 meters.

edit of the mean kinetic energy, and mean squared vorticity taken every 10 cycles. Since there are no energy terms in the reduced HAIFA equations, there should be no change in mean square vorticity and the kinetic energy; any change is an indication of the errors induced into the code by the advection scheme. Table 3.1 gives the results of the first test run with the Crowley second-order advection scheme.

A correction procedure for the advection treatment has been suggested.<sup>[17]</sup> This improvement consists of limiting the value of the updated value to be between the maximum and minimum of the original values of the cell and nearest neighboring cells.

$$\min(C_{i-1}^n, C_i^n, C_{i+1}^n) \leq C^{n+1} \leq \max(C_{i-1}^n, C_i^n, C_{i+1}^n)$$

This technique has the advantage of smoothing the solution of the advection equation and thus improving stability and accuracy. However, it also has the disadvantage of not insuring conservation. A test run was made for this modified Crowley scheme with the same conditions as the test described previously. The results given in Table 3.2 show that to the limit of accuracy of the computer, the modified Crowley scheme conserved both kinetic energy and mean square vorticity.

TABLE 3.1  
 Test Advection Schemes  
 Crowley Second-Order

CYCLE	$\int_{KE}$	$\int_{\eta^2}$
0	$5.809652 \times 10^6$	$2.239996 \times 10^{-1}$
1	5.809652	2.239996
10	5.809647	2.240003
20	5.809634	2.240020
30	5.809616	2.240033
% Difference per cycle	$-2 \times 10^{-5}$	$+5 \times 10^{-5}$

TABLE 3.2  
 Crowley Second-Order with the Restriction:  
 $\min(C_{i-1}, C_i, C_{i+1}) < C\Delta t < \max(C_{i-1}, C_i, C_{i+1})$

CYCLE	$\int_{KE}$	$\int_{\eta^2}$
0	$5.809652 \times 10^6$	$2.233996 \times 10^{-1}$
1	"	"
10	"	"
20	"	"
30	"	"
% Difference per cycle	0	0

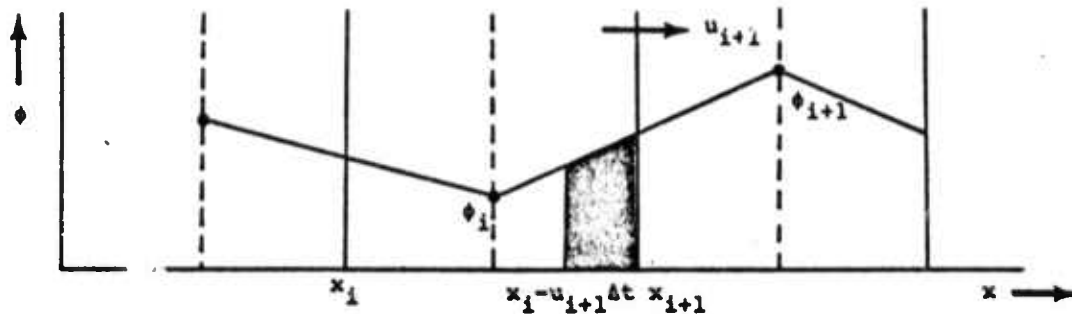
### 3.3.3 Triangular Zones in HAIFA

The addition of non-rectangular zones to the grid requires alteration of the code in three major areas. The Crowley advection scheme must be modified to include flow between rectangular and triangular zones. The Poisson solver must consider calculation of node-centered vorticities in the presence of triangular zones. Finally, needed space derivatives must be appropriately approximated in regions near triangular zones.

The practice of using triangular zones requires assumptions concerning the nature of the flow through the zone boundaries. We have assumed in this case that the flux is uniform along the unobstructed boundaries with all cell centered quantities located at the centroids of the cells. Clearly, there are other assumptions concerning the location for the cell centered quantities which could be made. These two assumptions, however, allow a simple adaptation of the flux scheme which seems to give qualitatively reasonable results. This scheme needs further testing, however, and further modifications may be required.

For completeness, the Crowley advection scheme [1] is described below for the case of rectangular zones. The case of triangular zoning follows immediately with results for left facing and right facing slopes presented. Since the Crowley scheme utilizes the splitting technique in which spatial dimensions are calculated sequentially, the scheme is derived for the one-dimensional case, it being a trivial matter to extend to two dimensions.

Assuming that the dynamic variable  $\phi$  varies linearly between cells we obtain the following pictorial representation.



where the ordinate represents the variable  $\phi$ , whose distribution is given by the piecewise continuous diagonal line. This assumption results in Crowley's second-order scheme. If  $\phi$  were fitted to a cubic between cells, the fourth-order scheme would be realized. The vertical bars represent cell boundaries in  $x$ , while the dashed lines indicate cell midpoints. The shaded area represents the material advected out of face  $x = x_{i+1}$  in a time  $\Delta t$ . The flux through this boundary is given by:

$$\begin{aligned}
 F_{i+1} &= \frac{1}{\Delta t} \int_{x_{i+1} - u_{i+1} \Delta t}^{x_{i+1}} \phi(x) dx = \frac{1}{\Delta t} \int_{x_{i+1} - u_{i+1} \Delta t}^{x_{i+1}} (a + bx) dx, \\
 &= \frac{1}{\Delta t} \left( ax + \frac{b}{2} x^2 \right) \Big|_{x_{i+1} - u_{i+1} \Delta t}^{x_{i+1}}, \\
 &= a u_{i+1} + b x_{i+1} u_{i+1} - \frac{b}{2} u_{i+1}^2 \Delta t. \quad (3.52)
 \end{aligned}$$

Under the assumption of linearity:

$$\begin{aligned} \phi_i &= a + b x_{i+1/2} & b &= \frac{\phi_{i+1} - \phi_i}{x_{i+3/2} - x_{i+1/2}} \\ & & \text{or} & \\ \phi_{i+1} &= a + b x_{i+3/2} & a &= \phi_i - b x_{i+1/2} \end{aligned} \quad (3.53)$$

For a constant  $\Delta x$ :

$$x_{i+1/2} = x_i + \Delta x/2 ,$$

$$x_{i+3/2} = x_{i+1} + \Delta x/2 ,$$

and

$$x_{i+3/2} - x_{i+1/2} = \Delta x, \quad (3.54)$$

Plugging in for  $a$  and  $b$  the flux becomes:

$$F_{i+1} = \frac{1}{2}(\phi_i + \phi_{i+1}) u_{i+1} - \frac{1}{2}(\phi_{i+1} - \phi_i) u_{i+1}^2 \frac{\Delta t}{\Delta x} \quad (3.55)$$

defining

$$\alpha = u_{i+1} \frac{\Delta t}{\Delta x} ,$$

we have

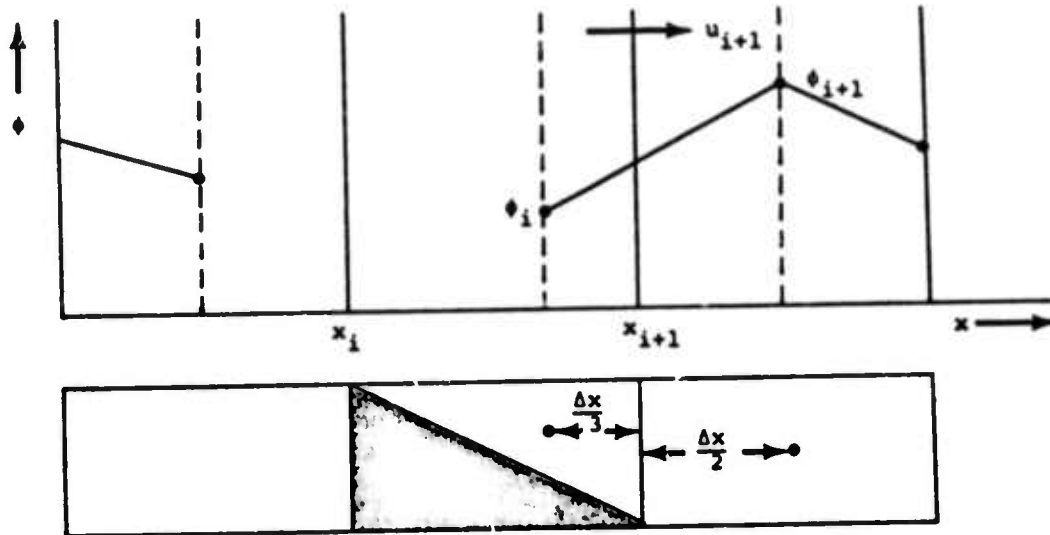
$$F_{i+1} \frac{\Delta t}{\Delta x} = \frac{\alpha}{2}(\phi_{i+1} + \phi_i) - \frac{\alpha^2}{2}(\phi_{i+1} - \phi_i) \quad (3.56)$$

Finally:

$$(\phi_i^{n+1} - \phi_i^n) = - \frac{\Delta t}{\Delta x} (F_{i+1} - F_i) \quad (3.57)$$

which is Crowley's result.

Upon introduction of triangular zones, the assumption of constant  $\Delta x$  is no longer valid. The scheme is altered as follows for a right facing zone:



The scheme is identical to the above case up to the assumption of linearity. We now have:

$$\phi_i = a + b x_{i+2/3} \quad b = \frac{\phi_{i+1} - \phi_i}{x_{i+3/2} - x_{i+2/3}}$$

or

$$\phi_{i+1} = a + b x_{i+3/2}$$

and

$$x_{i+3/2} - x_{i+2/3} = \frac{5}{6} \Delta x \quad (3.58)$$

Upon substitution for a and b we have:

$$F_{i+1} = \left( \frac{3}{5} \phi_i + \frac{2}{5} \phi_{i+1} \right) u_{i+1} - \frac{3}{5} (\phi_{i+1} - \phi_i) u_{i+1}^2 \frac{\Delta t}{\Delta x} \quad (3.59)$$

defining

$$\alpha = u_{i+1} \frac{\Delta t}{\Delta x}$$

then

$$F_{i+1} \frac{\Delta t}{\Delta x} = \frac{2\alpha}{5} (\phi_{i+1} + 1.5\phi_i) - \frac{3\alpha^2}{5} (\phi_{i+1} - \phi_i) \quad (3.60)$$

Finally:

$$(\phi_i^{n+1} - \phi_i^n) = - \frac{\Delta t}{\Delta x} (F_{i+1} - F_i) \quad (3.61)$$

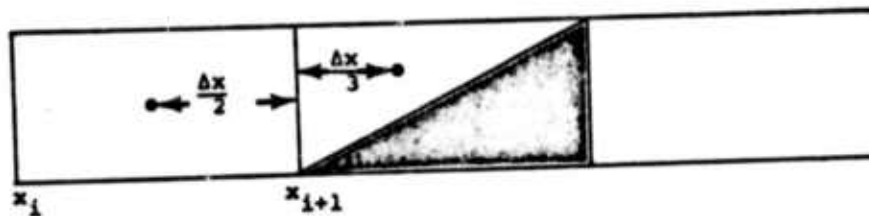
For the case of the left facing zone a similar derivation results in

$$F_{i+1} \frac{\Delta t}{\Delta x} = \frac{2\alpha}{5} (1.5\phi_{i+1} + \phi_i) - \frac{3\alpha^2}{5} (\phi_{i+1} - \phi_i) \quad (3.62)$$

and

$$(\phi_i^{n+1} - \phi_i^n) = - \frac{\Delta t}{\Delta x} (F_{i+1} - F_i) \quad (3.63)$$

where the reference grid is



The fact that adjacent cells in this derivation have centered values which are spatially non-aligned in the complementary dimension was ignored. The effect of this neglect is not negligible (on the order of 10 percent), but the law of diminishing returns applies.

Another necessary modification to the HAIFA code occurs in the Poisson solver routine. Specifically, the Poisson solver requires node-centered vortices in its solution for the stream function. Normally, the vorticity is carried as a cell-centered quantity so that it may be easily handled in the vorticity transport equation, and converted via an averaging process when the Poisson solver is called. With the introduction of triangular zones, this averaging process must be altered. Utilizing Figure 3.20 we define the following:

$$D = (\Delta x^2 + \Delta z^2)^{1/2} / 2 ,$$

and

$$B = \frac{2}{3} D .$$

Using these quantities, one performs a weighted averaging process on the four cell centered vorticities surrounding the point  $i, j$ .

We have

$$\begin{aligned} \eta_{i,j} &= \left( \frac{\eta_1}{D} + \frac{\eta_2}{D} + \frac{\eta_3}{D} + \frac{\eta_4}{B} \right) / \left( \frac{3}{D} + \frac{1}{B} \right) \\ &= 0.222(\eta_1 + \eta_2 + \eta_3) + 0.333 \eta_4 \end{aligned} \quad (3.64)$$

No further alteration of the Poisson solver is needed.

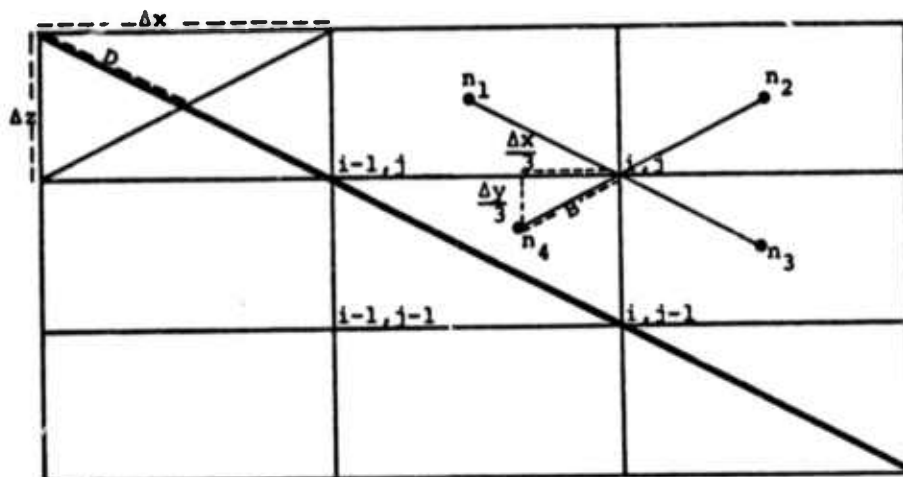
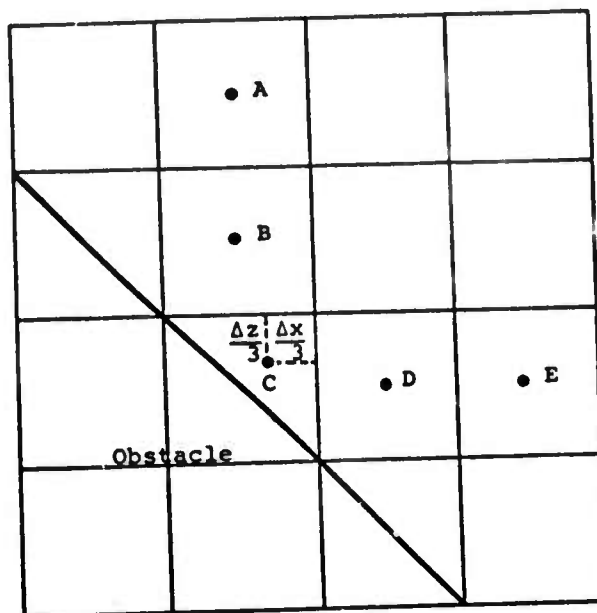


Figure 3.20. Determination of node-centered vorticity.

The final code alteration needed to effect incorporation of triangular zones is in the method of calculating the needed space derivatives. In the figure below, space derivatives calculated for cells B, C and D will be affected by the presence of triangular zone C.



The approximations used by HAIFA are summarized below, where  $\phi$  is any dynamic variable:

$$\frac{\partial \phi_C}{\partial x} = (\phi_D - \phi_C) / \frac{5}{6} \Delta x \quad , \quad \frac{\partial \phi_C}{\partial y} = (\phi_B - \phi_C) / \frac{5}{6} \Delta z$$

$$\frac{\partial \phi_D}{\partial x} = (\phi_E - \phi_C) / \frac{11}{6} \Delta x \quad , \quad \frac{\partial \phi_B}{\partial y} = (\phi_A - \phi_C) / \frac{11}{6} \Delta z. \quad (3.65)$$

Again, the spatial misalignment of the cell-centered quantities has been neglected in order to facilitate the calculation. Results have shown that this neglect does not noticeably affect the solution.

### 3.4 CORIOLIS TERMS IN HAIFA

The characteristic distance scale for the Coriolis force is  $L_f = u/f$ , where  $u$  is a typical wind speed and  $f$  is the Coriolis parameter (if  $u \sim 10$  m/s, we obtain  $L_f \sim 100$  km). When the mountain range is comparable to  $L_f$ , an appreciable modification of the gravity waves will result to form a complex system of gravity-inertia waves.

Since the Coriolis force induces a turning of the wind it is necessary to take into account several new factors in the calculations:

- (1) the component of the wind parallel to the mountain;
- (2) pressure gradients in directions parallel and perpendicular to the mountain must be included to establish geostrophic balance in the unperturbed flow; and
- (3) the vertical atmosphere structure is slightly modified to account for the Coriolis contribution to the hydrostatic balance condition.

In the following formulation we attempt to parallel the numerical treatment of the HAIFA code as closely as feasible in order to be able to compare the effects of the Coriolis terms with those pertaining to a non-rotating Earth.

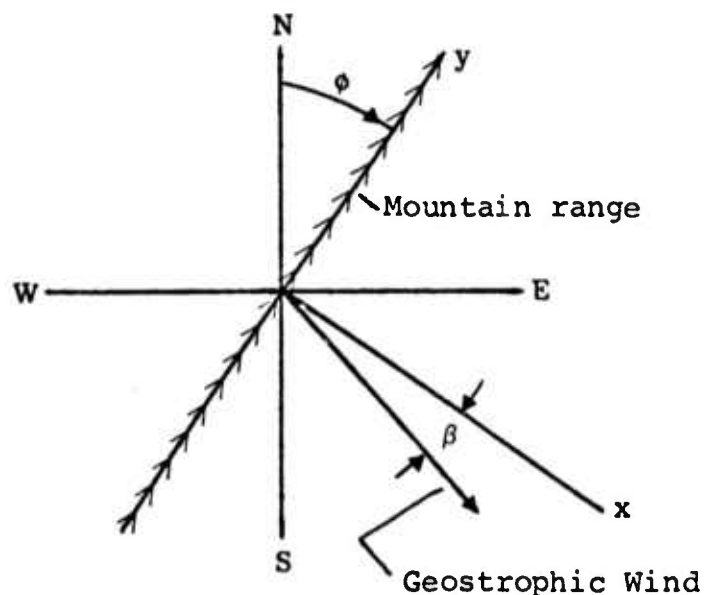
#### 3.4.1 Formulation

The differential equations of the dry atmosphere are formulated in a system of reference fixed to a rotating Earth. As discussed by Thompson<sup>[18]</sup> we incorporate the centrifugal terms into the definition of the local gravity to obtain

$$\frac{d\vec{U}}{dt} + 2\vec{\Omega} \times \vec{U} = -\frac{1}{\rho} \nabla P - \hat{k}g, \quad (3.66)$$

where  $\vec{U}$  is the velocity relative to the Earth's surface,  $\vec{\Omega}$  is the rotational velocity of the Earth,  $P$  is the pressure,  $\rho$  is the density of the atmosphere,  $g$  is the local acceleration of gravity which is assumed to act in the vertical direction  $\hat{k}$ . The time derivative is that evaluated following the fluid motion. The equations of mass and energy conservation are not affected by the Coriolis force.

Neglecting the curvature of the Earth's surface (and the resulting centrifugal terms associated with the relative velocity), Eq. (3.66) can be resolved into components. We choose a Cartesian coordinate system in which the x-axis lies in the surface and forms an angle  $\phi$  with the eastward direction, the y-axis lies in the surface at the same angle  $\phi$  with the northward direction, and the z-axis is perpendicular positive upward. We shall subsequently assume that the x-axis is perpendicular to the 2-D mountain range which is oriented at the angle  $\phi$  with the northward direction (see figure below). Denoting  $x$ ,  $y$ , and  $z$  components of the velocity by  $u$ ,  $v$ ,  $w$ , the component equations are:



$$\frac{du}{dt} - 2\Omega \sin\theta v + 2\Omega \cos\theta \cos\phi w = -\frac{1}{\rho} \frac{\partial P}{\partial x} ,$$

$$\frac{dv}{dt} + 2\Omega \sin\theta u - 2\Omega \cos\theta \sin\phi w = \frac{1}{\rho} \frac{\partial P}{\partial y} ,$$

$$\frac{dw}{dt} - 2\Omega \cos\theta (u \cos\phi - v \sin\phi) = -\frac{1}{\rho} \frac{\partial P}{\partial z} - g , \quad (3.67)$$

where  $\Omega$  is the magnitude of the rotational velocity,  $\theta$  is the latitude of the position, and the time derivatives are those formed following the fluid motion.

In the absence of the mountain barrier we consider the atmosphere to be in geostrophic balance; the motion is unaccelerated, the vertical velocity component  $w$  is zero, and the pressure gradients are just balanced by the Coriolis and gravity terms. Denoting the geostrophic state by subscripts  $g$  we obtain

$$-2\Omega \sin\theta v_g = -\frac{1}{\rho_g} \frac{\partial P_g}{\partial x} ,$$

$$2\Omega \sin\theta u_g = -\frac{1}{\rho_g} \frac{\partial P_g}{\partial y} ,$$

$$-2\Omega \cos\theta (u_g \cos\phi - v_g \sin\phi) + g = -\frac{1}{\rho_g} \frac{\partial P_g}{\partial z} . \quad (3.68)$$

Since the velocity of the unperturbed state is taken to be independent of  $x$  and  $y$ , Eq. (3.68) shows that the pressure at most need depend linearly on  $x$  and  $y$ .

When the mountain is present the pressure, density and velocity are perturbed from their geostrophic values. It

will be convenient to introduce the deviation  $P'$  of the pressure from the geostrophic value:

$$P' = P - P_g \quad . \quad (3.69)$$

We also introduce the Boussinesq approximation, in which the departure of density from the geostrophic value is taken into account only in the gravity term of Eq. (3.68). In all other terms, we use the geostrophic density:

$$\frac{du}{dt} - 2\Omega \sin\theta (v - v_g) + 2\Omega \cos\theta \cos\phi w = - \frac{1}{\rho_g} \frac{\partial P'}{\partial x} \quad ,$$

$$\frac{dv}{dt} + 2\Omega \sin\theta (u - u_g) - 2\Omega \cos\theta \sin\phi w = - \frac{1}{\rho_g} \frac{\partial P'}{\partial y} \quad ,$$

$$\frac{dw}{dt} - 2\Omega \cos\theta [(u - u_g) \cos\phi - (v - v_g) \sin\phi] = - \frac{1}{\rho_g} \frac{\partial P'}{\partial z} + \left(1 - \frac{\rho}{\rho_g}\right) g \quad . \quad (3.70)$$

These equations constitute the Boussinesq approximation for the equations of motion when the geostrophic flow, assumed steady and independent of  $x$  and  $y$ , is perturbed. Clearly, they are only approximately satisfied in a local region, since  $u_g$  and  $v_g$  are not constant on the synoptic scale.

We now consider the special case in which the initial and boundary equations are independent of the  $y$ -coordinate, corresponding to a uniform but obliquely incident wind encountering a two-dimensional ridge, the topography of which is independent of  $y$ . In this case, the initial and boundary conditions and the equations depend only on the coordinates  $x$  and  $z$ . The resulting 2-D equations derived from Eq. (3.70) are:

$$\begin{aligned}
\frac{\partial u}{\partial t} + u \frac{\partial u}{\partial x} + w \frac{\partial u}{\partial z} - 2\Omega \sin\theta (v - v_g) + 2\Omega \cos\theta \cos\phi w &= - \frac{1}{\rho_g} \frac{\partial P'}{\partial x} , \\
\frac{\partial v}{\partial t} + u \frac{\partial v}{\partial x} + w \frac{\partial v}{\partial z} + 2\Omega \sin\theta (u - u_g) - 2\Omega \cos\theta \sin\phi w &= 0 , \\
\frac{\partial w}{\partial t} + u \frac{\partial w}{\partial x} + w \frac{\partial w}{\partial z} + 2\Omega \cos\theta [(u - u_g)\cos\phi - (v - v_g)\sin\phi] &= \\
- \frac{1}{\rho_g} \frac{\partial P'}{\partial z} + \left(1 - \frac{\rho}{\rho_g}\right) g . & \quad (3.71)
\end{aligned}$$

Equations (3.71) are to be supplemented with the equations of incompressibility and the temperature equation. These latter equations are unchanged from those in Section 2.1.

There are two major modifications of the equations which have resulted from the treatment of the rotation of the Earth:

(1) The component of the wind parallel to the range influences both the  $x$  and  $z$  momentum equations through the Coriolis terms. The  $y$  momentum component equation is only weakly coupled to the others and may be solved in a similar way to the temperature equation.

(2) Additional terms from the Coriolis force enter the momentum equations giving rise to new terms in the vorticity equation.

### 3.4.2 Difference Equations

The difference equation formulation corresponding to Eq. (3.71) and supplementary equations can be chosen to parallel that of the HAIFA code. The equation for the  $y$ -component of

vorticity is obtained by cross-differentiation of the  $x$  and  $z$  components of the momentum, thereby eliminating the pressure from the equations entirely. The resulting equations are:

$$\frac{\partial \eta}{\partial t} + u \frac{\partial \eta}{\partial x} + w \frac{\partial \eta}{\partial z} - 2\Omega \sin \theta \left( \frac{\partial v}{\partial z} - \frac{\partial v_g}{\partial z} \right) - 2\Omega \cos \theta \sin \phi \frac{\partial v}{\partial x} = \frac{g}{\rho_g} \frac{\partial \rho}{\partial x} ,$$

$$\frac{\partial v}{\partial t} + u \frac{\partial v}{\partial x} + w \frac{\partial v}{\partial z} + 2\Omega \sin \theta (u - u_g) - 2\Omega \cos \theta \sin \phi w = 0 , \quad (3.72)$$

where the  $y$ -component of vorticity,  $\eta$ , is defined by

$$\eta = \frac{\partial u}{\partial z} - \frac{\partial w}{\partial x} .$$

A quantity,  $v'$ , is now introduced which is the difference between the  $y$ -component of wind velocity and the  $y$ -component of the geostrophic wind,

$$v' = v - v_g .$$

The system of equations that HAIFA solves now becomes

$$\nabla^2 \psi = \eta \quad ; \quad u = \frac{\partial \psi}{\partial z} \quad ; \quad w = - \frac{\partial \psi}{\partial x} \quad ;$$

$$\frac{\partial T'}{\partial t} + \frac{\partial (uT')}{\partial x} + \frac{\partial (wT')}{\partial z} = - w\Gamma \quad ;$$

$$\begin{aligned} \frac{\partial \eta}{\partial t} + \frac{\partial (u\eta)}{\partial x} + \frac{\partial (w\eta)}{\partial z} - 2\Omega \sin \theta \frac{\partial v'}{\partial z} \\ - 2\Omega \cos \theta \sin \phi \frac{\partial v'}{\partial x} = \frac{g}{\rho_g} \frac{\partial \rho}{\partial x} \quad ; \end{aligned}$$

$$\frac{\partial v'}{\partial t} + \frac{\partial (uv')}{\partial x} + \frac{\partial (wv')}{\partial z} = -w \frac{\partial u}{\partial z} \quad (3.73)$$

$$- 2\Omega \sin\theta (u - u_g) + 2\Omega \cos\theta \sin\theta w = 0 \quad .$$

The difference approximations for the above equations follows that of the basic HAIFA formulation. The time-dependent equations are solved in an explicit two-level formulation. The advection terms are obtained by using a high order conservation scheme in which the two directions are integrated by the splitting technique. Additional terms are all centered in space from quantities available at the current time cycle. The additional equation for  $v'$  is similar to the temperature equation in structure. The vorticity equation is modified by gradients in the velocity perturbation. Changes in  $v'$  are due to both forcing terms which are the result of the Coriolis force actions on the  $u$ - and  $w$ -components of velocity and advection of the  $v_g$ -component of geostrophic velocity in the vertical direction. Depending on the geostrophic wind structure the advection term could dominate the change in the  $v'$  parameter.

### 3.4.3 Initial Conditions

The initial conditions for HAIFA modified to include Coriolis forces are the same as basic HAIFA except that the angle between the mountain range and the north-south direction and the angle between the geostrophic wind and the mountain range must be specified.

The figure in Section 3.4.1 defines the parameters used to describe the orientation of the geostrophic wind and the mountain range. The angles,  $\phi$  and  $\beta$ , are both specified in degrees;  $\phi$  is the angle that the mountain range makes with the

north-south coordinate, and  $\beta$  is the angle the geostrophic wind makes with respect to the direction normal to the mountain range. The x- and y-axis in the code corresponds to the direction along the mountain range and normal to the mountain range, respectively.

The other parameter required in the Coriolis terms is the latitude,  $\theta$ , which is specified in the usual manner, in degrees from the equator.

The initial geostrophic wind,  $\vec{u}_g$ , is simply the wind which would be present without the mountain. This wind is assumed not to vary in the vertical direction. Thus, it is similar to the initial u velocity in BASIC HAIFA except that the wind is not necessarily normal to the mountain. Noting that

$$\vec{u}_g(z) = u(z)\hat{x} + v(z)\hat{y} \quad (3.74)$$

and referring to the figure above we can calculate the initial u- and v-velocities by

$$u(z) = \cos\beta |\vec{u}_g(z)| \quad (3.75)$$

$$v(z) = \sin\beta |\vec{u}_g(z)|$$

#### 3.4.4 Test Problem

Several preliminary runs were made using HAIFA with Coriolis forces. The first runs were made with the angular velocity,  $\Omega$ , set to zero and with the initial wind perpendicular to the mountains in an attempt to duplicate the double wave problem run with the basic HAIFA code.

After verifying that HAIFA with Coriolis forces duplicates the standard double wave problem, additional runs were made with the angular velocity,  $\Omega$ , set to its nominal value, and with the wind perpendicular to the mountain range (i.e.,  $\beta = 0$ ). The results of this run showed virtually no effects of the Coriolis terms incorporated in HAIFA. This result is not unexpected when we recall that the mountain range in the double wave problem is only 625 meters high and 4500 meters long.

However, problems simulating much larger mountains, for example, the Andes or the Sierras, should be significantly affected by the Coriolis forces, and the resulting lee waves produced would be a system of both inertia and gravity waves. These complex wave systems could appreciably change the drag from what one would expect considering only gravity waves.

### 3.5 HEURISTIC NUMERICAL MODEL OF TURBULENCE

In incompressible flow, whether laminar or turbulent, the equations of momentum and continuity, along with the boundary and initial conditions, suffice to establish completely the exact fluid motion. If the flow happens to be turbulent, however, the motion involves such small and rapid changes that, although it is in principle determinate, its actual calculation would impose an overwhelming computational burden and, in addition, the detailed initial conditions are not known.

The usual way around this difficulty is to average the equations of momentum and continuity to obtain mean flow quantities which are smooth. This results, of course, in an enormous simplification. Unfortunately, it also involves a significant and irretrievable loss of essential information. Consequently, owing to the presence of the unknown Reynolds stresses which are created by this averaging process, the averaged equations of momentum and continuity do not in themselves comprise a determinate set. Additional relations are required to fix the unknown Reynolds stresses. Equations can also be derived for the fluctuations and for averages of products of them. However, these equations form a coupled system involving ever higher order variances. No first-principles method for terminating this system of equations is known.

A plausible heuristic approach has been developed by Gawain and Pritchett.<sup>[19]</sup> Since the necessary supplementary relations cannot be established from the original equations by an analytic procedure, Gawain and Pritchett closed the system with the addition of empirical hypotheses. Their philosophy and rationale is quoted below:

"From another viewpoint, it may be stated that the averaged equations of motion show the effect of the Reynolds

stresses upon the mean flow. However, the reciprocal effect of the mean flow upon the Reynolds stresses is lost in the averaging process. Hence some adequate hypothesis must be found for representing this relation, at least approximately."

"For this purpose, a heuristic approach which seems plausible is to postulate a relation between the Reynolds stresses and the mean flow which is analogous to the relation that is known to govern the viscous stresses. The analogue of the ordinary molecular kinematic viscosity is the so-called eddy kinematic viscosity. The problem becomes, therefore, to determine empirically the general law which governs this mean effective eddy viscosity at every space/time point in the flow field."

"The eddy viscosity presumably depends on a number of variables, one of the most important of which is the local kinetic energy of turbulence. Therefore, it becomes necessary to find the space/time distribution of the turbulent energy. Fortunately, the governing energy equation can be deduced rigorously from the original equations of motion. However, the energy equation itself introduces two additional unknowns which can only be approximated in the same heuristic and empirical fashion as the eddy viscosity itself. The additional unknowns are the rate of dissipation of turbulent energy into heat, and the rate of turbulent diffusion of energy."

"Theory and experiment both show that the eddy viscosity, and the dissipation and diffusion functions as well, depend not only on the turbulent energy itself, but also on a local length scale parameter which can be associated with each space/time point in the flow field. Von Karman was perhaps the first to point out how a physically meaningful characteristic length can be defined in terms of local space derivatives of the mean velocity at any point in the flow.

In the present paper, the original approach of von Karman is further developed and refined. It now takes into account not only the velocity derivatives at the designated point itself, but also the values in the general vicinity of the point."

"By employing dimensional analysis, and by applying the available experimental data, we finally obtain three empirical expressions which determine to a reasonable approximation the eddy viscosity, the heat dissipation and the turbulent diffusion, respectively. These expressions also involve the turbulent energy, the local length parameter, and the distance to the nearest fixed wall (if any). Of course, these empirical expressions are amenable to further investigation and development."

"In this way a single consistent and determinate set of equations is established which applies in principle to any incompressible turbulent flow field. Only the boundary conditions differ for each specific application."

### 3.5.1 Formulation

The formulation of equations as developed by Gawain and Pritchett must be modified for flow of an incompressible fluid to flow of a fluid characterized by the Boussinesq approximation. Starting with the momentum and continuity equations shown below, the derivation of equations follows.

$$\frac{\partial u}{\partial x} + \frac{\partial w}{\partial z} = 0 \quad (\text{continuity}) \quad (3.76)$$

$$\frac{\partial u}{\partial t} + u \frac{\partial u}{\partial x} + w \frac{\partial u}{\partial z} = -\frac{1}{\rho_0} \frac{\partial p}{\partial x} + \nabla \cdot (K_v \nabla u) \quad (3.77)$$

$$\frac{\partial w}{\partial t} + u \frac{\partial w}{\partial x} + w \frac{\partial w}{\partial z} = -\frac{1}{\rho_0} \frac{\partial p}{\partial z} + \nabla \cdot (K_v \nabla w) - \frac{\rho}{\rho_0} g \quad (3.78)$$

} (momentum)

Here  $K_v$  is the molecular viscosity. The velocity components, the pressure, and density can be separated into mean and fluctuating parts,

$$u = \bar{u} + u'$$

$$w = \bar{w} + w'$$

$$p = \bar{p} + p'$$

$$\rho = \bar{\rho} + \rho'$$

These are to be inserted into the equations of motion and ensemble averaged. Eqs. (3.79) and (3.80) give the mean momentum equations.

$$\begin{aligned} \frac{\partial \bar{u}}{\partial t} + \bar{u} \frac{\partial \bar{u}}{\partial x} + \frac{\partial}{\partial x} (\overline{u'^2}) + \bar{w} \frac{\partial \bar{u}}{\partial z} + \frac{\partial}{\partial z} (\overline{u'w'}) \\ = - \frac{1}{\rho_0} \frac{\partial \bar{p}}{\partial x} + \nabla \cdot K_v \nabla \bar{u} \end{aligned} \quad (3.79)$$

and

$$\begin{aligned} \frac{\partial \bar{w}}{\partial t} + \bar{u} \frac{\partial \bar{w}}{\partial x} + \frac{\partial}{\partial x} (\overline{u'w'}) + \bar{w} \frac{\partial \bar{w}}{\partial z} + \frac{\partial}{\partial z} (\overline{w'^2}) \\ = - \frac{1}{\rho_0} \frac{\partial \bar{p}}{\partial z} + \nabla \cdot K_v \nabla \bar{w} + \frac{\rho}{\rho_0} g \end{aligned} \quad (3.80)$$

Following Gawain and Pritchett, the Reynolds stresses are postulated to be related to the strain rates of mean flow through

$$-\overline{u'_i u'_j} = -\frac{1}{3} \overline{u'_k u'_k} \delta_{ij} + \epsilon \left( \frac{\partial \bar{u}_j}{\partial x_i} + \frac{\partial \bar{u}_i}{\partial x_j} \right) \quad (3.81)$$

where  $\delta_{ij} = 0$  for  $i \neq j$ , and  $=1$  otherwise;  $\epsilon$  is called the eddy kinematic viscosity.

The postulate of Eq. (3.81) provides four necessary relationships,

$$\begin{aligned} -\overline{u'^2} &= -\frac{1}{3} \left( \overline{u'^2} + \overline{v'^2} + \overline{w'^2} \right) + 2\epsilon \frac{\partial \bar{u}}{\partial x} \\ -\overline{u'w'} &= \epsilon \left( \frac{\partial \bar{w}}{\partial x} + \frac{\partial \bar{u}}{\partial z} \right) \\ -\overline{w'^2} &= -\frac{1}{3} \left( \overline{u'^2} + \overline{v'^2} + \overline{w'^2} \right) + 2\epsilon \frac{\partial \bar{w}}{\partial z} \\ -\overline{w'u'} &= -\overline{u'w'} \quad . \end{aligned} \quad (3.82)$$

Applying the postulate of Eq. (3.81) to Eq. (3.79) and substituting the kinematic pressure

$$\phi = \bar{p} - \frac{1}{3} \left( \overline{u'^2} + \overline{v'^2} + \overline{w'^2} \right)$$

one has

$$\begin{aligned} \frac{\partial \bar{u}}{\partial t} + \bar{u} \frac{\partial \bar{u}}{\partial x} + \bar{w} \frac{\partial \bar{u}}{\partial z} &= -\frac{1}{\rho_0} \frac{\partial \phi}{\partial x} + (\epsilon + K_v) \nabla^2 \bar{u} \\ &+ 2 \frac{\partial \epsilon}{\partial x} \frac{\partial \bar{u}}{\partial x} + \frac{\partial \epsilon}{\partial z} \left( \frac{\partial \bar{w}}{\partial z} + \frac{\partial \bar{u}}{\partial z} \right) \quad , \end{aligned} \quad (3.83)$$

and for Eq. (3.80) one obtains

$$\begin{aligned} \frac{\partial \bar{w}}{\partial t} + \bar{u} \frac{\partial \bar{w}}{\partial x} + \bar{w} \frac{\partial \bar{w}}{\partial z} = & - \frac{1}{\rho_0} \frac{\partial \phi}{\partial z} + (\epsilon + K_v) \nabla^2 \bar{w} + \frac{\rho}{\rho_0} g \\ & + \frac{\partial \epsilon}{\partial x} \left( \frac{\partial \bar{w}}{\partial x} + \frac{\partial \bar{u}}{\partial z} \right) + 2 \frac{\partial \epsilon}{\partial z} \frac{\partial \bar{w}}{\partial z} . \end{aligned} \quad (3.84)$$

Equations (3.83) and (3.84) are reformulated in terms of the vorticity  $\eta$  and the stream function  $\psi$ , which satisfy the relations  $\eta = \frac{\partial u}{\partial z} - \frac{\partial w}{\partial x}$  and  $\nabla^2 \psi = \eta$ . The vorticity equation then has the form

$$\begin{aligned} \frac{d\eta}{dt} = & (\epsilon + K_v) \nabla^2 \eta - \frac{g}{\rho_0} \frac{\partial \rho}{\partial x} + \left( \frac{\partial^2 \epsilon}{\partial z^2} - \frac{\partial^2 \epsilon}{\partial x^2} \right) \left( \frac{\partial^2 \psi}{\partial z^2} - \frac{\partial^2 \psi}{\partial x^2} \right) \\ & + 4 \frac{\partial^2 \epsilon}{\partial x \partial z} \frac{\partial^2 \psi}{\partial x \partial z} + \frac{\partial \epsilon}{\partial z} \frac{\partial \eta}{\partial z} + \frac{\partial \epsilon}{\partial x} \frac{\partial \eta}{\partial x} + \frac{\partial \epsilon}{\partial x} \left[ \nabla^2 \frac{\partial \psi}{\partial z} \right] \\ & + \frac{\partial \epsilon}{\partial z} \left[ \nabla^2 \frac{\partial \psi}{\partial x} \right] . \end{aligned} \quad (3.85)$$

The energy equation is formed by multiplying the momentum equation by velocity. As before, the resultant equation is rewritten with mean and fluctuating terms, and the averaged energy equation is subtracted to yield the turbulent energy equation. It is convenient to express the result in Cartesian tensor notation,

$$\begin{aligned}
\frac{\partial}{\partial t} \left( \overline{\frac{u'_j u'_j}{2}} \right) + \frac{\partial}{\partial x_k} \left( \overline{u'_k \frac{u'_j u'_j}{2}} \right) = & - \overline{u'_j u'_k} \left( \frac{\partial \bar{u}_j}{\partial x_k} + \frac{\partial \bar{u}_k}{\partial x_j} \right) \\
& - \frac{K_v}{2} \overline{\left( \frac{\partial u'_j}{\partial x_k} + \frac{\partial u'_k}{\partial x_j} \right)^2} \\
& - \frac{\partial}{\partial x_k} \left[ \overline{u'_k \left( \frac{u'_j u'_j}{2} + \phi' \right)} \right] \\
& + K_v \frac{\partial}{\partial x_k} \left[ \frac{\partial}{\partial x_k} \left( \overline{\frac{u'_j u'_j}{2}} \right) + \frac{\partial}{\partial x_j} (u'_j u'_k) \right] \quad (3.86)
\end{aligned}$$

$\phi'$  is the perturbation of kinematic pressure, pressure/density. The terms on the right-hand side of the energy equation represent, respectively, turbulent energy production corresponding to the work done by the mean flow against the Reynolds stresses, dissipation of turbulent energy to heat, turbulent diffusion of energy, and molecular diffusion. For problems at high Reynolds number the last term is vanishingly small; it will be ignored hereafter.

Denoting by  $E$  the turbulent kinetic energy,

$$E = \overline{\frac{u'_j u'_j}{2}} = \frac{1}{2} (\overline{u'^2} + \overline{v'^2} + \overline{w'^2}) \quad (3.87)$$

and applying the postulate of Eq. (3.81) to Eq. (3.86), the turbulent energy equation becomes

$$\begin{aligned}
\frac{\partial E}{\partial t} + \frac{\partial}{\partial x_k} (\bar{u}_k E) = & \frac{\epsilon}{2} \left( \frac{\partial \bar{u}_j}{\partial x_k} + \frac{\partial \bar{u}_k}{\partial x_j} \right)^2 - \frac{K_v}{2} \overline{\left( \frac{\partial u'_j}{\partial x_k} + \frac{\partial u'_k}{\partial x_j} \right)^2} \\
& - \frac{\partial}{\partial x_k} \left[ \overline{u'_k \left( \frac{u'_j u'_j}{2} + \phi' \right)} \right] \quad (3.88)
\end{aligned}$$

At this point, neither the vorticity equation nor the turbulent energy equation are closed. It should also be noted here that the development of the turbulent energy equation (3.88) as described by Gawain and Pritchett neglects the temperature stratification term  $-\overline{\rho'u_1'} \frac{g}{\rho_0}$  on the right-hand side of the equation, which for our applications can be a significant effect. For the initial development of the turbulent scheme, however, this term was also ignored as it requires that the fluctuating density component be described in some heuristic and empirical fashion, i.e., that  $\overline{\rho'u_1'} \equiv \epsilon' \frac{\partial \rho}{\partial z}$ . The value of  $\epsilon'$  remains to be determined from experimental data in much the same manner as the kinematic eddy viscosity  $\epsilon$  itself needs to be determined.

To enable the kinematic eddy viscosity  $\epsilon$  to be determined, Gawain and Pritchett postulated the formulation

$$\epsilon = \alpha \lambda \sqrt{2E} \quad . \quad (3.89)$$

where  $\alpha$  is a dimensionless, slowly varying universal function not predictable from theory, but estimable from experimental data and  $\lambda$  is a length scale of turbulence in the vicinity of a point. Thus, there is a  $\lambda$  associated with every point of the flow field. It was hypothesized that the definition of  $\lambda$  in the vicinity of an arbitrary point should depend only on the mean flow conditions in a finite region surrounding that point. By use of a weighting function which falls off rapidly with increasing separation, dependence on all points in the flow field can be avoided.

The weighting function chosen was

$$\hat{w}(\vec{x}) = \frac{\exp\left(-\frac{\Delta\vec{x}\cdot\Delta\vec{x}}{\lambda^2(\vec{x})}\right)}{\int_{\text{all space}} \exp\left(-\frac{\Delta\vec{x}\cdot\Delta\vec{x}}{\lambda^2(\vec{x})}\right)} . \quad (3.90)$$

A strain rate tensor was defined,

$$\Gamma_{ij} = \frac{\partial \bar{u}}{\partial z} + \frac{\partial \bar{w}}{\partial x} . \quad (3.91)$$

Note that  $\Gamma_{ii} = 0$  for the incompressible case from continuity. Next a generalized strain rate,  $\Omega^2$ , and a generalized strain rate gradient,  $\Omega'^2$ , were defined as follows:

$$\Omega^2 = \frac{1}{2} \Gamma_{ij} \Gamma_{ij} \quad (3.92)$$

$$\Omega'^2 = \left(\frac{\partial \Omega}{\partial x_i}\right) \left(\frac{\partial \Omega}{\partial x_i}\right) \quad (3.93)$$

It was also found useful to define

$$(\Omega\Omega')^2 = \frac{1}{4} \left(\frac{\partial \Omega^2}{\partial x_i}\right) \left(\frac{\partial \Omega^2}{\partial x_i}\right) \quad (3.94)$$

$\lambda^2$  can be defined in terms of  $\Omega^2$  and  $(\Omega\Omega')^2$ :

$$\lambda^2(\vec{x}) = I^2(\vec{x})/J^2(\vec{x}) \quad (3.95)$$

where

$$I^2(\vec{x}) = \int_{\text{all space}} \hat{w}(\vec{x}, \vec{x}') \Omega^4(\vec{x}) dv' \quad (3.96)$$

$$J^2(\vec{x}) = \int_{\text{all space}} \hat{w}(\vec{x}, \vec{x}') (\Omega^4(\vec{x}))^2 dv' \quad (3.97)$$

and

$$\hat{w}(\vec{x}, \vec{x}') = \frac{\exp\left(-\frac{(\vec{x}-\vec{x}') \cdot (\vec{x}-\vec{x}')}{\lambda^2(\vec{x})}\right)}{\int_{\text{all space}} \exp\left(-\frac{(\vec{x}-\vec{x}') \cdot (\vec{x}-\vec{x}')}{\lambda^2(\vec{x})}\right)} \quad (3.98)$$

The last term in the turbulent energy equation (Eq. 3.88) is not in a form amenable to calculation. It was postulated to be expressible in the form

$$\overline{u'_k \left( \frac{u'_j u'_j}{2} + \phi \right)} = -\gamma \epsilon \left( \frac{\partial \epsilon}{\partial x_k} \right) \quad (3.99)$$

Dimensional considerations suggested to Gawain and Pritchett that the dissipation of turbulent energy into heat could be expressed in the form

$$\dot{E}_H = \frac{K_V}{2} \overline{\left( \frac{\partial u_j}{\partial x_i} + \frac{\partial u_i}{\partial x_j} \right)^2} = \frac{K_V (2E)}{\lambda_D^2} \quad (3.100)$$

which amounts to a definition of a dissipation length  $\lambda_D$ . To define  $\lambda_D$ , Gawain and Pritchett turned to the results of experimental studies at high Reynolds number, where heat dissipation effect tended to become independent of Reynolds number. Two lengths  $L_1$  and  $L_2$  were defined,

$$L_1^2 = \frac{K_V}{2E} \quad (3.101)$$

$$L_2^2 = \frac{2E}{J} \quad (3.102)$$

and the relation

$$\frac{L_1 L_2}{\lambda_D^2} = \beta \quad (3.103)$$

was postulated. The energy dissipation term becomes

$$\dot{E}_H = \beta (2E)^{7/6} J^{1/3} \quad (3.104)$$

The complete turbulent energy equation, including heuristic substitutes, is then written as follows:

$$\begin{aligned} \frac{\partial E}{\partial t} + \frac{\partial}{\partial x} (\bar{u}E) + \frac{\partial}{\partial z} (\bar{w}E) &= \alpha \lambda \sqrt{2E} \Omega^2 - \beta (2E)^{7/6} J^{1/3} \\ &+ \frac{\partial}{\partial x} \left( \alpha \gamma \lambda \sqrt{2E} \frac{\partial E}{\partial x} \right) + \frac{\partial}{\partial z} \left( \alpha \gamma \lambda \sqrt{2E} \frac{\partial E}{\partial z} \right) \end{aligned} \quad (3.105)$$

To complete the formulation, it is necessary to specify the computation of the three dimensionless coefficients,  $\alpha$ ,  $\beta$ , and  $\gamma$ . Gawain and Pritchett used the following expressions, based on experimental data:

$$\begin{aligned} \alpha &= 0.065 \{1 + \exp[-(y/\lambda - 1)^2]\} \\ 1/\beta &= 3.7 \{1 + \exp[-(y/\lambda - 1)^2]\} \\ \gamma &= 1.4 - 0.4 \exp[-(y/\lambda - 1)^2] \end{aligned} \quad (3.106)$$

where  $y$  is the distance to the nearest fixed boundary.

Thus, the modifications to the usual incompressible formulation required to incorporate the heuristic turbulence scheme of Gawain and Pritchett are

- (1) the revised vorticity equation [Eq. (3.85)], and
- (2) the inclusion of an heuristic equation for turbulent energy (Eq. (3.86)).

These modifications have been carried out, and the results are detailed in the following sections.

### 3.5.2 Numerics

The modifications to the vorticity equation were coded and incorporated using typical finite difference formulations, and treating the sum  $(K_v + \epsilon)$  as a total diffusion term.

The solution of the turbulent energy equation was carried out in a new code subpackage, subroutine TURB. The flow logic of this subroutine is displayed in Figure 3.21.

The turbulent energy code was exercised on various test problems in which it became apparent that a major calculational burden was imposed by the development of the  $I^2$  and  $J^2$  terms, and the associated weighting terms required for each grid point. This is despite the fact that the potentially expensive "exponential" evaluations can be reduced to a one pass computation, with tabular evaluation thereafter each cycle. The cost in computer time to simply form all the  $I^2$  and  $J^2$  terms, when only the nearest 36 cells are used in the weights, is about 12 seconds. The cost of a complete calculational cycle for the turbulent formulation approached 7 seconds in this case, nearly 10 times the cost of the BASIC HAIFA solution. In one test, the problem characteristics were such that the weights did not fall off sufficiently rapidly, and it was required to include

## SUBROUTINE TURB

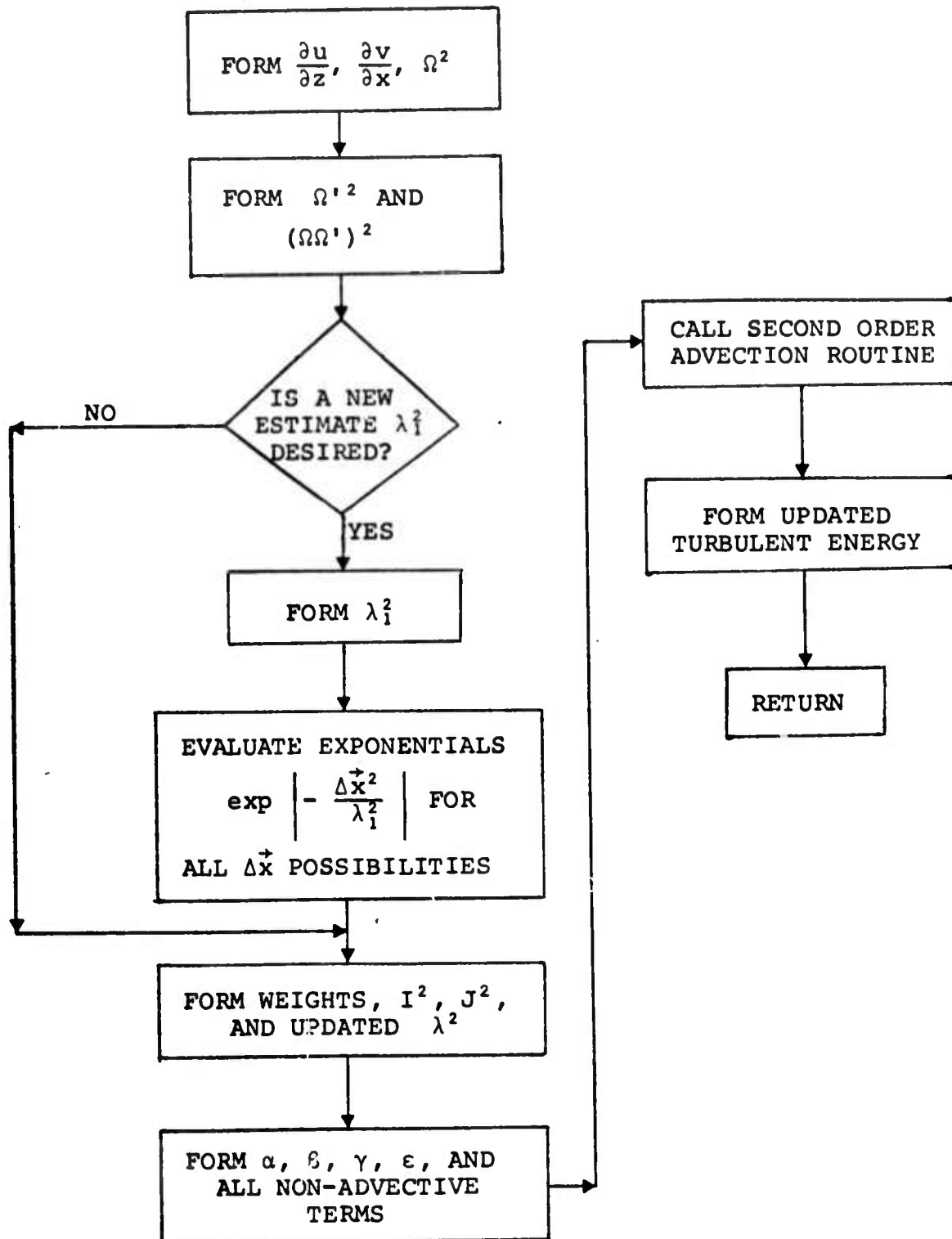


Figure 3.21. Flow Logic for Subroutine TURB

#### 4. BASIC HAIFA WAVE DRAG CALCULATIONS

Several problems have been calculated using the BASIC HAIFA code. The results of each are presented in this section and comparisons with other results are made where possible. An edit routine to determine the momentum flux (wave drag associated with gravity waves) was written and is described in detail in Appendix B.

Table 4.1 summarizes the initial conditions used for each problem. The boundary conditions in each case were those described in Section 2.4 of this report. The grid size consisted of 35 vertical cells by 64 horizontal cells.

##### 4.1 SINGLE WAVE PROBLEM

The atmospheric and horizontal velocity conditions to produce a single gravity wave were arrived at using the results presented on two-dimensional mountain lee waves by Palm and Foldvik. [8] They had established that if the quantity

$$\frac{S}{u^2} - \frac{1}{u} \frac{\partial^2 u}{\partial z^2} ,$$

where  $S$  is the stability of the atmosphere, has a value at the ground level which is at least 2.5 times as large as the minimum value (usually located 7-10 km above the ground),

TABLE 4.1  
SUMMARY OF INITIAL CONDITIONS USED FOR EACH PROBLEM

TEST PROBLEM	LAPSE RATE OF TEMPERATURE DISTRIBUTION	OBSTACLE/GRID SIZE	HORIZONTAL VELOCITY PROFILE
Single Wave	$\gamma = \frac{1}{2}\Gamma^*$	625 meters high $\times$ 4.5 kilometers long $\Delta x = 312.5$ meters $\Delta y = 1.5$ km	Exponential Velocity Profile shown in Figure 4.2.
Two Wave	$\gamma = \frac{1}{2}\Gamma$	441 meters high $\times$ 4.5 kilometers long $\Delta x = 441.0$ meters $\Delta y = 1.5$ km	Exponential Velocity Profile shown in Figure 4.2.
Uniform Velocity	$\gamma = \frac{1}{2}\Gamma$	1.0 kilometer high $\times$ 3 kilometers long $\Delta x = 1$ km $\Delta y = 1$ km	Velocity = 10m/sec
Inversion Layer I	$\gamma = \Gamma$ to 4.5 km $\Delta T = +4^\circ\text{C}$ @ 4.5 km $\gamma = \frac{1}{2}\Gamma$ above 4.5 km	1.5 kilometers high $\times$ 4.5 kilometers long $\Delta x = 1.5$ km $\Delta y = 1.5$ km	Exponential Velocity Profile to 13.5 km, $u$ at ( $z = 750\text{m}$ ) = 43 m/sec, $u$ at ( $z = 14.25$ km) = 146 m/sec.  $u =$ constant above 14.25 km (set equal to velocity at 14.25 km resulting from exponential profile).
Tropopause	$\gamma = 0.65\Gamma$ to 8.25 km $\gamma = 0$ above 8.25 km	1.5 kilometers high $\times$ 4.5 kilometers long $\Delta x = 1.5$ km $\Delta y = 1.5$ km	Exponential Velocity Profile to 8.25 km, $u$ at ( $z = 750\text{m}$ ) = 26 m/sec, $u$ at ( $z = 9.75$ km) = 60 m/sec.  $u =$ constant above 9.75 km (set equal to velocity at 9.75 km resulting from exponential profile).

\*  $\Gamma =$  adiabatic lapse rate --  $T_0$  for all problems assumed to be 300 °K.

the wave motion in the lower troposphere depends only on the wind profile and the stability. This condition is almost always satisfied when mountain waves occur. A diagram giving the expected wave lengths of lee waves under various stability and wind profiles was presented. In particular, regions of one and two waves were indicated. Using this diagram, a single wave of approximately 16 km in length was predicted for a lapse rate equal to one-half the dry adiabatic value (see Figure 4.1), and the exponential velocity profile shown in Figure 4.2.

The numerical results calculated using HAIFA are shown in Figures 4.3 through 4.6 as streamlines and vertical velocity contours at several times up to 1-1/4 hours. The measured wave length from Figure 4.4 or 4.6 is approximately 15 km. As can be observed from the results, only one wave did form during the time the problem was run. The cyclic boundary condition prevented any further computation due to disturbances created by the obstacle in the flow stream being introduced into the main flow upstream of the mountain. Some interference with the upper boundary positioned at 10.9 km may also be seen at the latest times.

The momentum edits  $\overline{u'v'}$  (see Appendix B) located one cell or 312.5 meters above the mountain top are shown in Figures 4.7 and 4.8 for various lengths used in obtaining the horizontal averages. The qualitative result obtained from these figures indicates a decrease in the edited quantity as the length used in the averaging length is increased, i.e., a lower amount of drag is created by the mountain. One exception appears, however; this can be noted as a cross over

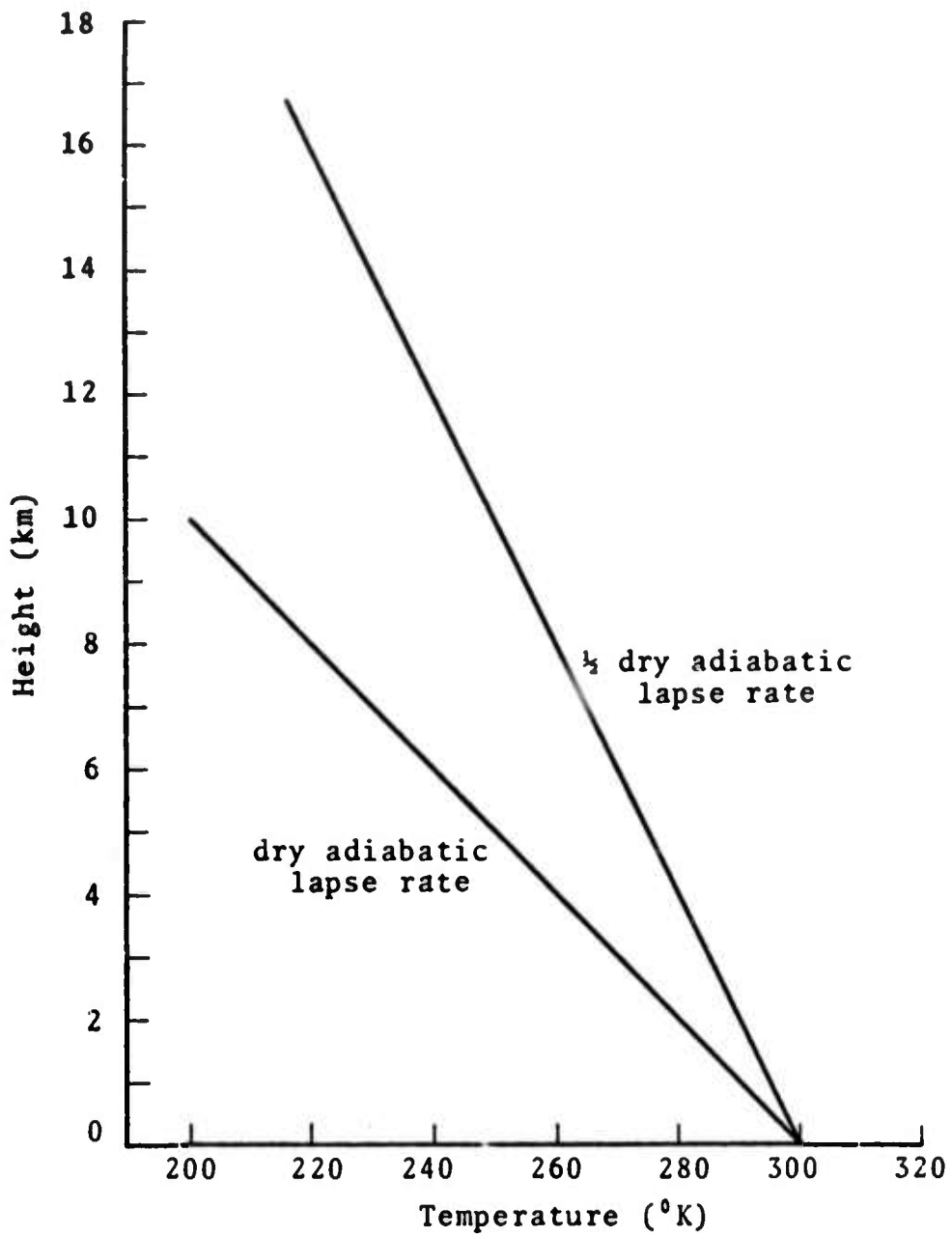


Figure 4.1 - Initial Temperature Profiles used in Test Problems.

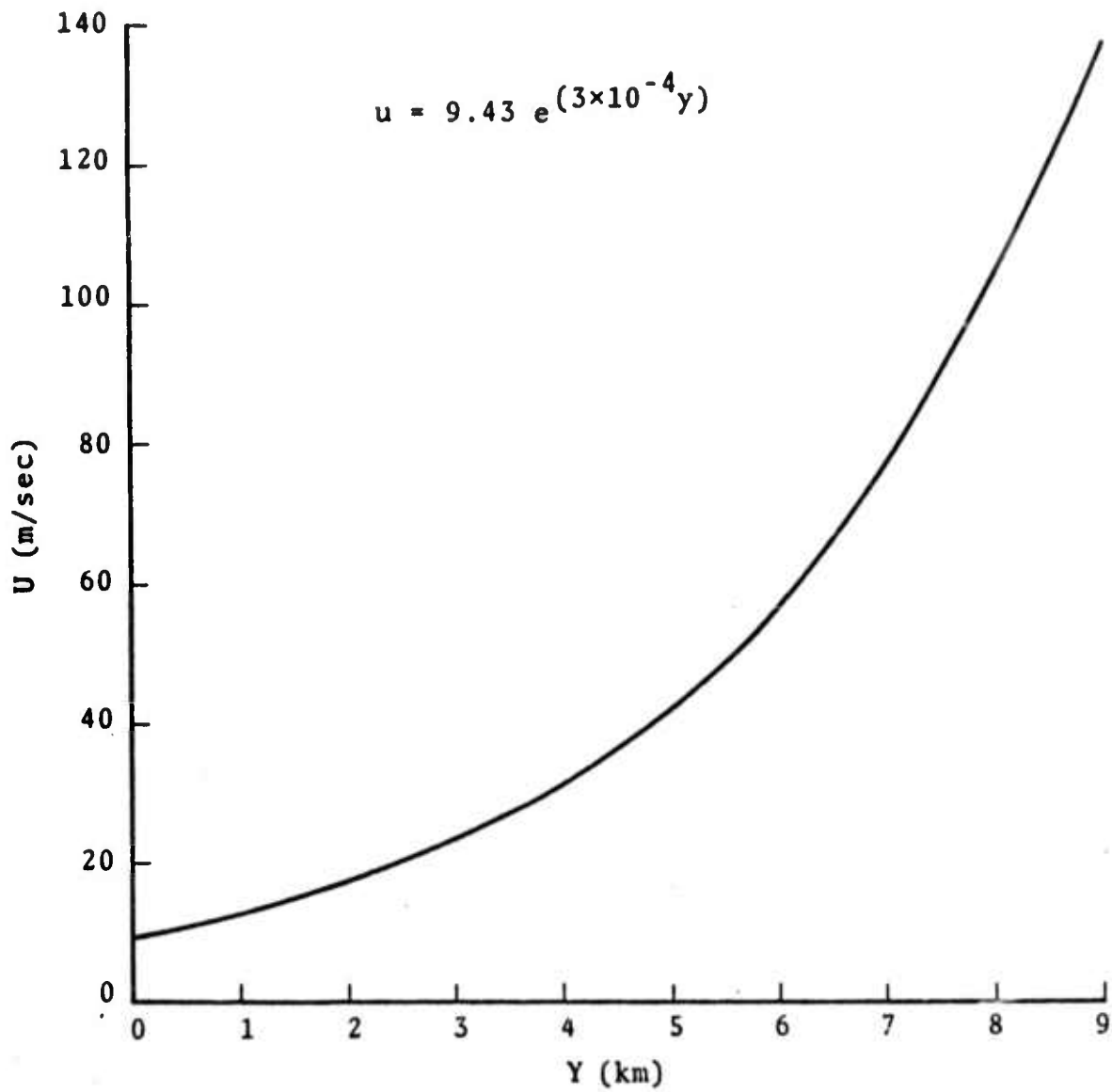


Figure 4.2 - Single Wave Velocity Profile.

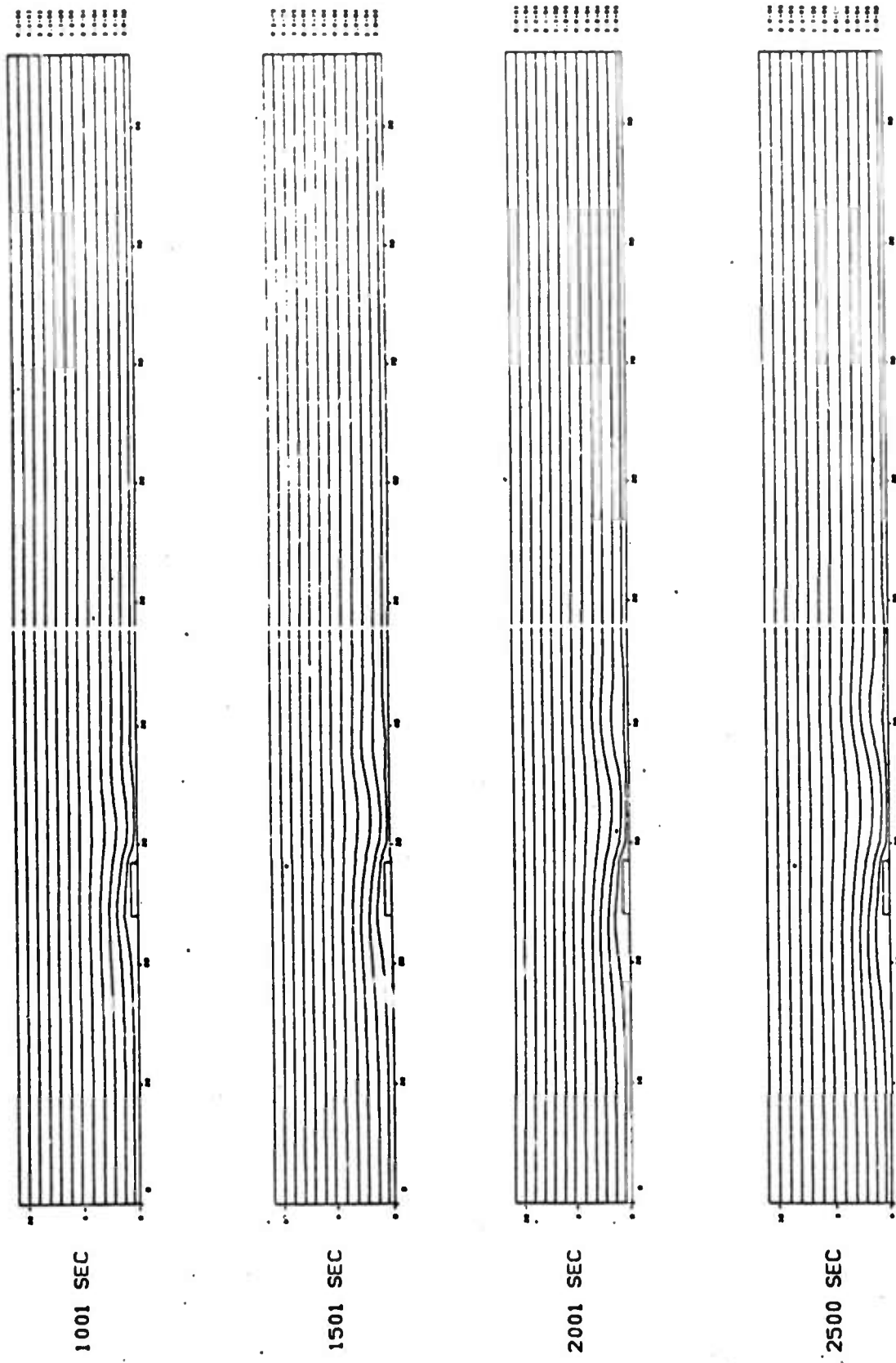


Figure 4.3 - Streamlines from Single Wave Problem.

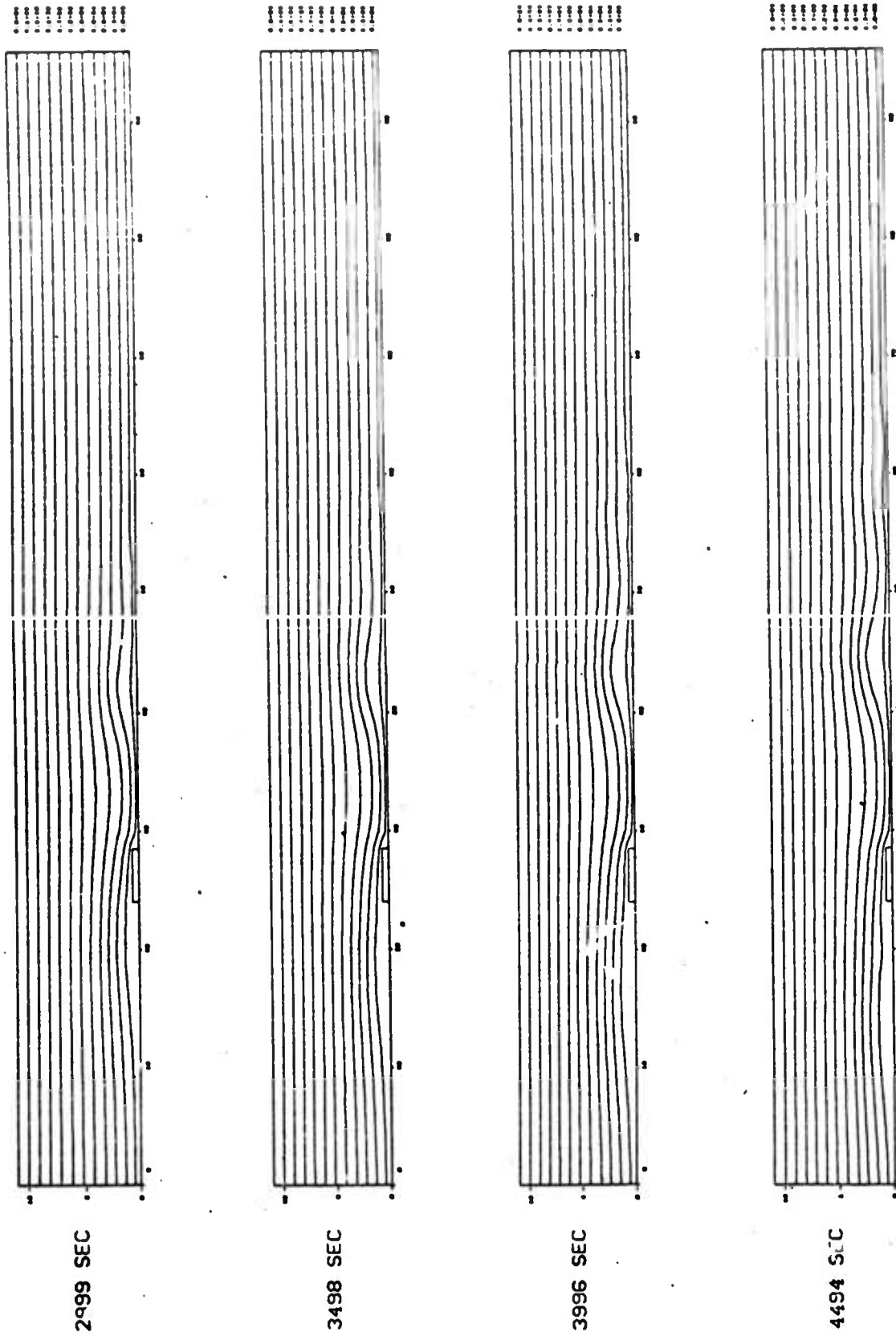


Figure 4.4 - Streamlines from Single Wave Problem (page 2).

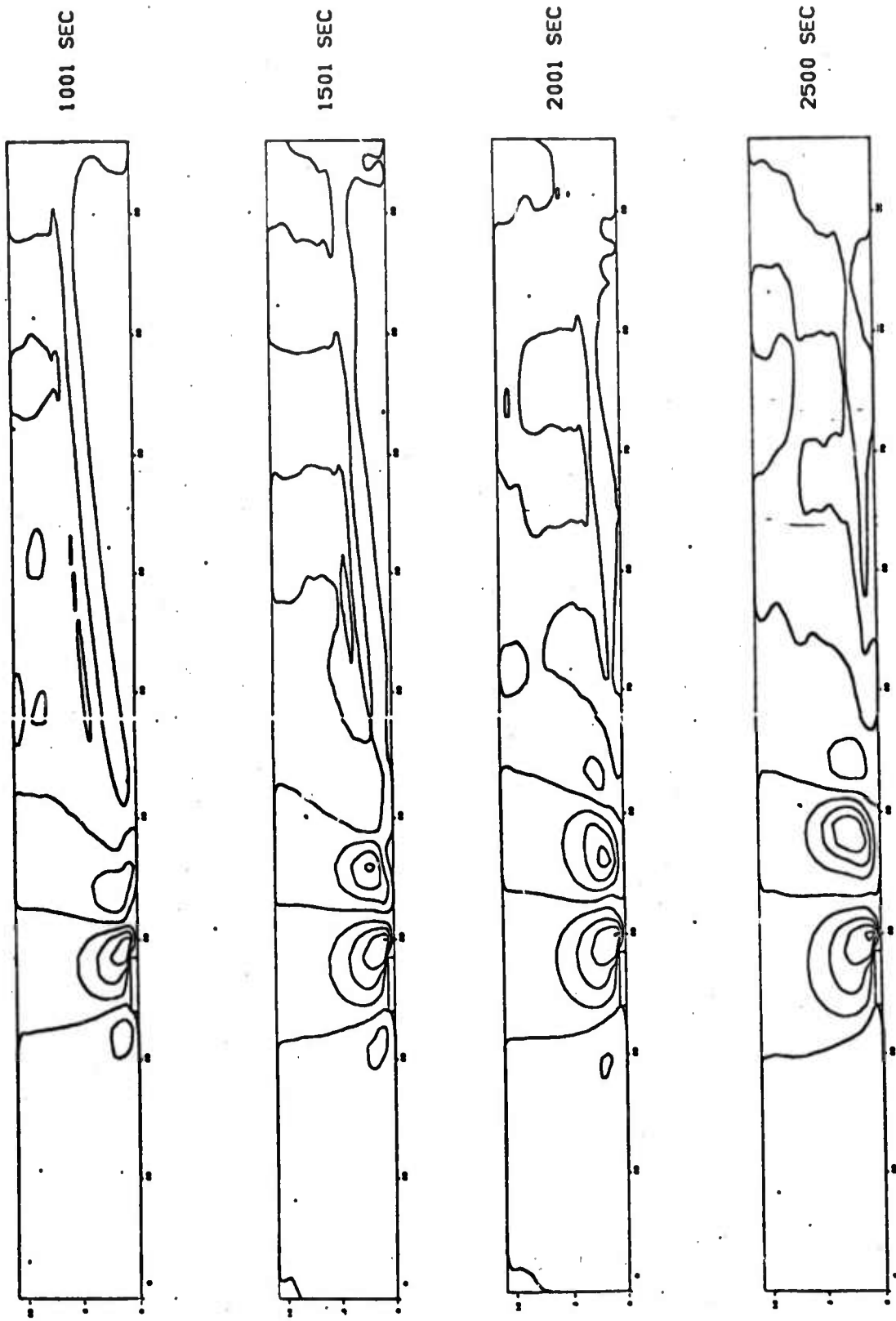


Figure 4.5 - Vertical Velocity Field from Single Wave Problem.

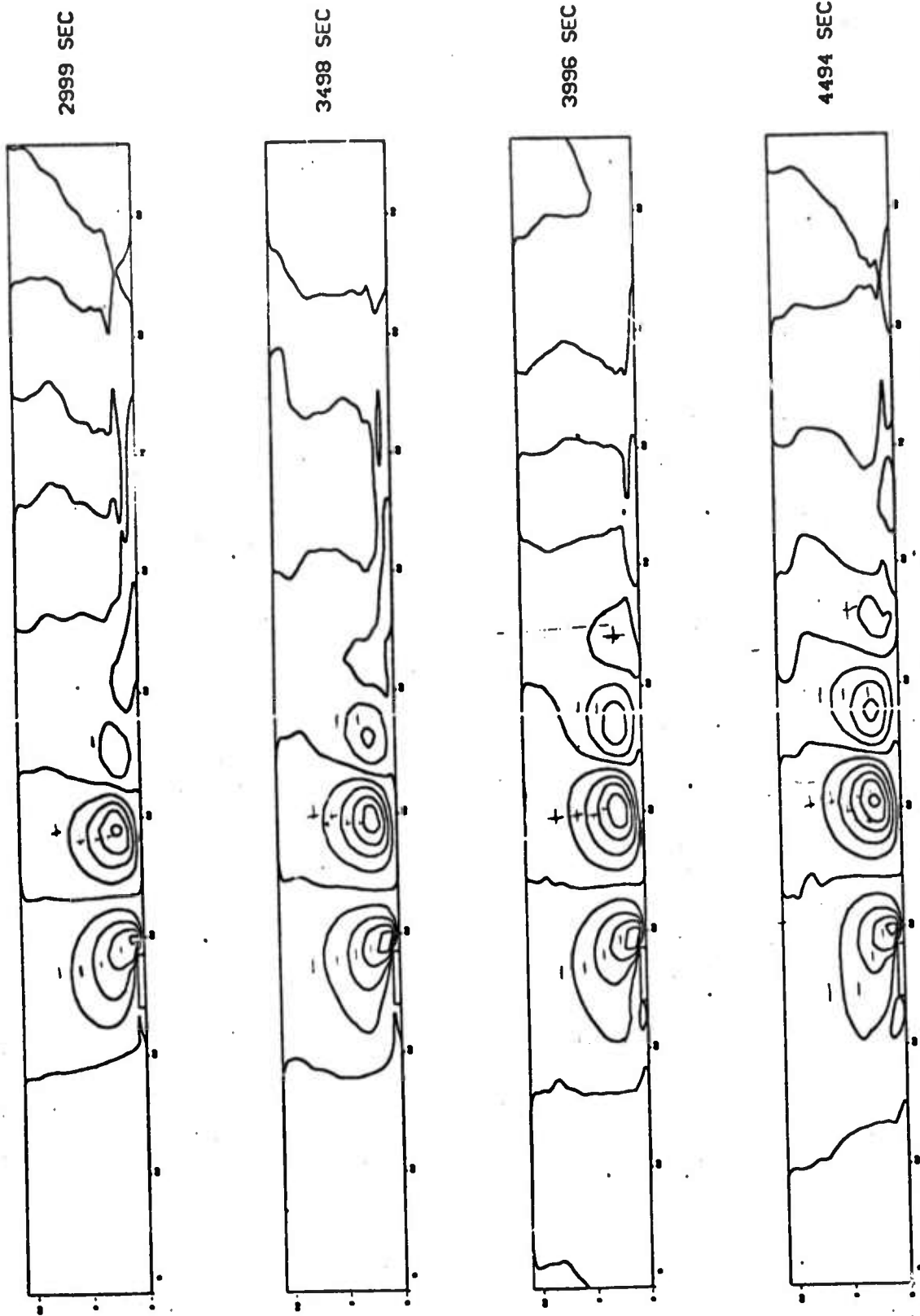


Figure 4.6 -- Vertical Velocity Field from Single Wave Problem (page 2).

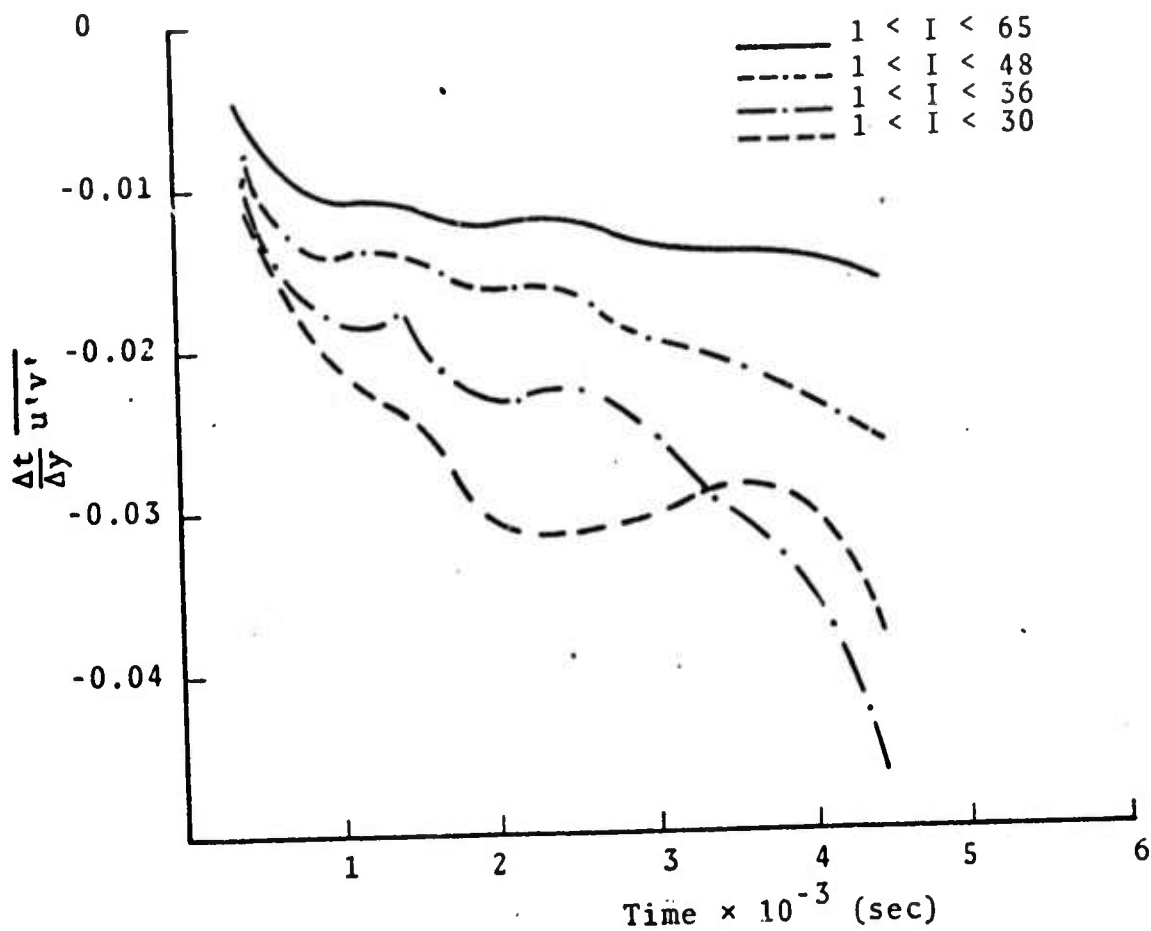


Figure 4.7 - Single Wave Problem Momentum Flux Edits.

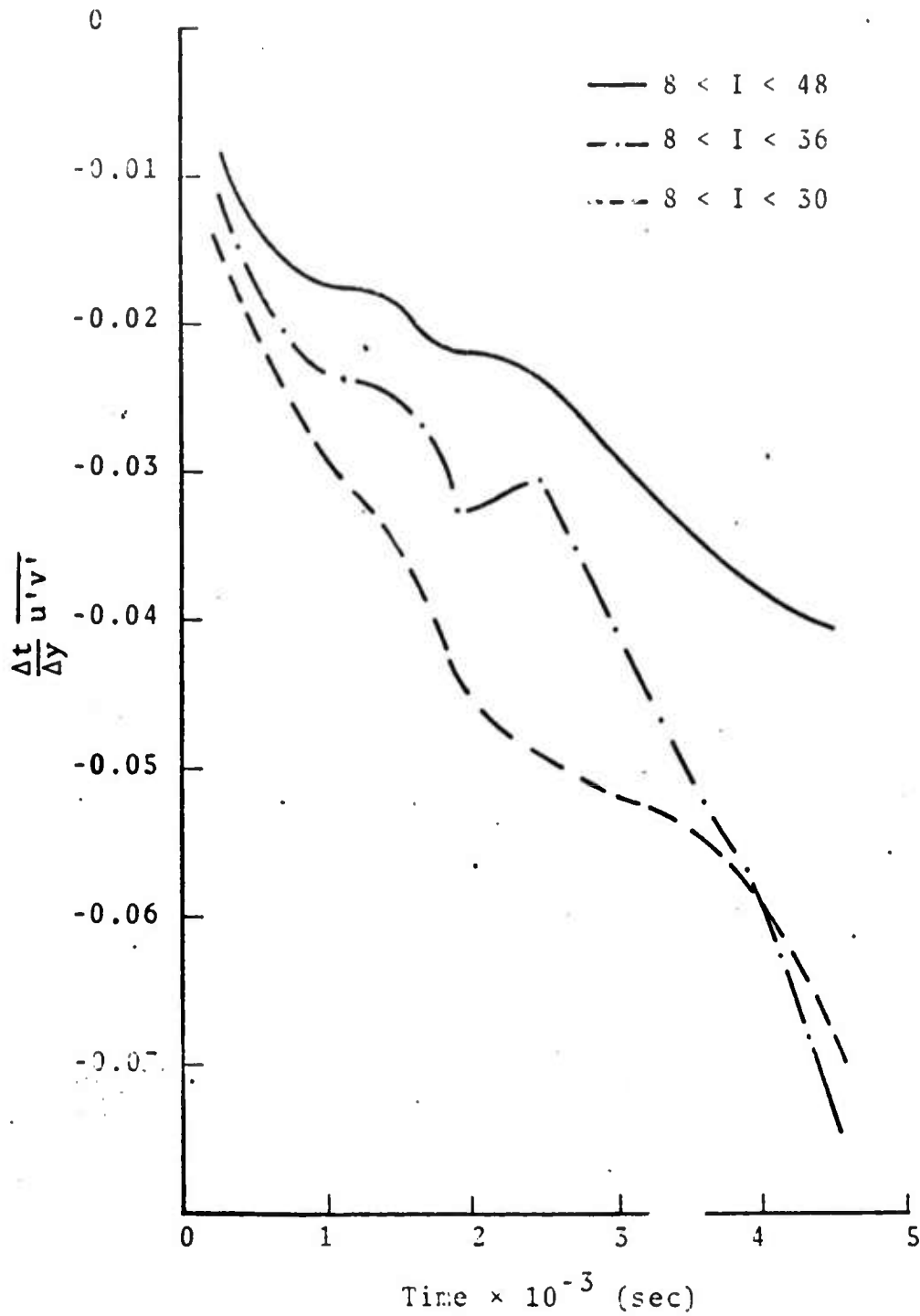


Figure 4.8 - Single Wave Problem Momentum Flux Edits (page 2).

of two of the curves occurring at approximately 3400 to 4000 seconds on either of the figures. The same phenomenon occurs when the averaging length is reduced by discounting zones from in front of the obstacle as well as the rear. While it is not clear what the averaging length should be in these cases or the interpretation of these results, it is clear that the magnitude of the edited quantity is only equal to the drag on the mountain if the inlet and outlet values of  $p$  and  $\rho u^2$  are identical. Since this is the case only when the total numerical grid length is used as the averaging length, due to the cyclic boundary conditions, a value for the drag on the mountain can only be estimated from the uppermost curve of Figure 4.7. The value of the drag reached at 4,445 seconds was approximately equal to 10 dynes/cm<sup>2</sup>. This value agrees qualitatively with measured values of the momentum flux reported by D. K. Lilly<sup>(20)</sup> for measurements at Boulder, Colorado.

One other important feature of the momentum flux edit is the oscillatory character of the values with time. This is thought to be related to the formation of the individual vertical velocity cells, i.e., as a new positive or negative cell is formed, the effect seems to be to increase or decrease the horizontal average of the vertical flux of horizontal momentum. This cyclic character is perhaps more clearly seen in the edits of the two wave problem discussed later.

Figure 4.9 shows the momentum edit as a function of height at a time of 4,445 seconds. The value goes to zero very quickly above the mountain. This indicates the solution is not yet approaching a steady state value since the drag for a steady problem would be constant with height.

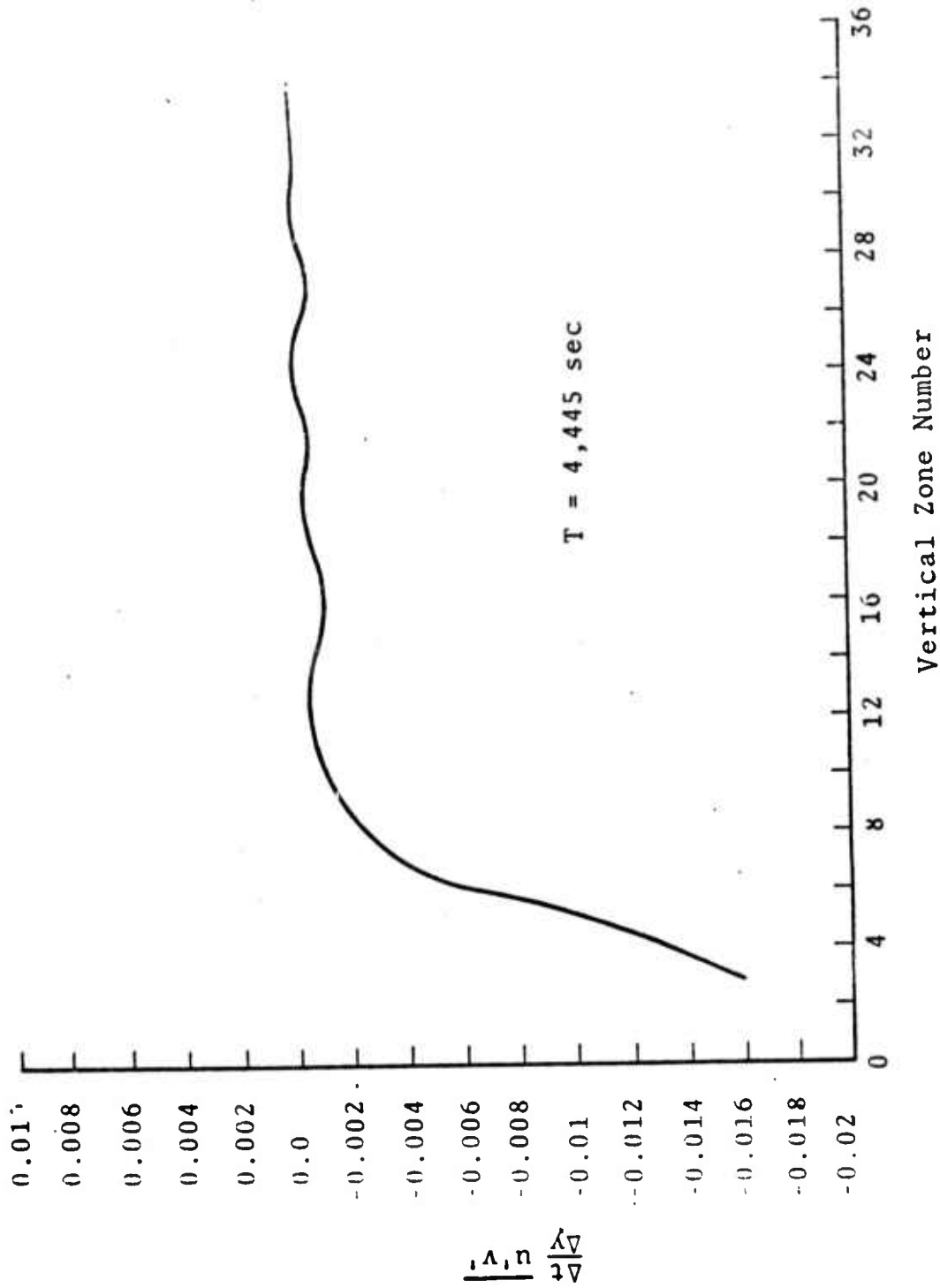


Figure 4.9 - Momentum Flux as a Function of Vertical Height.

## 4.2 TWO WAVE PROBLEM

This problem was run using a vertical grid size of 441 meters and an obstacle height of 441 meters. This placed the upper boundary at 15.4 km. The other initial conditions were identical to those noted in Section 4.1. They are reiterated in Table 4.2, and the initial horizontal velocity profile is shown in Figure 4.10.

TABLE 4.2  
TWO WAVE PROBLEM

PROBLEM TITLE	LAPSE RATE*	GRID CHARACTERISTICS	HORIZONTAL VELOCITY PROFILE
Two Wave	$\gamma = \frac{1}{2}\Gamma$	$\Delta x = 1500$ meters $\Delta z = 441$ meters Obstacle: Height = 441 meters Length = 4500 meters	Exponential profile as shown in Figure 4.10

\* Initial surface temperature = 300°K

$\Gamma$  = adiabatic lapse rate = 10°K/km

The linear analysis of Palm and Foldvik<sup>[8]</sup> indicates that under these conditions two waves should be present in the lee of the mountain - one wave of approximately 9.2 km wavelength and a second wave of approximately 25 km wavelength. The HAIFA calculation was run to a time of 4980 seconds. Computer plots of the streamlines and the vertical velocity profiles from the calculation at a time of 4691 seconds are shown in Figure 4.11. The shorter wave appears just above and behind the obstacle displaying a wavelength of approximately 10 km. A second wave appears behind the

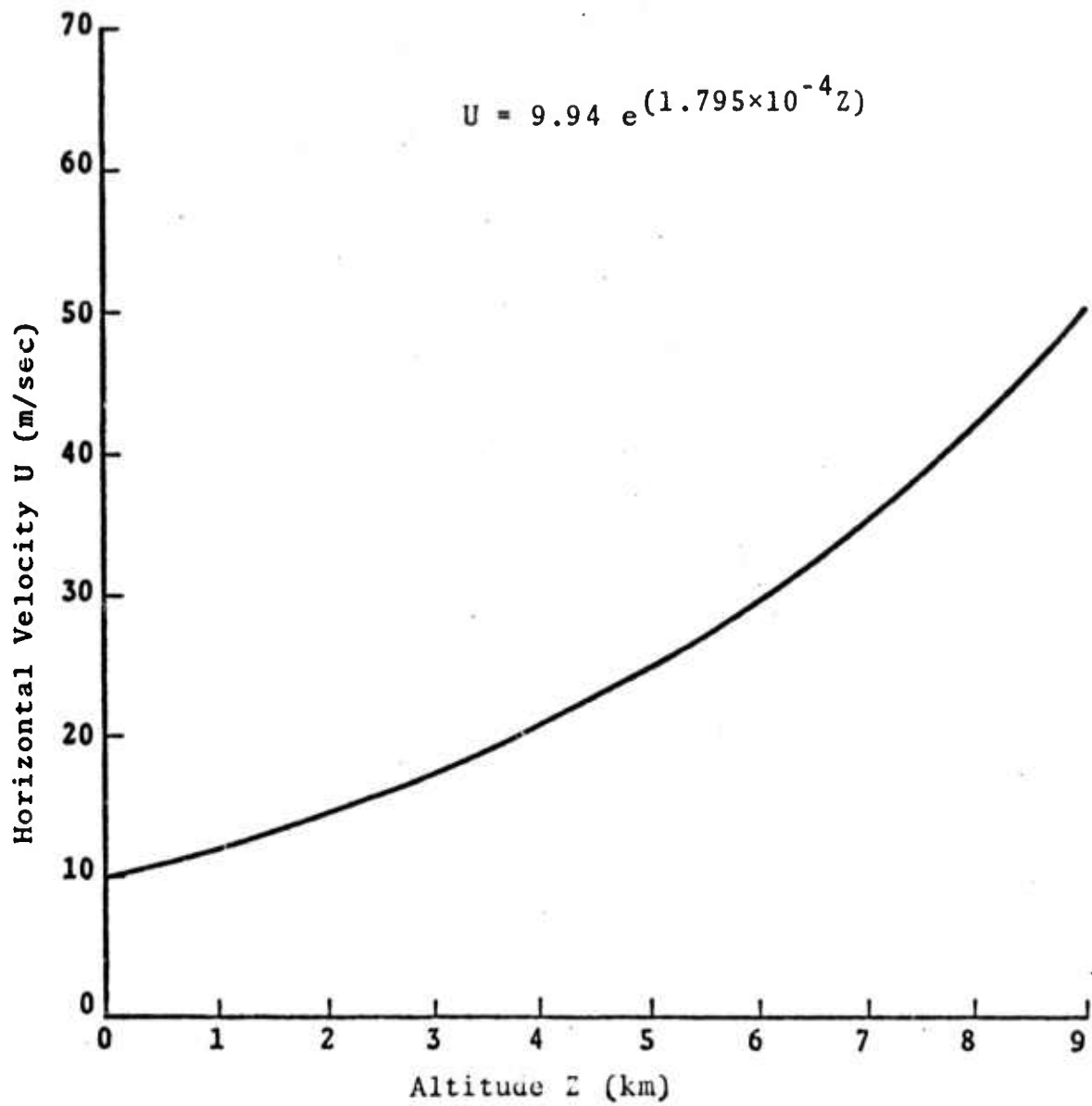


Figure 4.10. Initial velocity profile - two wave problem.

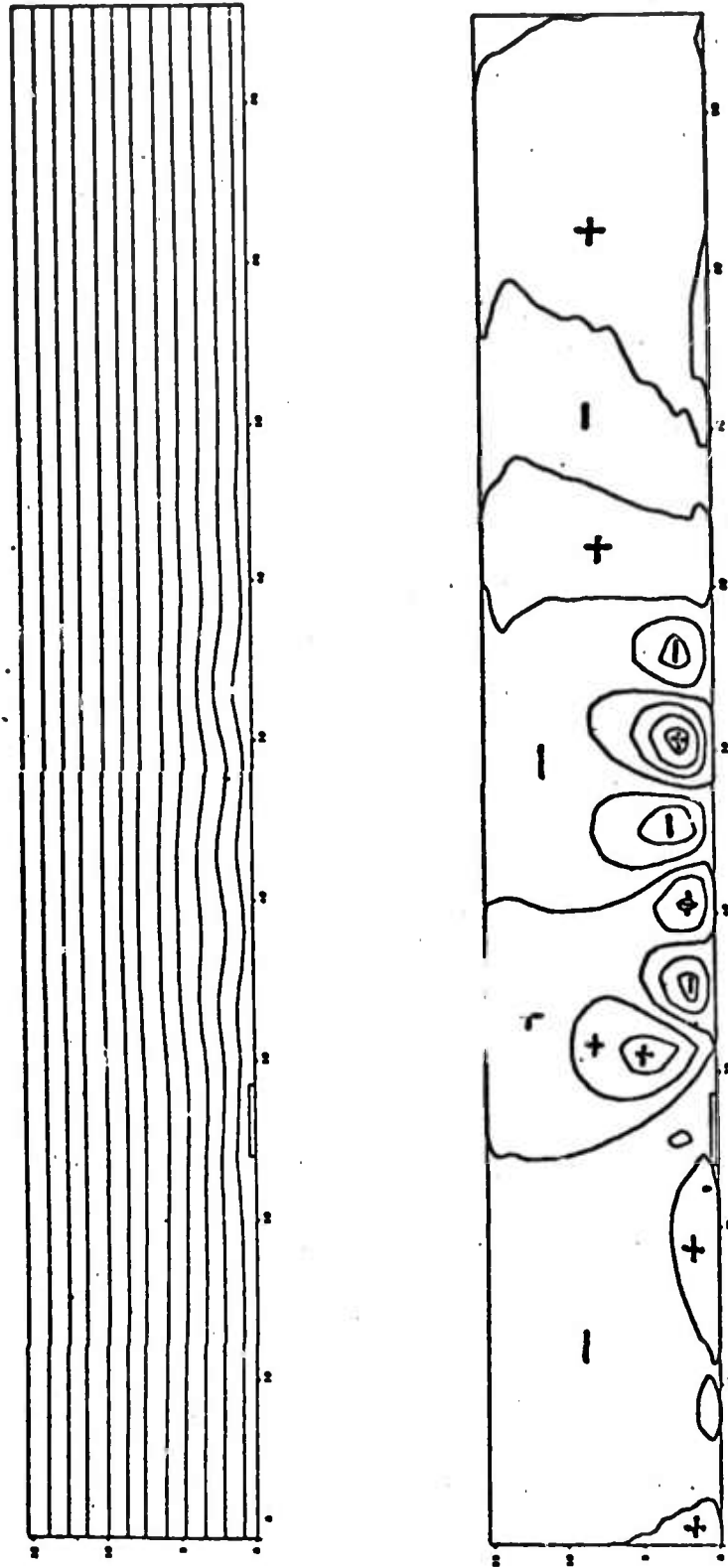


Figure 4.11. Streamlines and vertical velocity profiles for the two-wave problem.  
(time = 4691 seconds)

obstacle at a height of 7 to 8 km with a wavelength of approximately 25-35 km. Palm and Foldvik's analysis indicated the maximum amplitude of the wave would appear at 7.4 km. Consequently, the main features of the linear theory are obtained in the numerical calculation. These waves are distinctly indicated in the vertical velocity contour plots also shown in the figure.

#### 4.2.1 Wave Drag Results

In stratified flow over an obstacle the pressure is systematically higher on the upstream side, resulting in a drag force on the obstacle, and a corresponding drag of opposite sign on the air stream.

This drag force of the air on the mountain is obtained by integrating the momentum transport along the x-axis. For a symmetrical mountain of height H,

$$\text{Drag} = - \int_{-\infty}^{\infty} (\rho u'w')|_{z=H} dx ,$$

where  $u', w'$  = velocity perturbation quantities.

An edit routine was written to integrate the results obtained in these calculations. The results are presented as

$$\overline{\rho u'w'} = \frac{1}{2L} \int_{-L}^L \rho u'w' dx$$

where  $L$  is one-half the computational x-interval. The drag units  $\overline{\rho u'w'}$ , as presented here, are in dynes/cm<sup>2</sup>. The quantity  $L$  is 48 km. The values presented may be related to other studies where drag force is presented in dynes/cm by multiplying the values shown here by  $2L$ .

The momentum edits  $\overline{\rho u'w'}$ , located one cell above the mountain top, are shown as a function of time in Figure 4.12. The largest value of the drag which was reached at 1000 seconds, was approximately equal to 4 dynes/cm<sup>2</sup>. This value agrees qualitatively with measured values of the momentum flux reported by D.K. Lilly<sup>[20]</sup> for measurements at Boulder, Colorado (7 dynes/cm<sup>2</sup>). Palm and Foldvik, and Vergeiner<sup>[21]</sup> present calculated values of  $7 \times 10^6$  to  $2 \times 10^7$  dynes/cm for similar problems. The value of 4 dynes/cm<sup>2</sup> corresponds to  $3.8 \times 10^7$  dynes/cm and thus we also see qualitative agreement here.

The other important feature of the momentum flux edit is the oscillatory character of the values with time. It is thought to be related to the formation of the individual vertical velocity cells, i.e., as new positive or negative cells are formed, there is an increase or decrease in the horizontal average of the vertical flux of horizontal momentum.

Figure 4.13 presents the two-wave momentum flux as a function of height at several times. The momentum edits indicate a cyclic character at late times at a height of 3 to 5 km. The interaction of the long and short waves takes place in this altitude range and is thought to be responsible for this phenomenon.

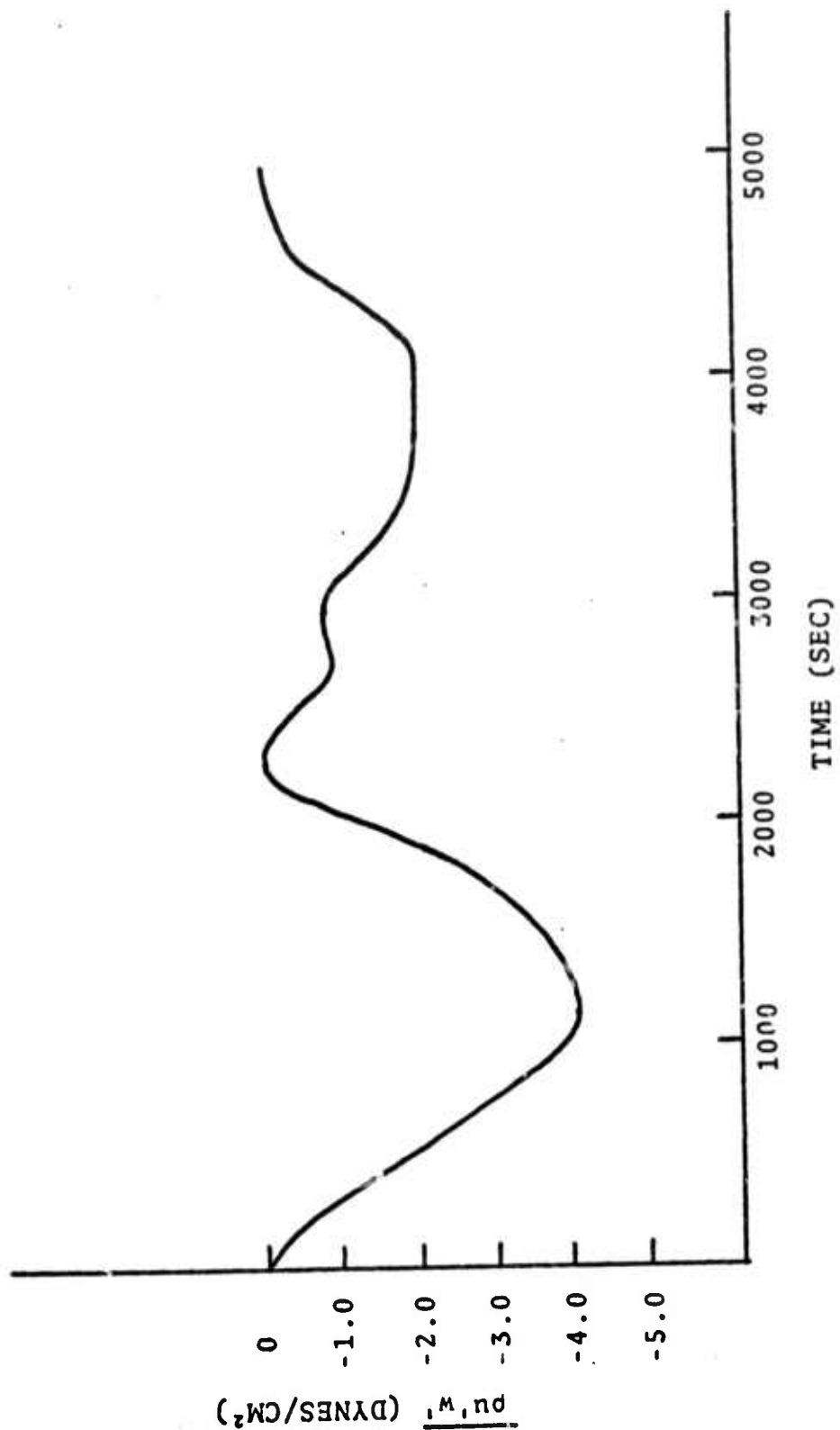


Figure 4.12. Two-wave problem - vertical transport of horizontal momentum above the obstacle.

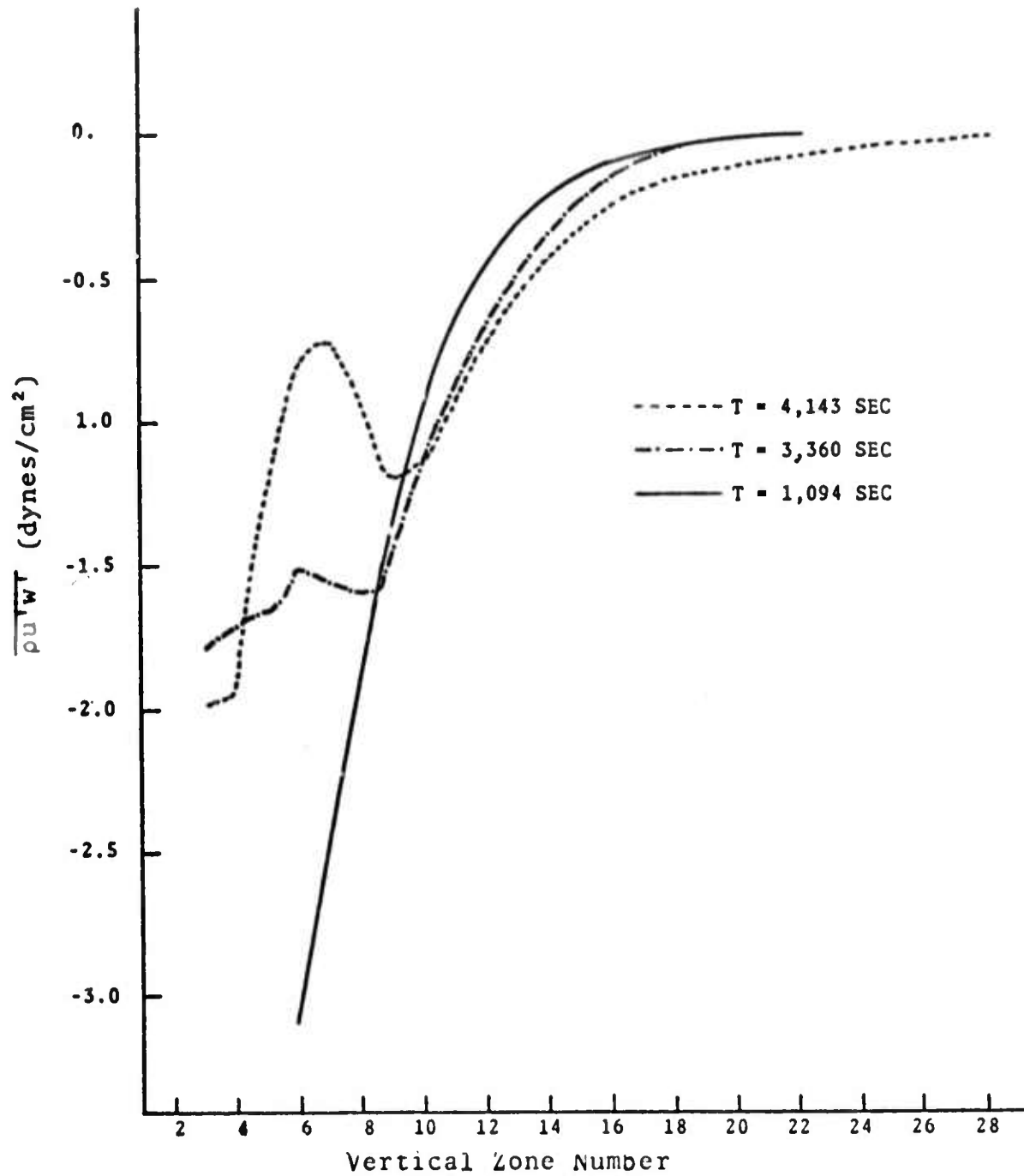


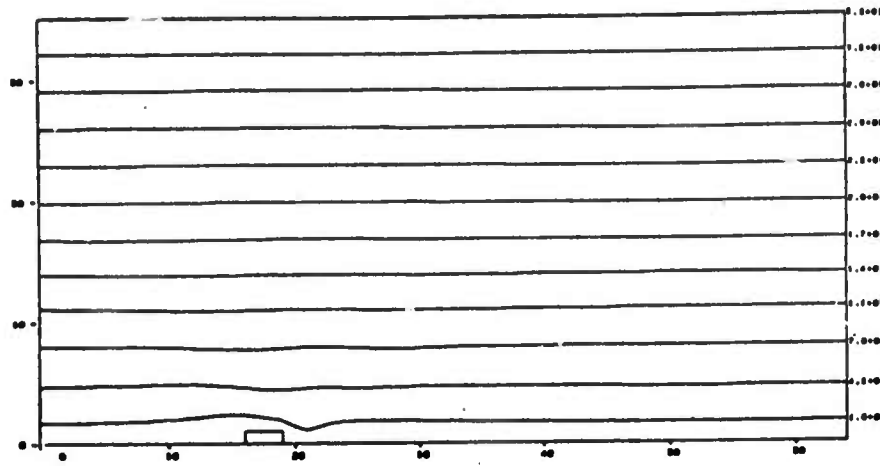
Figure 4.13. Momentum flux as a function of height for two-wave problem.

### 4.3 UNIFORM VELOCITY

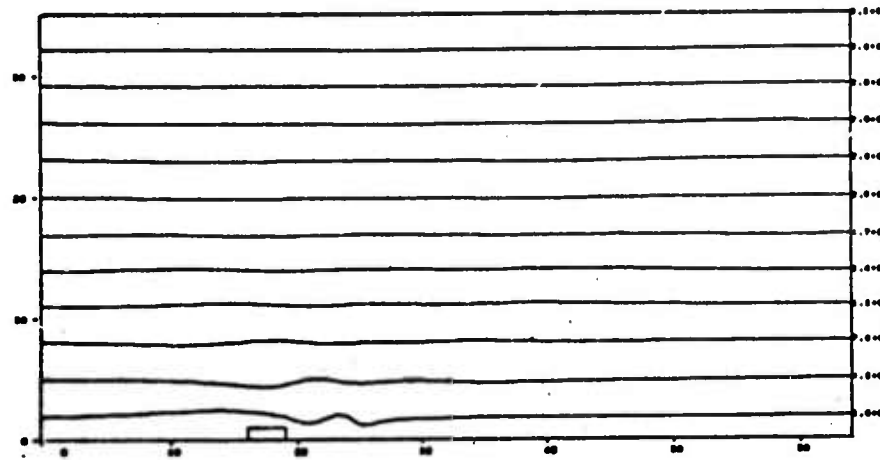
A problem using a velocity distribution uniform with height and equal to 10 m/sec perturbed by a one kilometer high mountain was completed. The lapse rate was set equal to one-half the dry adiabatic. Figures 4.14 through 4.17 show the resulting streamlines and vertical velocity cells formed under these conditions. Foldvik and Wurtele<sup>[22]</sup> have also investigated this problem, the results of which are shown in Figures 4.18 through 4.20. A comparison of their streamlines with our results show a continuous spectrum of waves is excited in both calculations, which when added together produce growing numbers of upwind-tilting troughs and crests extending to great heights. The figures showing the vertical velocity cells at the forward and rear of the obstacle show these upwind-tilting troughs and crests even more distinctly. Lyra<sup>[23]</sup> theoretically showed these same results using a linear analysis. His steady state analytical result for the streamlines and the vertical velocity field are shown in Figures 4.21 and 4.22. While there are certainly similarities in the results of Lyra, Foldvik and Wurtele, and the  $S^3$  calculation, there are also some significant differences. The four total streamline fields computed by Foldvik and Wurtele and shown in Figures 4.18 and 4.19 show a large amplitude wave just above the lee slope. The vertical velocity in this region is more than five times the upstream wind and the total horizontal velocity is negative at some grid points. This feature is not present in the linear theory and did not appear in the  $S^3$  computations.

One of the most significant items found in calculating this problem was a numerical instability associated with the flow when the normal stability criteria for the advective terms of the equations was used. An initial computation using this time step control produced a series of large wave length

457 SEC



937 SEC



1405 SEC

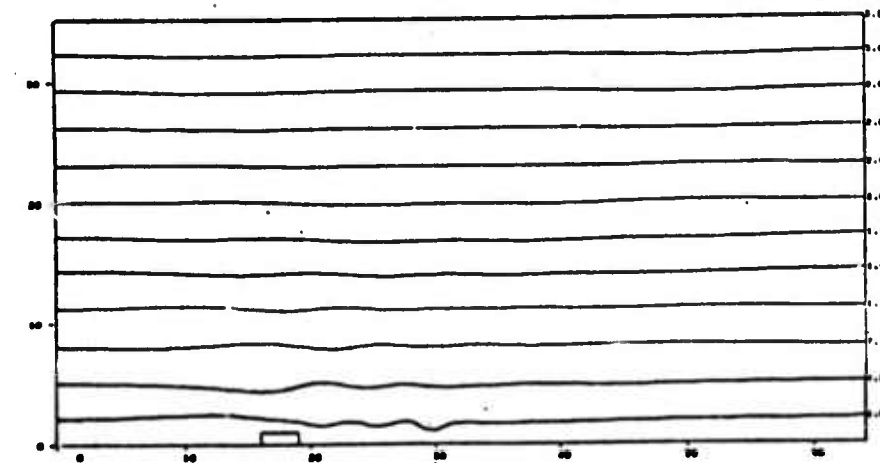
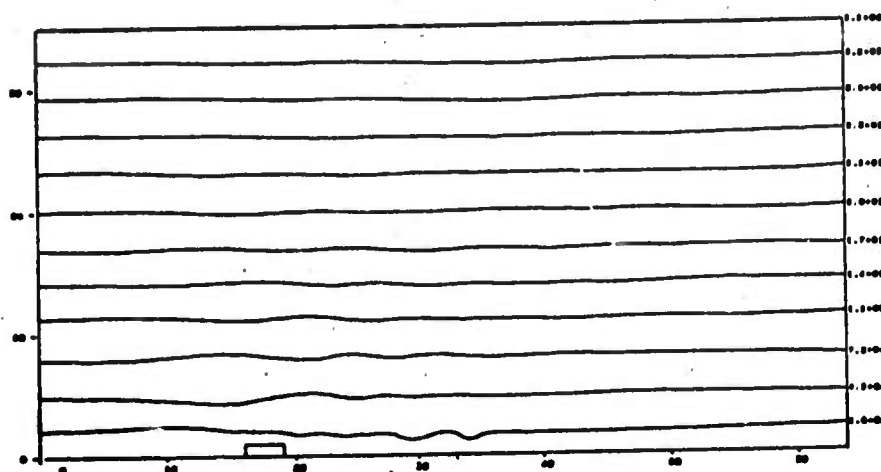


Figure 4.14 - Streamlines from Uniform Velocity Problem.

1885 SEC



2365 SEC

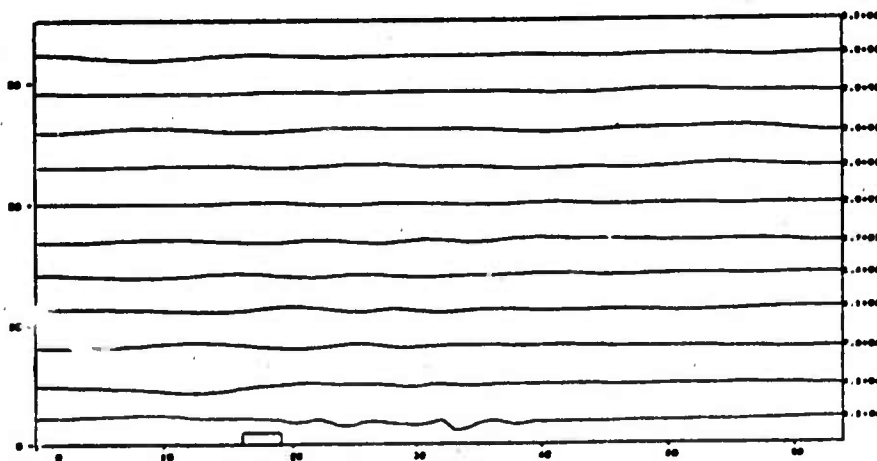
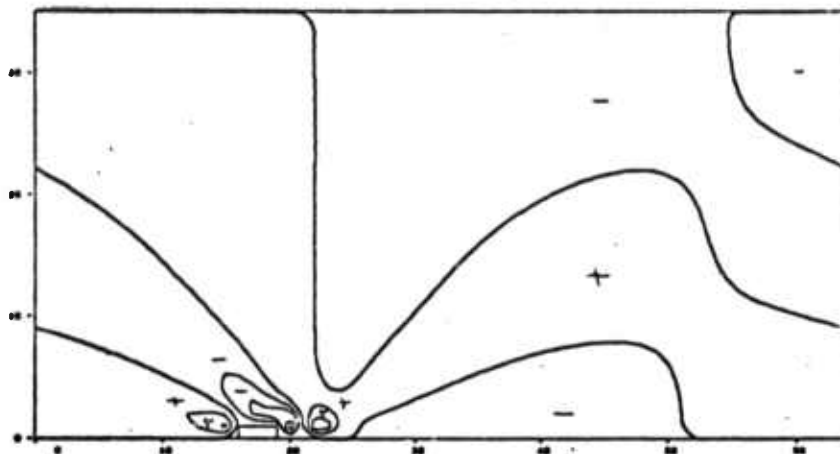
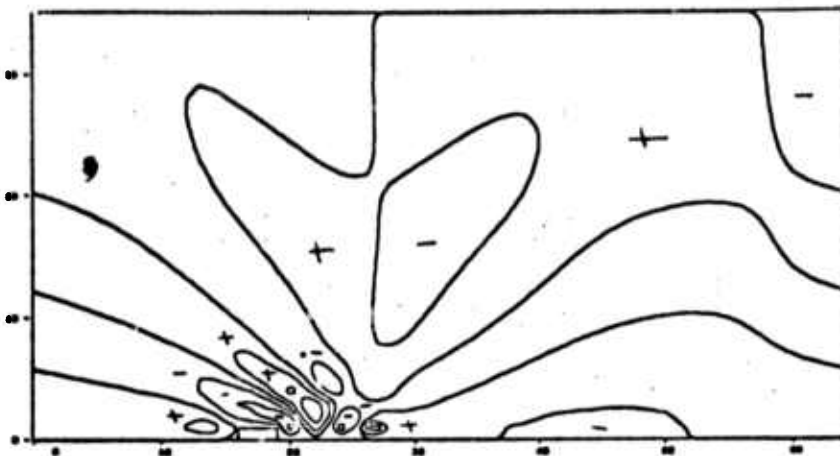


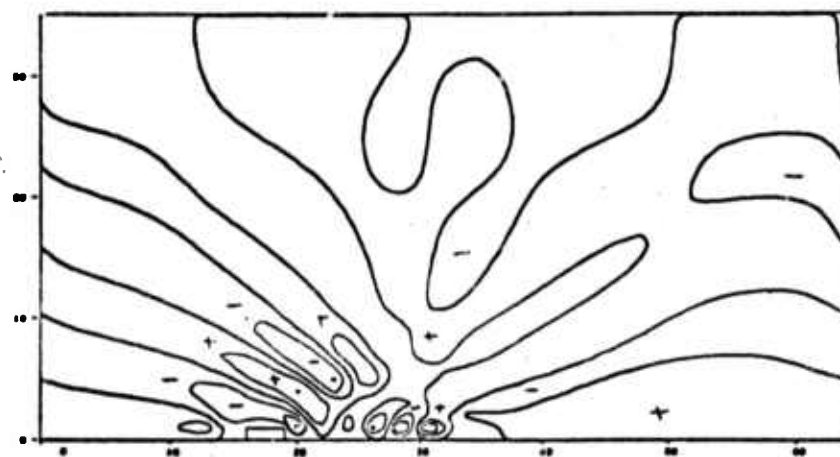
Figure 4.15 - Streamlines from Uniform Velocity Problem (page 2).



457 SEC

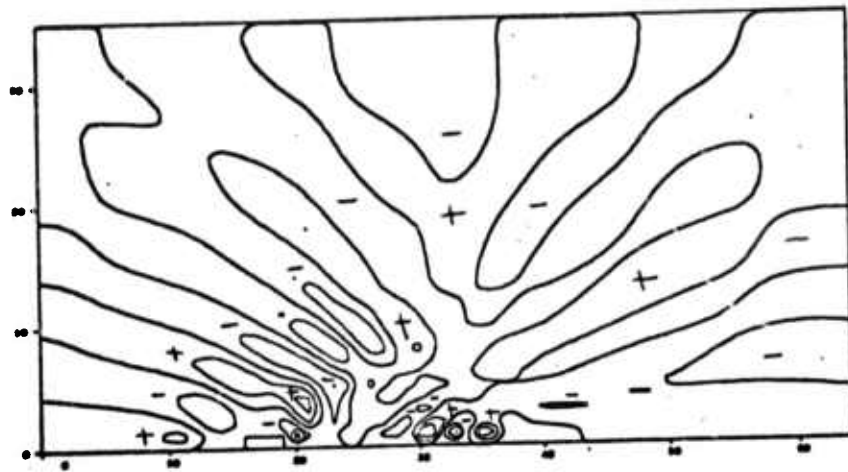


937 SEC

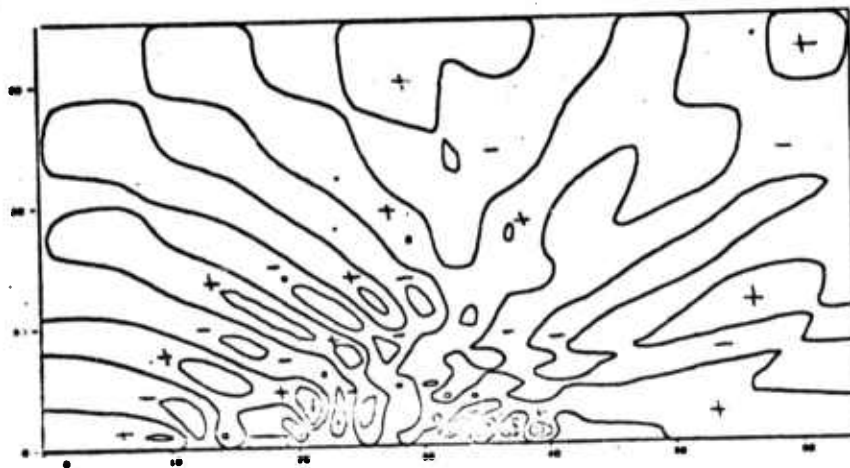


1405 SEC

Figure 4.16 - Vertical Velocity Field from Uniform Velocity Problem.



1885 SEC



2365 SEC

Figure 4.17 - Vertical Velocity Field from Uniform Velocity Problem (page 2).

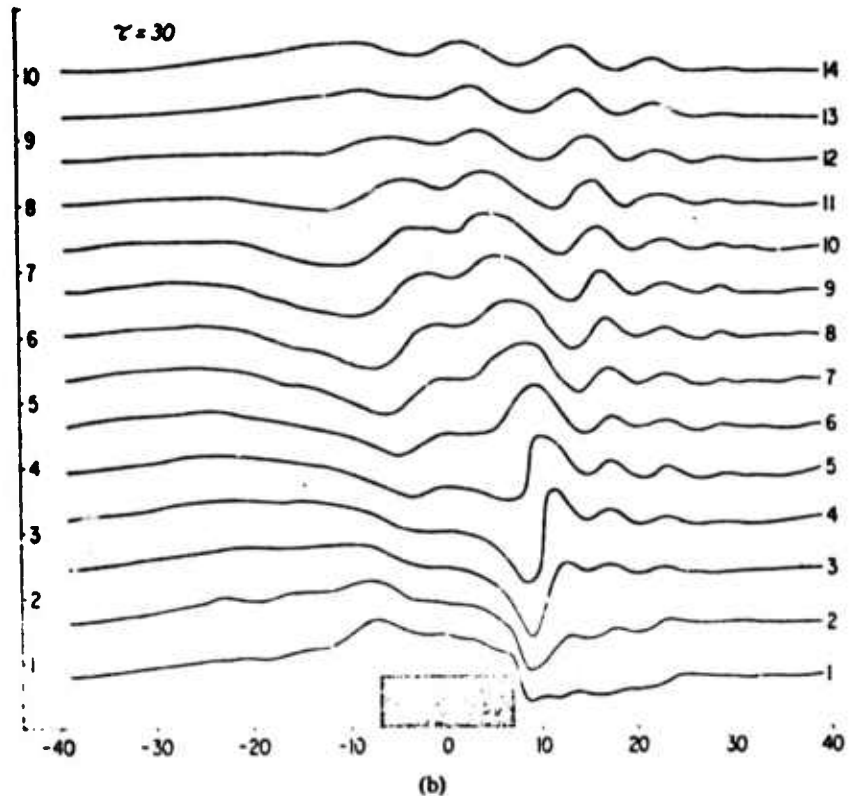
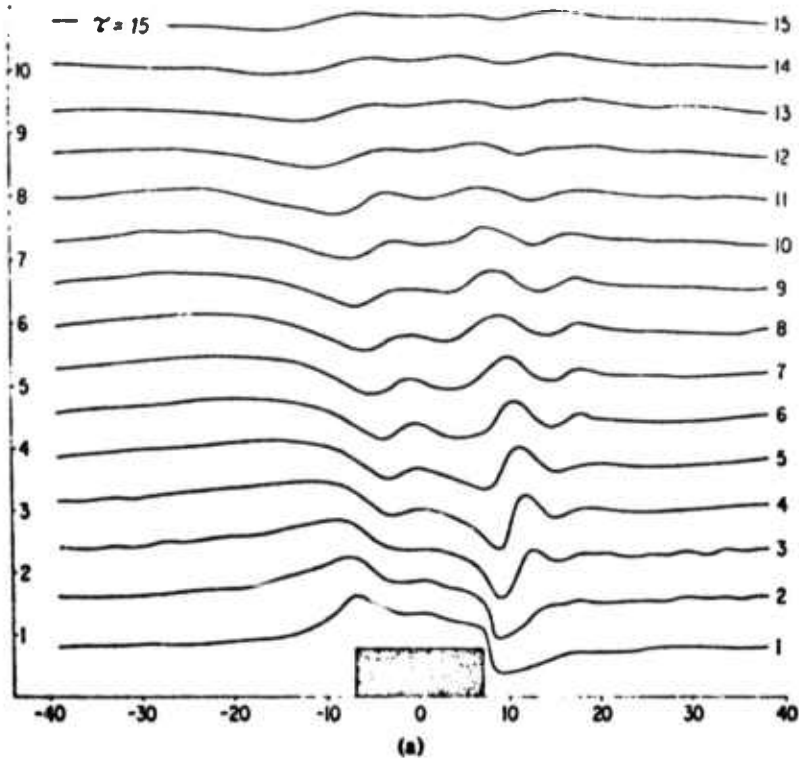


Figure 4.18 - Computed Streamlines from Foldvik and Wurtele at successive times for Uniform Velocity Problem.

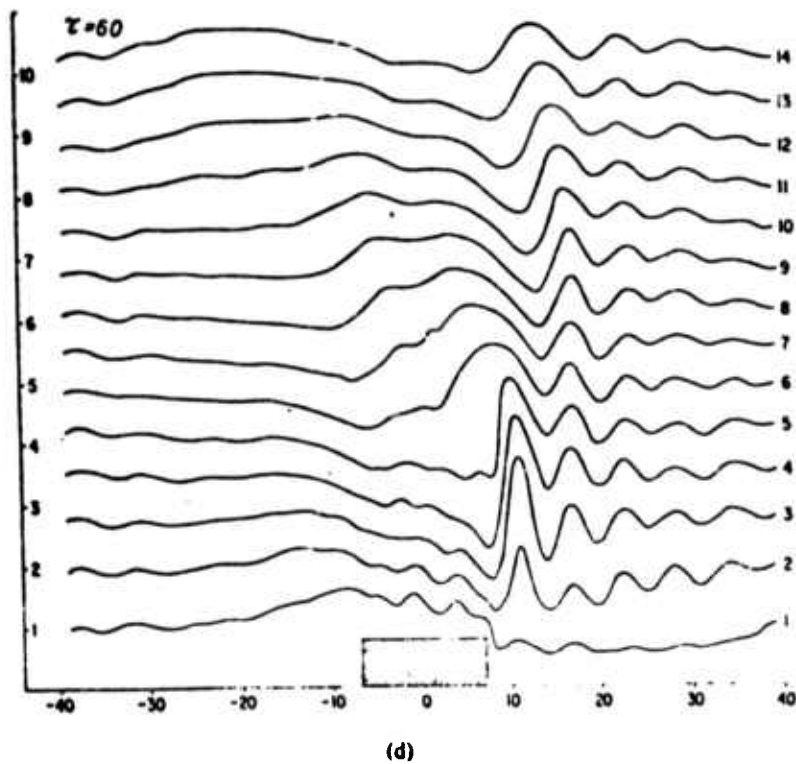
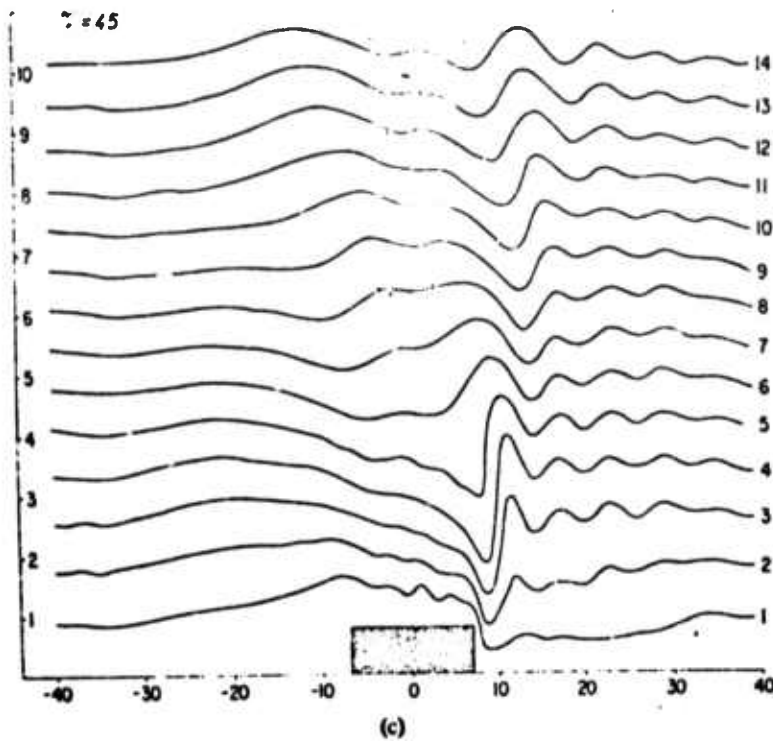


Figure 4.19 - Computed Streamlines from Foldvik and Wurtele at successive times for Uniform Velocity Problem (page 2).

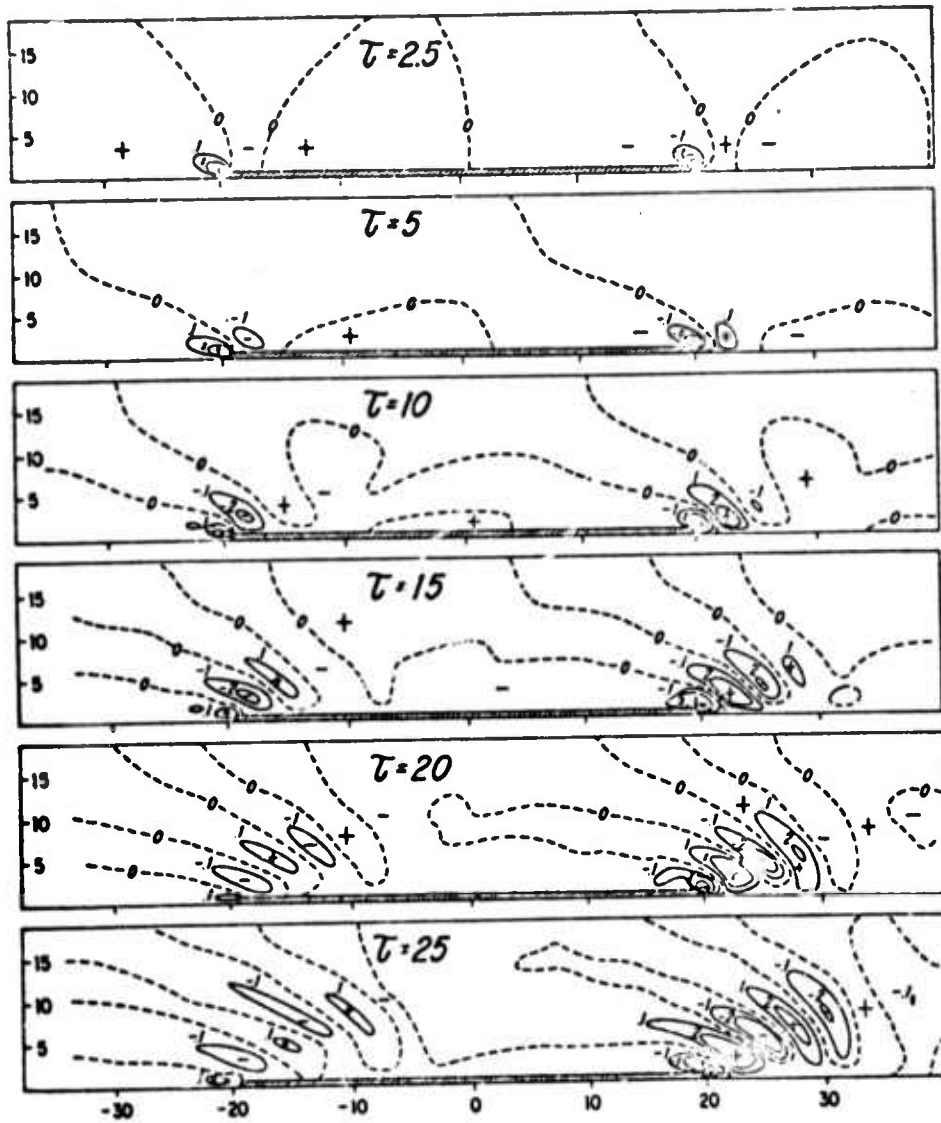


Figure 4.20 - Field of vertical motion computed under upwind conditions for successive times from Uniform velocity problem.

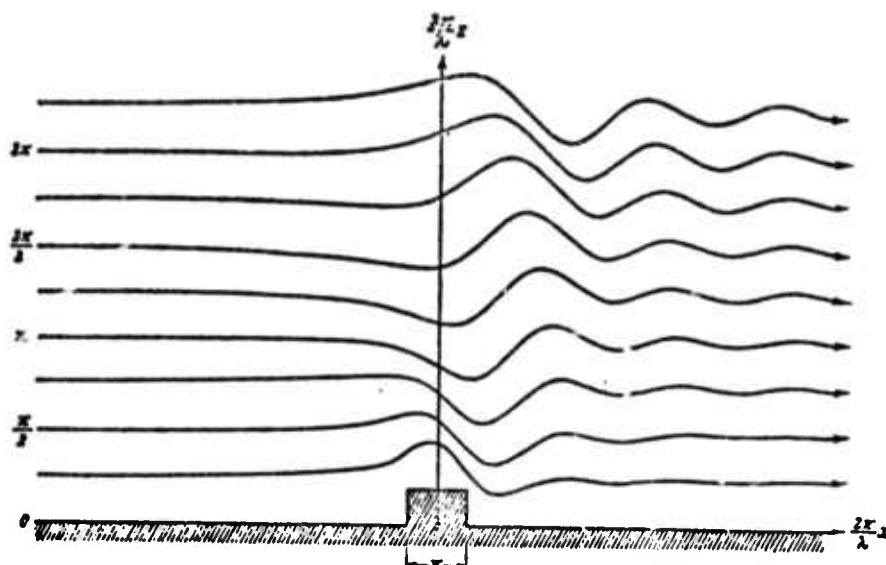


Figure 4.21 - Streamlines from the linear theory (after Lyra).

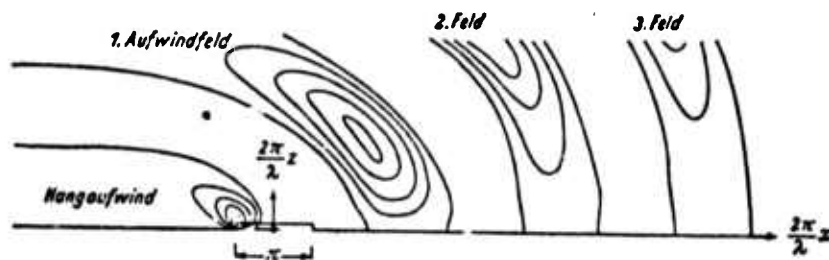


Figure 4.22 - Field of vertical velocity when  $U = \text{constant}$  with height (after Lyra). Isopleths for  $w > 0$  only.

high amplitude waves which propagated throughout the flow very quickly. The problem was recalculated by putting an upper limit on the time step which was based on the phase speed of the largest of these waves, i.e., a wave with a 50 km wavelength. This limited the time step to less than 14 seconds per cycle in order that the 50 km wave would not completely traverse a grid cell in one cycle. The actual limiting time step used in the recalculation was 12.0 seconds. The resulting wave pattern is the one shown in Figures 4.14 through 4.17 and previously discussed in this section. This new stability criteria, which had not been previously used, was not required in earlier problems due to either (1) the damping of the disturbances caused by the wind shear or (2) the high velocities in the single wave problem controlling the time step to an acceptable value. Later problems, the tropopause and inversion layers, exhibited this same instability.

#### 4.4 INVERSION LAYER I

The determination of the effect of an inversion layer in the atmosphere was calculated using the BASIC HAIFA code. The inversion layer was described as a positive 4°C temperature change over a 1.5 km height as shown in Figure 4.23. The other initial conditions are described in Table 4.1. The results, shown in Figures 4.24 through 4.27, indicate a small effect in the vertical velocity cells at heights corresponding to the inversion heights. The cells appear to be broader at a 5 km height than those seen in the two wave case for example. There also appear to be displacements in the vertical cells at this position. However, these may be due more to the change in the lapse rates at this position than the presence of the 4°C temperature increase.

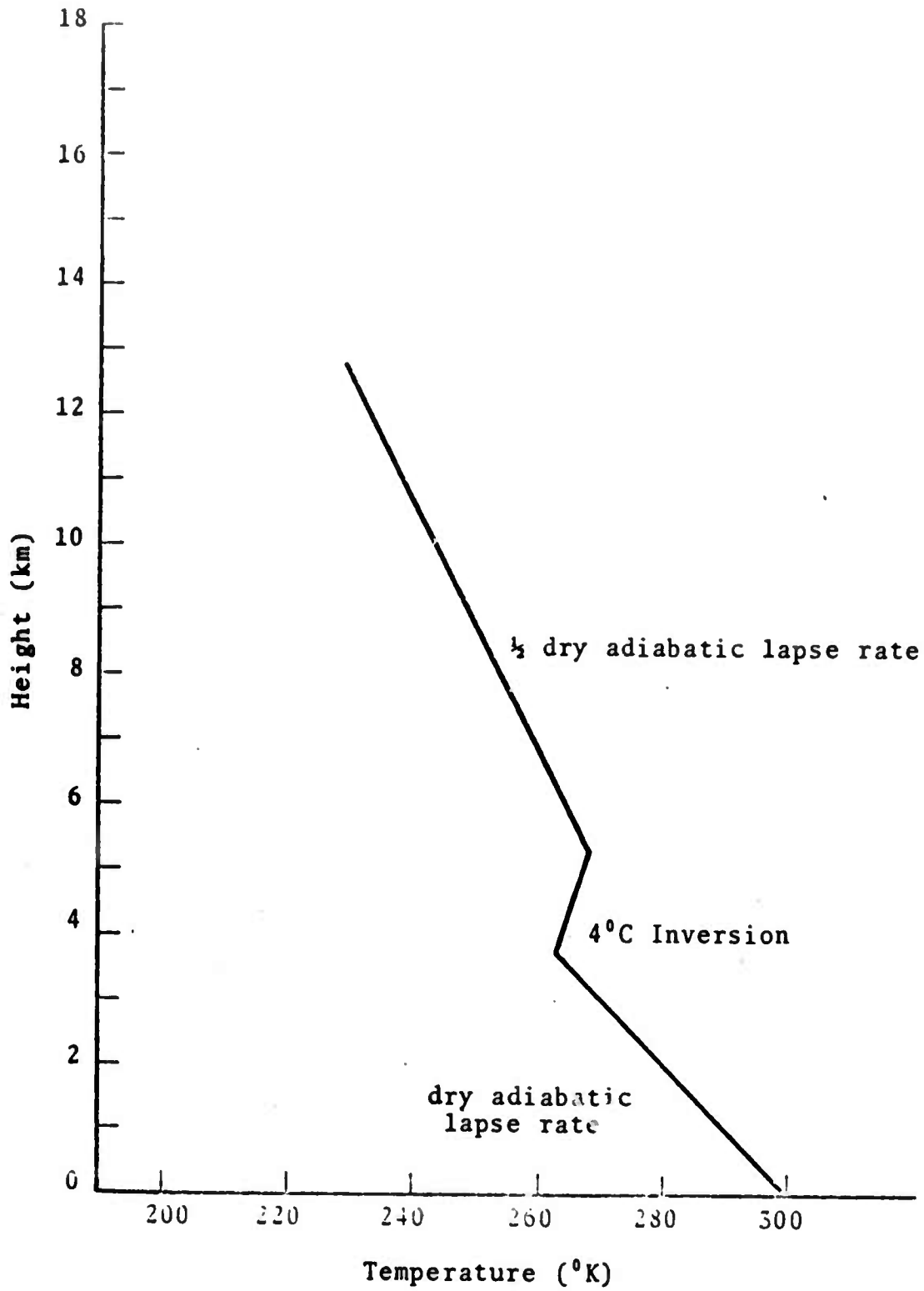
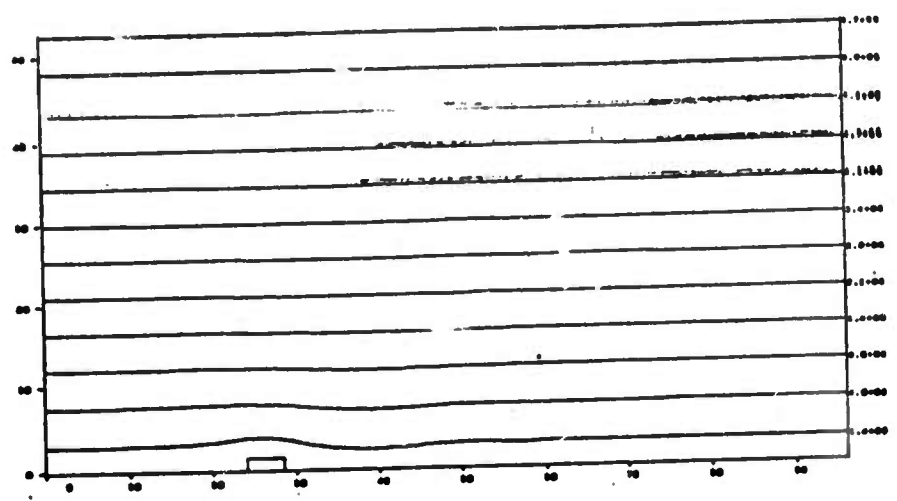


Figure 4.23 - Temperature Distribution used in Inversion Layer Problem.

591 SEC



996 SEC

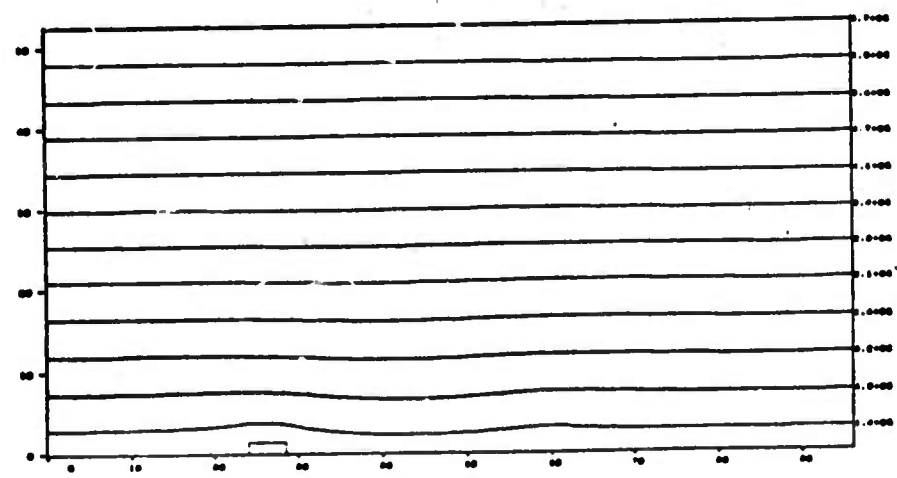
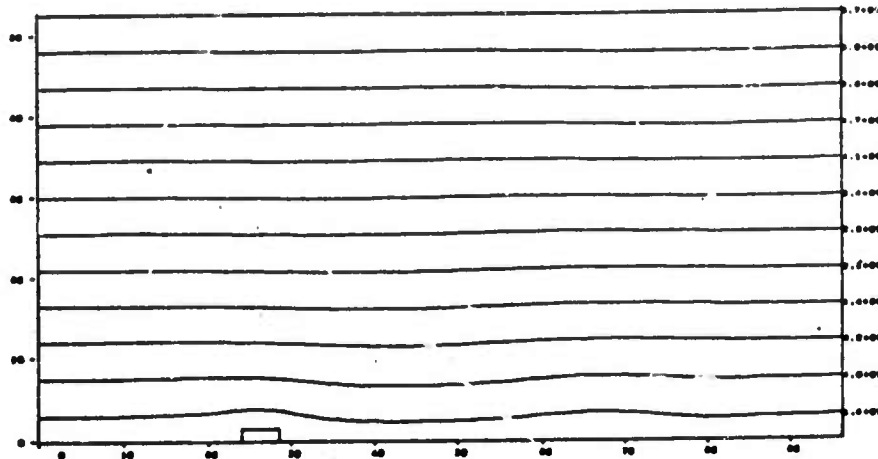


Figure 4.24 - Streamlines from Inversion Layer Problem.

1496 SEC



1946 SEC

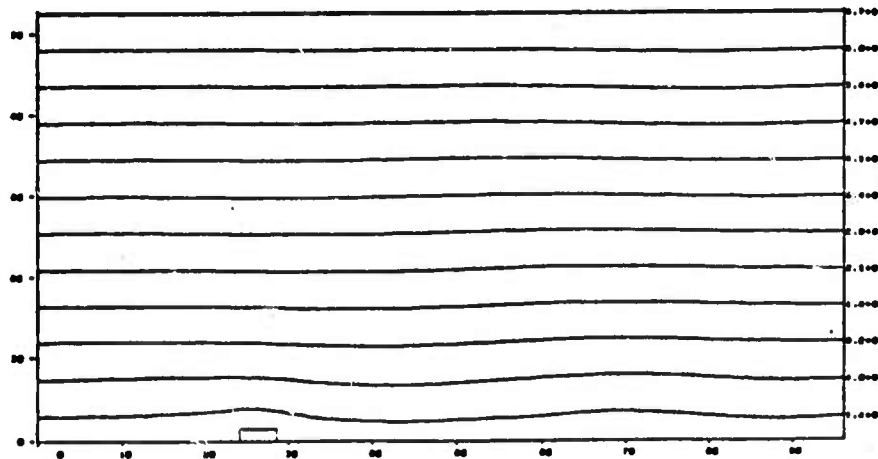
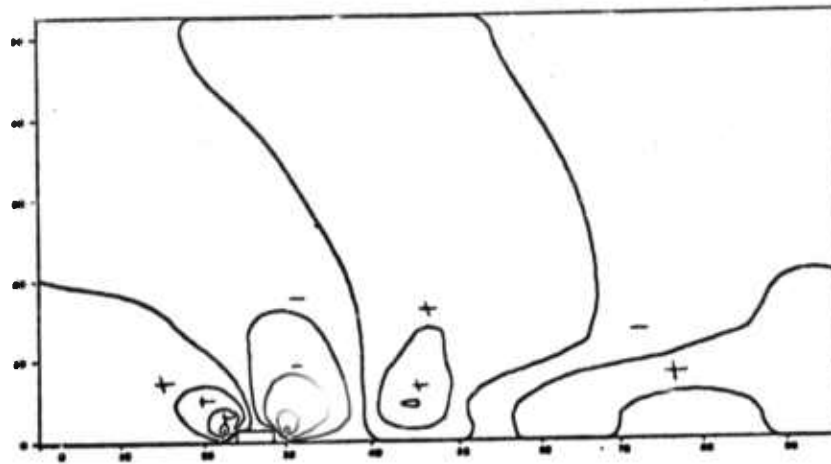
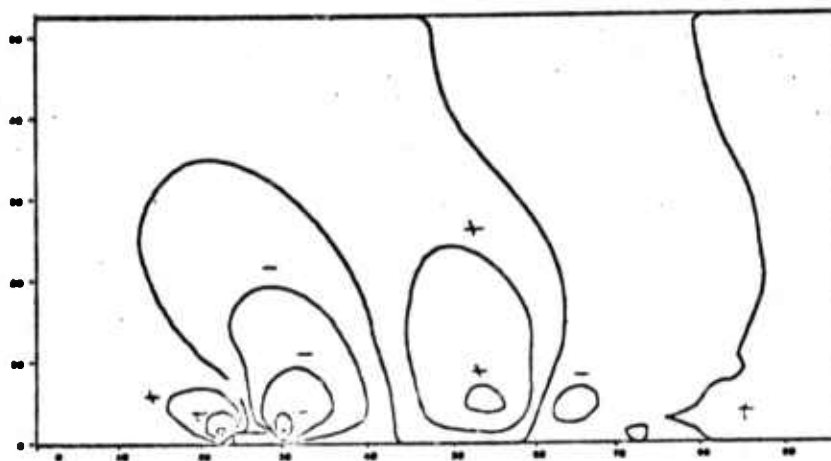


Figure 4.25 - Streamlines from Inversion Layer Problem (page 2).

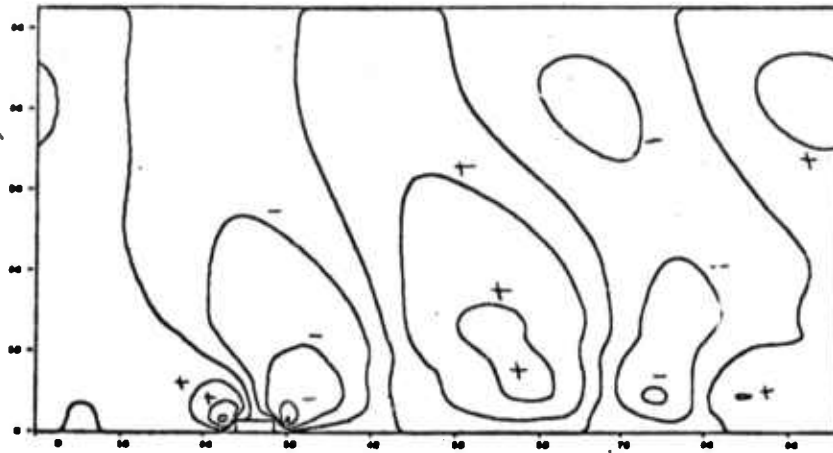


501 SEC

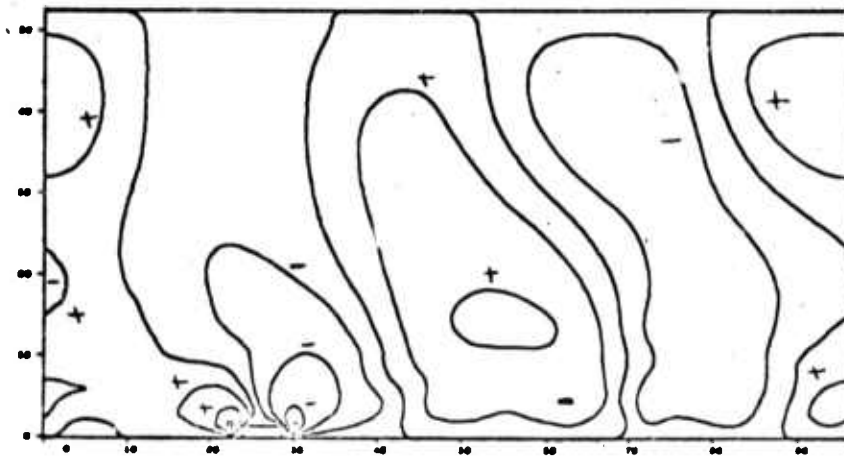


996 SEC

Figure 4.26 - Vertical Velocity Field from Inversion Layer Problem.



1496 SEC



1946 SEC

Figure 4.27 - Vertical Velocity Field from Inversion Layer Problem (page 2).

Because of the coarse zoning at the inversion layer, the definition of the flow is poor.

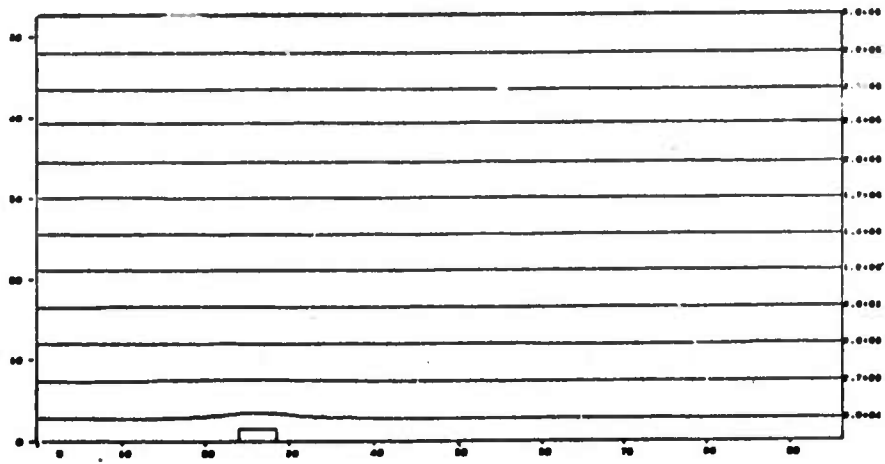
#### 4.5 TROPOPAUSE PROBLEM

The test calculation representing a tropopause problem consisted of initial conditions as described in Table 4.1. The calculated streamlines and vertical velocity contours are shown in Figures 4.28 through 4.31. The most noticeable characteristic of the resulting solution is the tilting of the vertical velocity cells toward the upwind direction. The streamline pattern for this problem did indicate, but not clearly, this same phenomena of the upwind tilting of the gravity peaks.

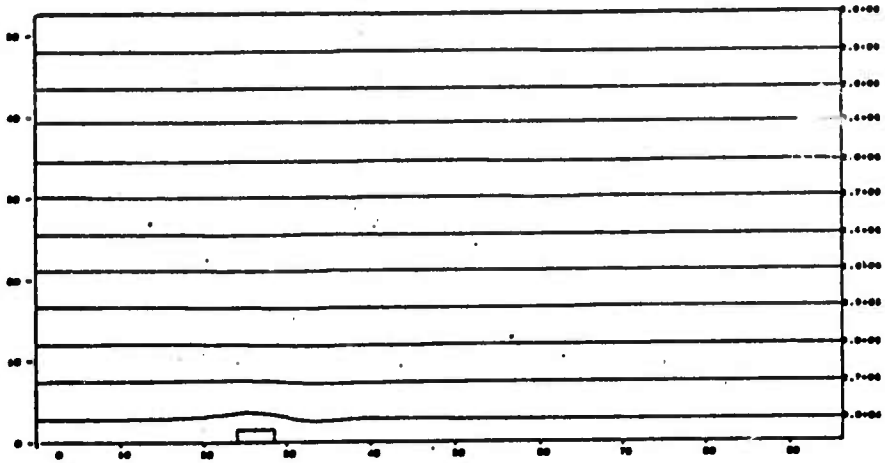
#### 4.6 SIERRA NEVADA LEE WAVE STUDY

Upon incorporation of triangular zoning and moisture effects in HAIFA, a study of the Sierra Nevada lee wave problem was undertaken. Experimental data was obtained from a study conducted by the University of California on lee wave phenomena occurring over the Owens Valley.<sup>[24]</sup> This study progressed over many months using sailplanes to record meteorological data over the valley. Rather complete temperature profiles were constructed for each day's work, with an accompanying description of the nature of any lee waves. Wind velocities were also measured, but no profiles could be constructed from the spotty data. Ambient conditions taken at two established weather stations were usually included in each day's report. The data set of February 16, 1952, (Figure 4.32) was chosen for the input conditions in the HAIFA runs. A strong lee wave was present on this day as shown by the streamline plots on Figure 4.33. The wavelength appears to be approximately 18 km at 2 km elevation, but increases to a 20 km wavelength at 6 km elevation.

87 SEC



287 SEC



487 SEC

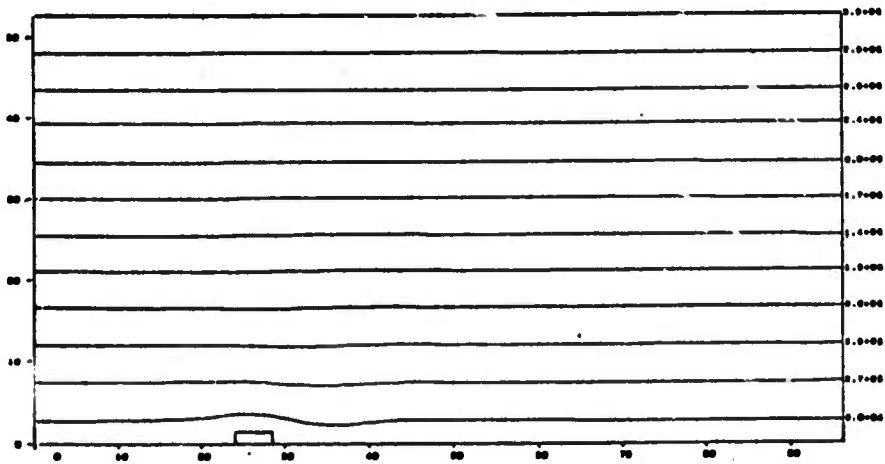
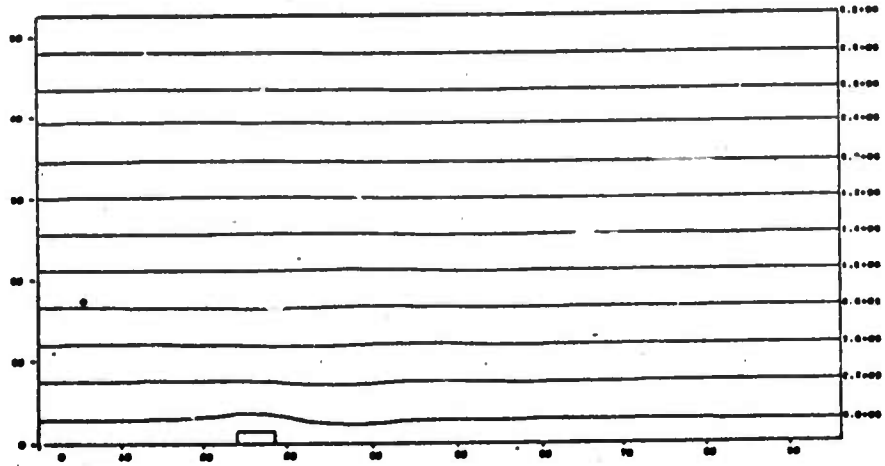


Figure 4.28 - Streamlines from Tropopause Problem.

687 SEC



887 SEC

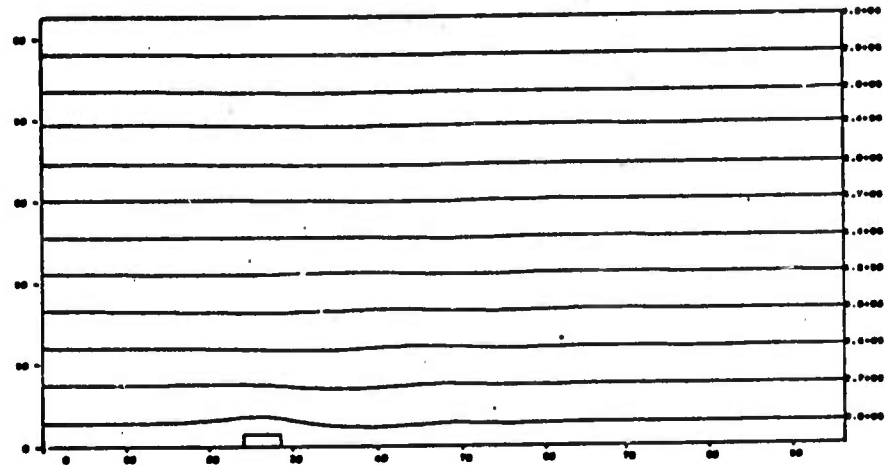
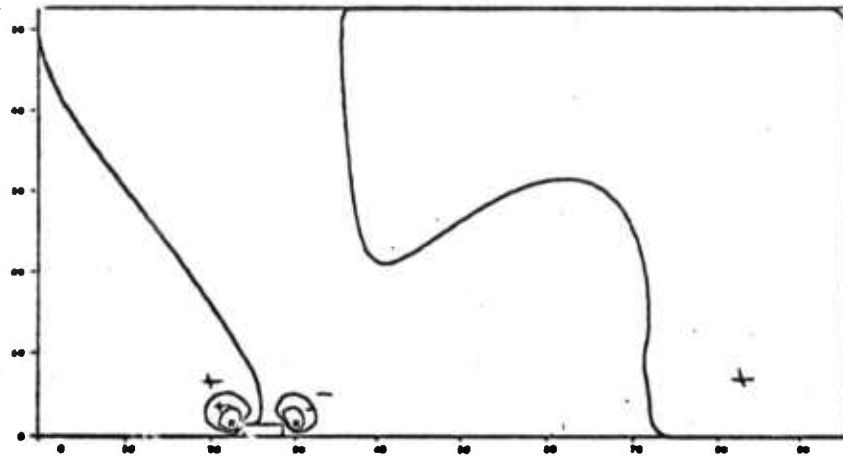
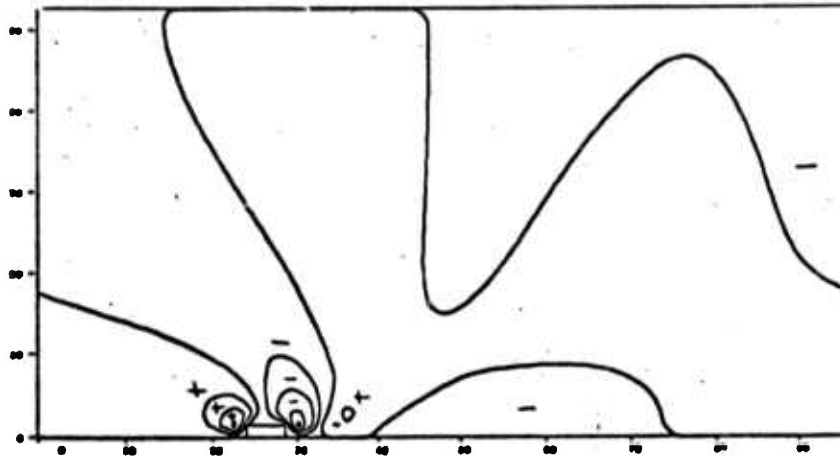


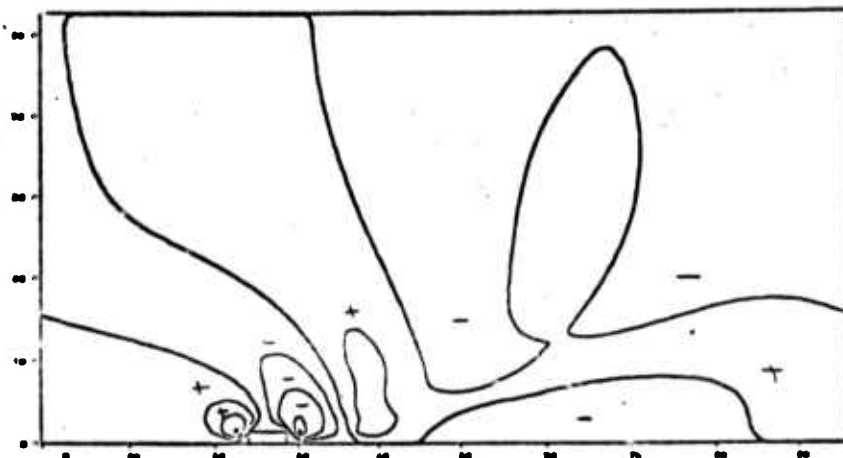
Figure 4.29 - Streamlines from Tropopause Problem (page 2).



87 SEC



287 SEC



487 SEC

Figure 4.30 - Vertical Velocity Field from Tropopause Problem.

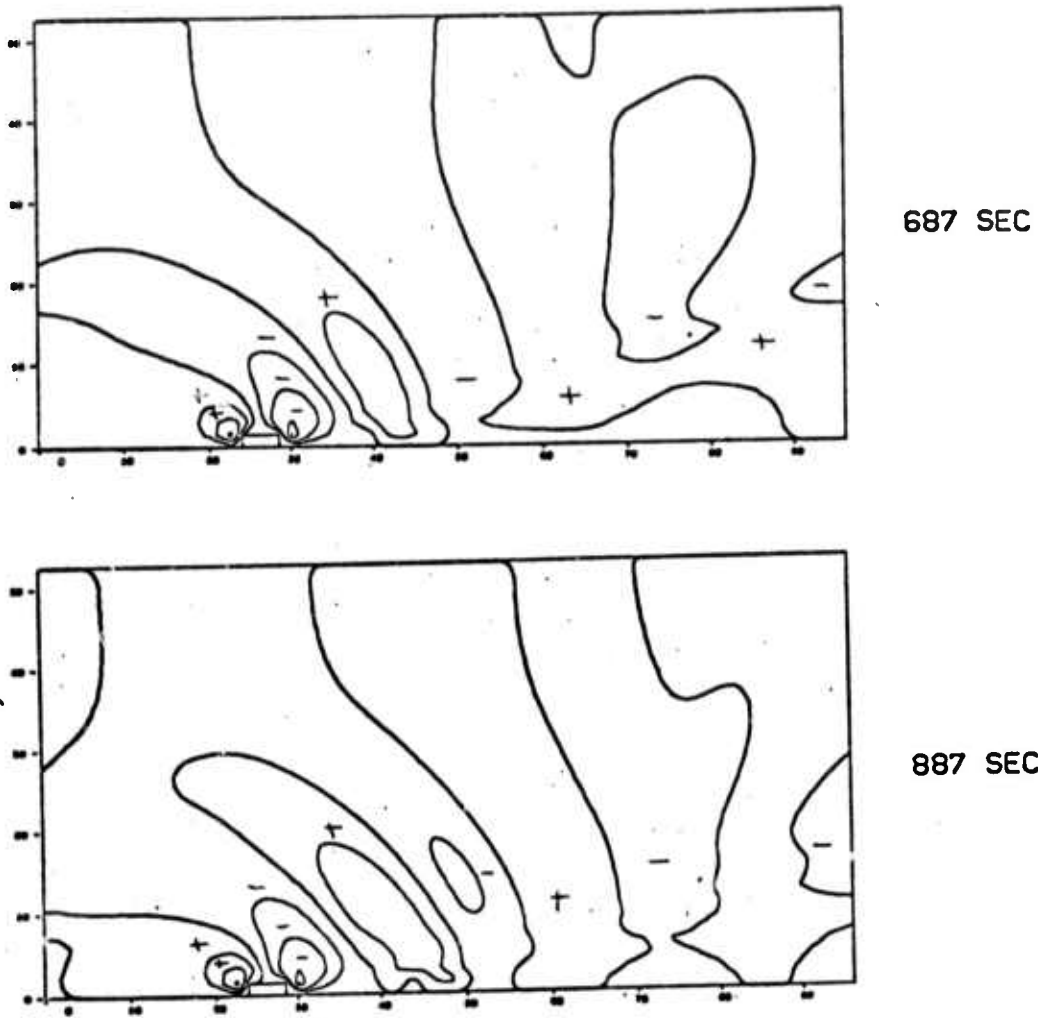


Figure 4.31 - Vertical Velocity Field from Tropopause Problem (page 2).

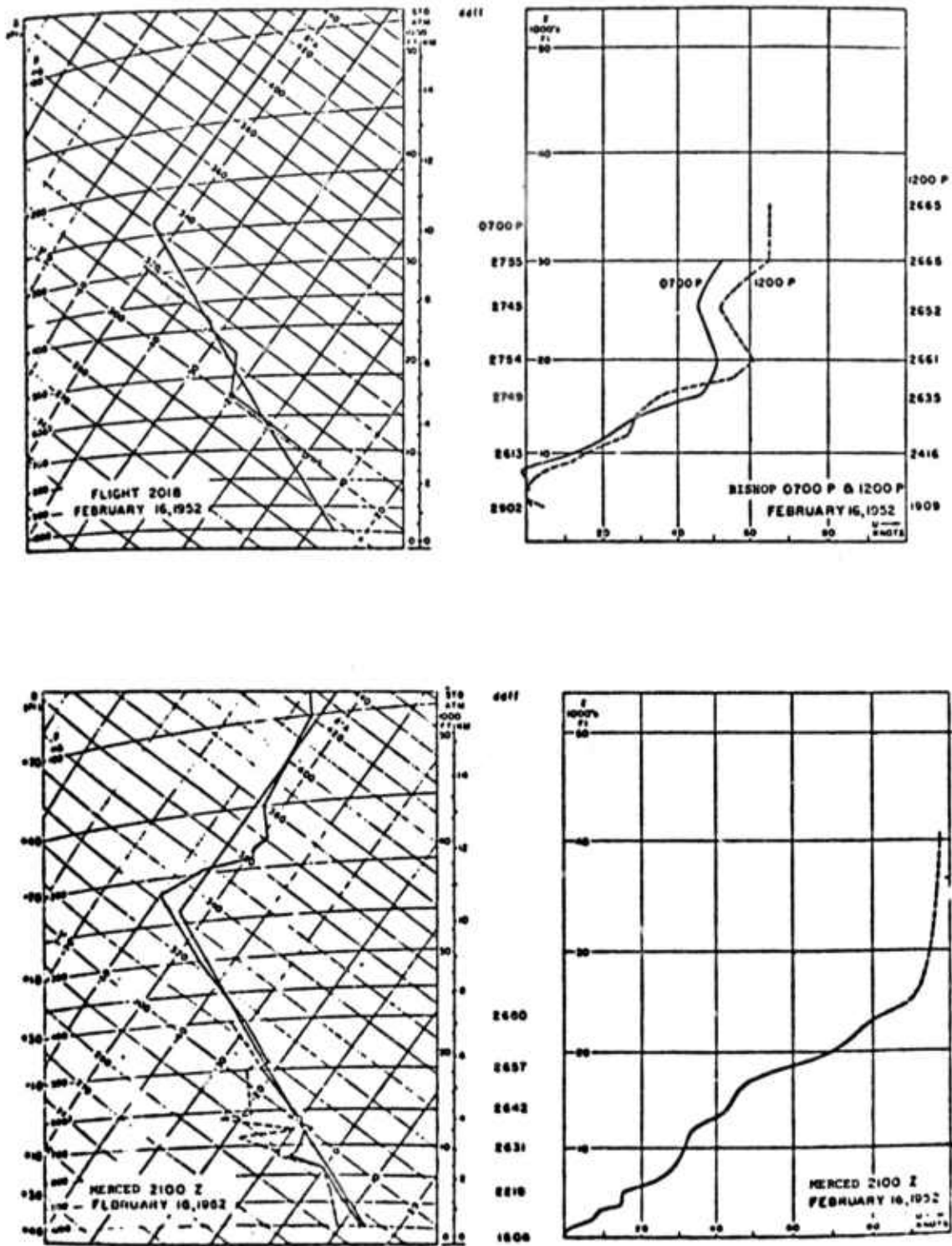


Figure 4.32 - Meteorological conditions for February 16, 1952, in the Owens Valley area.

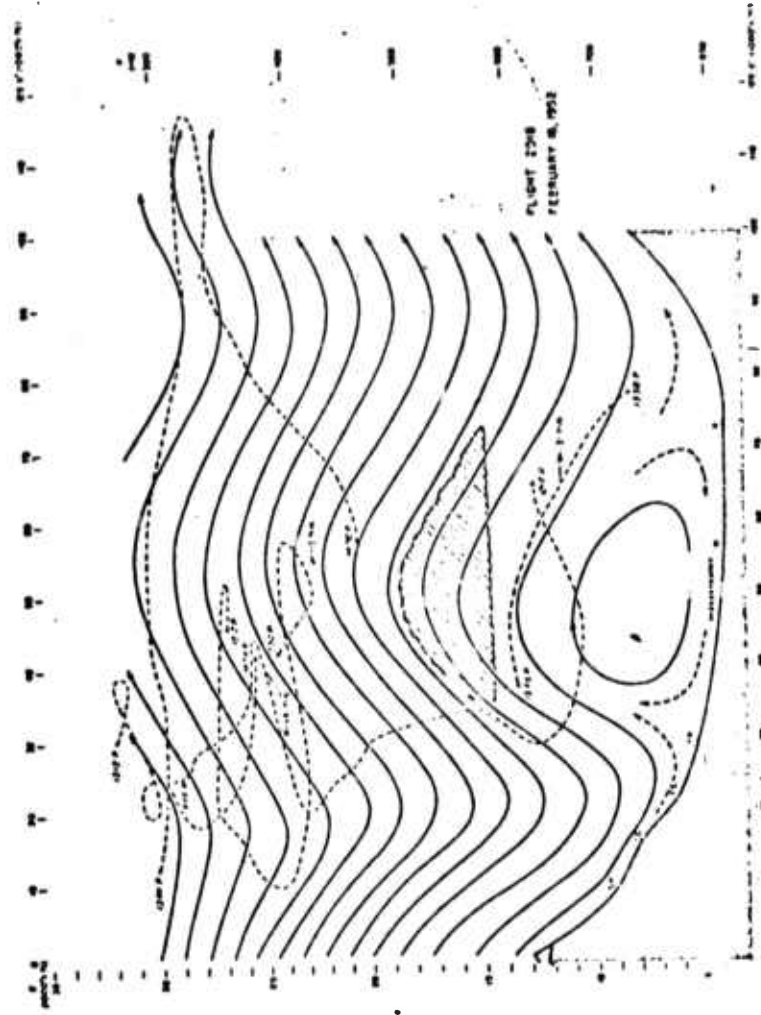


Figure 4.33 - Observed flow for February 16, 1952 over Owen's Valley.

HAIFA requires the specification of initial profiles of temperature, wind velocity, and in the case of the moist version of HAIFA, a moisture profile and specification of rain water production parameters. Since wind and moisture data were only available at the Merced weather station on the test day (west of the Sierra Nevada Range), the profiles of this station were used as input to HAIFA. A discussion of the appropriateness of this choice follows the presentation of results. The production term parameters describing auto-conversion, accretion, and evaporative processes were manipulated such that cloud water converted to rain water at the rate of 0.1 percent/second, rain water evaporation rates were zero and accretion assumed a negligible role compared to autoconversion. This arrangement is only one of many possibilities. It is, however, fairly representative of choices made by Liu and Orville in their cloud modeling work and is thought to be a good first choice. [10]

Upon examination of the typical cross section of the Sierra Nevada's Owens Valley (see Figure 4.34), it was thought that an appropriate choice of topography would be a symmetric triangular mountain of height 2 km with a base extending 16 km. The superposition of this choice on that of the real topography is seen in Figure 4.35. The HAIFA grid used in the study was composed of 35 cells in the vertical with a  $\Delta z$  of 500 m, yielding a total extent of 17.5 km. There were 64 cells in the horizontal, with a  $\Delta x$  of 2000 m, yielding an extent of 128 km. The top of the mountain model was located 30 km from the left edge of the grid.

The above HAIFA grid structure was used to simulate mountains at various elevations. This was accomplished by situating the base of the HAIFA grid at various elevations and

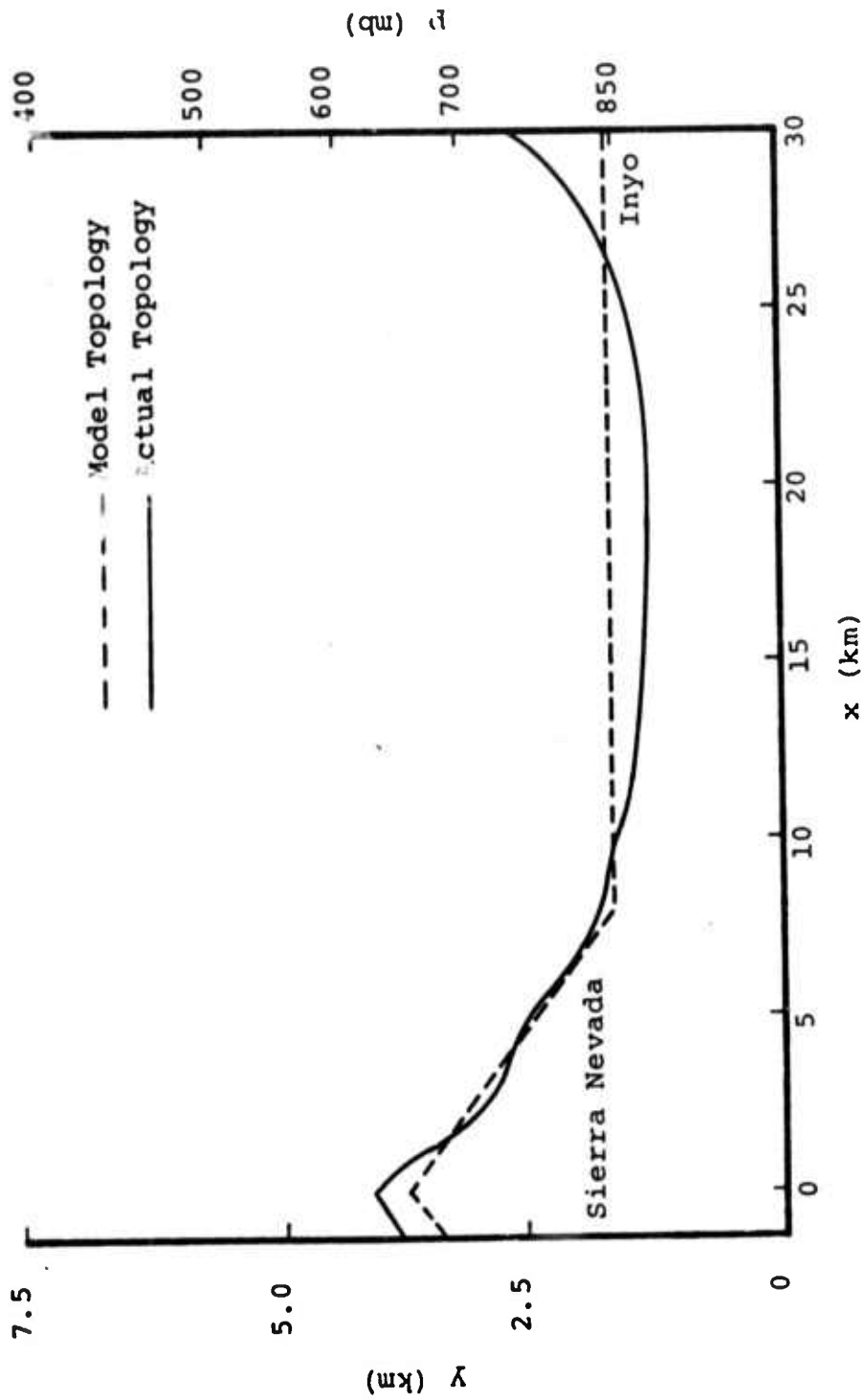


Figure 4.35 - Sierra Nevada cross-section with HAIFA approximation.

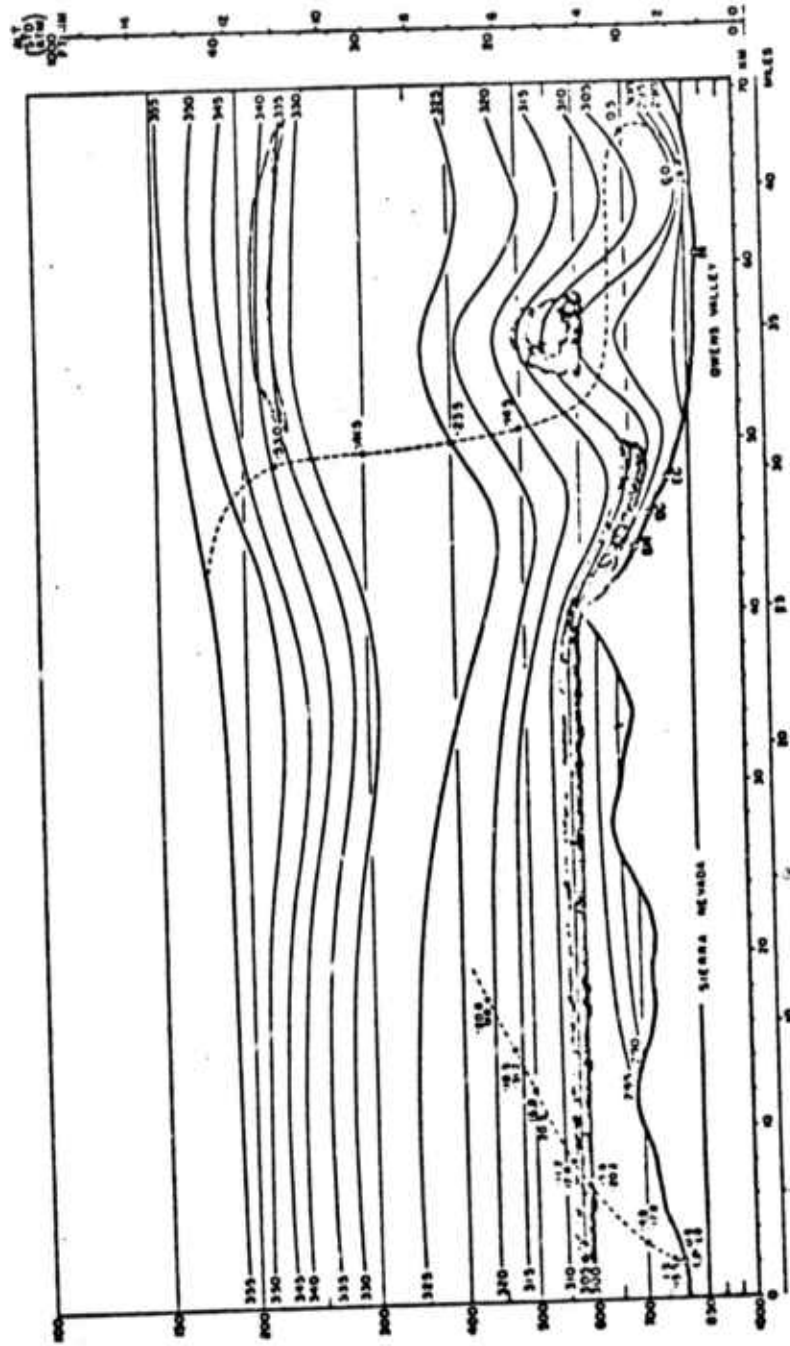


Figure 4.34 - Typical cross-section of Sierra Nevada at Owen's Valley.

allowing the HAIFA obstacle to represent only that part of the mountain which extends above the base elevation. The input profiles are picked up from the elevation at which the grid begins. Utilizing this procedure, two sets of runs were completed in the Sierra study. Each set consisted of two runs; the first run modeling a dry atmosphere, while the second run included moisture effects. The sets differed only in their grid base elevations. The first set located the grid base at sea level, thereby modeling a mountain of 2 km height. The second set positioned the grid base at 1.5 km elevation yielding a total mountain peak elevation of 3.5 km. Figure 4.32 depicts the actual weather data obtained at Merced. Wind data from Bishop and the temperature profile obtained from the flights over the valley are also presented. Figures 4.36a, b, and c represent the HAIFA input approximations to the Merced profiles. The approximations are tabulated in Table 4.3.

The results of set one indicate the basic validity of the HAIFA approach. The results of the dry run after a 2000 secs integration are presented in the streamline plots presented in Figure 4.37. A single well developed lee wave is present with a wavelength of approximately 10 km at an elevation of 2 km increasing to 15 km at 4 km. Three rotors are seen. The windward rotor is the result of blocking and is growing in time, as would be expected. Backflow extends almost 15 km. The two leeward rotors were formed from the splitting of a single larger rotor as time progressed. This is an expected result due to the traveling lee wave. Since there are no damping processes occurring in these HAIFA runs (other than truncation error diffusion), one would expect a series of rotors to form as any trapped waves progress downwind; the number and size of rotors produced being dependent on the strength of the flow field.

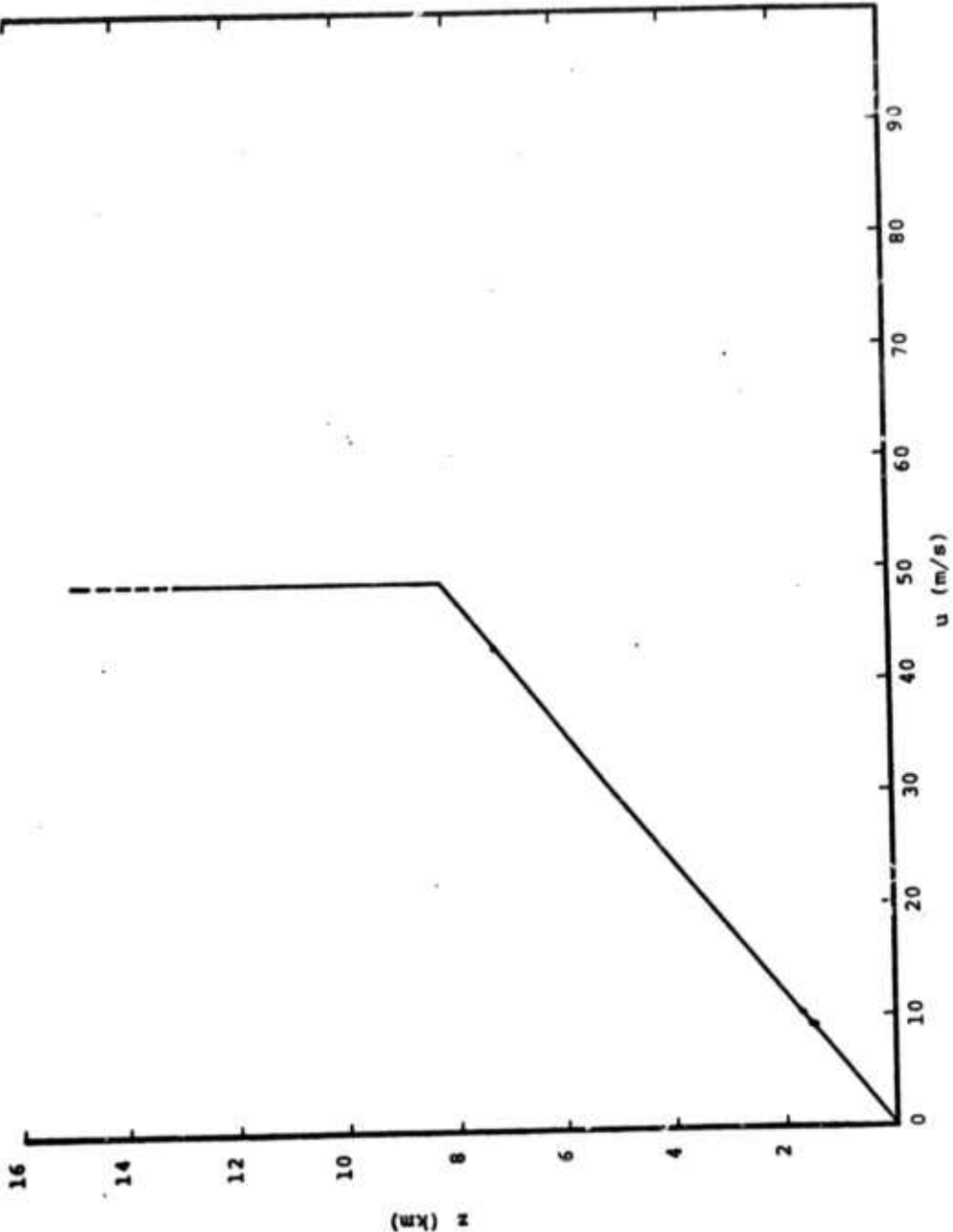


Figure 4.36a - Velocity profile, set 1.

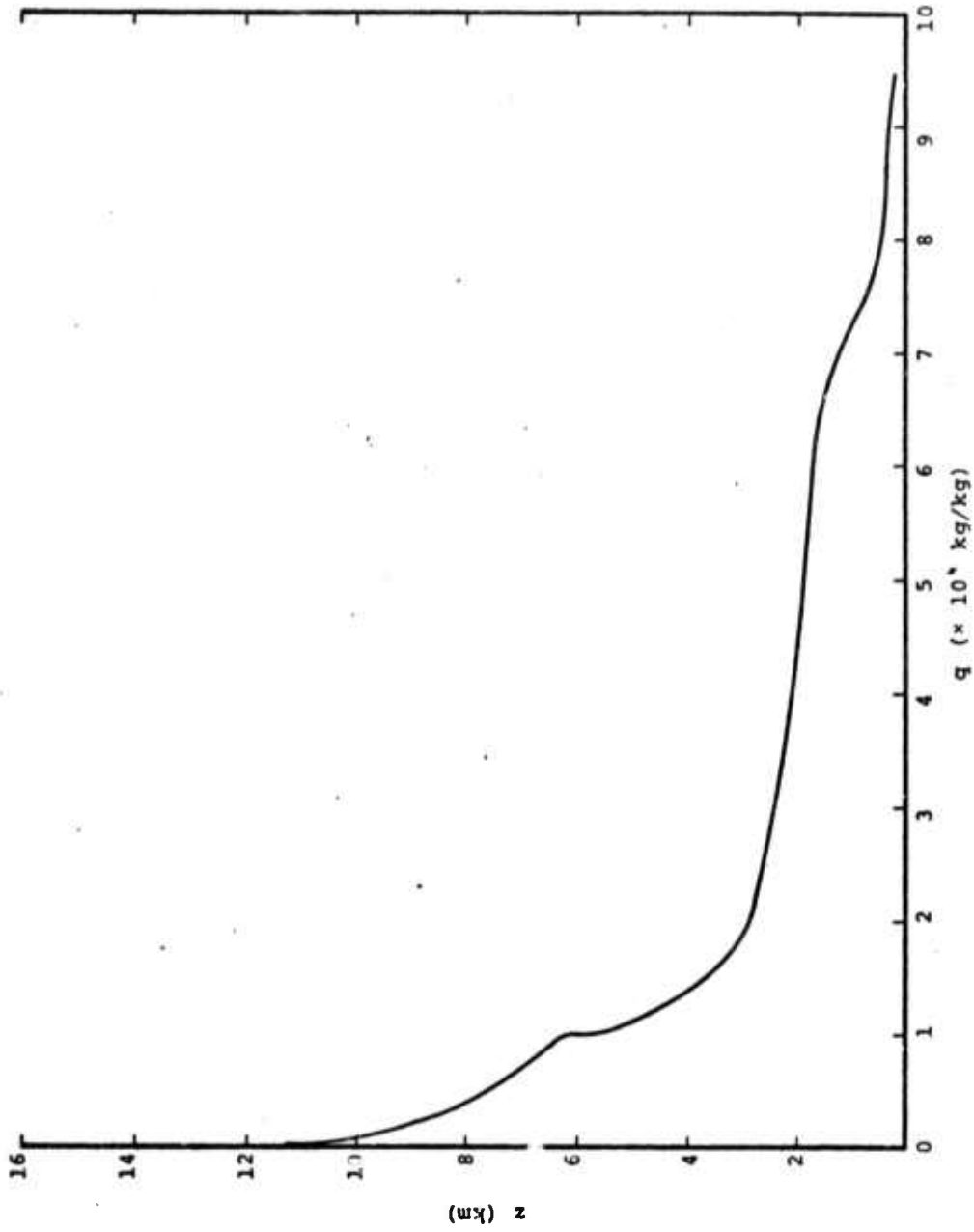


Figure 4.36b - Moisture profile, set 1.

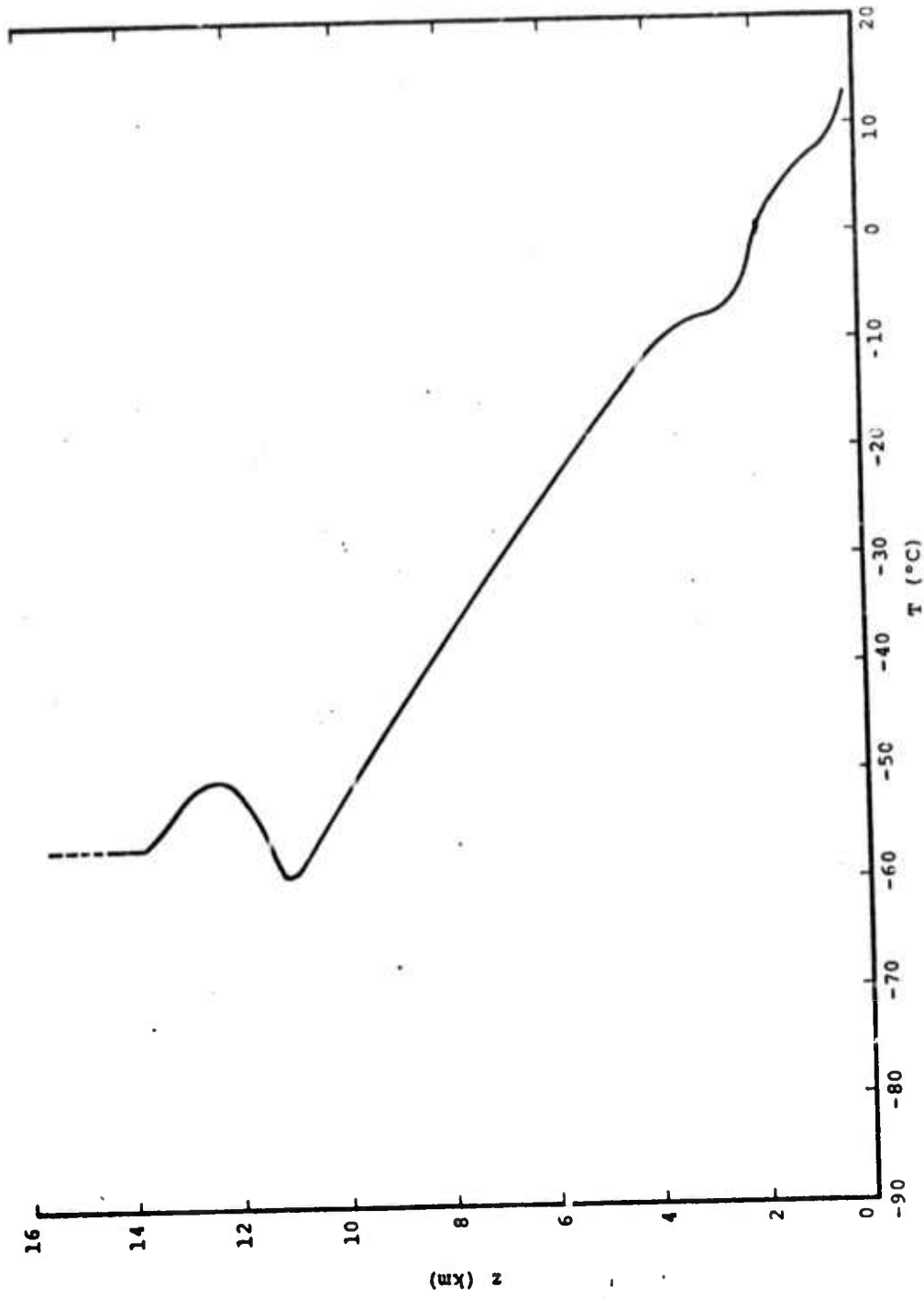


Figure 4.36c - Temperature profile, set 1.

Table 4.3  
HAIFA Input Profiles for Set 1

z (km)	q ( $\times 10^3$ kg/kg)	T ( $^{\circ}$ C)	u (m/s)
.25	9.50	13.0	1.48
.75	7.47	7.5	4.45
1.25	6.92	5.5	7.42
1.75	5.75	2.0	10.40
2.25	3.70	- 3.5	13.40
2.75	2.30	- 8.0	16.30
3.25	1.70	- 8.0	19.30
3.75	1.50	- 9.5	22.20
4.25	1.30	-12.7	25.20
4.75	1.20	-15.5	28.20
5.25	1.10	-19.0	31.10
5.75	1.00	-22.2	34.10
6.25	1.00	-25.7	37.10
6.75	0.79	-29.0	40.00
7.25	0.62	-32.2	43.00
7.75	0.46	-36.0	46.00
8.25	0.34	-39.5	49.00
8.75	0.25	-43.0	49.00
9.25	0.17	-47.0	49.00
9.75	0.13	-50.0	49.00
10.25	0.08	-54.5	49.00
10.75	0.06	-58.0	49.00
11.25	0.06	-58.0	49.00
11.75	0.12	-53.0	49.00
12.25	0.19	-50.0	49.00
12.75	0.18	-51.0	49.00
13.25	0.14	-54.0	49.00
13.75	0.11	-56.5	49.00
14.25	0.12	-56.5	49.00
14.75	0.13	-56.5	49.00
15.25	0.14	-56.5	49.00
15.75	0.15	-56.5	49.00
16.25	0.16	-56.5	49.00
16.75	0.18	-56.5	49.00
17.25	0.18	-56.5	49.00

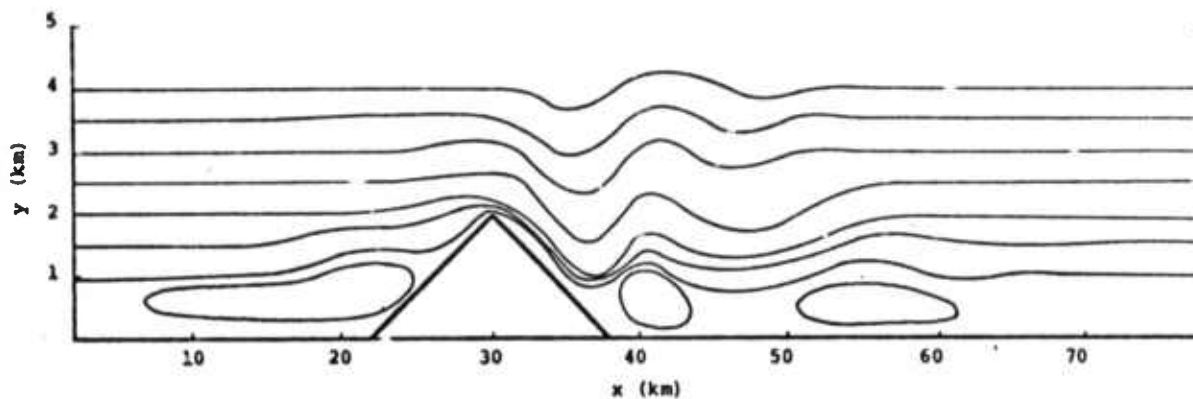


Figure 4.37 - Streamlines set 1, dry run, grid base at sea level,  $t = 2000$  sec.

The flow field in a moist atmosphere at 2000 secs is presented in Figure 4.38. In this case, we find two distinct lee waves - one at 2 km elevation has a wavelength of 8 km. The other, found at 4 km, displays a wavelength of approximately 20 km. This wavelength is in excellent agreement with that observed over the Owens Valley. As in the dry case, three rotors are observed. However, their structure is considerably different. The windward rotor is almost absent, while the leeward rotors have become much larger. In addition, the upper wave crest has advanced farther downwind than seen in the dry case.

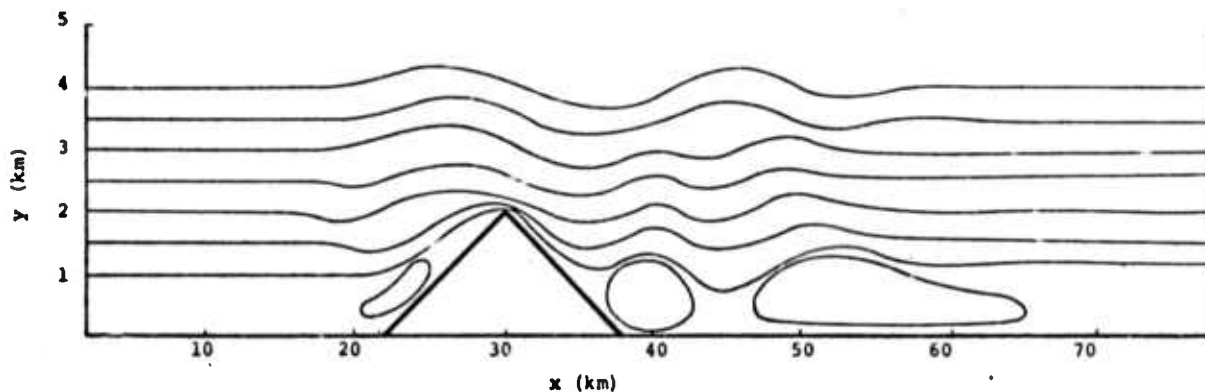


Figure 4.38 - Streamlines set 1, wet run, grid base at sea level,  $t = 2000$  sec.

Maximum cloud water concentrations are shown in Figure 4.39. These occur over the windward slope of the mountain and in the wave crests. This would be expected since the air at lower elevations is rather moist and warm. As this air is lifted by the flow, adiabatic cooling takes place and excess water vapor condenses out.

The second set of runs also utilized the Merced profiles. In this case, however, the grid base was situated at the floor of the Owens Valley. This yields a total mountain height of 3.5 km, a more realistic estimate of the true extent of the Sierra's. This set also consisted of two runs, one wet, one dry. The HAIFA approximated profiles are shown in Figures 4.40a, b, and c and tabulated in Table 4.4. These profiles are approximately the same as those used in set one except they are picked up at a 1.5 km elevation (elevation of Owens Valley). Also, the linear profiles, established in the intermediate atmospheric levels for wind and temperature, are continued to the top of the grid. This approximation eliminates calculational problems in the upper grid regions due to uniform flow. It is felt that this will not alter the solution in the region of interest, however.

The results of the dry run of set two at 2000 secs are presented in Figure 4.41. Only one lee wave appears with a wavelength of approximately 24 km agreeing qualitatively with observed data. Since the flow velocities are considerably higher than in set one, the longer wavelength is not surprising. Two small rotors are seen on the windward side. These would be expected to grow and merge at later times. A small rotor may be present under the leeward crest of the wave, but grid resolution prevents its detection.

The streamlines of the wet run at 2000 secs are presented in Figure 4.42. It appears as if the moisture has done little to affect the wave. Only one is present with a

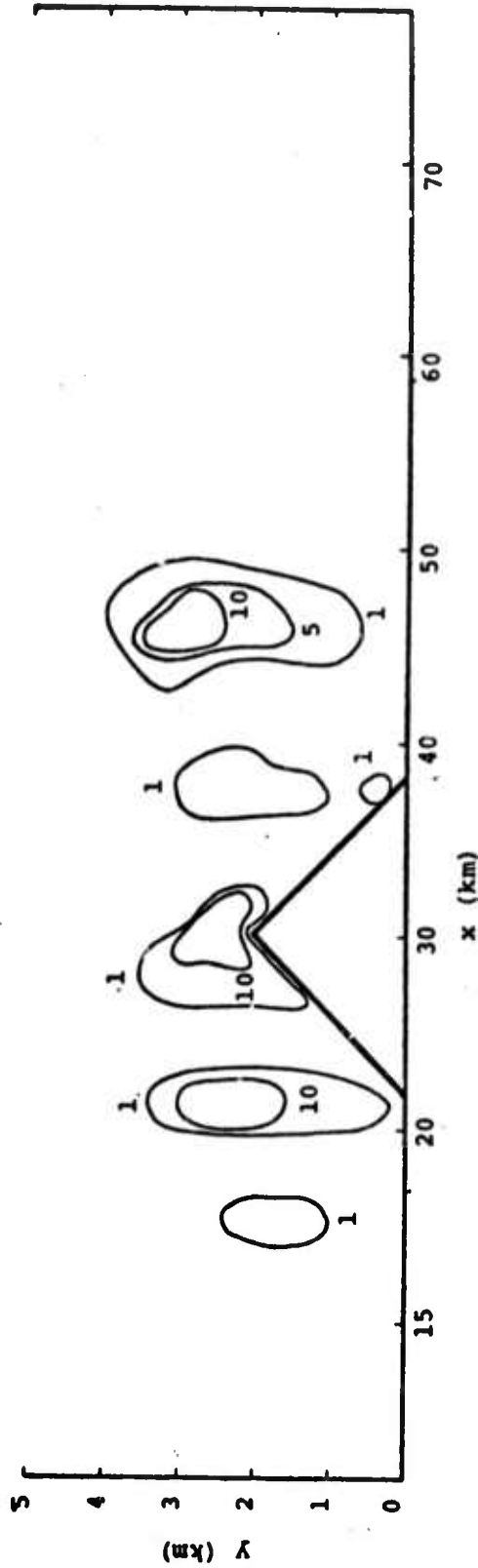


Figure 4.39 - Cloud water distribution, set 1, grid base at sea level, contours 1, 5, 10 ( $\times 10^4$  Kg/Kg),  $t = 2000$  sec.

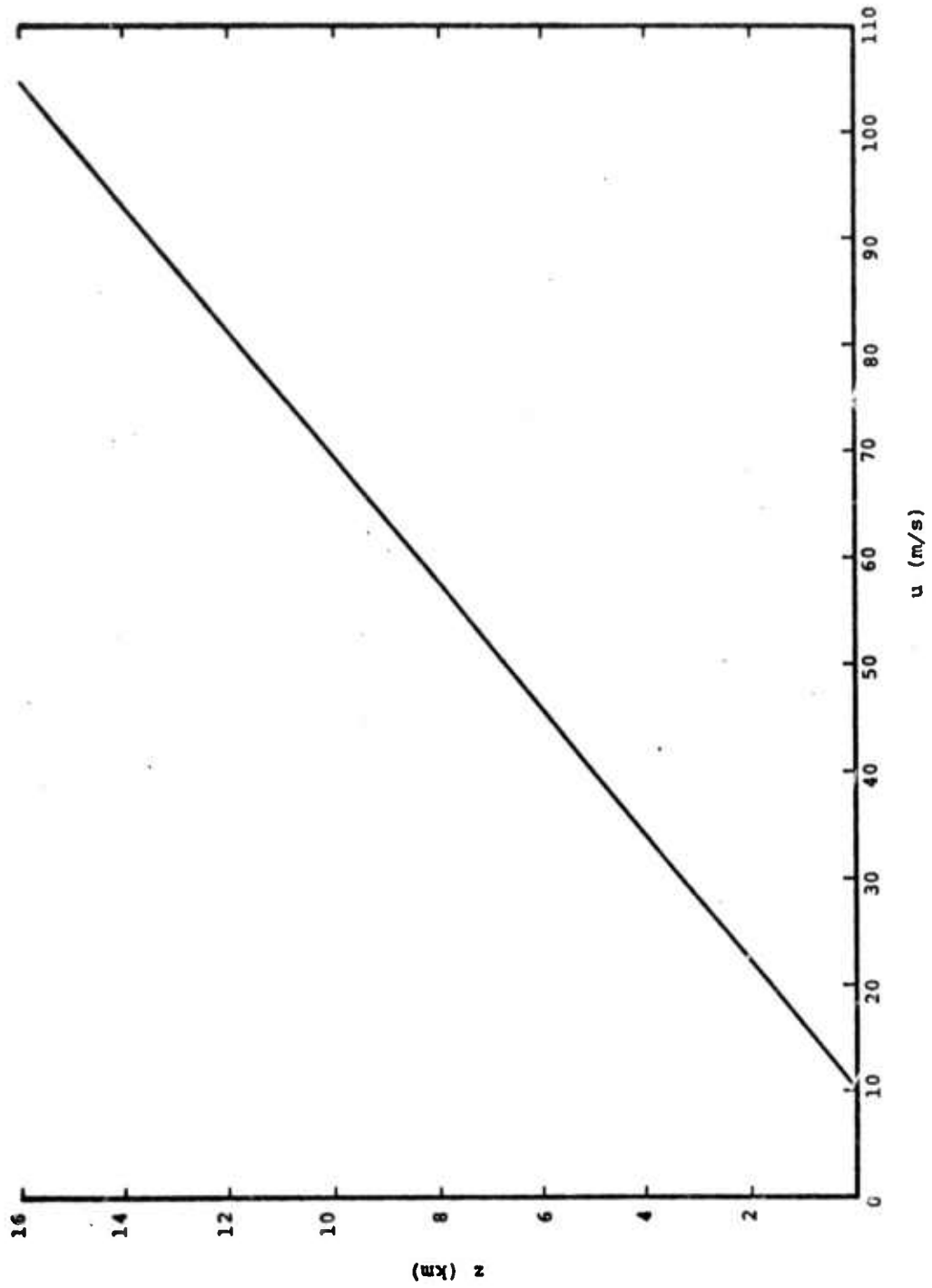


Figure 4.40a - Velocity profile, set 2.

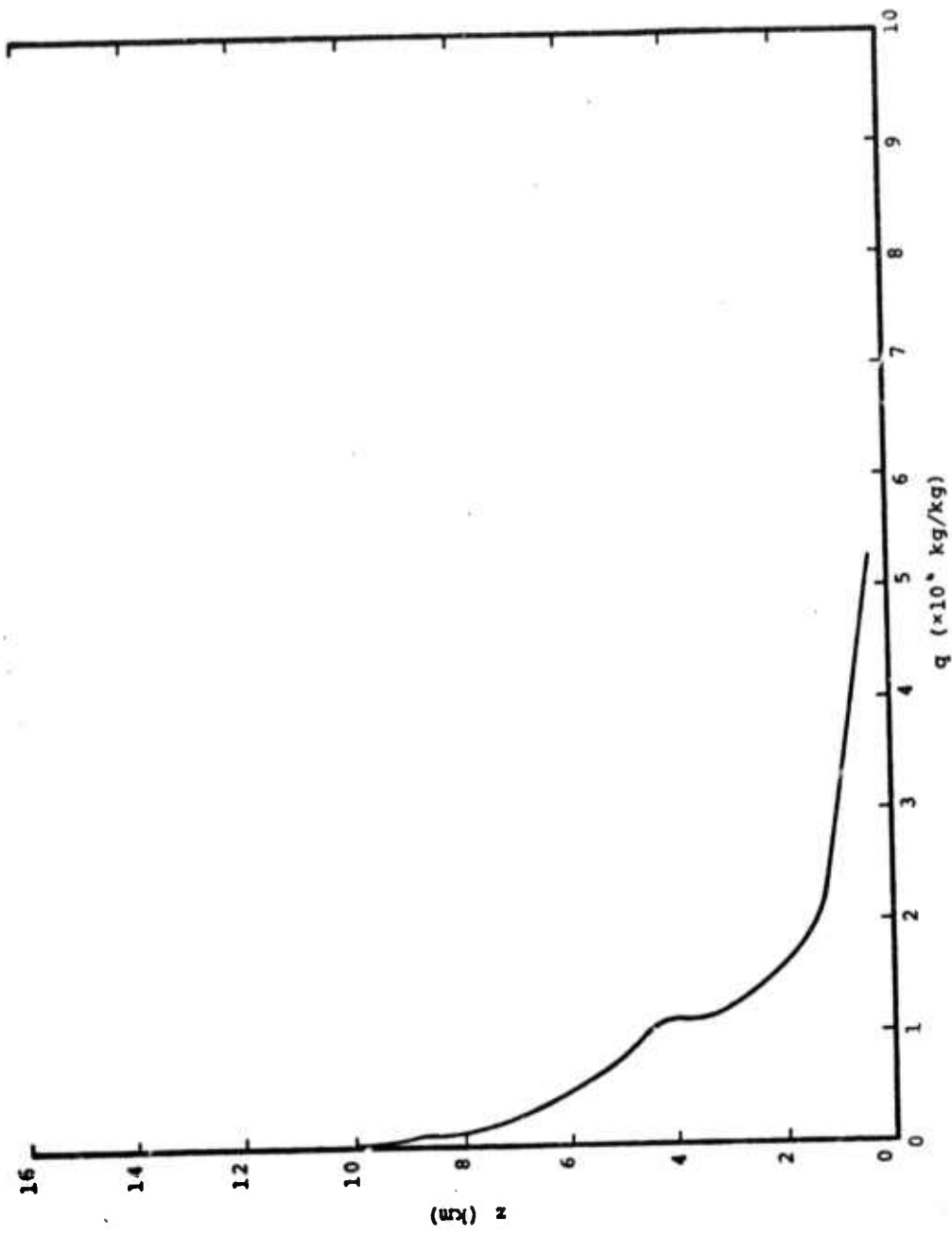


Figure 4.40b - Moisture profile, set 2.

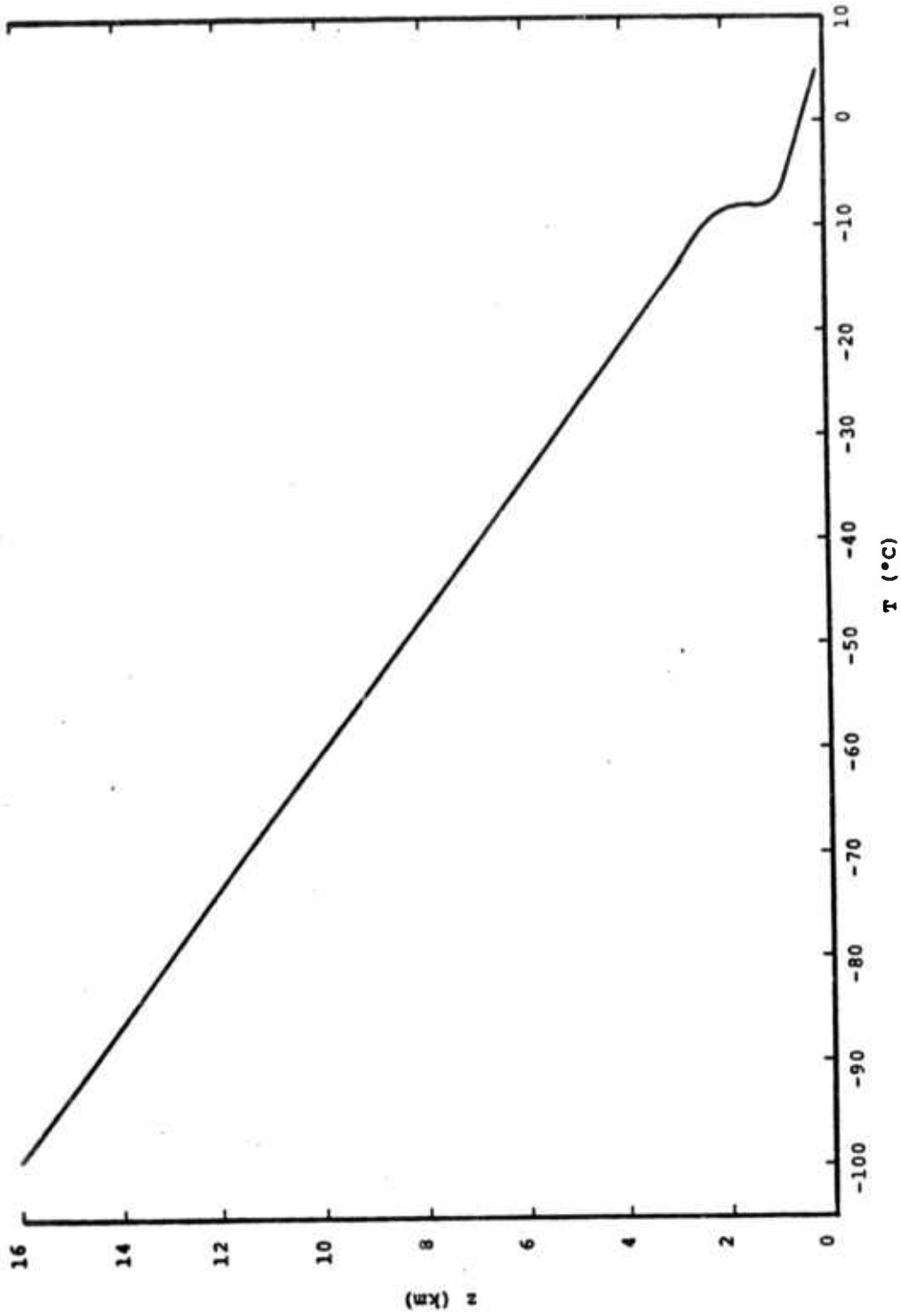


Figure 4.40c - Temperature profile, set 2.

Table 4.4  
HAIFA Input Profiles for Set 2

z (km)	q ( $\times 10^3$ kg/kg)	T ( $^{\circ}$ C)	u (m/s)
.25	5.28	3.4	11.5
.75	3.90	- 4.0	14.5
1.25	2.30	- 8.0	17.4
1.75	1.70	- 8.0	20.4
2.25	1.50	- 9.6	23.4
2.75	1.30	- 12.9	26.3
3.25	1.20	- 16.1	29.3
3.75	1.10	- 19.4	32.3
4.25	1.10	- 22.6	35.2
4.75	0.90	- 25.9	38.2
5.25	0.71	- 29.1	41.2
5.75	0.56	- 32.4	44.2
6.25	0.43	- 35.6	47.1
6.75	0.33	- 38.9	50.0
7.25	0.25	- 42.1	53.0
7.75	0.19	- 45.4	56.0
8.25	0.14	- 48.6	59.0
8.75	0.10	- 51.9	62.0
9.25	0.07	- 55.1	65.0
9.75	0.05	- 58.4	67.9
10.25	0.04	- 61.6	70.9
10.75	0.03	- 64.9	73.9
11.25	0.02	- 68.1	76.8
11.75	0.01	- 71.4	79.8
12.25	0.01	- 74.6	82.8
12.75	0.01	- 77.9	85.7
13.25	0.00	- 81.1	88.7
13.75	0.00	- 84.4	91.7
14.25	0.00	- 87.6	94.7
14.75	0.00	- 90.9	97.6
15.25	0.00	- 94.1	100.6
15.75	0.00	- 97.4	103.6
16.25	0.00	-100.6	106.5
16.75	0.00	-103.9	109.5
17.25	0.00	-107.1	112.5

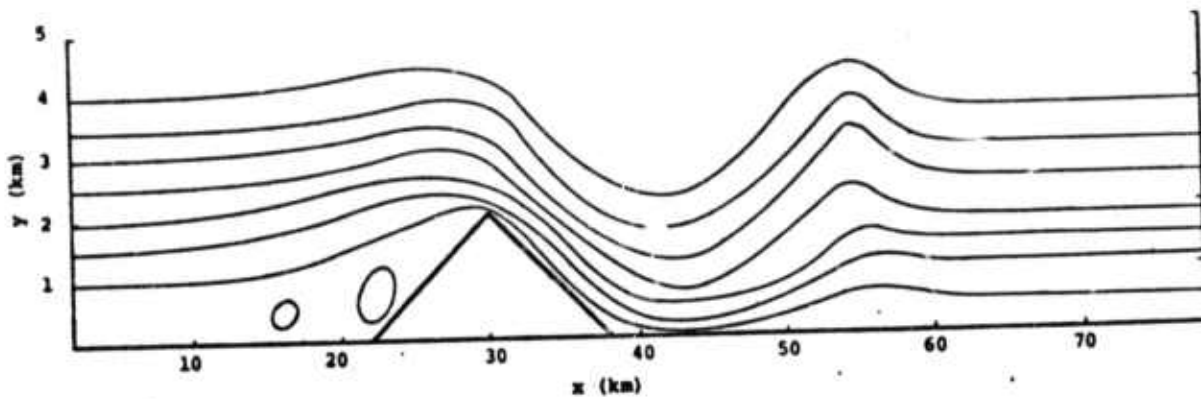


Figure 4.41 - Streamlines set 2, dry run, grid base at 1.5 km,  $t = 2000$  sec.

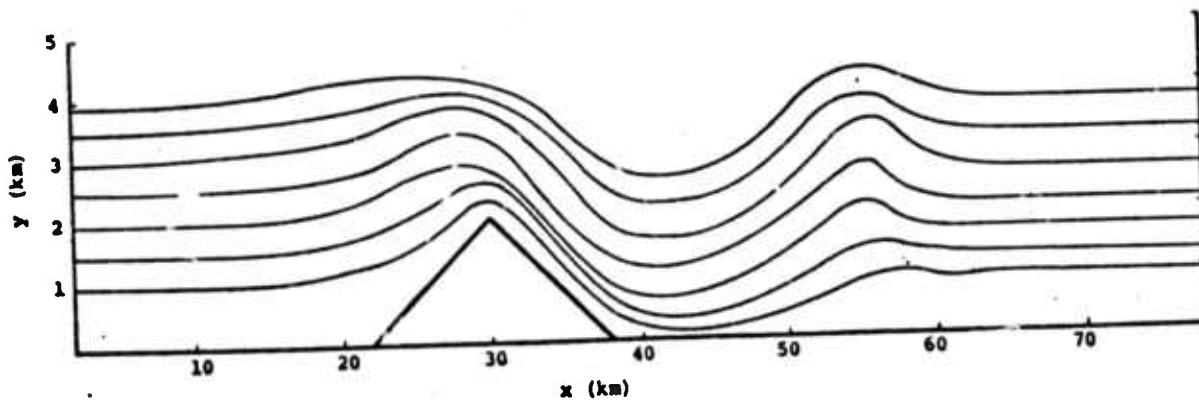


Figure 4.42 - Streamlines set 2, wet run, grid base at 1.5 km,  $t = 2000$  sec.

wavelength of around 24 km. Since there is considerably less moisture in this set (the moist lower atmosphere has been ignored in the profiles), it is not surprising. The rotors on the windward side have not appeared, although flow is very sluggish there, as seen from examination of wind field edits.

The cloud water (Figure 4.43) again congregates in regions of upward flow, predominantly on the windward slope and in the crest of the lee wave. Maximum values approach  $10^{-3}$  kg/kg. The much larger wave amplitudes present in this run serve to yield cloud water concentrations as large as that of the first run even though less moisture is available.

Momentum flux edits were performed on this set of runs. These are presented in Figures 4.44 and 4.45.

The two new edits exhibit a similar period with the moist run showing a consistently lower drag when plotted as a function of time. This appears to be the result of latent heat effects. The energetic processes which are introduced by the inclusion of moisture make interpretation difficult. It appears buoyant effects make the troughs in the streamlines shallower, thereby reducing the flux. More investigation is needed in this area.

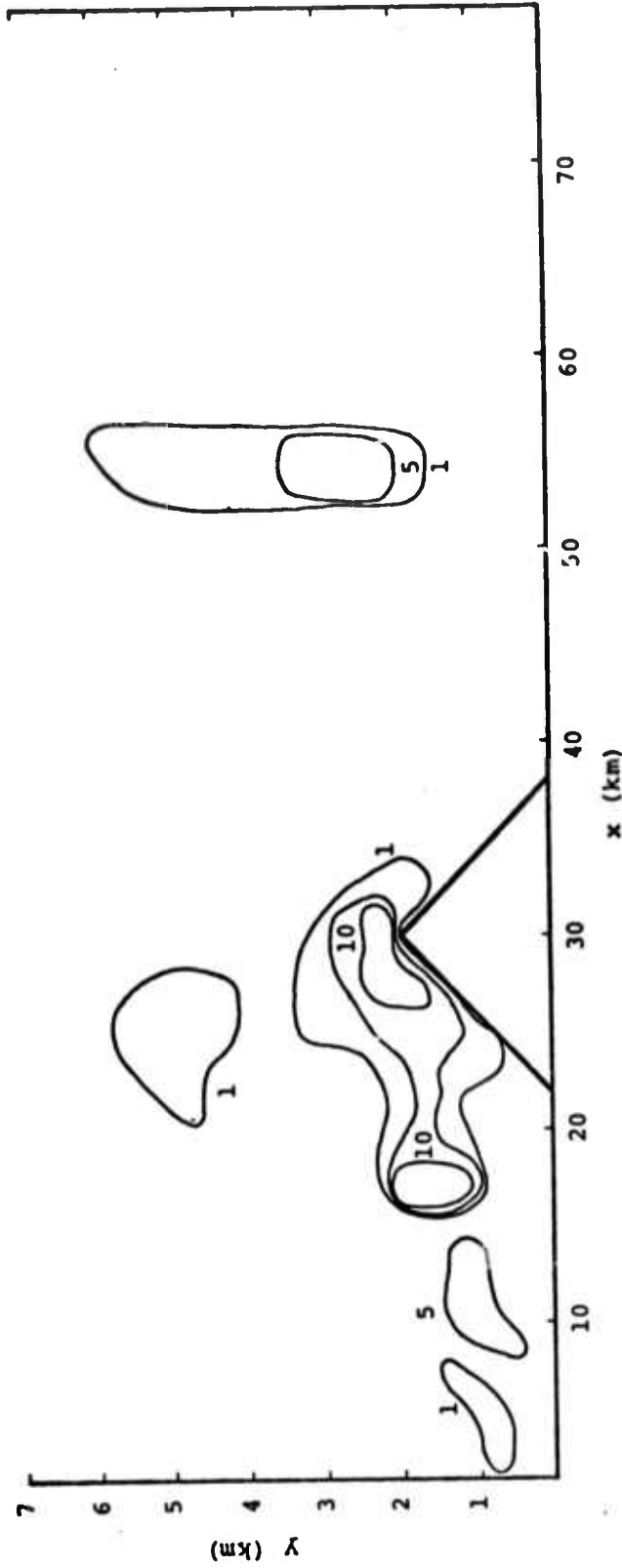


Figure 4.43 - Cloud water distribution, set 2, grid base at 1.5 km, contours 1, 5, 10 ( $\times 10^4$  Kg/Kg),  $t = 2000$  sec.

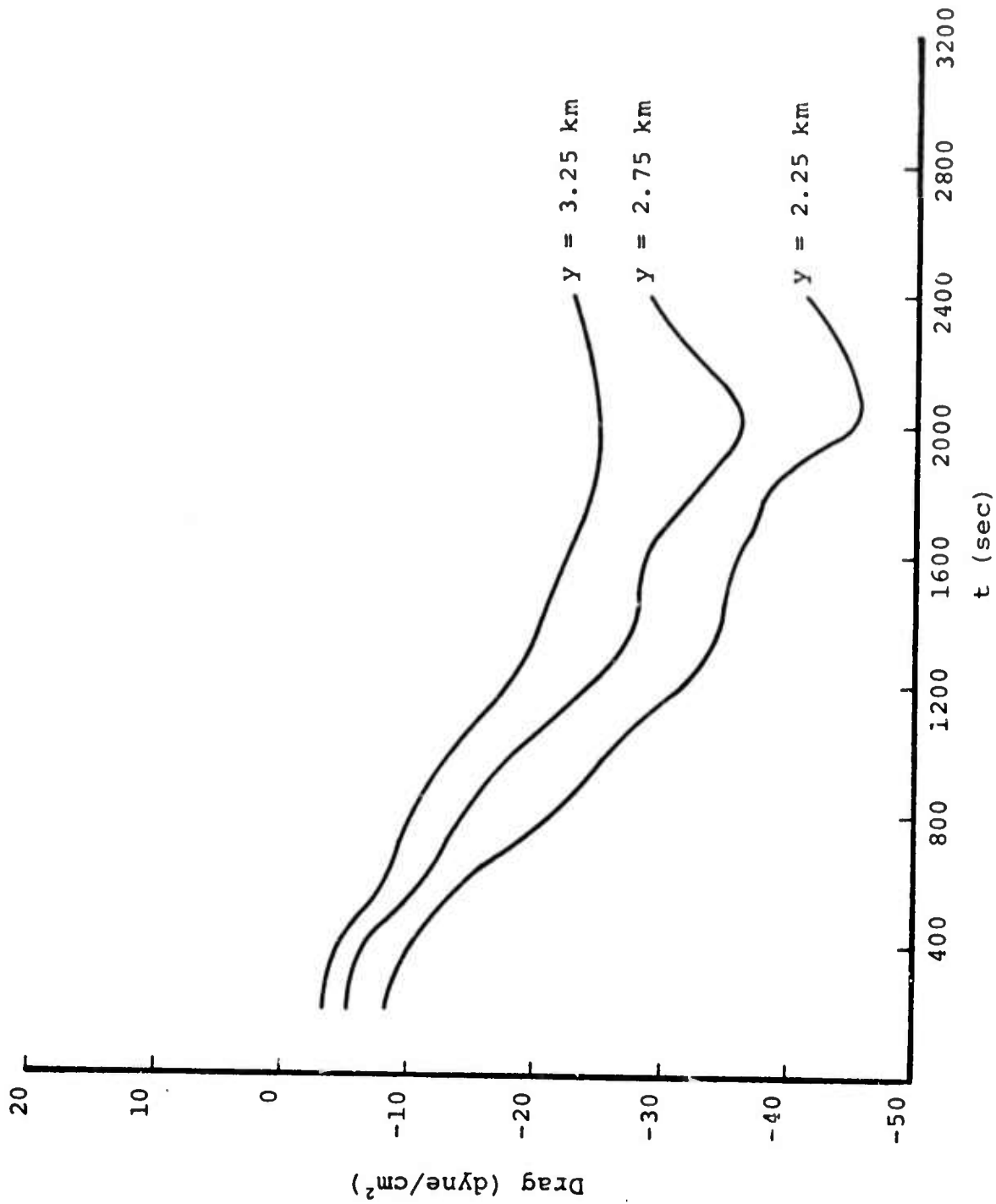


Figure 4.44 - Horizontal momentum flux dry run of set 2, grid base at 1.5 km.

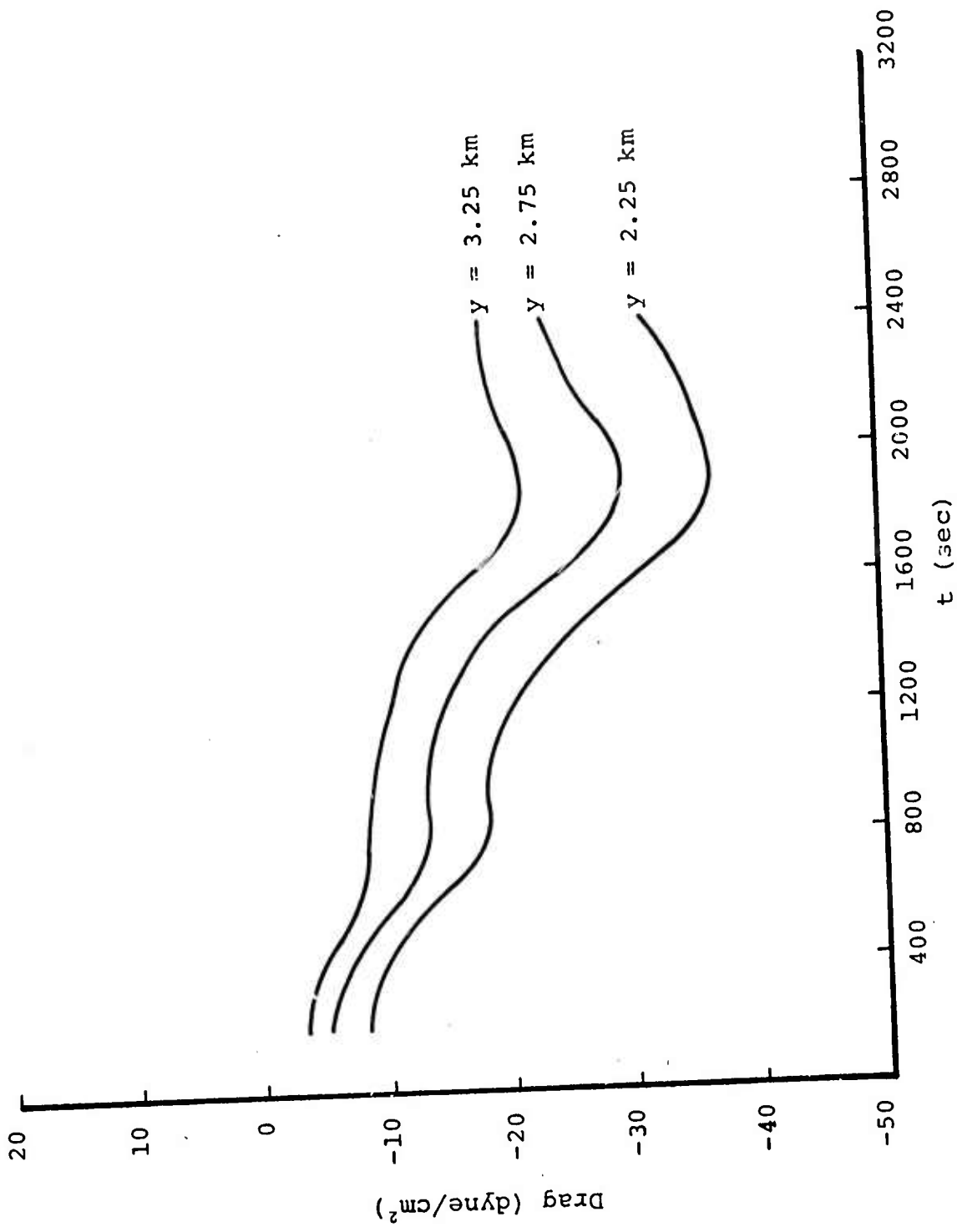


Figure 4.45 - Horizontal momentum flux wet run of set 2, grid base at 1.5 km.

The choice of the Merced profiles was dictated by their availability and not by their obvious applicability. Since Merced is located approximately 50 - 100 miles from the Owens Valley, the prevailing ambient conditions most probably do not reflect the true ambient conditions of the flow as it reaches the Sierra Nevada. In particular, the prevailing winds reported at Bishop on the same day (shown in Figure 4.32) show a marked deviation from those reported at Merced. Unfortunately, no temperature or moisture data was available that day for Bishop. The runs do indicate that the code is very sensitive to the input flow profile. The truncation of the Merced profiles at an elevation of 1.5 km for use in the set two runs is most probably an invalid procedure, resulting in much higher "ground" velocities than is found at 1.5 km on the Sierra Nevada. This artificially high flow may inhibit the formation of a large lee rotor at late integration times. A profile similar to that of Bishop's is probably more accurate.

## 5. LINEAR STEADY STATE CALCULATION OF WAVE DRAG

The calculation of the vertical flux of horizontal momentum (wave drag) using the HAIFA code has shown the phenomenon to be a complex time dependent process. On the other hand, the Mintz-Arakwa Global Circulation Model (GCM) is used to determine climatic changes over periods of time longer than hours. On this time scale the cyclic behavior of the wave drag parameters has undergone several oscillations, and it seems appropriate to use a time average of the wave drag in the GCM. For this reason a steady state treatment was derived.

Bretherton<sup>[25]</sup> and Danielson and Bleck,<sup>[26]</sup> among others, have published linear steady state analyses on the calculation of momentum transport by gravity waves. After an examination of both procedures, the analysis of Bretherton was chosen as the basis of the numerical model to be developed at Systems, Science and Software. The primary reason for the selection was that Bretherton had extended his analysis to three dimensions and arbitrary topography while the Danielson and Bleck model was more limited in scope.

In Section 5.1 a derivation of the Bretherton results is presented. The results of this analysis require that a topography data manipulation be performed, that an atmospheric response function be calculated, and that a stress integral be evaluated. These three calculations are described in

Sections 5.2.1, 5.2.2, and 5.2.3, respectively. In Section 5.2.4 the topographical data which we obtained for these calculations is described. In Section 5.2.5 test calculations using the linear steady state treatment are presented.

The linear steady state codes, as described in Section 5.2, turned out to be too expensive to incorporate directly into the GCM. Furthermore, the altitude dependence of the wind profiles as calculated in the two level GCM is not resolved in sufficient detail to warrant the additional expense. A vastly simplified model of the linear steady state model was, therefore, coded into a subroutine DRAG which has been delivered to RAND for use in their GCM. The simplifications and the program are described in Section 5.3. While this model has been simplified to the point of losing much of the sophistication and accuracy of the LSS code, we feel that its use in the GCM will provide a qualitatively correct estimate of the effects of wave drag on global circulation models.

### 5.1 A DERIVATION OF REYNOLDS STRESS FOR LINEAR-STEADY STATE FORMULATIONS

Bretherton gives without derivation the equations for the components of Reynolds stress corresponding to steady-state flow over three-dimensional (3D) topography in the linear approximation. In this section, the derivations of his result will be presented. We also generalize the equation for the vertical velocity and display correction terms to the Scorer parameter. The resulting equations (when sound waves are neglected) can then be incorporated into Bretherton's computational framework with little modification.

As a point of departure, the linearized steady state Navier Stokes equations for air without diabatic, Coriolis, or dissipative terms are adopted. We consider the perturbation to an unperturbed atmospheric state in which the atmosphere is stably stratified and the wind is steady and horizontal. The unperturbed wind may vary in strength and direction with altitude as given by the east-west and north-south components  $U(z)$  and  $V(z)$ .

The inviscid 3D equations of motion before we make the linear and steady-state approximations are:

$$\frac{dp}{dt} + \rho \left( \frac{\partial u}{\partial x} + \frac{\partial v}{\partial y} + \frac{\partial w}{\partial z} \right) = 0 \quad ,$$

$$\frac{du}{dt} + \frac{1}{\rho} \frac{\partial p}{\partial x} = 0 \quad ,$$

$$\frac{dv}{dt} + \frac{1}{\rho} \frac{\partial p}{\partial y} = 0 \quad ,$$

$$\frac{dw}{dt} + \frac{1}{\rho} \frac{\partial p}{\partial z} = -g \quad ,$$

$$\frac{dT}{dt} = \frac{1}{\rho C_p} \frac{dp}{dt} ,$$

$$p = \rho RT ,$$

where

$$\frac{d}{dt} = \frac{\partial}{\partial t} + u \frac{\partial}{\partial x} + v \frac{\partial}{\partial y} + w \frac{\partial}{\partial z} .$$

### 5.1.1 Linear Steady State Equations

The linear steady state equations for a small perturbation are obtained by separating the variables into a mean part which is a function of  $z$  only and a perturbation, and substituting these expressions into the above equations. The expressions for the variables are:

$$\rho = \bar{\rho}(z) + \rho_1 ,$$

$$u = U(z) + u_1 ,$$

$$v = V(z) + v_1 ,$$

$$w = w_1 ,$$

$$P = \bar{P}(z) + P_1 ,$$

and

$$T = \bar{T}(z) + T_1 .$$

The derived steady state equations are:

$$U\rho_x + V\rho_y + w\bar{\rho}_z + \bar{\rho}(u_x + v_y + w_z) = 0 , \quad (5.1)$$

$$Uu_x + Vu_y + wU_z + \frac{1}{\rho} P_x = 0 , \quad (5.2)$$

$$Uv_x + Vv_y + wv_z + \frac{1}{\rho} P_y = 0 \quad , \quad (5.3)$$

$$Uw_x + Vw_y + \frac{\rho g}{\rho} + \frac{1}{\rho} P_z = 0 \quad , \quad (5.4)$$

$$UT_x + VT_y + w(\bar{T}_z + \Gamma) = \frac{1}{\rho C_p} (UP_x + VP_y) \quad , \quad (5.5)$$

and

$$\frac{P}{\rho} = \frac{p}{\rho} + \frac{T}{\bar{T}} \quad . \quad (5.6)$$

The subscript "1" has been dropped in the above equations and the subscripts  $x$ ,  $y$ , and  $z$  are used to denote differentiation. The adiabatic lapse rate  $\Gamma = \frac{g}{C_p}$  has been introduced. In anticipation of the discussion of obliquely propagating plane waves, a transformation to a new coordinate system  $(x', y')$  rotated by an angle  $\phi$  with respect to the  $x, y$  system is completed, i.e.,

$$x = x' \cos \phi - y' \sin \phi$$

$$y = x' \sin \phi + y' \cos \phi$$

and

$$\frac{\partial \phi}{\partial x'} = \frac{\partial \phi}{\partial x} \cos \phi + \frac{\partial \phi}{\partial y} \sin \phi \quad ,$$

$$\frac{\partial \phi}{\partial y'} = - \frac{\partial \phi}{\partial x} \sin \phi + \frac{\partial \phi}{\partial y} \cos \phi \quad .$$

We also introduce the definitions:

$$U_n = U \cos \phi + V \sin \phi \quad ,$$

$$U_p = - U \sin \phi + V \cos \phi \quad ,$$

$$\text{and } u_n = u \cos\phi + v \sin\phi ,$$

$$u_p = -u \sin\phi + v \cos\phi .$$

The following identities are required in the derivation:

$$U_n \phi_{x'} + U_p \phi_{y'} = U \phi_x + V \phi_y ,$$

$$\frac{\partial u_n}{\partial x'} + \frac{\partial u_p}{\partial y'} = \frac{\partial u}{\partial x} + \frac{\partial v}{\partial y} .$$

Using these relations, the conservation equations become:

Continuity

$$U_n \rho_{x'} + U_p \rho_{y'} + w \bar{\rho}_z + \bar{\rho} [(u_n)_{x'} + (u_p)_{y'} + w_z] = 0 ; \quad (5.7)$$

Vertical Momentum

$$U_n w_{x'} + U_p w_{y'} + \frac{\rho g}{\bar{\rho}} + \frac{1}{\bar{\rho}} P_z = 0 ; \quad (5.8)$$

Energy

$$U_n T_{x'} + U_p T_{y'} + w(\bar{T}_z + \Gamma) = \frac{1}{\bar{\rho} C_p} (U_n P_{x'} + U_p P_{y'}) ; \quad (5.9)$$

Equation of State

$$P/\bar{P} = \rho/\bar{\rho} + T/\bar{T} . \quad (5.10)$$

The x and y momentum equations:

$$U_n u_{x'} + U_p u_{y'} + w U_z + \frac{1}{\bar{\rho}} P_x = 0 \quad (5.11)$$

and

$$U_n v_{x'} + U_p v_{y'} + w V_z + \frac{1}{\bar{\rho}} P_y = 0 , \quad (5.12)$$

respectively, are then combined in two ways:

$$\begin{aligned}
& U_n (u_{x'} \cos\phi + v_{x'} \sin\phi) + U_p (u_{y'} \cos\phi + v_{y'} \sin\phi) \\
& \quad + w(U_z \cos\phi + V_z \sin\phi) + \frac{1}{\rho} P_{x'} \\
& = U_n (u_n)_{x'} + U_p (u_n)_{y'} + w(U_n)_z + \frac{1}{\rho} P_{x'} = 0 ; \quad (5.13)
\end{aligned}$$

and

$$\begin{aligned}
& U_n (-u_{x'} \sin\phi + v_{x'} \cos\phi) + U_p (-u_{y'} \sin\phi + v_{y'} \cos\phi) \\
& \quad + \frac{1}{\rho} P_{y'} + w(-U_z \sin\phi + V_z \cos\phi) \\
& = U_n (u_p)_{x'} + U_p (u_p)_{y'} + w(U_p)_z + \frac{1}{\rho} P_{y'} = 0 \quad . \quad (5.14)
\end{aligned}$$

The above equations are to be expected; they are the result of transforming the equations by rotation to the  $x'$  and  $y'$  directions. They are obtained by the substitutions:

$$\begin{aligned}
U_n & \rightarrow U , & U_p & \rightarrow V , \\
u_n & \rightarrow u , & u_p & \rightarrow v , \\
x' & \rightarrow x & \text{and } y' & \rightarrow y
\end{aligned}$$

into the original equations.

### 5.1.2 Boundary Condition

The bottom boundary condition for the mountain flow problem results from linearization of the statement that the wind is parallel to the surface at all points,

$$w(0) = U \frac{\partial h}{\partial x} + V \frac{\partial h}{\partial y} = U_n \frac{\partial h}{\partial x'} + U_p \frac{\partial h}{\partial y'} \quad (5.15)$$

where  $h(x,y)$  = height of the ground surface.

We now introduce Fourier components of the topography such that:

$$\hat{h}(k,l) = \frac{1}{2\pi} \int_0^X \int_0^Y h(x,y) e^{-i(kx + ly)} dx dy$$

and

$$h(x,y) = \frac{1}{2\pi} \iint \hat{h}(k,l) e^{i(kx + ly)} dk dl .$$

Since both the equations and the boundary conditions are linear, we may consider a single wave component, corresponding to particular values of  $k$  and  $l$ ,

$$\hat{h}(k,l) e^{i(kx + ly)}$$

and superpose the resulting calculated wave drag.

$$\text{Introducing } \tan\phi = \frac{l}{k} , \quad x = x' \cos\phi - y' \sin\phi ,$$

$$y = x' \sin\phi + y' \cos\phi ,$$

$$\kappa = \sqrt{k^2 + l^2} \quad \text{and} \quad \cos\phi = \frac{k}{\kappa} ,$$

one arrives at the result that

$$kx + ly = \kappa x' .$$

Consequently, the disturbance is

$$\hat{h}(\kappa, \phi) e^{i\kappa x'} ,$$

corresponding to corrugations in the  $x'$  direction and having no  $y'$  dependence. All of the perturbation quantities are also independent of  $y'$  for this mode and the linearized

conservation equations become:

$$U_n \rho_{x'} + \bar{w} \bar{\rho}_z + \bar{\rho} [(u_n)_{x'} + w_z] = 0 \quad ,$$

$$U_n (u_n)_{x'} + w (U_n)_z + \frac{1}{\rho} P_{x'} = 0 \quad ,$$

$$U_n w_{x'} + \frac{\rho g}{\rho} + \frac{1}{\rho} P_z = 0 \quad ,$$

and

$$U_n T_{x'} + w (\bar{T}_z + \Gamma) = \frac{1}{\rho C_p} U_n P_{x'} \quad ,$$

with the boundary condition

$$w(0) = U_n h_{x'} \quad .$$

These equations do not contain  $U_p$  or  $u_p$ . (However,  $u_p$  apparently is not zero or constant with  $x'$  or  $z$  if  $U_p' \neq 0$  since  $U_n (u_p)_{x'} + w (U_p)_z = 0$ .)

Substituting the spatial dependence  $e^{ikx'}$  into the above equations, we obtain:

$$ik U_n \bar{\rho} + \hat{w} \bar{\rho}_z + \bar{\rho} (ik \hat{u}_n + \hat{w}_z) = 0 \quad ,$$

$$ik U_n \hat{u}_n + \hat{w} (U_n)_z + \frac{ik}{\rho} \hat{P} = 0 \quad ,$$

$$ik U_n \hat{w} + \frac{\hat{\rho} g}{\rho} + \frac{\hat{\rho}_z}{\rho} = 0 \quad ,$$

$$ik U_n \hat{T} + \hat{w} (\bar{T}_z + \Gamma) = \frac{ik}{\rho C_p} \hat{P} \quad ,$$

$$\hat{\omega}(0) = ik\hat{h} \quad ,$$

and

$$\frac{\hat{p}}{\bar{p}} - \frac{\hat{T}}{\bar{T}} - \frac{\hat{\rho}}{\bar{\rho}} = 0$$

where the quantity  $\hat{\phi}$  denotes the coefficient of the Fourier component of  $\phi$  with wavenumbers  $k$  and  $l$ .

These equations are precisely the same as the 2D equations presented in Reference 27 as Equations (5.4a) - (5.4e), except for the replacements:

$$\kappa \rightarrow k$$

$$U_n \rightarrow U$$

and

$$\hat{u}_n \rightarrow \hat{u} \quad .$$

Therefore, we can incorporate the results of Equation (5.8) (Ref. 27) to obtain the equation for the vertical velocity  $\hat{w}$ :

$$\begin{aligned} \hat{w}_{zz} - \left(s + \frac{\mu_z}{\mu}\right)\hat{w}_z + \left[-\mu\kappa^2 + \frac{g}{U_n^2} \left(s + \frac{\mu_z}{\mu}\right) \right. \\ \left. + \frac{(U_n)_z}{U_n} \left(s + \frac{\mu_z}{\mu}\right) - \frac{(U_n)_{zz}}{U_n}\right]\hat{w} = 0 \end{aligned} \quad (5.16)$$

where

$$\mu = 1 - \left(\frac{U_n}{C_s}\right)^2, \quad s = -\frac{\bar{\rho}_z}{\bar{\rho}} \quad \text{and} \quad S = \frac{\bar{T}_z + \Gamma}{\bar{T}},$$

and  $C_s$  is the sound speed.

The  $\hat{w}_z$  term can be eliminated by the transformation:

$$x = \left(\frac{\bar{\rho}}{\mu}\right)^{1/2} \hat{w} \quad (5.17)$$

to give

$$x_{zz} + \left\{ -\mu\kappa^2 + \frac{g}{U_n^2} \left( s + \frac{\mu_z}{\mu} \right) + \frac{(U_n)_z}{U_n} \left( s + \frac{\mu_z}{\mu} \right) - \frac{(U_n)_{zz}}{U_n} + \frac{1}{4} \left( s + \frac{\mu_z}{\mu} \right)^2 + \frac{1}{2} \left( s + \frac{\mu_z}{\mu} \right)_z \right\} x = 0. \quad (5.18)$$

This equation can be compared with the corresponding 3D equations of Bretherton (Equation 49) and Sawyer<sup>[28]</sup> (Equation 10). The leading terms are seen to agree with the exception of terms which are normally very small. In particular, the approximation  $\mu = 1$  is justified, since the atmospheric motions are strongly subsonic. Consequently, the equations become:

$$\hat{w} = \left( \frac{\bar{\rho}}{\rho_0} \right)^{-\frac{1}{2}} \omega,$$

and

$$\omega_{zz} + \left\{ -\kappa^2 + \frac{gS}{U_n^2} + s \frac{(U_n)_z}{U_n} - \frac{(U_n)_{zz}}{U_n} + \left( \frac{s}{2} \right)^2 + \frac{s_z}{2} \right\} \omega = 0 \quad (5.19)$$

where  $\rho_0$  is the unperturbed atmospheric density at the surface.

We now consider the drag force on the lower boundary resulting from a particular Fourier component of the topography  $k, l$ . For this component  $\frac{\partial h}{\partial y'} = 0$  and

$$F_{x'} = -\frac{1}{XY} \iint P \frac{\partial h}{\partial x'} dx' dy' = \frac{1}{XY} \iint h \frac{\partial P}{\partial x'} dx' dy'$$

where  $X, Y$  are the horizontal grid limits. Substituting

from the momentum equations we obtain:

$$F_{x'} = - \frac{1}{XY} \iint \bar{\rho} h \left( U_n \frac{\partial u_n}{\partial x'} + w \frac{\partial U_n}{\partial z} \right) dx' dy' ,$$

where all quantities are evaluated at  $z = 0$ . Using the bottom boundary condition  $w(0) = U_n h_{x'}$ , and integrating by parts,

$$F_{x'} = \frac{1}{XY} \iint \bar{\rho} U_n h_{x'} u_n dx' dy' = \frac{1}{XY} \iint \bar{\rho} w(0) u_n dx' dy' .$$

Consequently, the drag is equal to the Reynold's stress evaluated at the surface. In the direction parallel to the wavefront ( $y'$ ),  $F_{y'} = 0$ .

For the same Fourier component we now calculate the vertical dependence of the Reynold's stress and energy flux. The equations are simplified by eliminating the temperature and the density perturbations in favor of the vertical displacement,  $\xi$ . Following Eliassen and Palm,<sup>[29]</sup> the equations become:

$$\bar{\rho} \left( U_n \frac{\partial u_n}{\partial x'} + w U_n' \right) + \frac{\partial P}{\partial x'} = 0 , \quad (5.20)$$

$$\bar{c} \left( U_n \frac{\partial w}{\partial x'} + v_0^2 \xi \right) + \frac{\partial P}{\partial z} + \gamma g p = 0 , \quad (5.21)$$

$$\frac{\partial u_n}{\partial x'} + \frac{\partial w}{\partial z} - \gamma g w + \frac{\gamma U_n}{\bar{\rho}} \frac{\partial P}{\partial x'} = 0 , \quad (5.22)$$

and

$$w = U_n \frac{\partial \xi}{\partial x'} , \quad (5.23)$$

where  $\gamma$  characterizes the compressibility of the air  $\gamma = \frac{d\rho}{dP}$  and  $\gamma^{-\frac{1}{2}}$  is the sound speed, and  $\Gamma = \frac{d\bar{\rho}}{d\bar{P}}$  is the density gradient of the unperturbed atmosphere. The static stability of the atmosphere is described by the Brunt-Vaisala frequency,  $v_0$ , given by  $v_0^2 = (\Gamma - \gamma)g^2$ . These quantities are considered to be constants characteristic of the atmosphere. In terms of them, the density perturbation  $\rho$  is given by:

$$\rho = \frac{v_0^2}{g} \bar{\rho} \xi + \gamma P \quad .$$

We obtain the wave energy equation by forming the sum of the products, Equation (5.20) times  $u_n$ , Equation (5.21) times  $w$ , and Equation (5.22) times  $P$ . The result is:

$$\frac{\partial}{\partial x'} (EU_n + Pu_n) + \frac{\partial}{\partial z} (Pw) = - \bar{\rho} (U_n)_z u_n w \quad ,$$

where

$$E = \frac{1}{2} \bar{\rho} (u_n^2 + w^2 + v_0^2 \xi^2 + \frac{\gamma P^2}{\bar{\rho}^2})$$

is the wave energy. Integrating over the domain we obtain:

$$\frac{\partial}{\partial z} \iint P w \, dx' dy' = - (U_n)_z \bar{\rho} \iint u_n w \, dx' dy' \quad . \quad (5.24)$$

We can obtain another relation between these two quantities by multiplying Equation (5.20) by  $(\bar{\rho} U_n u_n + P)$ :

$$\begin{aligned} \frac{\partial}{\partial x'} \left( \frac{\bar{\rho}^2 U_n^2}{2} u_n^2 + \bar{\rho} U_n u_n P + \frac{P^2}{2} \right) \\ + \bar{\rho} (U_n)_z \left( \bar{\rho} U_n u_n w + Pw \right) = 0 \quad . \end{aligned}$$

Integrating over the domain we obtain:

$$\iint Pw \, dx' dy' = - \bar{\rho} U_n \iint u_n w \, dx' dy' \quad . \quad (5.25)$$

Comparing Equations (5.24) and (5.25) we conclude that:

$$\frac{\partial \left( \bar{\rho} \iint u_n w \, dx' dy' \right)}{\partial z} = 0 \quad ,$$

so that the Reynold's stress is independent of altitude if  $U_n \neq 0$ . Consequently, the momentum flux is constant with  $z$  and equal to the surface drag force in the absence of a critical layer where  $U_n = 0$ .

Since the quantity most readily available describing the perturbed motion is the vertical velocity from Equation (5.19), it is desirable to express the Reynold's stress in terms of the quantity  $w$ . We again follow Eliassen and Palm, using the continuity equation for a Fourier component in the  $\phi$ -direction. Multiplying Equation (5.22) by  $\frac{\partial w}{\partial x'}$ , we obtain:

$$\frac{\partial w}{\partial x'} \frac{\partial w}{\partial z} = - \frac{\partial u_n}{\partial x'} \frac{\partial w}{\partial x'} + \frac{\gamma g}{2} \frac{\partial w^2}{\partial x'} - \frac{\gamma U_n}{\rho} \frac{\partial P}{\partial x'} \frac{\partial w}{\partial x'} \quad .$$

Taking into account the dependence of each of the perturbed quantities on  $x'$  as  $e^{ikx'}$ , plus the result in Equation (5.14), this becomes after integration:

$$\kappa^2 \iint u_n w \, dx' dy' (1 - \gamma U_n^2) = - \iint \frac{\partial w}{\partial x'} \frac{\partial w}{\partial z} \, dx' dy' \quad .$$

Neglecting the small quantity  $\gamma U_n^2$  compared to 1, the average value of the Reynold's stress is expressed in terms of  $w$  as:

$$\frac{\bar{\rho}}{XY} \iint u_n w \, dx' dy' = - \frac{\bar{\rho}}{\kappa^2 XY} \iint \frac{\partial w}{\partial x'} \frac{\partial w}{\partial z} \, dx' dy' .$$

This quantity, the Reynold's stress in the  $x'$  direction due to the  $k, l$  component, can now be expressed in terms of  $w$  from the definition  $w = \text{Re} \left\{ \omega \left( \frac{\bar{\rho}}{\rho_0} \right)^{-\frac{1}{2}} e^{i\kappa x'} \right\}$  :

$$F_{x'} = \frac{\bar{\rho}}{XY} \iint u_n w \, dx' dy' = - \frac{\rho_0}{2\kappa} \text{Im} \left\{ \omega^* \omega_z \right\} , \quad (5.26)$$

where  $\omega^*$  is the complex conjugate of  $\omega$  and  $\text{Im}$  denotes the imaginary part. It can readily be shown, from Equation (5.19) for  $\omega$ , that this quantity is strictly constant as a function of  $z$ .

The value of  $w$  in Equation (5.26) depends on the topography through the boundary condition at the surface,

$$w(0) = U_n \frac{\partial h}{\partial x'} .$$

Due to the linearity of the formulation, it is convenient to arrange Equation (5.26) into a topography-independent factor,

$$F = \frac{1}{2} \text{Im} \left\{ \omega^* \omega_z \right\} / \omega^*(0) \omega(0) \quad (5.27)$$

and a factor that depends on topography

$$\omega^*(0) \omega(0) = U_n^2(0) \kappa^2 \hat{n}^* \hat{n} = \frac{U_n^2(0) \kappa^2}{4\pi^2} A X Y \quad (5.28)$$

$$F_{x'} = - \frac{\rho_0 U_n^2(0)}{4\pi^2} F A X Y . \quad (5.29)$$

X and Y are the spatial dimensions of the surface grid cell, and A and I will be discussed later. We not integrate over all wave numbers k, l to obtain the drag components:

$$F_x = \int_{-\infty}^{\infty} \int_{-\infty}^{\infty} \rho u w dx dy = 4\pi^2 \rho_0 \int_{-\infty}^{\infty} \int_{-\infty}^{\infty} \frac{1}{2k} \text{Im}(\omega^* \omega_z) dk dl ,$$

and

$$F_y = \int_{-\infty}^{\infty} \int_{-\infty}^{\infty} \rho v w dx dy = 4\pi^2 \rho_0 \int_{-\infty}^{\infty} \int_{-\infty}^{\infty} \frac{1}{2l} \text{Im}(\omega^* \omega_z) dk dl .$$

These are obtained by taking components of the Reynold's stress in the x' direction. In terms of  $\kappa$  and  $\phi$  the drag components are:

$$F_x = 4\pi^2 \int_{-\pi}^{\pi} \int_0^{\infty} F_{x'} \cos\phi d\phi \kappa dk ,$$

and

$$F_y = 4\pi^2 \int_{-\pi}^{\pi} \int_0^{\infty} F_{x'} \sin\phi d\phi \kappa dk .$$

Substituting and taking account that contributions from  $-k$  and  $k$  are the same,

$$F_x = -2\rho_0 \int_{-\pi/2}^{\pi/2} \int_0^{\infty} U_n^2(0) \cos\phi \kappa^2 F A d\phi dk$$

and

$$F_y = -2\rho_0 \int_{-\pi/2}^{\pi/2} \int_0^{\infty} U_n^2(0) \sin\phi \kappa^2 F A d\phi dk . \quad (5.30)$$

Equation (5.30) corresponds to Equation (54) of Bretherton and forms the basis for the linear steady-state calculations. The derivation shows that, even though the surface air density enters the equation, the density change with altitude is taken into account. Additional correction terms have been derived in Equation (5.19) which, under most circumstances, are small compared with the terms originally taken into account by Bretherton.

## 5.2 LSS:A 3-D STEADY STATE WAVE DRAG CALCULATION

In Section 5.1 it was shown that the linear steady state equations may be solved to calculate the wave drag. The expression for the drag (Equation 5.30) contains an atmospheric response function,  $F$ , described in Section 5.2.1, and a topography function,  $A$ , described in Section 5.2.2. These two functions are integrated over a domain in Fourier wave number space ( $k, l$  space). The integration is described in Section 5.2.3. Finally, in Section 5.2.4 the topography data we have acquired is described.

### 5.2.1 Atmospheric Response Function, $F(k,l)$

The function  $F(k,l)$  is given in Bretherton's [25] equation 52. This may be derived from Equation 5.16 by setting  $\mu=1$ ,  $\mu_z=0$ ,  $s=0$ .

$$F = \frac{1}{2i} \left\{ \frac{d\hat{w}}{dz} \hat{w}^* - \frac{d\hat{w}^*}{dz} \hat{w} \right\} / \hat{w}(0) \hat{w}^*(0) \quad (5.31)$$

Here  $\hat{w}$  is a solution to the Scorer equation,

$$\frac{d^2 \hat{w}}{dz^2} + (\ell^2(z) - \kappa^2) \hat{w} = 0 \quad (5.32)$$

We now discuss the boundary conditions to be used in solving this equation.

### 5.2.1.1 Choice of Vertical Velocity at Upper Boundary

The solution of the vertical velocity equation requires boundary conditions to be imposed both at the ground and at the top of the atmosphere. In order to perform a marching calculation, a specific value of the complex vertical velocity is assigned at the top of the atmosphere. The resulting wave drag is independent of this value, a result which we wish to demonstrate below. In order to do so, we evaluate the quantity  $F$  containing all of the vertical velocity terms. According to Bretherton, we must consider the two cases for which different boundary conditions at the top of the atmosphere  $z=H$  are prescribed.

Before considering these two cases, however, we develop a general solution of the Scorer equation with which we can more easily consider the boundary conditions. The real and imaginary parts of the vertical velocity each obey the same linear second order equation

$$\frac{d^2 u}{dz^2} + (\ell^2 - \kappa^2)u = 0 \quad . \quad (5.33)$$

A general solution of this equation contains two coefficients

$$u = a_1 u_1 + a_2 u_2 \quad (5.34)$$

where  $u_1$  and  $u_2$  are linearly independent. We choose the functions  $u_1$  and  $u_2$  to be solutions of Eq. (5.33) having the following boundary conditions:

$$u_1(H) = 1 \quad , \quad \left. \frac{du_1}{dz} \right|_H = 0 \quad , \quad (5.35)$$

$$u_2(H) = 0 \quad , \quad \left. \frac{du_2}{dz} \right|_H = 1 \quad .$$

As mentioned above, the real and imaginary parts of  $\hat{w}$ , the vertical component of the perturbation velocity, each have the form of Eq. (5.34).

We now discuss the simpler of the two cases in which  $\kappa^2 > \ell^2(H)$ , for which we have trapped wave solutions and the contributions to the Reynold's stress are discrete (as given by Eq. (61) of Bretherton). The boundary condition at the top of the atmosphere  $z=H$  in this case, is Eq. (50a) of Bretherton:

$$\frac{d\hat{w}}{dz} = -\sqrt{\kappa^2 - \ell^2(H)}\hat{w} .$$

Assuming an initial value of  $\hat{w}$  at  $z=H$  of  $\hat{w}(H) = u_0 + iv_0$ , the initial values of the derivatives are

$$\left. \frac{dw_R}{dz} \right|_H = -\sqrt{\kappa^2 - \ell^2(H)}u_0 ,$$

$$\left. \frac{dw_I}{dz} \right|_H = -\sqrt{\kappa^2 - \ell^2(H)}v_0 .$$

We can now determine the coefficients  $a_1$  and  $a_2$  in Eq. (5.34):

$$w_R = u_0(u_1 - \sqrt{\kappa^2 - \ell^2(H)}u_2) , \tag{5.36}$$

$$w_I = v_0(u_1 - \sqrt{\kappa^2 - \ell^2(H)}u_2) .$$

Thus, we find that the real part of the velocity  $w_R$  and the imaginary part  $w_I$  are proportional to each other at every altitude  $z$ . Consequently, it is only necessary to perform one integration of the Scorer equation to evaluate either one of them.

It is now possible to construct the term containing all of the velocity dependence of the Reynold's stress, given by Bretherton's Eq. (60);

$$\int F(\kappa) d\kappa = \frac{\pi}{2\kappa} \frac{\left| \frac{d\hat{w}}{dz} \right|_0^2}{\int_0^H |\hat{w}|^2 dz} = \frac{\pi}{2\kappa} \frac{\left( \frac{dw_R(0)}{dz} \right)^2 + \left( \frac{dw_I(0)}{dz} \right)^2}{\int_0^H (w_R^2 + w_I^2) dz} .$$

In terms of the expressions of Eq. (5.36), we obtain

$$\int F(\kappa) d\kappa = \frac{\pi}{2\kappa} \frac{\left( \frac{du_1}{dz} - \sqrt{\kappa^2 - \ell^2(H)} \frac{du_2}{dz} \right)_{z=0}^2}{\int_0^H (u_1 - \sqrt{\kappa^2 - \ell^2(H)} u_2)^2 dz} . \quad (5.37)$$

The salient feature of Eq. (5.37) is that the values of  $u_0$  and  $v_0$  do not appear; the trapped wave contribution to the Reynold's stress is independent of the assumed velocity amplitude at  $z=H$ .

For the case of waves which leak into the stratosphere, corresponding to  $\kappa^2 \leq \ell^2(H)$ , the boundary condition (given by Eq. (50b) of Bretherton) is

$$\frac{d\hat{w}}{dz} = + i\sqrt{\ell^2(H) - \kappa^2} \operatorname{sgn}(U_n) \hat{w} .$$

Substituting the assumed boundary values at  $z=H$ , the derivative condition becomes

$$\left. \frac{dw_R}{dz} \right|_H = - \sqrt{\ell^2(H) - \kappa^2} \operatorname{sgn}(U_n) v_0 ,$$

$$\left. \frac{dw_I}{dz} \right|_H = \sqrt{\ell^2(H) - \kappa^2} \operatorname{sgn}(U_n) u_0 .$$

The general solutions satisfying these boundary conditions are

$$\begin{aligned} w_R &= u_1 u_0 - \sqrt{\ell^2(H) - \kappa^2} \operatorname{sgn}(U_n) u_2 v_0 , \\ w_I &= u_1 v_0 + \sqrt{\ell^2(H) - \kappa^2} \operatorname{sgn}(U_n) u_2 u_0 . \end{aligned} \quad (5.38)$$

In contrast to the first case, these two solutions are linearly independent and require that two integrations of the Scorer Equation be performed.

In order to evaluate the term containing all of the dependence on the vertical velocity in the Reynold's stress, we compute the quantity  $F$  (see Equation (5.31)):

$$F = \frac{1}{2i} \left\{ \frac{d\hat{w}}{dz} \hat{w}^* - \frac{d\hat{w}^*}{dz} \hat{w} \right\} / \hat{w}(0) \hat{w}^*(0) ,$$

where  $w^*$  denotes the complex conjugate of  $w$ . The numerator of  $F$  is independent of altitude and can be evaluated at  $z=H$  from the boundary values given above. The result is

$$\begin{aligned} \frac{1}{2i} \left\{ \right\} &= \sqrt{\ell^2(H) - \kappa^2} \operatorname{sgn}(U_n) \hat{w}(H) \hat{w}^*(H) \\ &= \sqrt{\ell^2(H) - \kappa^2} \operatorname{sgn}(U_n) (u_0^2 + v_0^2) . \end{aligned} \quad (5.39)$$

Using this result, and forming the denominator of Eq. (5.39) from the solutions of Eq. (5.38) evaluated at  $z=0$ , we obtain for  $F$

$$F = \frac{\sqrt{\ell^2(H) - \kappa^2} \operatorname{sgn}(U_n)}{u_1^2(0) + (\ell^2(H) - \kappa^2) u_2^2(0)} . \quad (5.40)$$

This expression is also independent of the assumed boundary values  $u_0$  and  $v_0$ . Consequently, we have shown that the Reynold's stress does not depend on the chosen values of vertical velocity at the top of the atmosphere.

## 5.2.2 The Topography Spectrum Function Code

### 5.2.2.1 The Equations

The spectrum function code performs the primary task of determining a spectrum function distribution in wavenumber space associated with a Fourier representation of the horizontal dependence of the topography. Bretherton<sup>[25]</sup> defines a spectrum function, A;

$$A(k,l) = \frac{4\pi^2}{XY} \hat{h}^* \hat{h} \quad (5.41)$$

where X and Y represent the spatial extent of the topographic region in the east-west and north-south directions.  $\hat{h}$  is the Fourier transform of the surface height and the asterisk indicates conjugation. The Fourier transform is defined as

$$\hat{h}(k,l) = \frac{1}{4\pi^2} \int_0^X \int_0^Y h(x,y) e^{-i(kx+ly)} dx dy \quad (5.42)$$

These two equations are solved in this code.

### 5.2.2.2 Numerical Method

The approach taken in this code is as follows: First, surface height data are obtained from the appropriate data tape. Next, these data are Fourier transformed to obtain the spectrum. Finally, the spectrum function distribution is calculated according to Eq. (5.41).

The topography data are composed of  $m \times n$  data "points" falling within the rectangle specified by the user at problem generation time. It must be remembered that each "point" is, in fact, an average value to be associated with a small rectangle about the point in question. Thus, the surface height may be thought of as a step-function representation of the topography. A sample  $5 \times 4$  grid shown in Figure 5.1 demonstrates this more clearly. Each of the numbers appearing within the cells represents the average height within the cell.

The nature of the data representation has implications for the Fourier transform. First, the discrete data can be represented by a discrete number of spectral components. Second, the resolution in spectral space is a function of the resolution in real space, and a lack of spectral resolution can therefore reduce the accuracy of the wave drag calculation. Particularly at trapped wavenumbers this uncertainty results in a corresponding uncertainty in the trapped wave drag contribution. The use of 5' data allows resolution of wavelengths of the order of 10 km, which are comparable with the wavelengths of the predominant trapped waves. We propose to examine the desirability of using even more highly resolved data.

The fact that the topography can be considered discrete is fortunate from a calculational point of view, however. Calculation of the Fourier transform requires a large amount of time due to the large number of trigonometric evaluations and manipulations of the data. The fast Fourier transform (FFT), which is an algorithm to optimize the direct calculation of the Fourier transform, is used to calculate the topography spectrum function. The algorithm requires that the function be defined at a discrete set of points spaced at equal intervals in each dimension. A FORTRAN subroutine based on the Cooley-Tukey

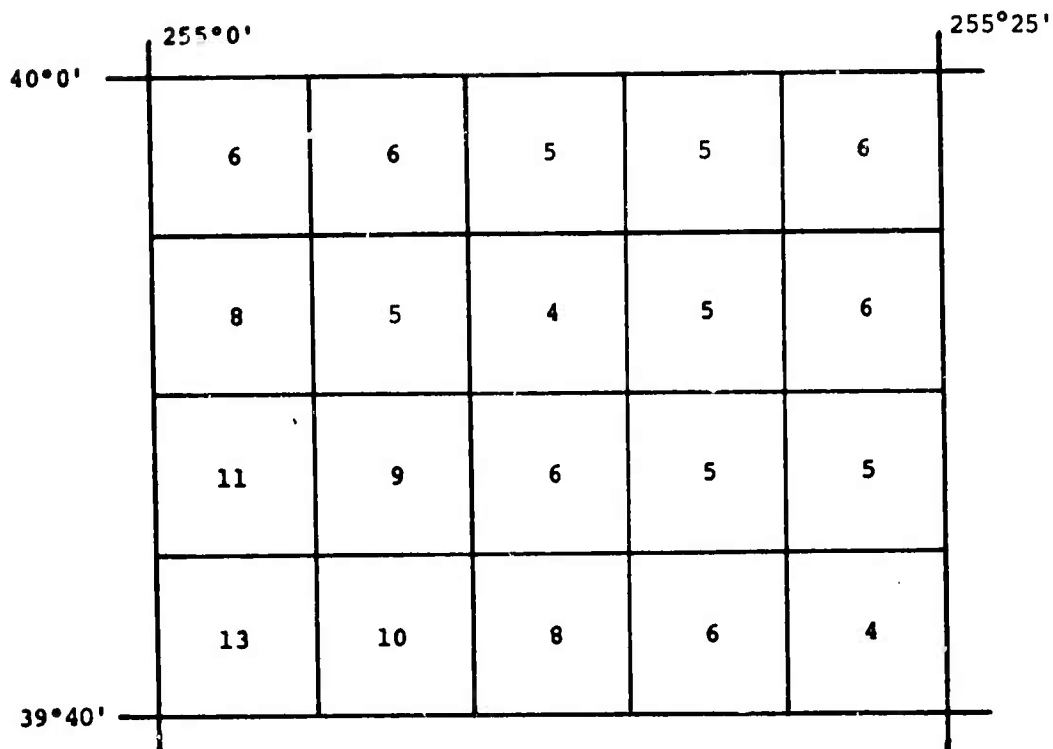


Figure 5.1 - A hypothetical topographical grid extending 25'x20'. The numbers represent mean values for the cell. Grid resolution is 5 minutes.

algorithm was obtained from the University of California at San Diego and has been used satisfactorily in the applications described below.

The finite Fourier transform requires some adaptation before it is applicable to the topography data. This can be seen from the finite difference expression for the Fourier integral which is given by

$$\hat{h}(k, l) = \frac{1}{4\pi^2} \sum_{s=0}^{m-1} \sum_{u=0}^{n-1} h(s\Delta x, u\Delta y) e^{-i(ks\Delta x + lu\Delta y)} \Delta x \Delta y \quad (5.43)$$

The FFT routine calculates

$$\tilde{a}_{rt} = \frac{1}{mn} \sum_{s=0}^{m-1} \sum_{u=0}^{n-1} a_{su} e^{-2\pi i \left( \frac{rs}{m} + \frac{tu}{n} \right)} \quad (5.44)$$

We see then that if we identify  $a_{su}$  with the height function as follows

$$a_{su} = \frac{m\Delta x \ n\Delta y}{4\pi^2} h(s\Delta x, u\Delta y) \quad (5.45)$$

and define

$$k = \frac{2\pi r}{m\Delta x} \quad 0 \leq r < \frac{m}{2} \quad (5.46)$$

$$k = \frac{2\pi(r-m)}{m\Delta x} \quad \frac{m}{2} \leq r < m$$

$$l = \frac{2\pi t}{n\Delta y} \quad 0 \leq t < \frac{n}{2} \quad (5.47)$$

$$l = \frac{2\pi(t-n)}{n\Delta y} \quad \frac{n}{2} \leq t < n$$

then the FFT routine will return the Fourier transform as defined in Eq. (5.42). The wavenumbers associated with the transform are given by Eqs. (5.46) and (5.47).

The topo data tapes, however, do not contain values associated with boundary points of the area in question. Instead, the data are associated with averages over elementary rectangles and lie in the interior of the area as illustrated by Figure 5.1. It is also necessary that the number of data points along each spatial dimension be an integer power of 2. In order to take account of this displacement of the data from the boundary points, a redefinition of the Cooley-Tukey coefficients is required:

$$a_{su} = \frac{m\Delta x n\Delta y}{4\pi^2} h[(s+\frac{1}{2})\Delta x, (u+\frac{1}{2})\Delta y] \quad (5.48)$$

Following the calculation of the FFT coefficients a subsequent calculation to form the topography transform is carried out:

$$\hat{h}_{kl} = \tilde{a}_{rt} e^{-\frac{1}{2}i(k\Delta x + l\Delta y)} \quad (5.49)$$

This transformation of terms allows one to approximate the integral of Eq. (5.42) without having to use boundary points.

The steps of the spectrum function calculation, consequently, are as follows: The topography data are interpolated to obtain new values corresponding to the next higher integer power of 2 equally spaced points in each direction. These

values are pre-processed according to Eq. (5.48). The FFT is executed and the resulting array is then processed as in Eq. (5.49) to obtain the Fourier transform of the height. The spectrum function is then straightforwardly calculated according to Eq. (5.41).

The spectrum function, together with the associated  $k, l$  wavenumbers, is written into a file for future use. The final task of the code is to print a tabulation of  $A(k, l)$ . Contour maps of the topography and spectrum function are also plotted. Additionally, a contour map of the log of the spectrum function is made.

### 5.2.2.3 Spectrum Function Calculations

Several calculations were run with the spectrum function code to determine the sensitivity of the model to the spatial resolution. The study consisted of an examination of ten geographic areas in the United States differing widely in topography and location. Topography data from the DMA magnetic tapes having 5' resolution were used and the resulting spectrum functions were calculated. These same topographic data were then resolved to 10', by combining 5' values, and the spectrum functions were determined again. The resulting set of data can be investigated to determine the behavior of  $A$  as a function of differing topographies and also determine the sensitivity of  $A$  to topographical resolution.

A representative sample of terrains was selected; these data consisted of contiguous rectangles within a strip of land across the U.S. from  $34^{\circ}20'$  to  $37^{\circ}0'$  north latitude and from  $94^{\circ}20'$  to  $121^{\circ}$  west longitude. This strip includes the rugged topography of the High Sierra and Rocky Mountains, the flat plains of the midwest, and the Appalachian mountains of the east.

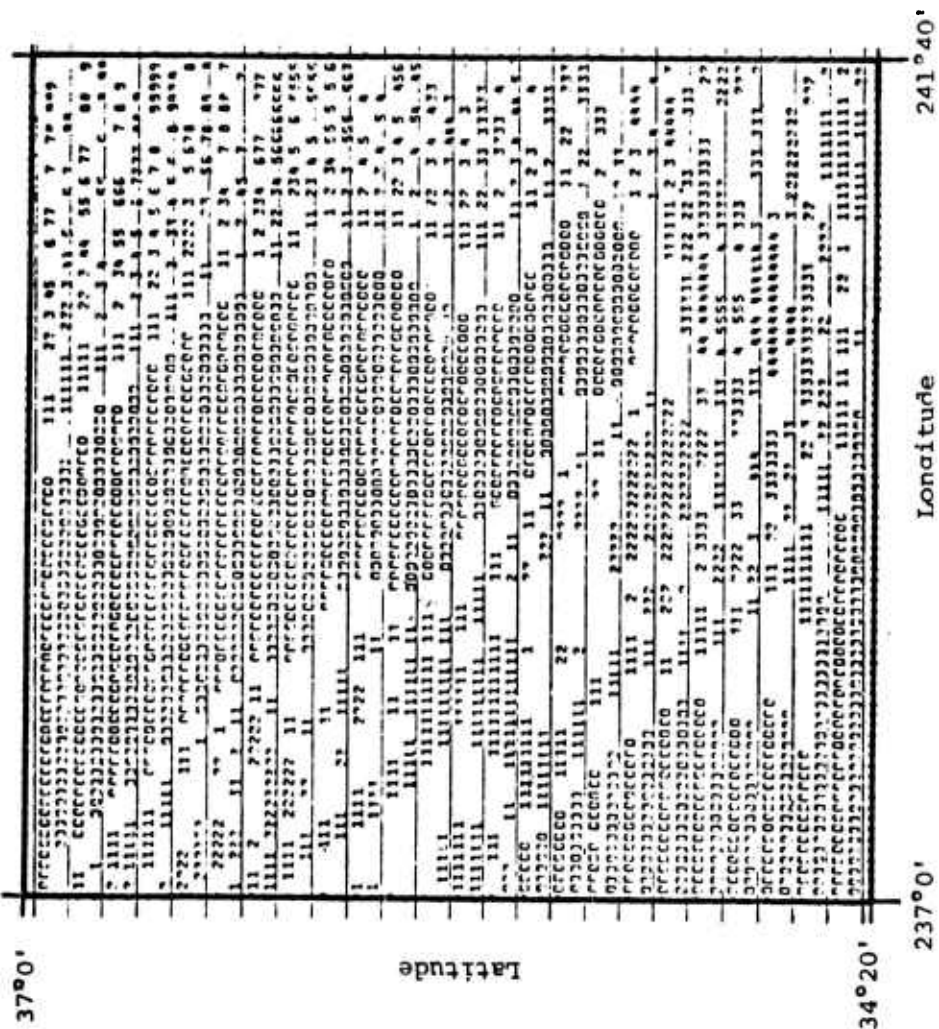
The strip was composed of 10 contiguous topographical grids 2°40' on a side (corresponding to 32×32 data points for each grid at 5' resolution). This set of grids constitutes a preliminary cross-section of characteristic topographies.

Figures 5.2 through 5.5 show contour maps of one geographic area and its associated spectrum function located in the rectangle 118°20' to 121° west longitude, 34°20' to 37°0' latitude at both 5' and 10' resolution. This area corresponds to the first grid in the set of grids and encompasses portions of the San Joaquin Valley, Sierra-Nevada mountains, and the coastal ranges of California. Figure 5.2 presents the contour map at 5' resolution, and Figure 5.3 is the corresponding calculated spectrum function. Figure 5.4 presents the contour map for the 10' resolution data, and Figure 5.5 shows the corresponding spectrum function.

The figures contain computer produced contours. Actual contours could be constructed by connecting like numbers; the actual value (h or A) corresponding to the plotted numbers are given by the formula

$$V_{\text{actual}} = V_{\text{min}} + (V_{\text{max}} - V_{\text{min}}) [(N \pm \frac{1}{2}) \pm \frac{1}{2}] / 10 .$$

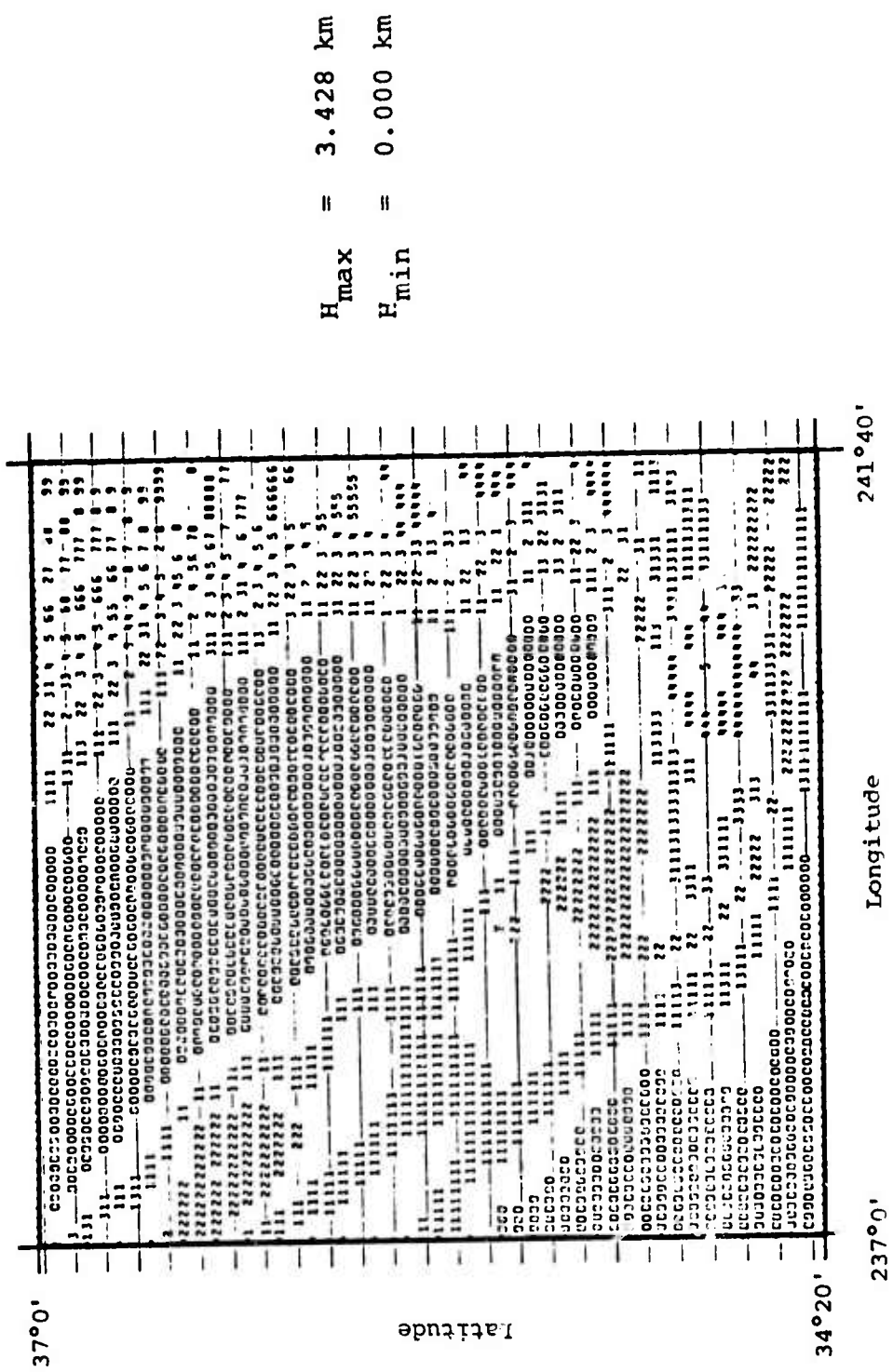
The quantities  $V_{\text{max}}$ ,  $V_{\text{min}}$  refer to maximum and minimum values of the variable and  $N$  is the plotted symbol. The  $\pm \frac{1}{2}$  indicates the range in  $V_{\text{actual}}$  corresponding to a particular symbol. The blank fields appearing in the plots correspond to contour levels intermediate between the symbols which are left blank for visual clarity. A(0,0) appearing on the spectrum



H<sub>max</sub> = 3.559 km  
 H<sub>min</sub> = 0.000 km

Figure 5.2 - San Joaquin-Sierra Nevada topography contour map derived from 5' resolution data.





H<sub>max</sub> = 3.428 km  
 H<sub>min</sub> = 0.000 km

37°0'

Latitude

5-31

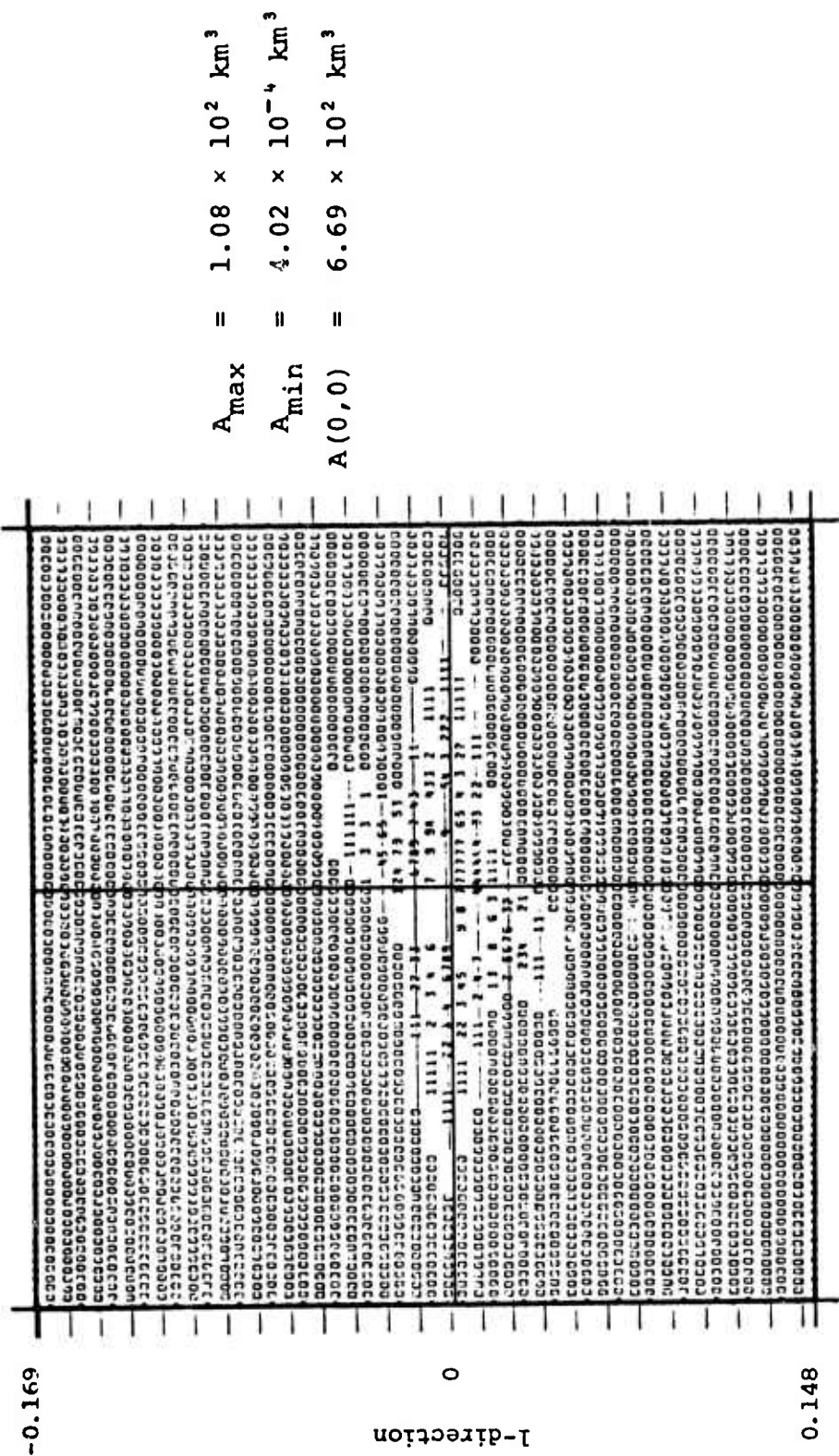
34°20'

Longitude

237°0'

241°40'

Figure 5.4 - San Joaquin-Sierra Nevada topography contour map derived from 10' resolution data.



$$A_{\max} = 1.08 \times 10^2 \text{ km}^3$$

$$A_{\min} = 4.02 \times 10^{-4} \text{ km}^3$$

$$A(0,0) = 6.69 \times 10^2 \text{ km}^3$$

Figure 5.5 - Spectrum function distribution using topography data from Figure 5.4.

function plots is the value of the spectrum function at  $k=0$ ,  $l=0$ . Due to its large value it has omitted in the contouring so that resolution could be improved.

The presence of the San Joaquin Valley (having a pronounced north-west to south-east axis) in the grid introduced an interesting asymmetry to the topography. Upon examination of the graph we find that these regularities in the topography are reflected in the spectrum function. The topography consists primarily of two ridges rising above a flat plain. One feature extends north-south near the right edge of the topography graph and the other crosses the graph at approximately a  $45^\circ$  angle. These two ridges correspond to the two finger-like extensions seen in the spectrum function plot of Figures 5.2 and 5.4. The horizontal extension corresponds mainly to the irregularities in the N-S ridge while the diagonal arm reflects the diagonal ridge.

Due to the symmetry properties of  $A$ , the graphs exhibit a reflected symmetry through the origin. (Note: Due to the number of contour intervals and the slight displacement of the graphs of topography and spectrum function, exactly the same plot character may not appear in the reflected plot.) We also see the same characteristic features appearing in both  $A$  plots. The resolution of Figure 5.3 hampers further comparisons between the spectrum functions corresponding to 5' and 10' resolution.

Examination of the other topographic regions of the set reveals that frequently a prominent topographical feature will be reflected in a clearly observable corresponding feature of the  $A$  distribution.

### 5.2.3 Computer Code for Calculation of Reynold's Stress

#### 5.2.3.1 Reduction of Domain of Integration

This result, which reduces the amount of calculation in forming the Reynold's stress components by a factor 2, is incorrectly justified by Bretherton. In fact, as will be shown below, the simplification results from the integrand being the same at the wave numbers  $(k,1)$  and  $(-k,-1)$  representing a reflection in the origin of wave number space, rather than as stated by Bretherton that  $(\kappa,\phi)$  is the same as  $(\kappa,-\phi)$ .

Several factors enter in the Reynold's stress integrand; we examine the behavior of each of these when the transformation  $(-k,-1) \rightarrow (k,1)$  is carried out. First, we examine the differential equation for the vertical velocity and its boundary conditions.

$$\kappa^2(-k,-1) = k^2 + 1 = \kappa^2(k,1)$$

$$U_n(-k,-1) = \frac{-1}{\kappa}(U\kappa + V1) = -U_n(k,1) \quad (5.50)$$

$$\ell^2(-k,-1) \equiv \frac{N^2}{U_n^2} - \frac{d^2 U_n}{U_n dz^2} = \ell^2(k,1) .$$

i.e., the Scorer parameter, being an even function of  $U_n$ , is invariant under the transformation. Consequently, the Scorer equation and its elementary solutions, depending only on  $\ell^2 - \kappa^2$ , are also invariant. Using this result, which establishes that  $u_1$  and  $u_2$  of Eq. (5.35) are invariant, and considering the transformation properties of Eq. (5.40) for  $F$ , we find that

$$F(-k,-1) = -F(k,1) \quad (5.51)$$

We now consider the topographic factor of the Reynold's stress given by Eq. (47) of Bretherton.

$$\hat{h}(-k, -l) = \frac{1}{4\pi} \int_0^X \int_0^Y h(x, y) e^{-i(-kx-ly)} dx dy$$

$$= \hat{h}^*(k, l) .$$

Forming the spectrum function  $A = \frac{4\pi^2}{XY} \hat{h} \hat{h}^*$ , we obtain the transformation property

$$A(-k, -l) = \frac{4\pi^2}{XY} \hat{h}(-k, -l) \hat{h}^*(-k, -l) = A(k, l) .$$

These quantities can be combined to form the integrands of the two horizontal components of the Reynold's stress:

$$\begin{Bmatrix} \rho u w \\ \rho v w \end{Bmatrix} = \rho_0 U_n^2(0) \kappa^2 A F \begin{Bmatrix} \cos \phi \\ \sin \phi \end{Bmatrix} = \rho_0 U_n^2(0) \kappa A F \begin{Bmatrix} k \\ l \end{Bmatrix} .$$

The transformation  $(-k, -l) \rightarrow (k, l)$  is seen to leave the integrand invariant:

$$\rho u w(-k, -l) = \rho u w(k, l)$$

$$\rho v w(-k, -l) = \rho v w(k, l) .$$

Consequently, the result given in Bretherton's Eq. (54) is confirmed; namely that

$$\int_0^{2\pi} d\phi = 2 \int_0^{\pi} d\phi .$$

### 5.2.3.2 The Equations

The equations incorporated in the code are substantially those of Bretherton. [25] A slight modification has been made to the trapped wave integrals, however. A factor of  $\kappa$  in the numerator of the sums which was omitted by Bretherton, has been incorporated into the code.

### 5.2.3.3 Numerical Method

The flow diagram for the Reynold's stress calculation is shown in Figure 5.6. A trapezoidal integration scheme is currently being employed in the evaluation of the stress integrals. The integration uses a constant increment  $\Delta\kappa$  and  $\Delta\phi$  of  $\kappa$  and  $\phi$ . The integration over  $\kappa$  is currently carried out for each value of  $\phi$ , although the order of calculations can be changed to increase the efficiency code. First, the Scorer parameter profile is calculated for the current value of  $\phi$ . Values of  $\hat{w}$  are then successively calculated for all  $\kappa$ -values. The values at  $z=0$  are then tested to determine whether there are nearby trapped waves. If the test is negative and  $\kappa \leq \ell(H)$  then the region is defined to be part of the continuous spectrum and the stress integrals are incremented using Bretherton's Eq. (54). If the criterion for a trapped wave is met, a search to localize it more accurately is begun.  $\kappa$ -values between  $\kappa - \Delta\kappa$  and  $\kappa$  are searched until the denominator of the  $F$  expression is minimized to within a user-prescribed accuracy. If  $\kappa > \ell(H)$ , the trapped wave occurs at a  $\kappa$ -value for which the perturbation velocity  $\hat{w}$  at  $z=0$  vanishes. Since the real and imaginary parts of the solution for  $\kappa > \ell(H)$  are proportional to each other, they both must vanish together. This property simplifies the search scheme for the trapped wave considerably.

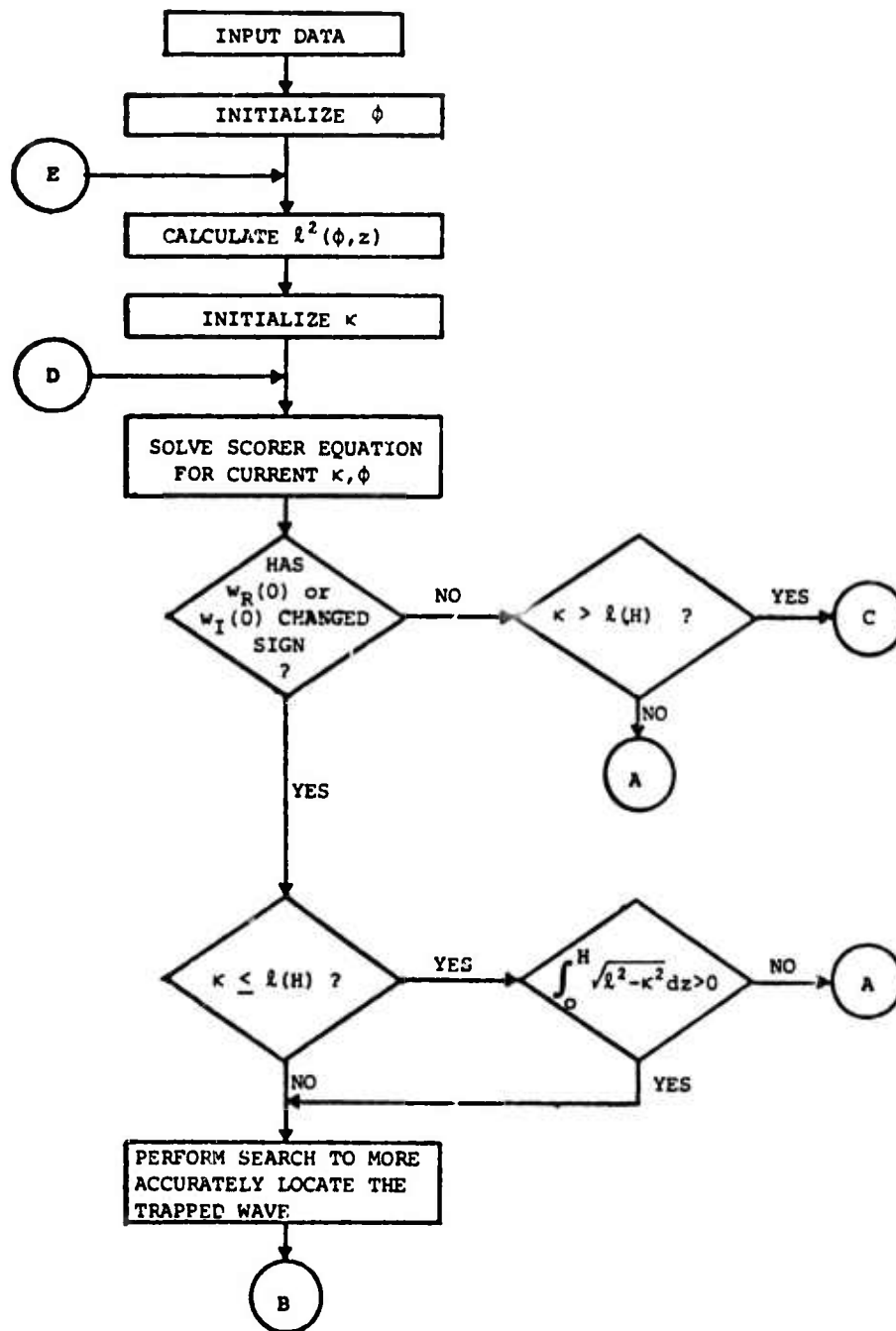


Figure 5.6 - General flow diagram of drag code.

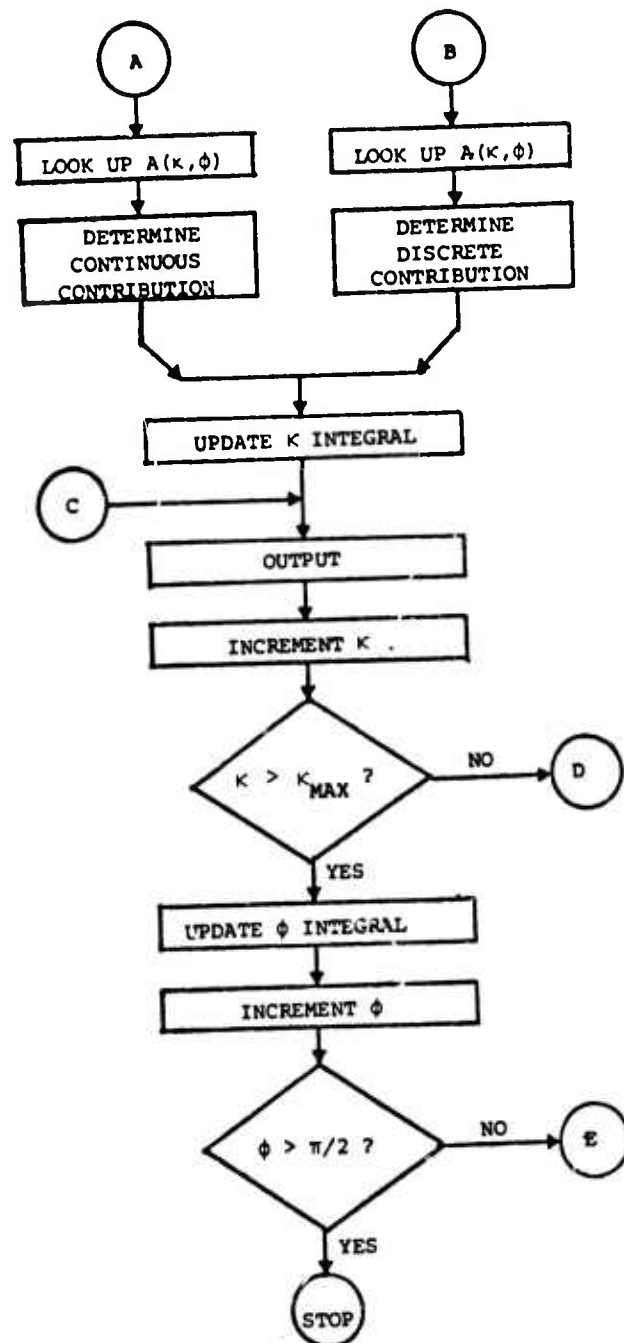


Figure 5.6 - (continued)

Figure 5.7 depicts the typical  $\kappa$ -dependence of the Scorer equation solutions at  $z=0$ . Let  $\kappa_i$  be the  $\kappa$ -value of the trapped wave. We also denote by  $w_1$  and  $w_2$  the real parts of the Scorer equation solution for  $\kappa-\Delta\kappa$  and  $\kappa$  at  $z=0$ . An iterative search is performed which utilizes linear interpolation between  $w_1$  and  $w_2$  to obtain a more accurate guess at  $\kappa_i$ . Using this value of  $\kappa$  and its corresponding  $w_R(0)$  another linear interpolation is performed using the member of the old pair of  $w$ 's of opposite sign to the new value. The search converges quite rapidly and usually requires only a few iterations. The criterion for convergence of the search is a user-specified value of the permissible change in the "s" term of Bretherton's Eq. (61). It was found to be superior to a test of  $w_R(\kappa, \phi)$  compared with a small number which was found to be unreliable due to possible rounding errors in  $\hat{w}$  where the amplitude of  $\hat{w}$  is very large. Care must be taken in choosing the size of  $\Delta\kappa$  since it might be possible for  $\hat{w}(\kappa, \phi)$  to change sign twice within the interval and a trapped wave would be missed. Present  $\Delta\kappa$  are very conservative, and it is felt that this situation will not arise very often.

For values of  $\kappa \leq \ell(H)$ , the real and imaginary parts of the solution to Scorer's equation are linearly independent. Consequently, the real and imaginary parts will not simultaneously vanish at  $z=0$  for any  $\kappa$ -value. Both may simultaneously become quite small, however. When this condition occurs, a peak in the  $F$  distribution will be present. The height of the peak is a function of  $\hat{w}^*(0) \hat{w}(0)$ , and its "Q", corresponding to the width of the peak, is a function of the depth of the region in which the solution of the Scorer equation undergoes exponential decrease. A large value of "Q" corresponds to trapped waves with a very slight upwards energy leak.

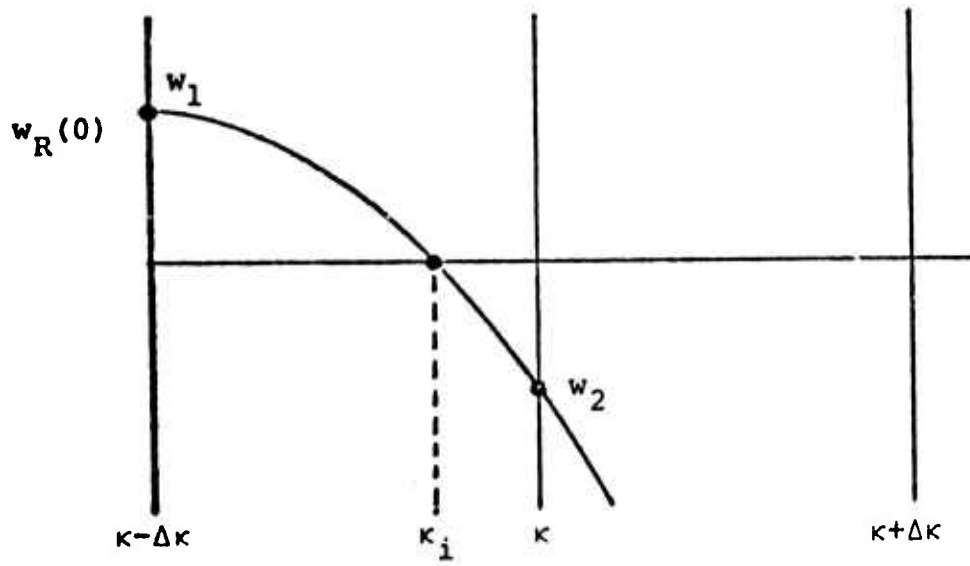


Figure 5.7 - Typical dependence on wavenumber of the solution of the Scorer equation at  $z=0$ ,  $w_R(0)$  vs.  $\kappa$ .

Consequently, a trapped wave in the region of  $\kappa \leq \ell(H)$  must satisfy two conditions. First, the value of  $\hat{w}^*(0) w(0)$  must have a local minimum. And second, the peak in the value of  $F$  must be sharply localized. Bretherton suggests that the first condition can be recognized by examining the quantity  $\arg[\hat{w}(\kappa, \phi)]$  for sudden changes as a function of  $\kappa$ . This, in effect, requires either the real or the imaginary part of  $\hat{w}$  at  $z=0$  to change sign. This is a necessary condition for a trapped wave to exist. For  $\kappa > \ell(H)$  it is also a sufficient condition. However, for  $\kappa \leq \ell(H)$  the second condition discussed above must also be met. A sharply localized peak of  $F$  requires that a resonant behavior of  $\hat{w}$  occur. This, in turn, calls for a sufficiently deep atmospheric layer in which gravity waves are reflected so that the leakage of energy into the stratosphere is small. This condition can be quantified in terms of the quantity.

$$\int_0^H \sqrt{\ell^2(z) - \kappa^2} dz ,$$

which is a measure of the exponential decrease of  $\hat{w}$  due to wave reflection. When

$$\int_0^H \sqrt{\ell^2(z) - \kappa^2} dz > \sigma$$

where  $\sigma$  is a user-specified number, the resonance in  $F$  is judged to be sufficiently sharp to perform the integration over it analytically. If the above condition is not met, the integration is to be performed numerically. In this case, the integrand changes sufficiently slowly that an accurate numerical quadrature can be performed with a reasonable integration step  $\Delta\kappa$ .

Since the extent and strength of the region of exponential decay in the solution to Scorer's equation increases with increasing  $\kappa$ , the resonances (if any) lying below  $\kappa=l(H)$  will exhibit sharper and sharper peaks as  $\kappa$  increases. Through the choice of  $\sigma$  the user has control over the extent of the spectrum to be considered as continuum. A small value of  $\sigma$  will require that rather broad lines are treated analytically, while a large value will treat quite sharp lines as continuous.

Tests of this section of the code have been carried out for several choices of atmospheric parameters in order to determine an optimum value of  $\sigma$  for accuracy and speed of calculation.

#### 5.2.4 Topography

Topography data were obtained from the Defense Mapping Agency (DMA) and are contained on two sets of magnetic tapes. The first set contains elevations area-averaged over 30'x30' rectangles for the entire globe. The second set contains elevations area-averaged over 5'x5' rectangles for most of North America and Europe.

An examination of these tapes indicated that a restructuring of the data format would allow much faster access to particular pieces of information. As a result, the reading of all available 30' data now requires 30 seconds of CPU time as compared to 600 seconds previously.

The new tapes, resulting from the above restructuring, are arranged in a common format for both the 30' and 5' data sets. The 30' set requires two tapes, one for the northern hemisphere and one for the southern hemisphere. The 5' set consists of one tape covering the northern hemisphere. The data are written in logical records having 1444 word length for 30' data and 4324 words for 5' data. Each logical record represents topographical data at a particular latitude for a

full 360° of longitude. These records are written on the tapes sequentially starting at the northernmost latitude of each hemisphere. At the head of each logical record are written the starting latitude and longitude of the strip, where longitude is measured east of Greenwich. Associated with each data point is a code number which contains information about the nature of the topography; i.e., whether sea bed, lake, all land, etc. This coded information is the same as that in the DMA description of their tapes. In addition to the code data, however, another indicator has been added to denote missing data. It was found that occasional gaps in data occurred on the DMA tapes. Since the Fourier transform routine requires complete data, a flag is set whenever the missing topography is encountered and the run is terminated. Usually, this requires obtaining the data from other sources and inserting it into the data tape. The case can then be rerun in the usual manner.

#### 5.2.5 Test Calculations

##### 5.2.5.1 Comparison of Transient and Steady-State Wave Drag

After the completion of the 3-D steady-state code, two test problems were run. The first investigated a generalization of the triangular mountain of the previous section (see Section 4.6) by calculating a triangular ridge 128 km in length. The second calculation was applied to the actual Sierra Nevada-Owen's Valley topography and is described below in detail.

The Sierra Nevada is a single unbroken range approximately 400 miles in length and 50 to 80 miles wide. At the Owen's Valley we find the main crest running nearly North-South. Elevations along the crest are around 12,000 ft. with numerous peaks rising above 14,000 ft. The eastern scarp is abrupt and quite straight. Owen's Valley is to the east at an

average elevation of 4,000 ft. and of a nearly uniform width of approximately 15 miles. The east wall of Owen's Valley is a fault block range called the Inyo Mountains to the south and the White Mountains to the north. The elevation of the Inyo Mountains is 7,000-11,000 ft. while the White Mountains rival the Sierras in height.

Figures 5.8 and 5.9 show the topography of the Owen's Valley region. Figure 5.8 is a contour map of the data used in the second 3-D calculation. Figure 5.9 shows three east-west transects at the indicated latitudes. The asterisk indicates the position of Owen's Valley. Both figures were made from data derived from the 5' x 5' topography tapes described in Section 5.2.4.

The steady-state runs utilized the wind and temperature profile data obtained from the Merced weather station and employed in the previous studies. The calculations indicate a principal trapped wave having a wavelength of approximately 19 km. This agrees well with the value observed in the Owen's Valley under the same meteorological conditions of 18-20 km. The wave drag results are shown superimposed on the transient HAIFA results in Figure 5.10. Two-dimensional steady-state calculation results utilizing the east-west transects of Figure 5.9 are also presented. As can be seen, the results of the 3-D runs agree quite closely, revealing a possible insensitivity to the topography.

The 2-D runs, however, differ by as much as a factor of 3. Since the real topography calculations and idealized topography 3-D calculations agree closely, one may assume that the idealized topography is a good characterization of the real topography. The differences between the 2-D and 3-D results can thus be attributed to the sensitivity of Reynold's stress to the topographic variability exhibited in Figure 5.9.

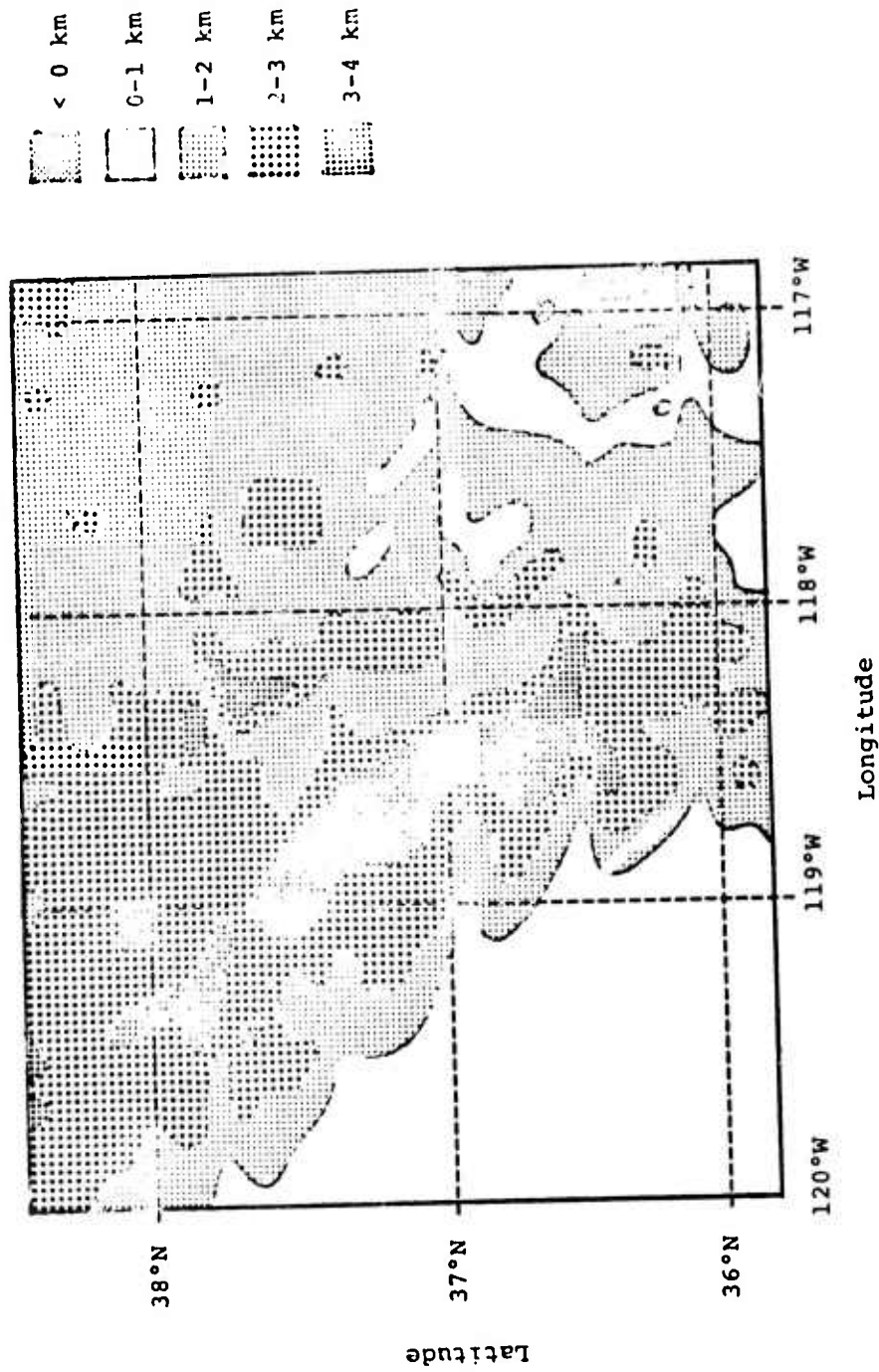


Figure 5.8 - Contour map of the Sierra Nevada-Owen's Valley region showing contours at 1 km intervals. Data are obtained from Defense Mapping Agency 5'x5' topography tables.

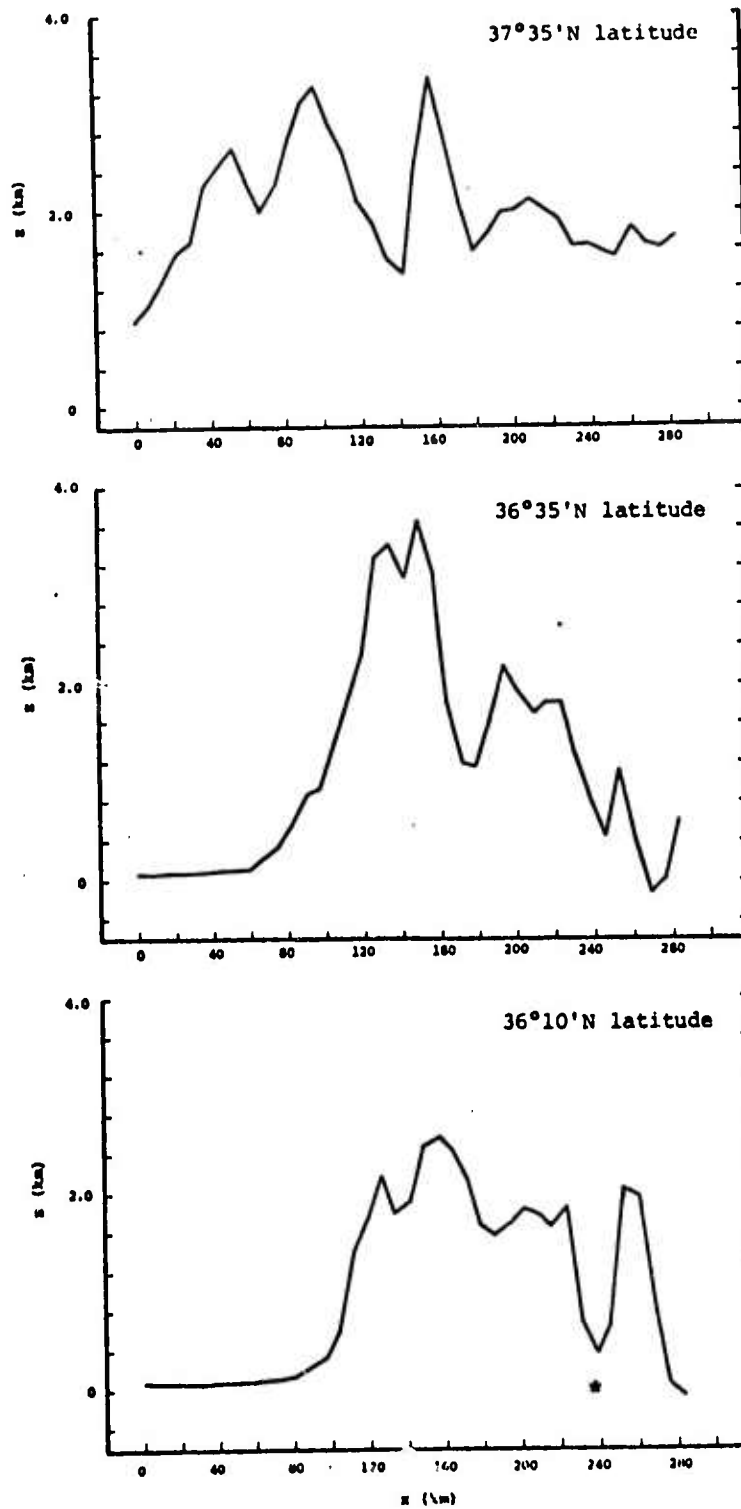


Figure 5.9 - 2-D cross-sections of Sierra topography from  $120^{\circ}\text{W}$  through  $116^{\circ}50'\text{W}$  longitude. Asterisk indicates Owen's Valley.

LEGEND

- 2-D LSS calculation of HAIFA  
triangular mountain
- X 3-D LSS calculation of HAIFA  
triangular ridge
- O 2-D LSS calculation along 36°10'  
36°10'N transect
- 2-D LSS calculation along  
36°35'N transect
- △ 2-D LSS calculation along  
37°35'N transect
- ◇ 3-D LSS calculation of area  
from 35°50'N to 38°25'N and  
120°W to 116°50'W

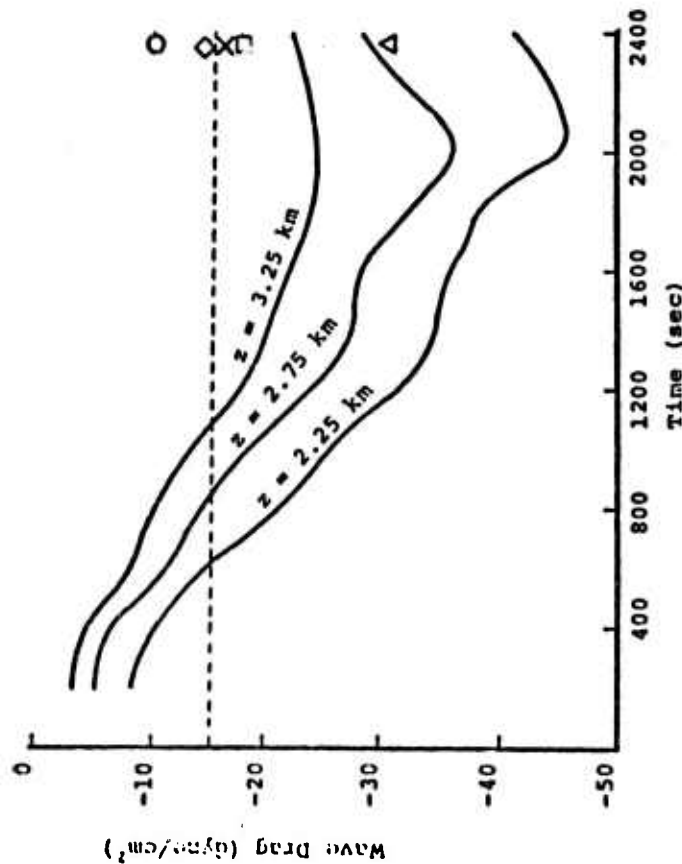


Figure 5.10 - Vertical flux of horizontal momentum from HAIFA calculation (See Section 4.6), compared with steady-state calculations.

### 5.2.6 Test Calculations to Parameterize the Wavedrag

The amplitude of the waves generated on the leeward side of mountains and the mechanism for the dissipation of these waves will depend strongly on the atmospheric wind and temperature profiles. In the linearized theory, the propagation of wave energy in the wave with horizontal wavenumbers  $(k,l)$  is dependent on the Scorer parameter profile in the atmosphere. The Scorer parameter  $^2(z) = N^2/U_n^2 - U_n^{-1}$  is a function of the atmospheric stability,  $N$ , and the velocity component,  $U_n$ , parallel to the wavevector. The amplitude of the waves that the atmosphere can support is determined by a solution of the equation.

$$(d^2w/dz^2) + (\ell^2(z) - \kappa^2) w = 0 \quad (5.52)$$

subject to the boundary conditions imposed by the model used. [25-29]  
 In equation (5.52),  $\kappa^2 = k^2 + l^2$ . The local magnitude of the Scorer parameter,  $\ell^2(z)$ , with respect to the square of the magnitude of the wavevector.  $\kappa^2$ , will determine the amplification of a particular wavenumber. When the wind speed in the direction of the wavevector is very high, horizontal energy and momentum is pumped into that wavenumber, and the wave will grow in amplitude in that layer. Conditions producing amplification of wave energy ( $\kappa^2 > \ell^2(z)$ ) also occur when the lapse rate approaches the adiabatic lapse rate. The longer waves will not be as greatly influenced by changes in the resonance characteristics of the lower atmosphere, and much of this wave energy will pass through the troposphere forcing the natural modes of the stratosphere.

The generation and dissipation of lee waves in an atmosphere will depend upon the fine structure of the wind field and the temperature profile. The response characteristics of the atmosphere to a disturbance with wavenumber  $(k,l)$  is determined by the local stability of the atmosphere, the wavelength of the disturbance, and the angle the wavevector makes with the meridional and zonal winds. The most favorable conditions for the generation of high amplitude waves occur with strong low-level winds and a low-level inversion. The dissipation of the waves will occur at regions of low Richardson's number, that is, regions of high stress. The effect of horizontal stress on the wave is to turn the wavevector in the horizontal direction. [30] As the intrinsic frequency of the wave,  $\omega - U_n k$ , goes to zero, the amplitude decreases and the momentum is given to the flow-field. Hence, an accurate description of the momentum transport to the atmosphere requires a detailed atmospheric temperature and wind velocity profile.

The modeling of the wavedrag associated with mountains is restricted by the lack of vertical and horizontal resolution of a global circulation model. We can resolve the topography to the 5' or 30' grid data available, but we rely on the atmospheric variables from the GCM for a definition of the atmospheric profiles of temperature and wind velocity. The wind vectors and temperatures are resolved to only the 4° by 5° grids used in the GCM. The strong low-level inversions (which, in any case, could not be resolved in the vertical by a two-level model) are generally the result of the movement of a warm air mass over a cold air mass. The resolution of frontal activity cannot be obtained explicitly from the GCM. However, arguments for the occurrence of inversions and a parameterization of the inversion level may be possible from a study of the movement of synoptic scale air masses in the GCM. We have not had the opportunity to attempt such a parameterization in this research program. In characterizing

the stress integrals, we have chosen to fit the GCM wind speed and temperature data at the two levels with prescribed vertical profiles which will be described subsequently. The Scorer parameter profile for each wavevector then followed from the definition of the Scorer parameter and the atmospheric response was determined by integration of equation (5.52) through the atmosphere subject to the boundary conditions at the top of the atmosphere given in equation (5.53). The wind profiles, the temperature profiles, and the Scorer parameter, are of necessity considerably smoothed due to the poor resolution of the GCM. Since the Scorer parameter is considerably smoothed, we might have alternately chosen to express the Scorer parameter in terms of the mathematical forms which give analytic solutions to the Scorer equation. Application of these analytic solutions to multilayer models for the one-dimensional problem has been given by Palm and Foldvik and Vergeiner. [8,21] The same solutions are applicable to our problem if the Scorer parameter is treated as a function of the wavevector of each of the components of the topography spectrum function. The Scorer equation admits analytic solutions when the Scorer parameter is treated as a constant through the layer, as an exponential function of height, or if it is taken to be

$$k^2(z) \equiv k_0^2 - \frac{2}{(z+\alpha)^2} \quad (5.53)$$

where  $k_0$  and  $\alpha$  are constants determined for each level. The form given in equation (5.53) has been applied by Vergeiner. We will discuss in Section 5.3 how we intend to use an analytic solution in the Rand GCM subroutine to calculate the two components of the wave drag. We did not feel justified in using these analytic models during this phase of the research because of the need to study the sensitivity of the atmospheric response function to the changes in the atmospheric variables.

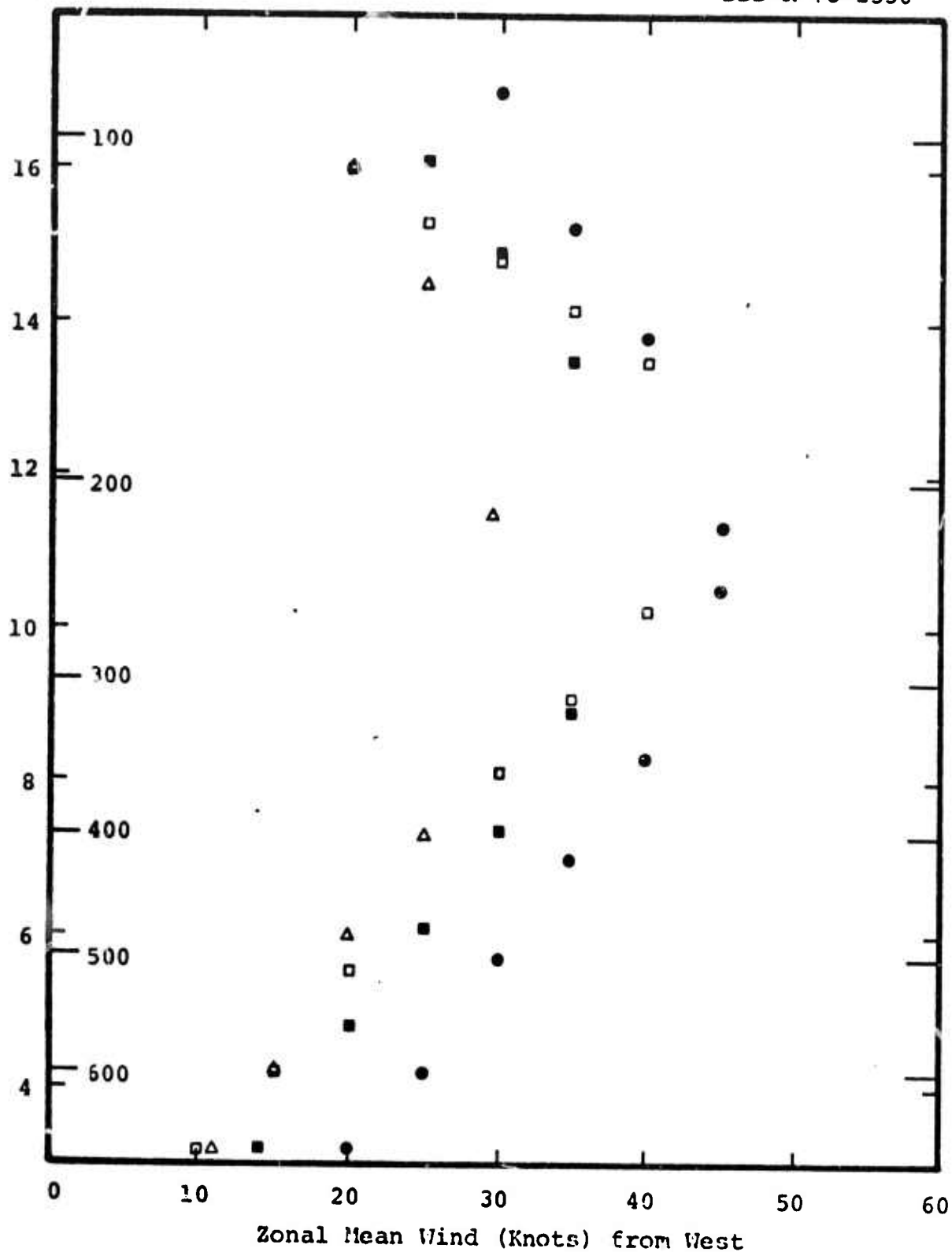
We have described the difficulties involved in obtaining the meridional and zonal wind profiles. We inspected the wind data that were available on National Weather Service tapes.<sup>[31]</sup> We obtained data available on microfilm from the National Center for Atmospheric Research, and reviewed the seasonally averaged wind profiles available from the National Weather Records Center.<sup>[32]</sup> We also consulted with meteorologists to obtain suggestions on how the wind profiles might be deduced from the two-level model.

In Figures 5.11 and 5.12 we have reproduced typical seasonally averaged data from the National Weather Records Center data for the midlatitudes over mountainous terrain. Each component is characterized by peak speeds near the tropopause and can be approximated by a second-degree polynomial.

Wind speed and direction data obtained from the National Center for Atmospheric Research are reproduced in Figure 5.13. These data represent soundings over the Rocky Mountains taken over a period of approximately one hour.

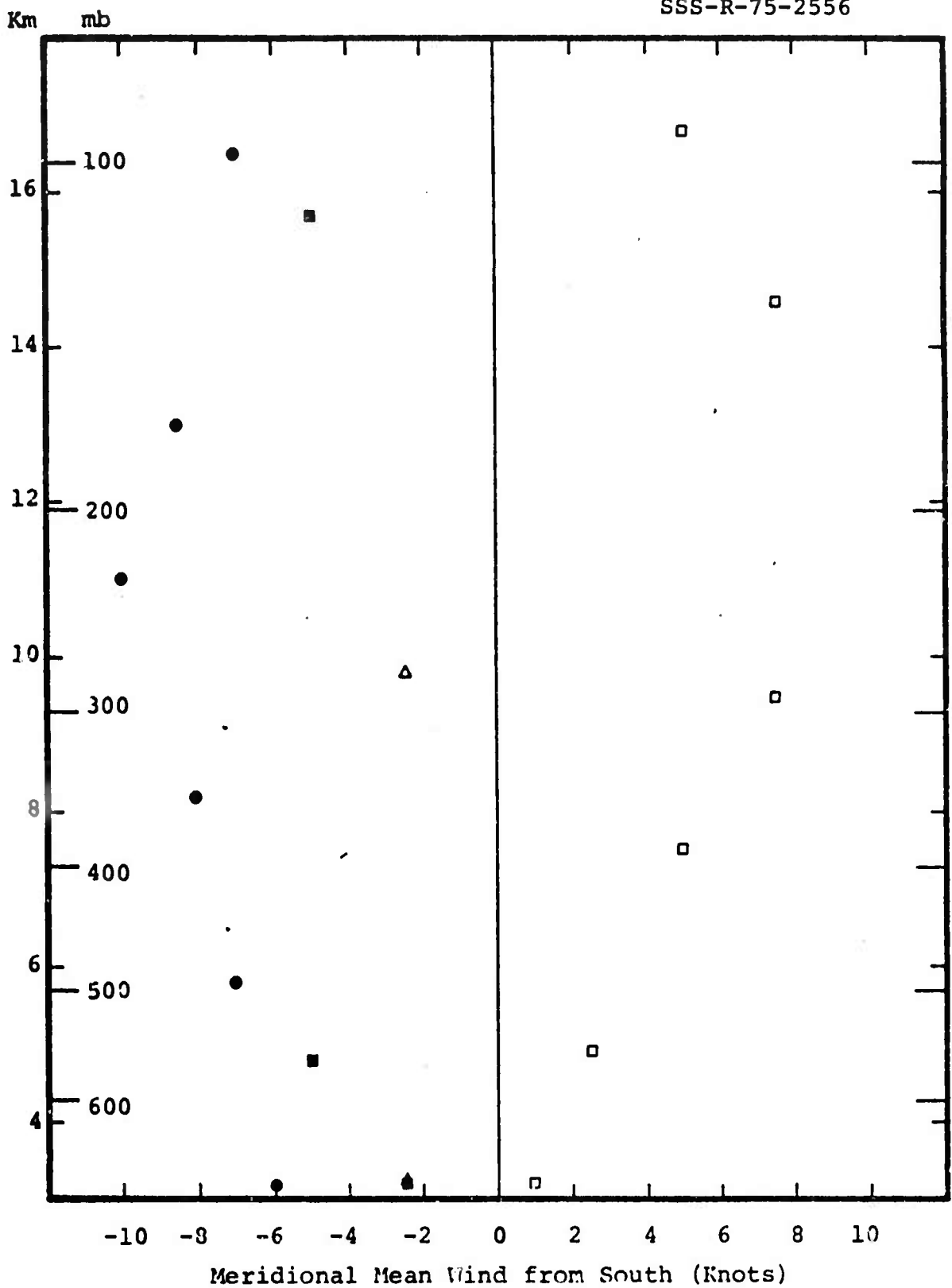
Finally, in Figures 5.14 to 5.16 we have reproduced data taken from the National Weather Service tapes for the meridional and zonal winds and the temperature profiles over West Virginia. The data are represented by the dots and the data points have been fitted with a smooth curve.

In the present study the solution of the Scorer equation was obtained by an integration of the equation through the atmosphere in the z-coordinate system. To use the GCM data required a transformation from the  $\sigma$ -coordinate system to the z-coordinate system and extrapolation of the data to other points in the atmosphere. The temperature, given at the  $\sigma = 1/4$  and  $\sigma = 3/4$  levels, was extrapolated in a pressure coordinate system by letting



- Dec - Jan - Feb
- ▲ Mar - Apr - May
- Jun - Jul - Aug
- Sep - Oct - Nov

Figure 5.11 - Seasonally averaged zonal mean wind at 110°W 45°N from U.S. Department of Commerce Technical Paper 41.



- Dec - Jan - Feb
- ▲ Mar - Apr - May
- Jun - Jul - Aug
- Sep - Oct - Nov

Figure 5.12 - Seasonally averaged meridional mean wind for 110°W 45°N from U.S. Dept. of Commerce Technical Paper 41.

B WAMFLEX 12 MAR 73 UPSTREAM SOUNDING

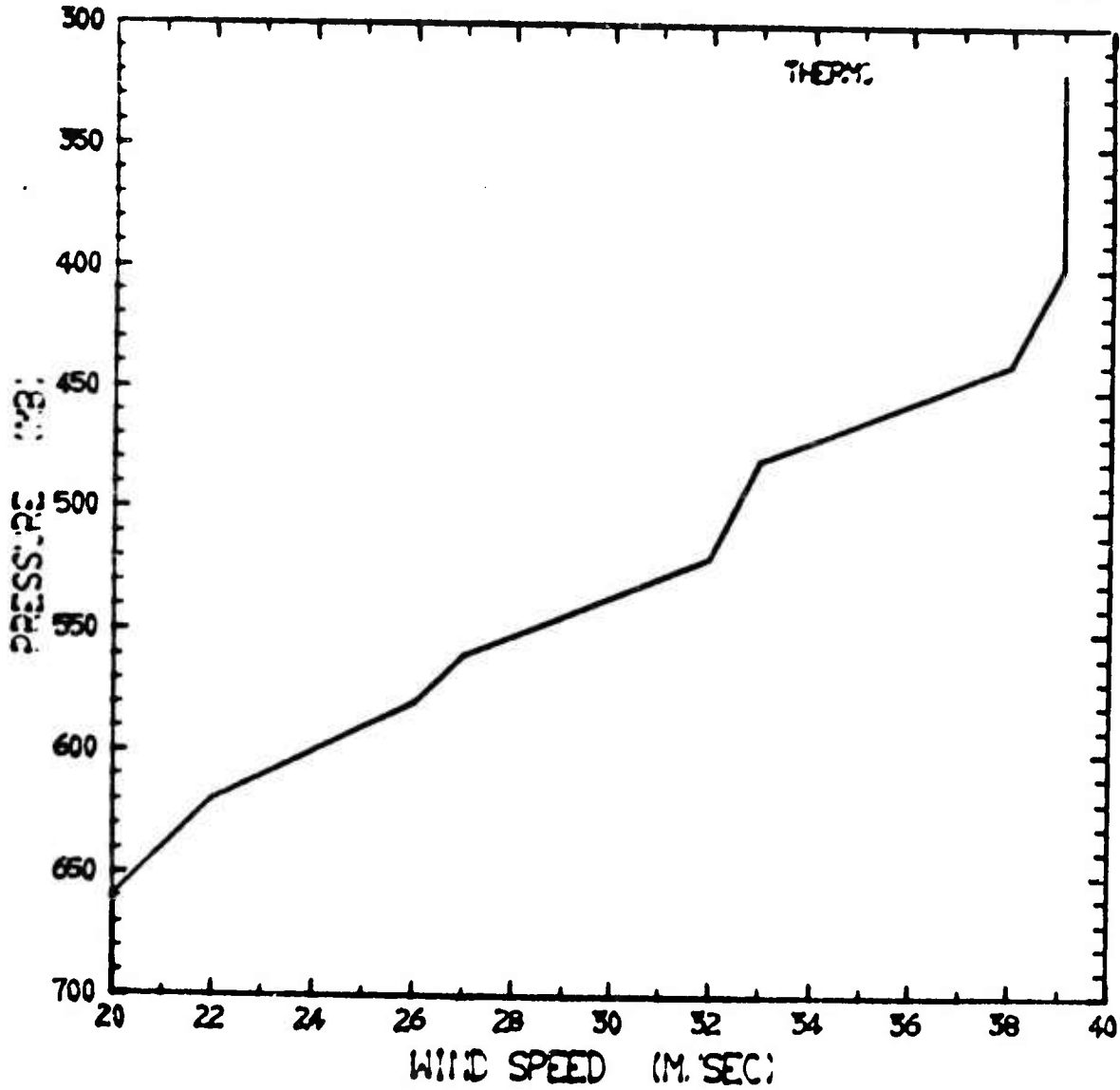


Figure 5.13a - Wind speed data from NCAR for March 12, 1973.

B WAMFLEX 12 MAR 73 UPSTREAM SOUNDING

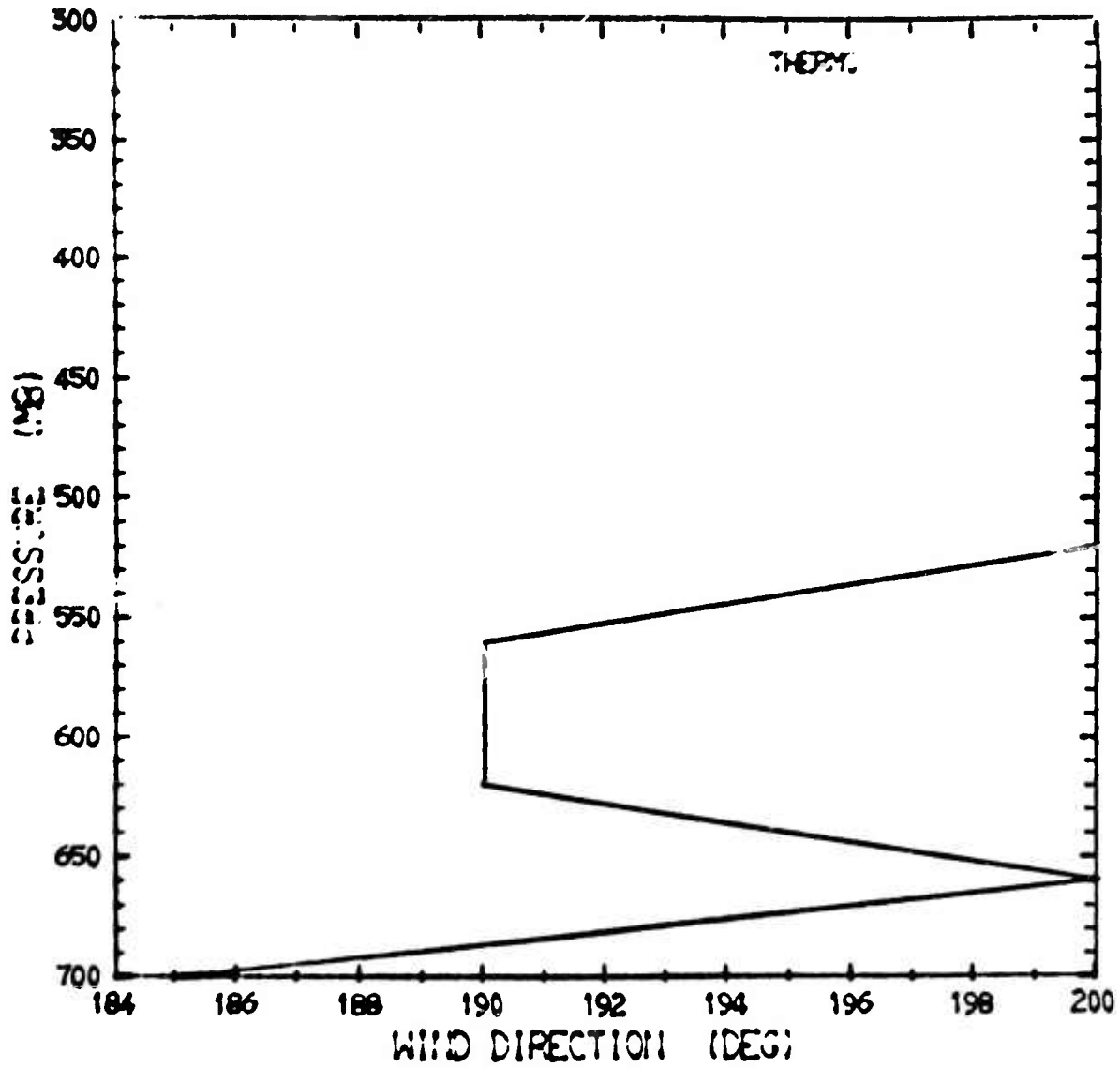


Figure 5.13b - Wind direction data from NCAR for March 12, 1973.

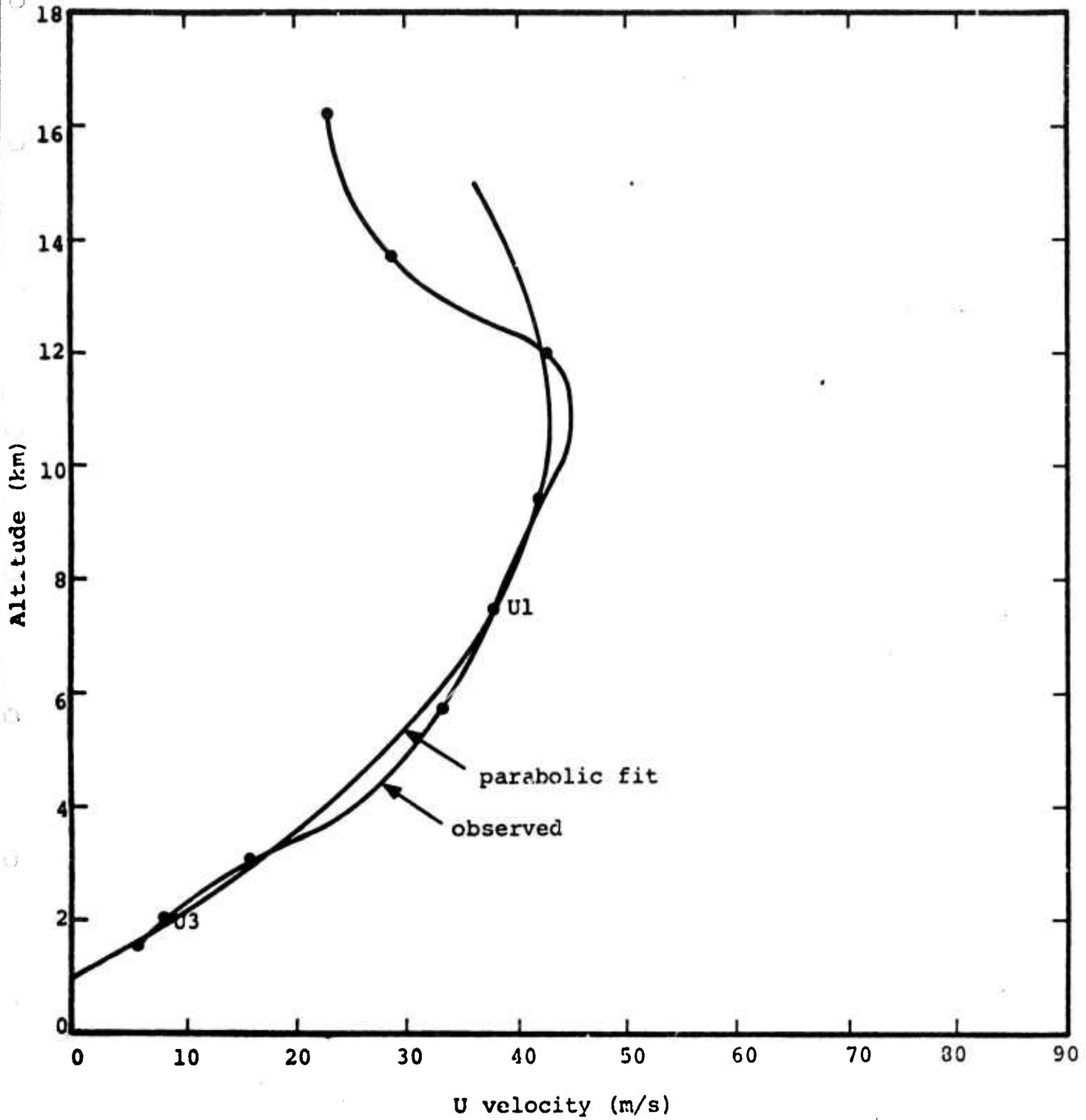


Figure 5.14 - The zonal wind profile for West Virginia from the National Weather Service tapes.

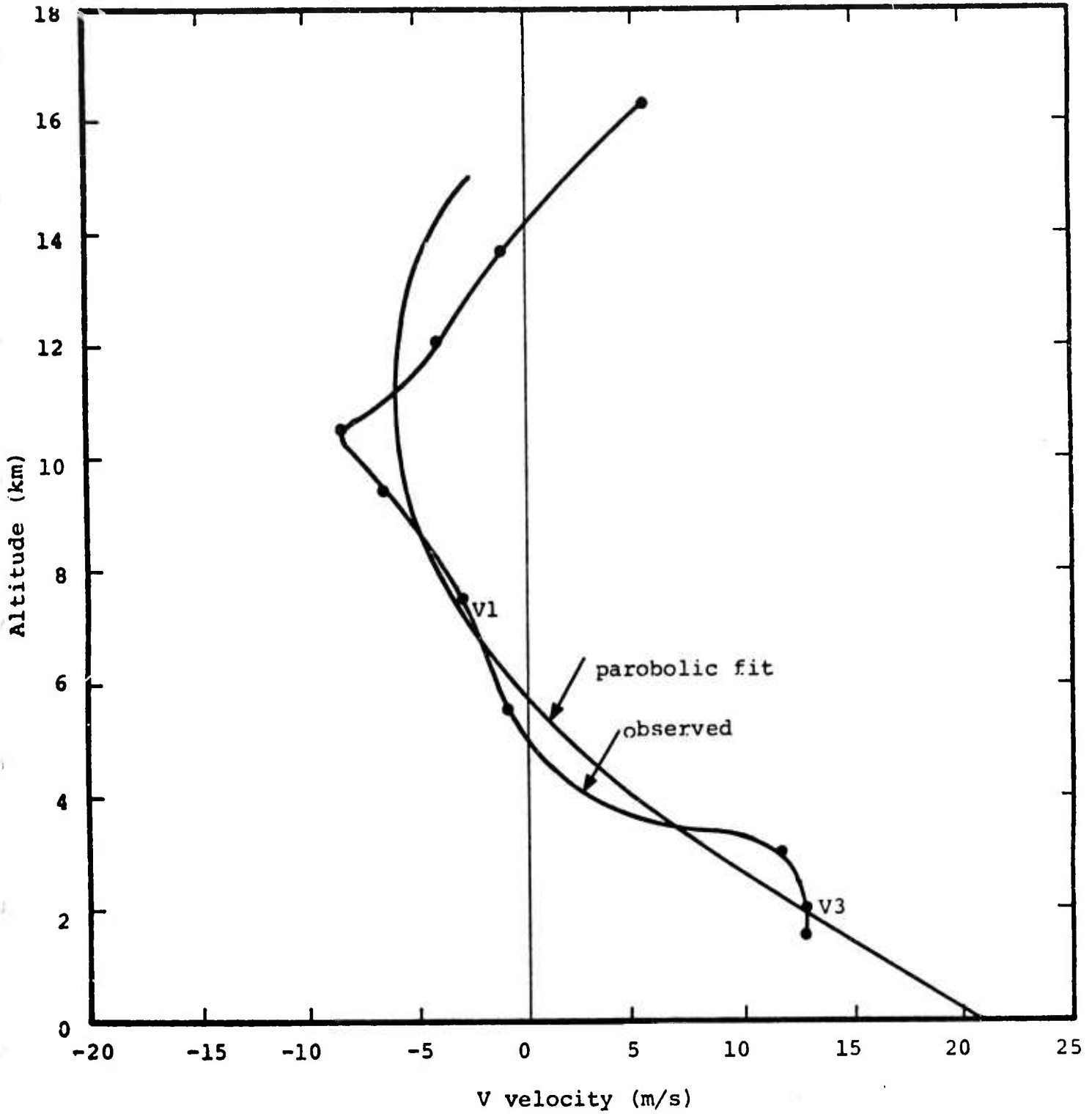


Figure 5.15 - The meridional wind profile for West Virginia from the National Weather Service tapes.

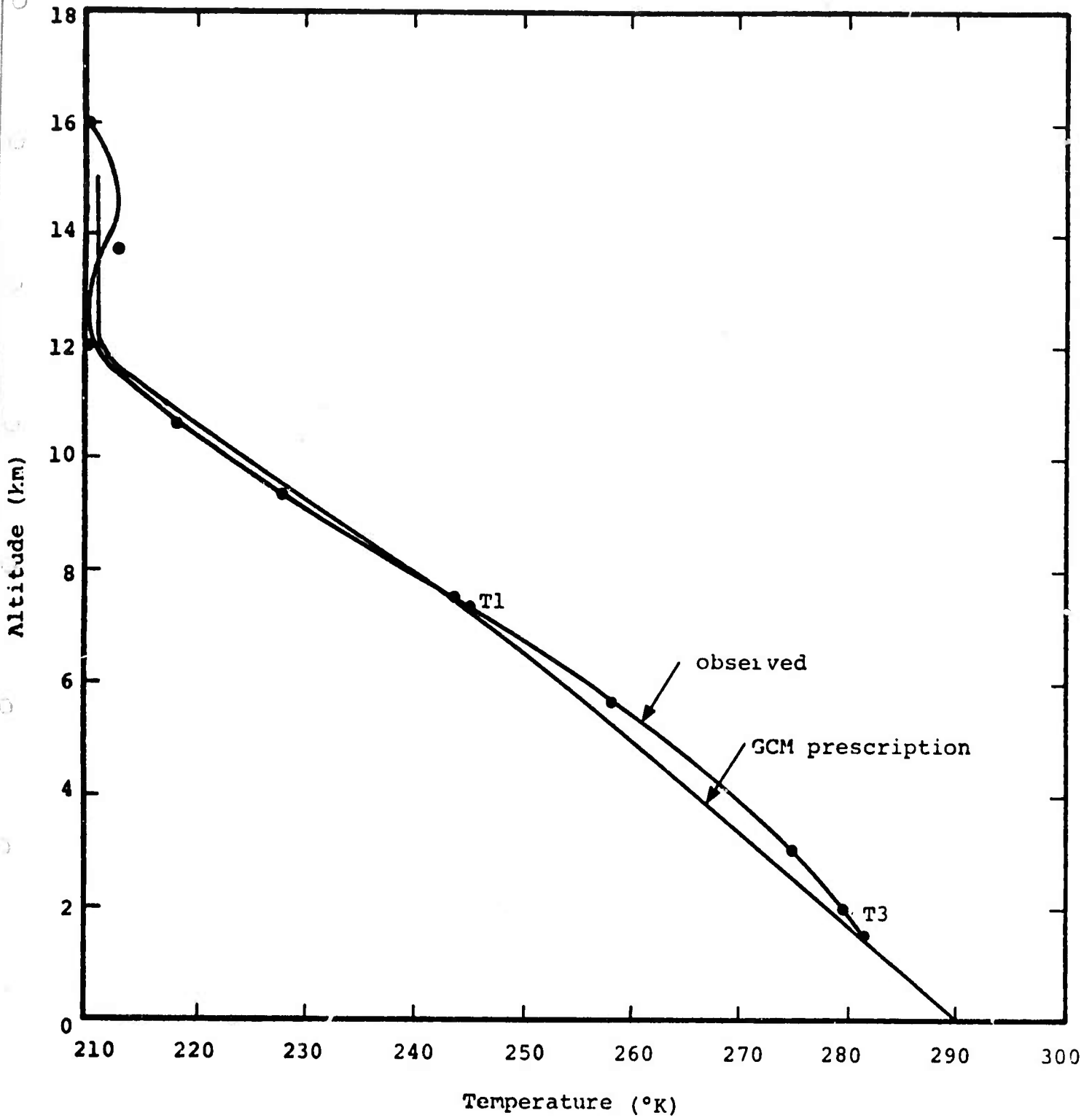


Figure 5.16 - The temperature profile for the West Virginia data taken from the National Weather Service tapes.

$$T(p) = \frac{p^{k_1}}{p_3^{k_1-p_1 k_1}} \left\{ \frac{T_1}{p_1^{k_1}} \left[ p_3^{k_1-p_1 k_1} \right] + \frac{T_3}{p_3^{k_1}} \left[ p^{k_1-p_1 k_1} \right] \right\} \quad (5.54)$$

below the 200-mb level and assuming an isothermal layer above this level. In equation (5.54),  $k_1 = 0.286$ , and subscripts 1 and 3 denote the variables at the  $\sigma = 1/4$  and  $\sigma = 3/4$  levels, respectively. The transformation from the p-coordinates to the z-coordinates followed by successive application of the hydrostatic equation written in finite difference form. The pressure profile obtained in this manner from the West Virginia data is given in Figure 5.17.

The profiles of the meridional and zonal winds were obtained by a parabolic fit, in z-coordinates, of the wind data points at  $\sigma = 1/4$ ,  $\sigma = 3/4$ , and a third point obtained by a reflection of the  $\sigma = 1/4$  data point about the 200-mb pressure level. This profile closely approximates the profiles of the seasonally averaged meridional and zonal winds in the midlatitude. In Figures 5.14 to 5.16 we have applied the extrapolation schemes to the West Virginia wind and temperature profiles. In this particular example, very high surface winds are predicted by this model. We did not correct for the high surface winds because in general this was not a problem. The only advantage of this prescription for the winds is that it provides an extrapolation above 200 mb which is not given by the linear extrapolation in the GCM. A prescription for the wind field which more accurately treats the variability of the winds with height would require a lengthy statistical treatment of the available wind data in terms of the two levels of the GCM. The additional information gained by such a prescription would undoubtedly be lost in the parameterization required to reduce the computing time to levels compatible with the GCM. A simple modeling of the wind field is consistent with the requirements of a simple mathematical expression for the Scorer parameter to

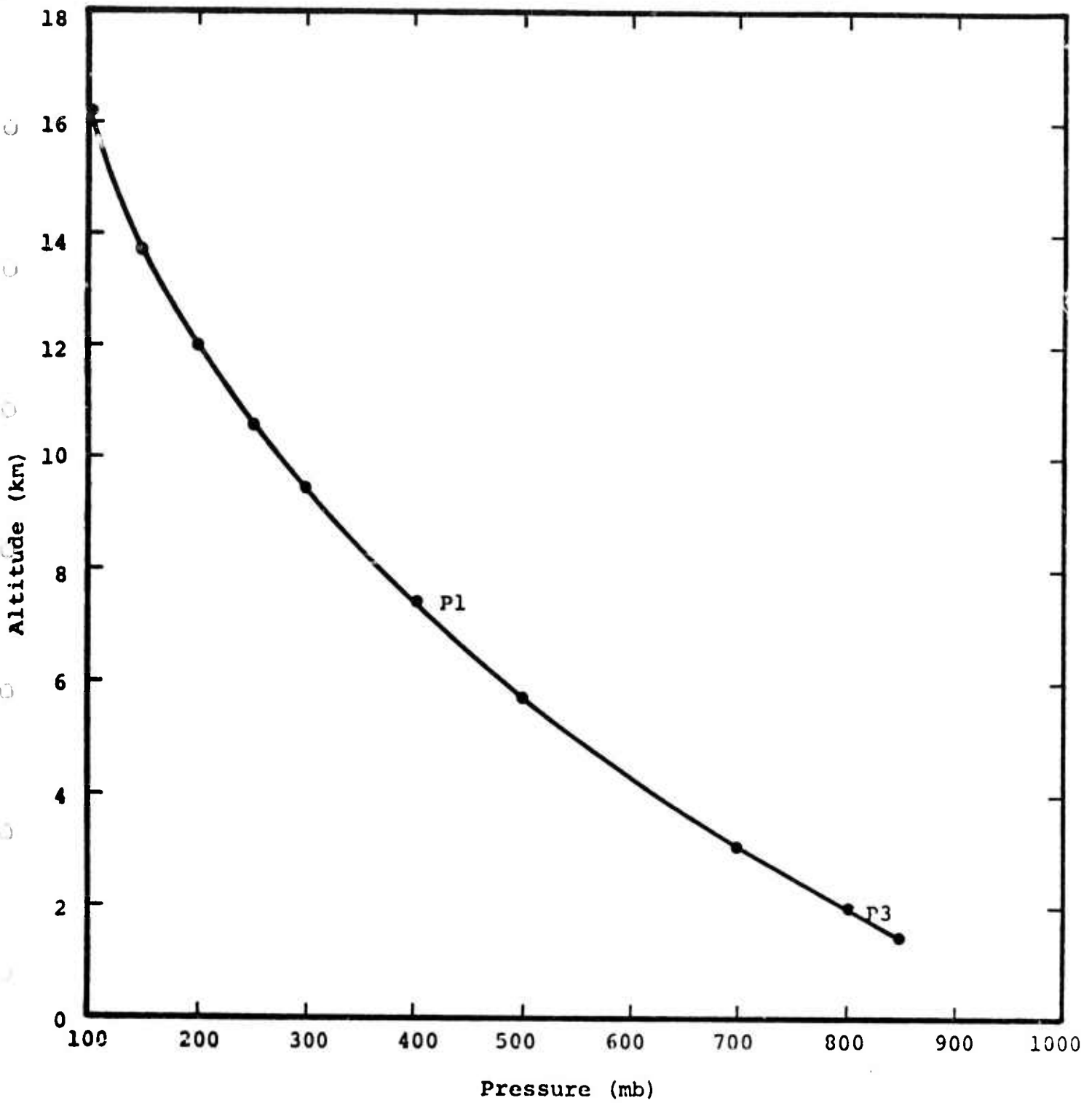


Figure 5.17 - The pressure profile for West Virginia from the National Weather Service tapes.

obtain an analytic solution of the Scorer equation. In general, in the absence of very stable conditions, the Scorer parameter will be much larger than the wavenumbers resolvable in the topography spectrum. Any local decrease of the Scorer parameter will have a greater influence on the shorter wavelengths than on the long wavelengths. Other investigators have found that these trapped waves do not increase the wave drag significantly. [25,33]

The temperatures at the  $\sigma = 1/4$  and  $\sigma = 3/4$  levels have been extrapolated to other levels by assuming that the potential temperature is linear in  $p^{k_1}$ , where  $k_1 = 1 - 1/\gamma$  and  $\gamma$  is the ratio of specific heats for the atmosphere. We have extended this to the 200-mb level, and then we have assumed an isothermal atmosphere above this level. The extrapolation of the temperature is the same as used in the GCM.

The temperature profile enters explicitly in the Scorer equation through the stability. It also enters into the wind profile through the transformation of the  $\sigma$ -coordinate system to the  $z$ -coordinate system by the hydrostatic equation. The smoothing of the temperature profile should also have a more significant effect on the shorter wavelengths than on the long wavelengths.

We have considered the ten topographic grids and the 15 atmospheres listed in Tables 5.1 and 5.2. All of the grids listed in Table 5.2 were  $2^\circ 40'$  on a side. In addition, another computer run was made of the stress integral on a  $4^\circ$  by  $5^\circ$  grid with the northwest corner located at  $121^\circ$  W  $37^\circ$  N. The smaller grids were selected for the economy of calculating fewer values of the atmospheric response function. The atmospheres were taken from selected mountainous areas of a GCM run. Four atmospheres were taken from this GCM run, and the remaining 11 atmospheres are perturbations or permutations of these four sets of data.

TABLE 5.1  
TOPOGRAPHIES INVESTIGATED

TOPOGRAPHY	NORTHERN LATITUDE	SOUTHERN LATITUDE	WESTERN LONGITUDE	EASTERN LONGITUDE
1	37°N	34° 20'N	121°W	118° 20'W
2	37°N	34° 20'N	118° 20'W	115° 40'W
3	37°N	34° 20'N	115° 40'W	113°W
4	37°N	34° 20'N	113°W	110° 20'W
5	37°N	34° 20'N	110° 20'W	107° 40'W
6	37°N	34° 20'N	107° 40'W	105°W
7	37°N	34° 20'N	105°W	102° 20'W
8	37°N	34° 20'N	102° 20'W	99° 40'W
9	37°N	34° 20'N	99° 40'W	97°W
10	37°N	34° 20'N	97°W	94° 20'W

The topography spectrum function, the atmospheric response function, and the stress integral are discussed in the next three sections. Our objective was to parameterize the stress integral; therefore, much of the discussion in the third section is devoted to the investigation of individual components of the stress integral and their dependence on the atmospheric response function and the topography spectrum function.

#### 5.2.6.1 The Topography Spectrum Function

Very little time was spent trying to characterize the topography spectrum function in terms of the features of the terrain. We decided early in the parameterization that the

TABLE 5.2  
ATMOSPHERES STUDIED

ATMOSPHERE	$P_s$	$T_1$	$T_3$	$U_1$	$U_3$	$V_1$	$V_3$
1	906.4	231	263	29.3	7.88	-0.97	0.82
2	826.0	234	262	33.6	14.80	4.57	-0.69
3	906.4	231	263	29.3	7.96	-0.97	0.82
4	906.4	231	263	29.3	8.27	-0.97	0.82
5	826.0	234	262	33.6	15.00	4.57	-0.69
6	826.0	234	262	33.6	14.60	4.57	-0.69
7	826.0	234	262	33.6	15.50	4.57	-0.69
8	826.0	234	262	33.6	14.10	4.57	-0.69
9	826.0	234	262	33.6	16.30	4.57	-0.69
10	826.0	234	262	33.6	13.30	4.57	-0.69
11	906.4	231	263	33.6	14.80	-0.97	0.82
12	906.4	231	263	29.3	7.88	4.57	-0.69
13	743.8	214	237	-4.95	-2.89	11.47	5.85
14	738.9	239	267	10.95	5.14	13.23	-4.93
15	743.8	239	267	-4.95	-2.89	11.47	5.85

spectrum function could be calculated and stored for the grids on which the wave drag was to be calculated. The two-dimensional spectrum of the real topography is not easily related to features of the terrain.

The topography spectrum function is, by definition,

$$A(k,l) = \frac{4\pi^2}{XY} \hat{h}^*(k,l) \hat{h}(k,l) \quad (5.55)$$

where  $X$  and  $Y$  are the dimensions of the grid and  $h(k,l)$  is the two-dimensional Fourier transform of the topography,

$$\hat{h}(k,l) = \frac{1}{4\pi^2} \int_0^X \int_0^Y h(x,y) e^{i(kx+ly)} dx dy. \quad (5.56)$$

The function  $A(k,l)$  depends strongly on the amplitude of a Fourier component of the topography and will therefore vary over many orders of magnitude. The 5' topography data which we have over North America provides resolution of the topography spectrum to a wavenumber of  $0.3 \text{ km}^{-1}$  in the midlatitudes.

#### 5.2.6.2 The Atmospheric Response Function

From a physical point of view the atmospheric response function represents a measure of the kinetic energy that must be transferred from the mean flow to the vertical at the ground level to propagate one unit of kinetic energy to the level at which the integration of the Scorer equation begins. Resonances in the atmospheric response function will occur when the kinetic energy, transferred into the vertical at the ground level, required to propagate one unit of energy into the stratosphere approaches zero.

The atmospheric response function may be written as

$$F(\kappa, \phi) = \frac{2\sqrt{k^2(H) - \kappa^2}}{w_R^2(0) + w_I^2(0)} \text{sgn}[U_n(H)] \quad , \quad (5.57)$$

where  $W$  is obtained by integrating Scorer's equation through the atmosphere with boundary conditions

$$W_R(H) = W_I(H) = 1 .$$

Equation (5.57) illustrates one of the weaknesses of the model. The atmospheric response is a function of the height at which the integration of the Scorer equation begins. The dependence on the depth of the atmosphere appears explicitly in the numerator of Eq. (5.57). Of greater significance is the dependence of the denominator on the initial height,  $H$ , chosen to begin the numerical integration of the Scorer equation. Typically, the stability is on the order of  $2 \times 10^{-4} \text{ sec}^{-2}$ , and in some layers of the atmosphere, particularly near the ground, the wind speed is on the order of 1 m/sec. The Scorer parameter is then  $2 \times 10^{-4} \text{ m}^{-2}$ , and large variations of  $w(0)$  will then occur when changes in  $z$  on the order of  $(\pi/2)(1.4 \times 10^{-2} \text{ m})$  or approximately 100 m are made. Perhaps because of this and for obvious reasons of computer economy, Bretherton defines a critical layer at points in the atmosphere where the Scorer parameter,  $l^2(z)$ , is greater than  $2.5 \times 10^{-5} \text{ m}^{-2}$ . His integration then begins from this point and no larger values of the Scorer parameter occur in the integration.

To be consistent in our studies we always began the integration at 15 km above sea level. The depth of the atmosphere was then determined by the average height of the terrain.

In addition to those atmospheres listed in Table 5.2, we investigated other atmospheres earlier in the contract period to characterize the behavior of the atmospheric response function. These atmospheres were obtained by making a linear interpolation between the data points taken from National Weather

Service tapes. Results of one of these runs are shown in Figures 5.18 to 5.23. The atmospheric response function was run for 50 values of the wave vector magnitude,  $\kappa$ , and for 19 angles between  $-90^\circ$  and  $90^\circ$  from the direction of the zonal wind. The atmospheric response function is invariant under the transformation from  $(k, l)$  to  $(-k, -l)$ . Critical layers for this atmosphere occurred for angles around  $77^\circ$ . For  $70^\circ \leq \phi \leq 90^\circ$ , the Scorer parameter is much larger than the magnitude of the wave vector and  $F(k, l)$  is virtually independent of  $\kappa$ .

When atmospheric layers exist where  $\lambda^2(z) < \kappa^2$ , energy will be pumped into that mode which propagates to that layer and in phase with the atmospheric response at that layer. The resonances which occur in the continuous spectrum in Figures 10 to 13 are associated with wave vectors such that  $\lambda^2(z) < \kappa^2$  for a segment of the atmosphere. These resonances will not have any effect on the stress calculated with the topography data that is available to us. With 5' resolution the maximum resolvable wavenumber in the topography spectrum is  $0.3 \text{ km}^{-1}$  in the midlatitudes. In the upper atmosphere, where winds of sufficient strength may be present to make the Scorer parameter comparable to  $\kappa^2$ , the stability is typically  $4 \times 10^{-4} \text{ sec}^{-2}$ . The winds required to give a Scorer parameter comparable to our maximum resolvable wavenumber are on the order of 65 m/sec. Without better resolution in the atmospheric variables it is unlikely that the lapse rates or the winds required to have a resonance in the atmospheric response function will be found.

In the absence of these resonances the atmospheric response is nearly independent of  $\kappa$  for a constant  $\phi$ . Over the entire range of  $(\kappa, \phi)$  the atmospheric response changes by less than two orders of magnitude compared to the topography spectrum which may vary over seven orders of magnitude or more. These observations considerably simplify the treatment of the stress integrals and make it possible to neglect many of the terms in the integral of the stress.

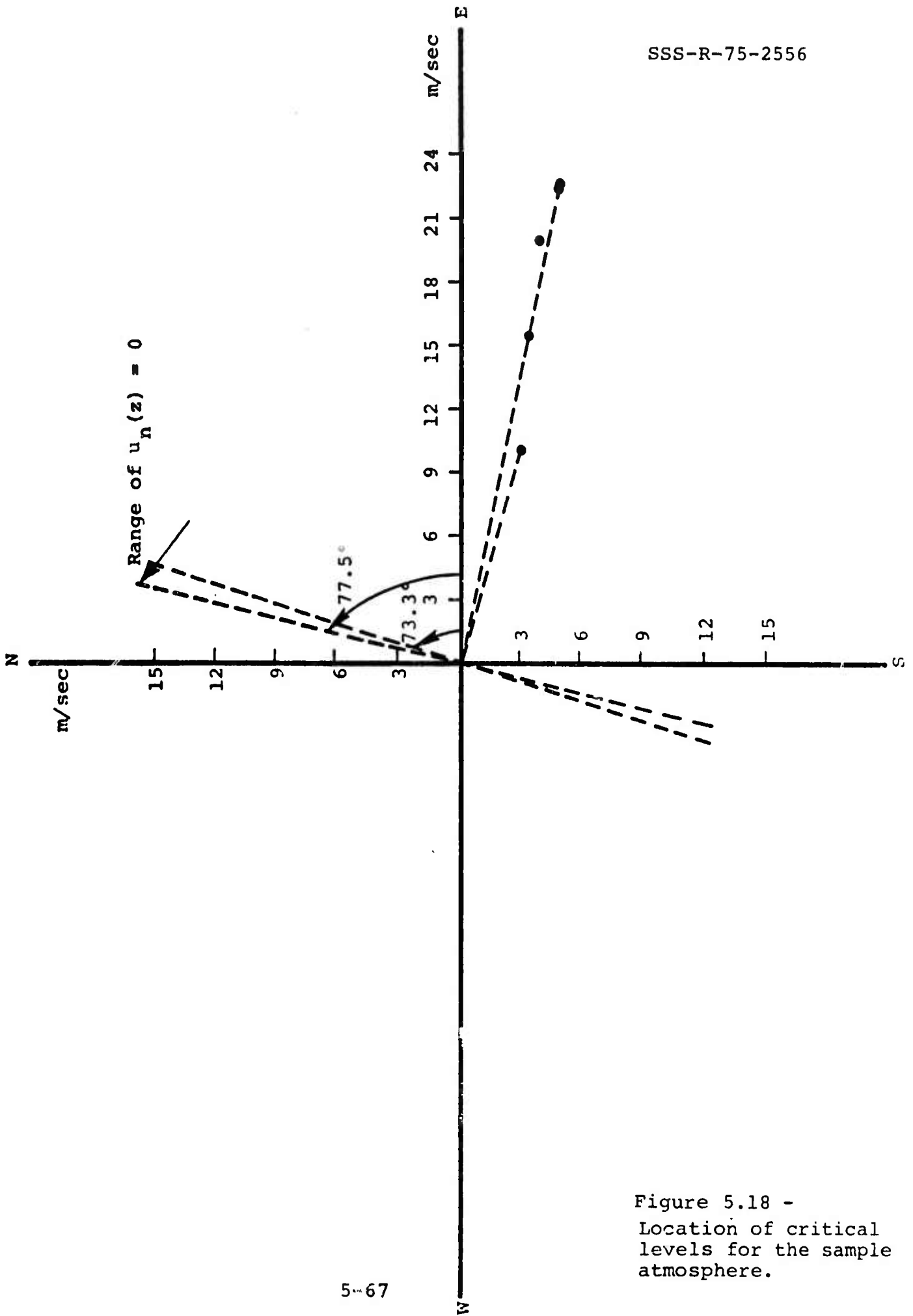


Figure 5.18 -  
Location of critical  
levels for the sample  
atmosphere.

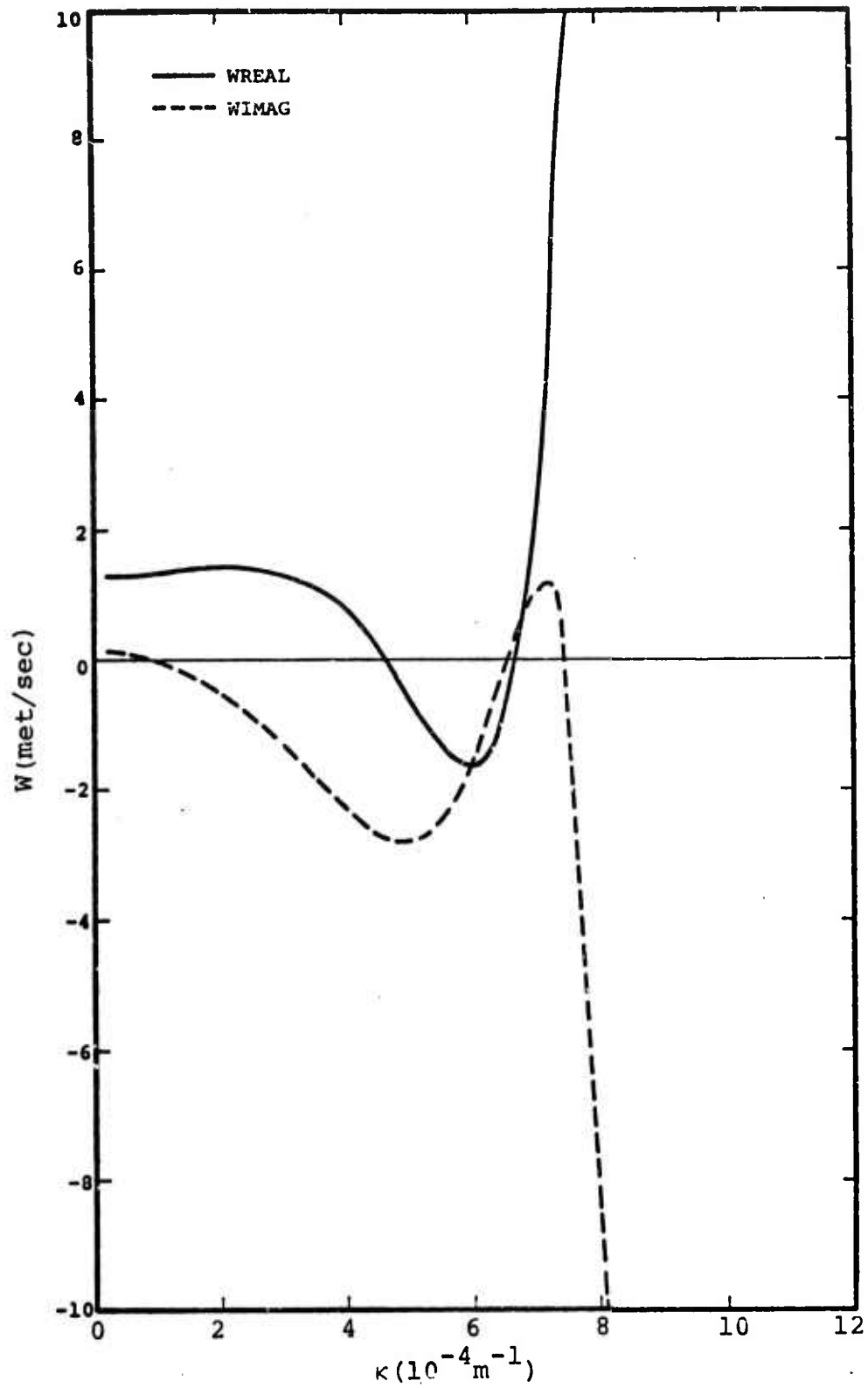


Figure 5.19 - The real and imaginary parts of the ground level wave amplitude for  $\phi = 0$ .

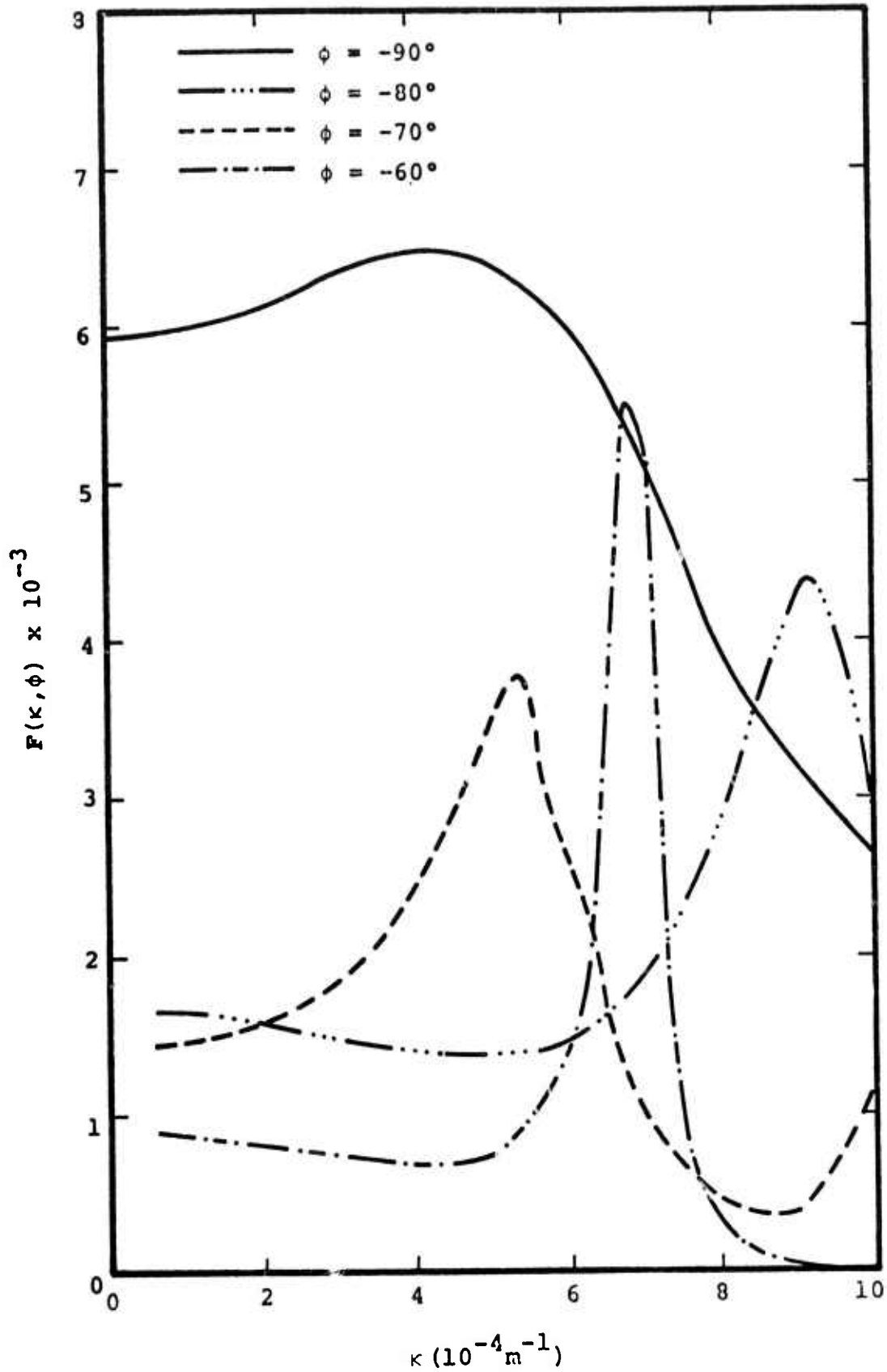


Figure 5.20 - Wavenumber dependence of the atmospheric response function for fixed angles of the wavevector.

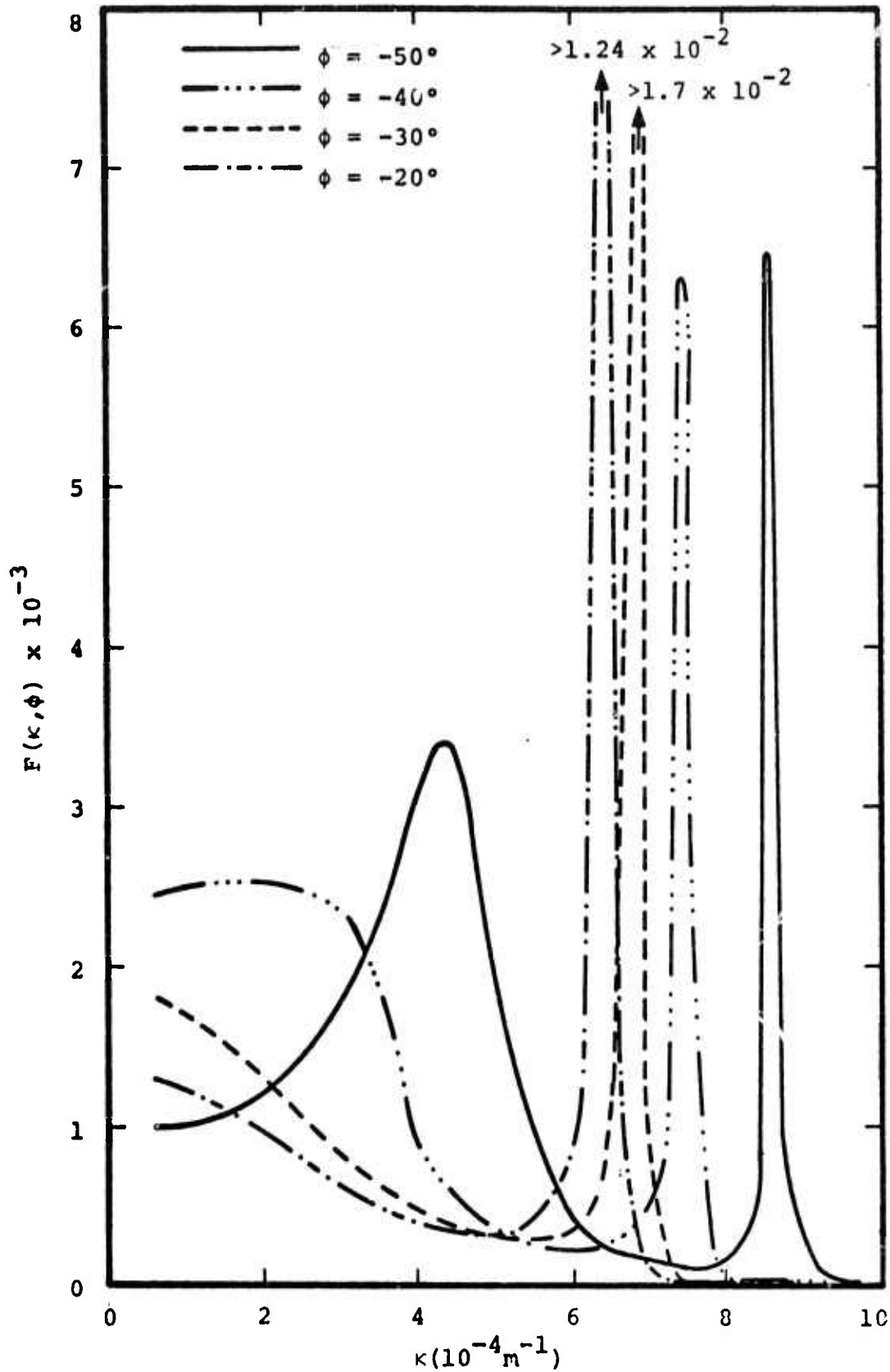


Figure 5.21 - Wavenumber dependence of the atmospheric response function for fixed angles of the wavevector.

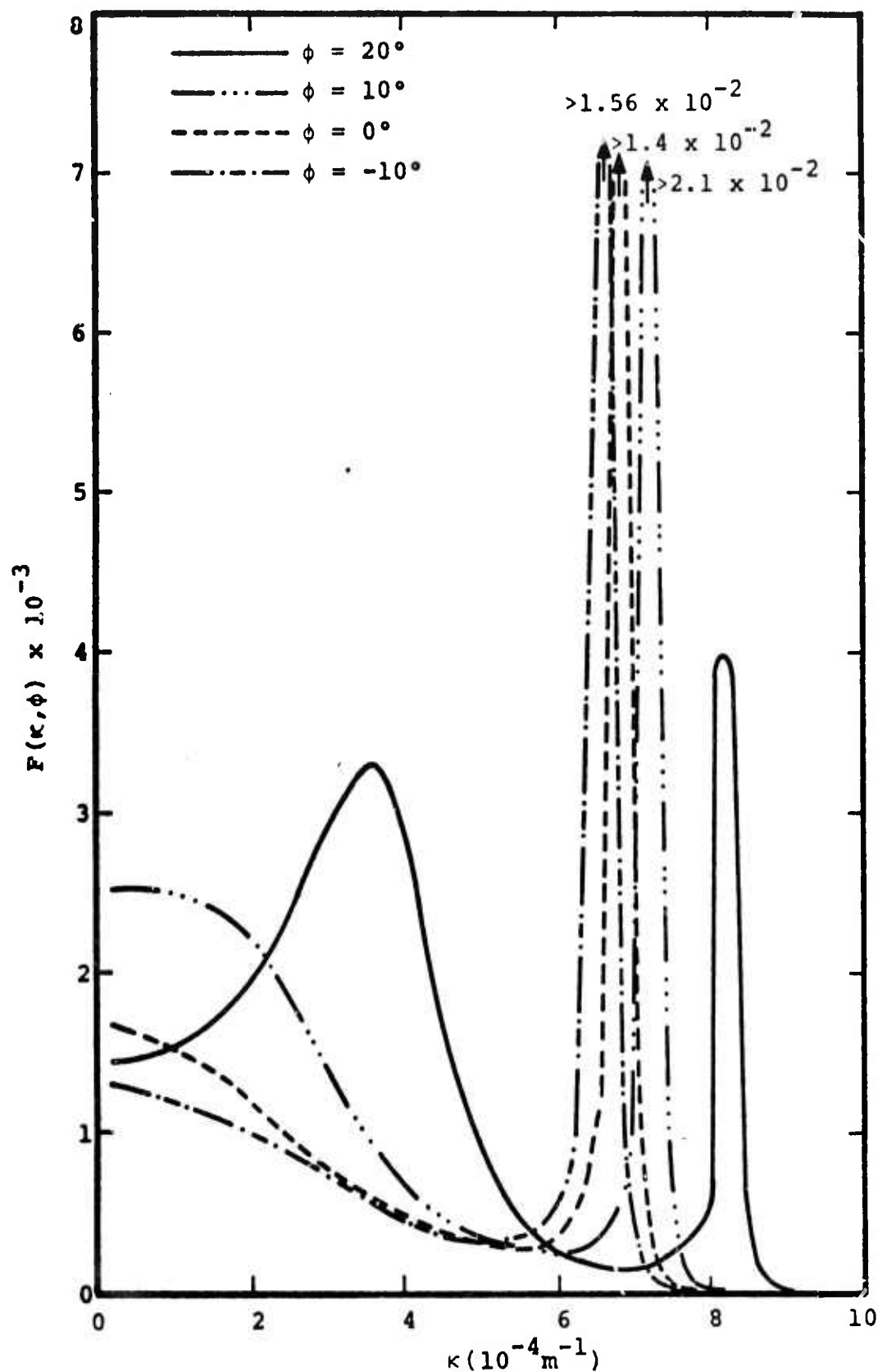


Figure 5.22 - Wavenumber dependence of the atmospheric response function for fixed angles of the wavevector.

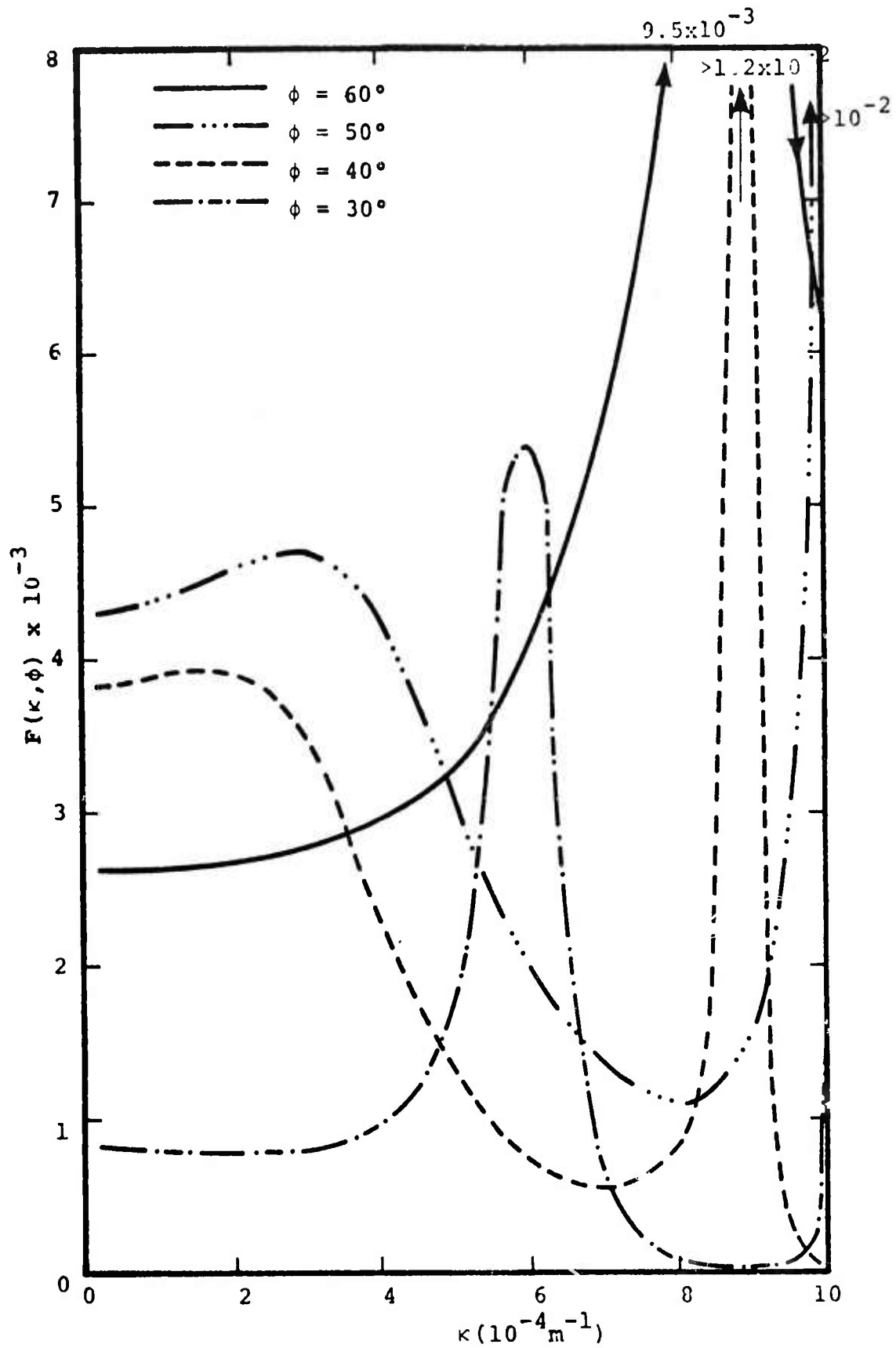


Figure 5.23 - Wavenumber dependence of the atmospheric response function for fixed angles of the wavevector.

Before the beginning of the parameterization of the wave drag it was necessary to reduce the computing time required for the atmospheric response function. At the start of this study the computing time required to calculate the atmospheric response function for the 500 wavenumbers, required to integrate the stress integral, was 1100 seconds. By a judicious optimization of the code and a simplification of the numerical methods involved in the solution of the Scorer equation we reduced the time required to calculate the 500 values of  $F(\kappa, \phi)$  to 20 seconds for our parameterization study. This optimization produced less than a 3% change in the magnitude of the calculated atmospheric response function.

#### 5.2.6.3 Parameterization of the Stress Integral

The code to calculate the two components of the stress was written to perform the integration in horizontal wave number space; the range and resolution of the wave numbers being determined by the resolution of the topography used to calculate the topography spectrum function. The atmospheric response function was calculated at each point that the spectrum function was calculated. The integrals for the two components of the stress are

$$\overline{\rho u w} = 2\rho(0) \int_0^{k_c} \int_{-l_c}^{l_c} U_n^2(0) A(k,l) F(k,l) k \, dk dl \quad (5.58)$$

and

$$\overline{\rho v w} = 2\rho(0) \int_0^{k_c} \int_{-l_c}^{l_c} U_n^2(0) A(k,l) F(k,l) l \, dk dl \quad (5.59)$$

where the limits of integration in wavenumber space are determined by the resolution of the topography.

Our purpose in studying the stress integral was to reduce the number of calculations of the atmospheric response function required to calculate the stress.

A reduction of the time required to solve the Scorer equation will not, by itself, simplify the wave drag calculation to the extent necessary to meet the requirements of the GCM. The actual computing time that can be devoted to the calculation of the wave drag in the GCM will depend upon the persistence of the wave drag and the number of cycles that will not require a recalculation of the drag. We have found that the wave drag is on the order of 6 to 7 dynes/cm<sup>2</sup> on a 4° by 5° grid with the northwest corner located at 121°W 37°N. If an upper limit of 10 dynes/cm<sup>2</sup> is taken and we assume that all of the momentum is taken out of the lower layer of the GCM (typically 3 km in depth) then the change in the wind speed in the lower layer will be on the order of 1 m/sec/hour of application of this stress. The meridional component of the wind velocity is typically 5 to 10 m/sec in the lower layer, hence the wave drag should be recalculated at least every hour in the GCM. Further studies of the persistence of the drag will be performed on the final version of the wave drag subroutine.

The running time for older versions of the GCM is typically 17 min of computer time per day of calculation. If we increase this running time by 5% for the initial parameterization then 2 sec of computing time will be available for each calculation if the calculation is performed once in an hour. Our calculations have shown that the magnitude of the stress will only be significant when large mountains are present in a GCM grid. We have specified the grids that will require a calculation of the wave drag in Figure 5.24. There are on the order of 400 of these grids. With 2 sec of computing time available for each cycle, we can use  $5 \times 10^{-3}$  sec to compute the drag for each grid.

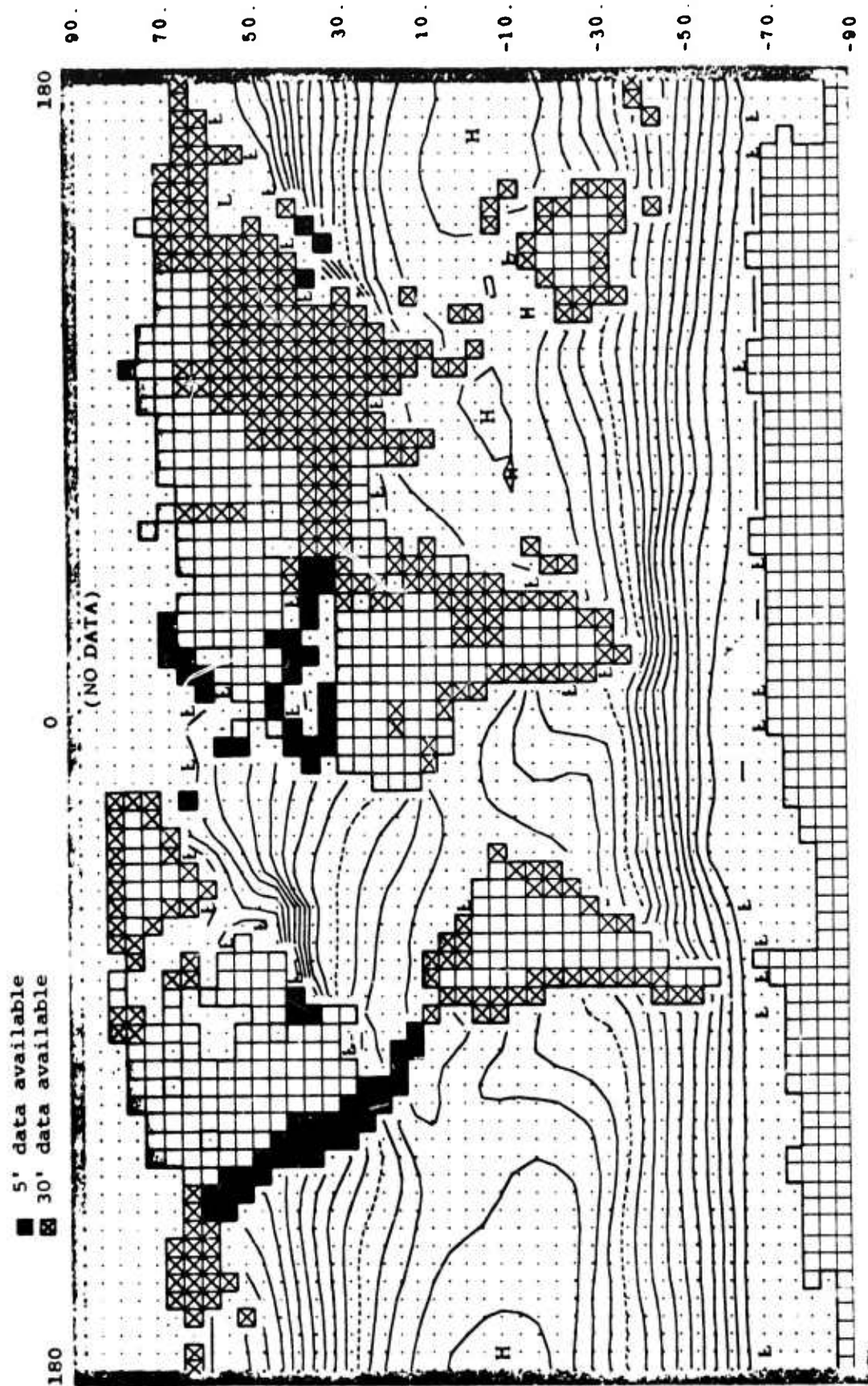


Figure 5.24 - The topography grids containing the mountainous terrain around the world. See text in Section 3 for further clarification of the location of these grids.

To utilize the resolution of our 5' topography data to the fullest on the GCM 4° by 5° grids, a 64 by 64 grid is required (the fast Fourier transform requires the number of grids to be powers of 2). The symmetry properties of the atmospheric response function and the topography spectrum function, which were discussed previously, reduce the number of grids required for the calculation of the stress integrals to 32 by 64. The simplest analytic solution of the Scorer equation is the sinusoidal solution. The sine function and the cosine function require approximately 30  $\mu$ sec of computing time on the UCLA 360/91. In a two-level model approximately 10 calculations of the sine or cosine function are required for each wavenumber component of the stress. Hence, with the simplest analytic model fewer than 16 solutions of the Scorer equation can be obtained for the calculation of the two components of the stress.

The first task that was completed after the development of the stress integral code was to calculate the stress integrals for a series of topography grids. Two atmospheres were chosen from a run of the Rand GCM and the stress was calculated over six topography grids. The two atmospheres are listed as atmospheres 1 and 2 in Table 5.2. The first five topography grids and the last grid listed in Table 1 were involved in the calculation. The component of the drag in the direction of the zonal wind has been illustrated in Figure 5.25 for atmosphere 1. The results of the drag calculation for the other component of the stress and the two components for the other atmosphere are tabulated in Table 5.3. The westernmost grid includes the Coast Range, the San Joaquin Valley and parts of the Sierra Nevada range. It is a grid with extreme variations in height. The next grid includes parts of the Sierra Nevadas and Death Valley. The easternmost edge of TOPO5 is just west of the San Juan Mountains and the Sangre de Cristo Mountains in New Mexico. The grids represented by TOPO4 and

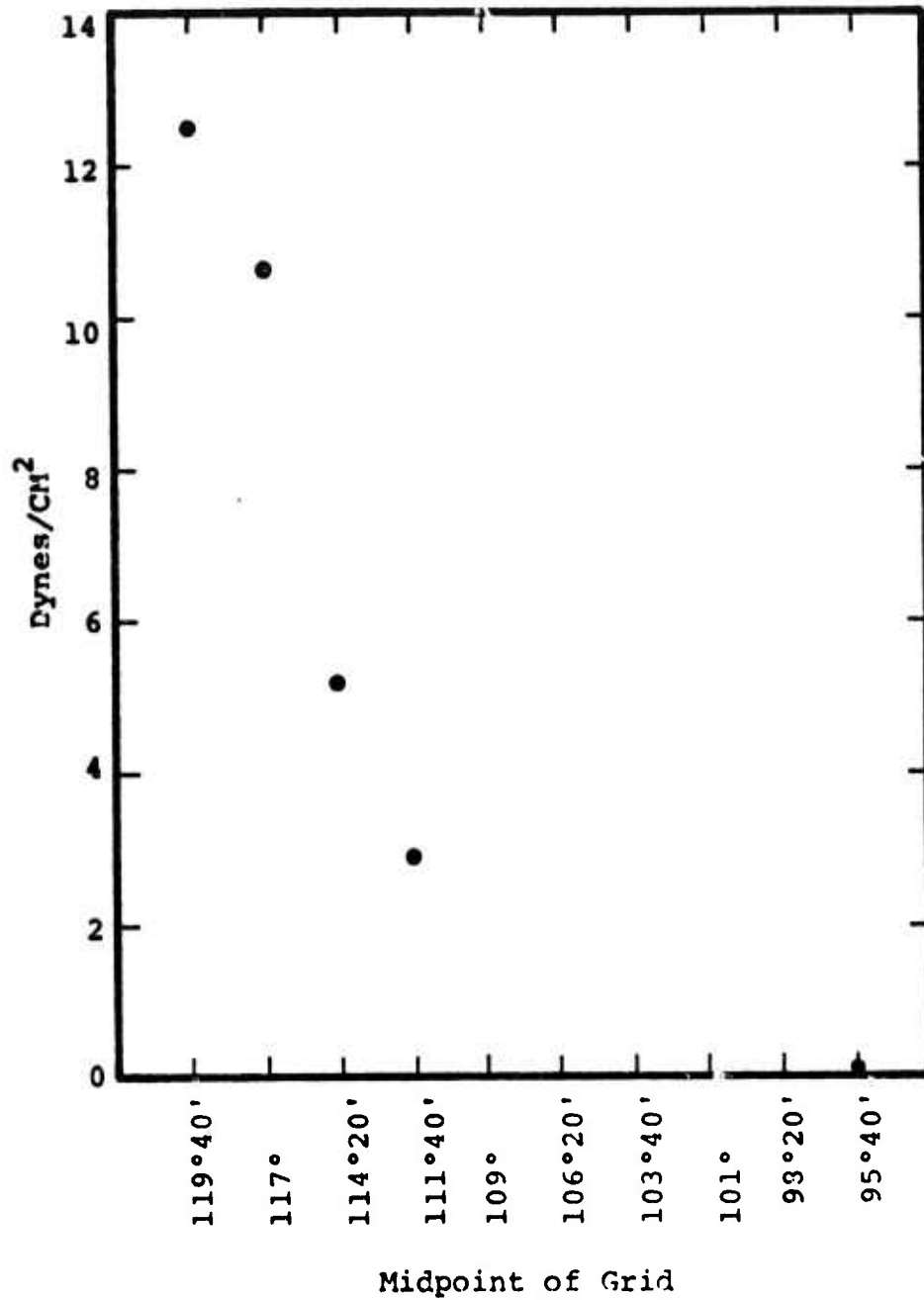


Figure 5.25 - The wavedrag as a function of the topography grid for atmosphere 1.

TABLE 5.3  
THE RESULTS OF THE STRESS PARAMETERIZATION

ATMOSPHERE LOCATION	ZONAL STRESS	MERIDIONAL STRESS	$\rho_{uw}/\rho_{kA}$	$\rho_{vw}/\rho_{l A}$	$\frac{(\rho_{uw})(\rho_{l A})}{(\rho_{vw})(\rho_{kA})}$
<b>Atmosphere 1</b>					
Topography 1	-12.5	4.22	-0.0968	0.0656	-1.48
Topography 2	-10.6	4.13	-0.112		
Topography 3	- 5.18	1.38	-0.0953		
Topography 4	- 2.95	1.52	-0.113		
Topography 5	- 1.40	0.596	-0.11		
<b>Atmosphere 2</b>					
	- 0.061	0.0294	-0.0795	0.039	-2.06
Topography 1	13.96	-5.83	0.107	0.0908	1.18
Topography 2	11.62	-5.59	0.122		
Topography 3	5.77	-3.13	0.106		
Topography 4	2.69	-2.18	0.103		
Topography 5	1.39	-0.92	0.109		
<b>Atmosphere 3</b>					
Topography 1	-12.38	4.15	-0.096	0.0646	-1.48
Topography 2	-10.39	4.17	-0.109		
<b>Atmosphere 4</b>					
Topography 1	-11.50	4.70	-0.089	0.0731	-1.22
Topography 2	- 8.54	3.84	-0.090		
<b>Atmosphere 5</b>					
Topography 1	14.90	-5.28	0.115	-0.082	1.40
<b>Atmosphere 6</b>					
Topography 1	13.37	-5.20	0.103	-0.081	-1.27
<b>Atmosphere 7</b>					
Topography 1	15.74	-5.57	0.121	0.087	1.39
<b>Atmosphere 8</b>					
Topography 1	8.90	-5.08	0.0687	-0.0791	0.87
<b>Atmosphere 9</b>					
Topography 1	15.78	-6.27	0.122	-0.097	-1.26
<b>Atmosphere 10</b>					
Topography 1	- 4.27	-5.30	0.033	-0.082	-0.402

TABLE 5.3, continued

ATMOSPHERE LOCATION	ZONAL STRESS	MERIDIONAL STRESS	$\rho_w/\rho_A$	$\rho_w/\rho 1 A$	$\frac{(\rho_w)(\rho 1 A)}{(\rho_w)(\rho_A)}$
Atmosphere 11 Topography 1	13.35	1.10	0.103	0.017	6.06
Atmosphere 12 Topography 1	-11.12	-2.74	-0.086	-0.043	2.0
Atmosphere 13 Topography 1	7.1	-2.98	0.055	-0.046	1.20
Atmosphere 14 Topography 1	7.73	-0.48	0.060	$-7.4 \times 10^{-3}$	8.1
Atmosphere 15 Topography 1	2.80	-1.37	0.022	-0.021	1.05

TOPO5 are south of the very rugged region of the Rockies in Utah and Colorado. The last grid, TOPO10, contains sections of Arkansas and Oklahoma.

The early runs that were made of the topography spectrum function and atmospheric response function indicated that  $F(k,l)$  was nearly constant compared with the highly varying spectrum function. It was found that the topography spectrum function was large for small wavenumbers and fell off rapidly as the wavenumbers increased. If the spectrum function is localized in wavenumber space then the product  $U_n^2(0) F(k,l)$  should be nearly constant for the wavenumbers which dominate the stress integral. If this is true, then dividing the stress integral in Eq. (5.58) by

$$2\rho(0) \int_0^{k_c} \int_{-1_c}^{1_c} kA(k,l) dkdl \quad (5.60)$$

and the stress integral in Eq. (5.59) by

$$2\rho(0) \int_0^{k_c} \int_{-1_c}^{1_c} |1| A(k,l) dkdl \quad (5.61)$$

should produce a function which is independent of the topography. In Table 5.3 we have tabulated these functions in the fourth and fifth columns. The first two atmospheres, which were run on the five topographies indicate that the ratio of Eq. (5.58) and Eq. (5.60) has an rms deviation about the mean of 7% although the drag varies by an order of magnitude over the five topographies. On TOPO10 the variation is more significant but this can be attributed to the spectrum function being less localized because there are no significant features in the topography.

We had an error in the integration routine for Eq. (5.60) and did not obtain much data on this function for the meridional stress. We suspect that this function will not be as constant for the meridional stress as for the zonal stress because the dominant features of the topography tend to run north-south (with the possible exception of the Himalayas); therefore, the spectrum function on the  $l$ -axis and on off-axis points is not as large as the values of the spectrum function along the  $k$ -axis when large mountains running north-south are in a grid. Some additional work is required to decide how the parameterization of the meridional component of the stress will be treated.

In Table 5.4 we have tabulated the wavenumbers which dominate the stress integral. Most of the zonal component of the stress is contributed by the wavenumbers for which  $l=0$ . In this case  $U_n$  becomes the zonal wind component and  $F(k,l)$  is essentially constant if the Scorer parameter is large.

To simplify the calculation of the stress it would be desirable to store the integral in Eq. (5.59) for each grid and calculate a single value of  $U_n^2 F$  for each atmosphere. In Table 5.5 we have tabulated the calculated value of  $U_n^2 F$  for each of the atmospheres that we have considered for the wavenumber  $(5.21 \times 10^{-5}, 0)$ . We have also formed the product of  $U_n^2 F$  with the integral in Eq. (5.59) and have compared it with the calculated stress. For most of the atmospheres tabulated the ratio of the stress to the product  $U_n^2 F \rho k A$  is between 1.3 and 2.5. Hence, at least for the meridional component of the stress it appears that the wave drag can be calculated to within approximately a factor of two by calculating the atmospheric response function for a single wavenumber.

We have also tabulated, for some of the atmospheres, the momentum flux which is dissipated at critical layers in

TABLE 5.4  
 THE MAGNITUDE OF  $U_n^2$  FOR THE WAVEVECTORS  
 WHICH DOMINATE THE STRESS INTEGRAL  
 (All units are CGS)

a. Atmosphere 5, Topography 1

$(k, l)$	$\xi^2(H)$	$\xi^2(0)$	$U_n^2(0)$	H	$U_n^2 F$	$U_n^2 AFK$
$(2.6 \times 10^{-7}, 2.1 \times 10^{-7})$	$1.03 \times 10^{-10}$	$5.71 \times 10^{-10}$	$2.95 \times 10^5$	$1.34 \times 10^6$	3.87	0.23
$(5.2 \times 10^{-7}, -4.2 \times 10^{-7})$	$1.03 \times 10^{-10}$	$5.71 \times 10^{-10}$	$2.95 \times 10^5$	$1.34 \times 10^6$	3.88	1.19
$(2.6 \times 10^{-7}, 0)$	$5.15 \times 10^{-11}$	$1.11 \times 10^{-7}$	$1.52 \times 10^{-5}$	$1.34 \times 10^6$	8.31	2.56
$(5.2 \times 10^{-7}, 0)$	$5.15 \times 10^{-11}$	$1.11 \times 10^{-7}$	$1.52 \times 10^{-5}$	$1.34 \times 10^6$	8.37	2.71
$(7.8 \times 10^{-7}, 0)$	$5.15 \times 10^{-11}$	$1.11 \times 10^{-7}$	$1.52 \times 10^{-5}$	$1.34 \times 10^6$	8.43	1.77
$(1.0 \times 10^{-6}, 0)$	$5.15 \times 10^{-11}$	$1.11 \times 10^{-7}$	$1.52 \times 10^{-5}$	$1.34 \times 10^6$	8.45	1.43
$(1.3 \times 10^{-6}, 0)$	$5.15 \times 10^{-11}$	$1.11 \times 10^{-7}$	$1.52 \times 10^{-5}$	$1.34 \times 10^6$	8.34	0.84
$(1.6 \times 10^{-6}, 0)$	$5.15 \times 10^{-11}$	$1.11 \times 10^{-7}$	$1.52 \times 10^{-5}$	$1.34 \times 10^6$	7.96	0.39
Total drag in these wavenumbers						
					11.12	

TOTAL WAVE DRAG = 14.9 dynes/cm<sup>2</sup>

TABLE 5.4, continued  
 b. Atmosphere 11, Topography 1

$(k, l)$	$\rho^2(H)$	$\rho^2(0)$	$U_n^2(0)$	H	$U_n^2$	$U_n^2AFK$
$(2.6 \times 10^{-7}, 2.1 \times 10^{-7})$	$7.57 \times 10^{-11}$	$5.6 \times 10^{-9}$	$2.64 \times 10^4$	$1.42 \times 10^6$	2.60	0.80
$(2.6 \times 10^{-7}, 0)$	$4.83 \times 10^{-11}$	$1.14 \times 10^{-9}$	$1.32 \times 10^5$	$1.42 \times 10^6$	7.76	2.39
$(5.2 \times 10^{-7}, 0)$	$4.83 \times 10^{-11}$	$1.14 \times 10^{-9}$	$1.32 \times 10^5$	$1.42 \times 10^6$	7.86	2.55
$(7.8 \times 10^{-7}, 0)$	$4.83 \times 10^{-11}$	$1.14 \times 10^{-9}$	$1.32 \times 10^5$	$1.42 \times 10^6$	7.99	1.68
$(1.0 \times 10^{-6}, 0)$	$4.83 \times 10^{-11}$	$1.14 \times 10^{-9}$	$1.32 \times 10^5$	$1.42 \times 10^6$	8.06	1.36
$(1.3 \times 10^{-6}, 0)$	$4.83 \times 10^{-11}$	$1.14 \times 10^{-9}$	$1.32 \times 10^5$	$1.42 \times 10^6$	7.96	0.80
$(1.6 \times 10^{-6}, 0)$	$4.83 \times 10^{-11}$	$1.14 \times 10^{-9}$	$1.32 \times 10^5$	$1.42 \times 10^6$	7.49	0.37
				Total drag in these wavenumbers		9.95
				TOTAL DRAG = 13.3 dynes/cm <sup>2</sup>		

TABLE 5.4, continued  
 c. Atmosphere 12, Topography 1

$(k, l)$	$\ell^2(H)$	$\ell^2(O)$	$U_n^2(O)$	H	$U_n^2 F$	$U_n^2 AFK$
$(2.6 \times 10^{-7}, 2.1 \times 10^{-7})$	$2.89 \times 10^{-8}$	$7.74 \times 10^{-9}$	$1.90 \times 10^4$	$1.42 \times 10^4$	-3.75	-1.15
$(5.2 \times 10^{-7}, -4.2 \times 10^{-7})$	$2.89 \times 10^{-8}$	$7.74 \times 10^{-9}$	$1.90 \times 10^4$	$1.42 \times 10^4$	-3.75	-0.22
$(2.6 \times 10^{-7}, 0)$	$3.06 \times 10^{-4}$	$6.02 \times 10^{-10}$	$2.39 \times 10^5$	$5.68 \times 10^4$	-4.53	-1.40
$(5.2 \times 10^{-7}, 0)$	$3.06 \times 10^{-4}$	$6.02 \times 10^{-10}$	$2.39 \times 10^5$	$5.68 \times 10^4$	-4.53	-1.47
$(7.8 \times 10^{-7}, 0)$	$3.06 \times 10^{-4}$	$6.02 \times 10^{-10}$	$2.39 \times 10^5$	$5.68 \times 10^4$	-4.53	-0.95
$(1.0 \times 10^{-6}, 0)$	$3.06 \times 10^{-4}$	$6.02 \times 10^{-10}$	$2.39 \times 10^5$	$5.68 \times 10^4$	-4.53	-0.77
$(1.3 \times 10^{-6}, 0)$	$3.06 \times 10^{-4}$	$6.02 \times 10^{-10}$	$2.39 \times 10^5$	$5.68 \times 10^4$	-4.53	-0.46
$(1.6 \times 10^{-6}, 0)$	$3.06 \times 10^{-4}$	$6.02 \times 10^{-10}$	$2.39 \times 10^5$	$5.68 \times 10^4$	-4.53	-0.22
Total drag in these wavenumbers						-6.63
TOTAL DRAG = $11.12 \text{ dynes/cm}^2$						

TABLE 5.5  
ANALYSIS OF TREATING  $U_n^2 F$  TO BE A CONSTANT VALUE

ATMOSPHERE LOCATION	(k,l)	$U_n^2 F(k,l)$	$U_n^2 F(\rho kA)$	$\rho_{uw}$	$\frac{\rho_{uw}}{[U_n^2 F(\rho kA)]}$
( $2.6 \times 10^{-7}$ , $2.1 \times 10^{-7}$ )					
Atmosphere 1		-4.53	- 5.9	-12.54	2.12
Topography 1		-4.53	- 4.3	-10.68	2.48
Topography 2		-4.53	- 2.46	- 5.18	2.10
Topography 3		-4.53	- 1.19	- 2.96	2.48
Topography 4		-4.53	- 0.58	- 1.40	2.41
Topography 5		4.53	- 0.035	- 0.061	1.74
Topography 10					
Atmosphere 2					
Topography 1		7.76	10.1	13.96	1.38
Topography 2		7.76	7.38	11.61	1.57
Topography 3		7.76	4.22	5.77	1.37
Topography 4		7.76	2.04	2.69	1.32
Topography 5		7.76	1.00	1.39	1.39
Atmosphere 3					
Topography 1		-4.55	- 5.91	-12.38	2.10
Topography 2		-4.55	- 4.31	-10.39	2.41
Atmosphere 4					
Topography 1		-3.89	- 5.05	-11.50	2.28
Topography 2		-3.89	- 3.68	- 8.54	2.32
Atmosphere 5					
Topography 1		8.37	11.0	14.9	1.35
Atmosphere 6					
Topography 2		7.00	9.1	13.4	1.47

TABLE 5.5, continued

ATMOSPHERE LOCATION	(k, l)	$U_n^2 F(k, l)$	$U_n^2 \overline{(DkA)}$	$\rho_{uw}$	$\frac{\rho_{uw}}{[U_n^2 \overline{(DkA)}]}$
Atmosphere 7 Topography 1	$(2.6 \times 10^{-7}, 2.1 \times 10^{-7})$	8.81	11.5	15.7	1.37
Atmosphere 8 Topography 1		3.29	4.28	8.90	2.08
Atmosphere 9 Topography 1		8.05	10.5	15.78	1.50
Atmosphere 10 Topography 1		1.10	1.43	- 4.27	2.99
Atmosphere 11 Topography 1		7.86	1.43	- 4.27	2.99
Atmosphere 12 Topography 1		-4.53	10.2	13.35	1.31
Atmosphere 13 Topography 1		2.98	3.87	7.10	1.83
Atmosphere 14 Topography 1		3.87	5.03	7.73	1.54
Atmosphere 15 Topography 1		$9.37 \times 10^{-1}$	1.22	2.80	2.29

the lower layer and that which gets through to the upper layer. These results are given in Table 5.6. One of the difficulties with a two-layer model is deciding where the momentum which propagates into the stratosphere comes from. We are making the assumption that since the momentum flux would not be present in the absence of the mountains that the momentum must be taken from the lower layer. It is obvious that momentum will, in fact, be taken from both layers but it is quite difficult to decide what the contribution is from each layer.

#### 5.2.6.4 Summary of Parameterization Attempts

The above examples show that parameterization of the wavedrag by a simple procedure is not very successful. Errors on the order of 100 percent are routine and, we feel, unacceptable. Other studies were done which showed that substituting equally valid parabolic fits to the two velocity points of the GCM could vary the results by a factor of two as well. There was little sensitivity of the results to varying temperature profiles.

It was therefore decided to avoid the parameterization errors entirely, and use instead a simple analytical solution to Scorer's equation to reduce the computational time. This procedure is described in more detail in Section 5.3.

### 5.3 DRAG - A SUBROUTINE FOR A TWO-LEVEL GLOBAL CIRCULATION MODEL

One of the purposes of the S<sup>3</sup> climatology program was to produce a computer program for use with the RAND Mintz-Arakawa GCM. The development of this subroutine proceeded by making use of the more elaborate time dependent model in the HAIFA code to evaluate the simpler LSS model described

TABLE 5.6  
VERTICAL DISTRIBUTION OF THE MOMENTUM FLUX

ATMOSPHERE LOCATION	$\overline{p_{uw}}UP$	$\overline{p_{wd}}DOWN$	$\overline{p_{wv}}UP$	$\overline{p_{wv}}DOWN$
Atmosphere 1 Topography 1	$1.88 \times 10^{-2}$	-12.1	$1.18 \times 10^{-1}$	3.99
Atmosphere 2 Topography 10	$4.28 \times 10^{-4}$	$-6.13 \times 10^{-2}$	$2.19 \times 10^{-3}$	$2.72 \times 10^{-2}$
Atmosphere 5 Topography 1	15.1	$-2.23 \times 10^{-1}$	-3.0	-2.28
Atmosphere 6 Topography 1	13.63	$-2.58 \times 10^{-1}$	-2.94	-2.36
Atmosphere 7 Topography 1	15.89	$-1.52 \times 10^{-1}$	-3.39	-2.18
Atmosphere 8 Topography 1	9.21	$-3.04 \times 10^{-1}$	-2.64	-2.44
Atmosphere 9 Topography 1	15.92	$-1.35 \times 10^{-1}$	-4.14	-2.13
Atmosphere 10 Topography 1	4.72	$-4.50 \times 10^{-1}$	-2.64	-2.66
Atmosphere 11 Topography 1	13.38	$-2.76 \times 10^{-2}$	$2.63 \times 10^{-1}$	$8.34 \times 10^{-1}$
Atmosphere 12 Topography 1	$1.40 \times 10^{-1}$	-11.26	$-4.6 \times 10^{-1}$	-2.28
Atmosphere 13 Topography 1	7.10	$-2.12 \times 10^{-3}$	-2.97	$-4.68 \times 10^{-3}$
Atmosphere 14 Topography 1	7.65	$8.09 \times 10^{-2}$	$-5.89 \times 10^{-1}$	$1.12 \times 10^{-1}$
Atmosphere 15 Topography 1	2.80	$-1.51 \times 10^{-3}$	-1.36	$-3.31 \times 10^{-3}$

above, and finally, by making additional assumptions consistent with approximations already made in the GCM to simplify the model even further. This resultant code is called DRAG and is the subject of this section. At the risk of repetition of some of the material in other sections of this report, we summarize the Bretherton treatment as well as all the steps necessary to arrive at the final version of the code in order that the present section will essentially stand alone and serve as a User's Guide to the DRAG program.

5.3.1 Wave Drag Contribution to the Atmospheric Momentum Equations

The momentum equation for the earth's atmosphere may be written

$\frac{\partial \rho \bar{V}}{\partial t}$	$+ \nabla \cdot \rho \bar{V} \bar{V}$	$+ \nabla P$	$+ \nabla \cdot \bar{\tau}$	
total rate of change of momentum	rate of change due to convec- tion	rate of change due to pressure gradient	rate of change due to viscous forces	
$- \rho \bar{g}$	$+ \alpha \bar{\Omega} \times \bar{V}$	$= \bar{W} \bar{D}$		(5.59)
rate of change due to gravity	Coriolis force	wind wave drag		

In this equation  $\bar{V}$  corresponds to the wind velocity vector,  $\rho$  is the density, and  $P$  is the pressure. The viscous force term  $\nabla \cdot \bar{\tau}$  includes effects of air-air friction and air-ground friction.

Over mountains, the air flow is characterized by three types of flow shown in Figure 5. The streamlines of the ambient flow are deflected as they flow over the mountains and mountain lee waves are formed. These waves continue far downstream and rise high above the mountains until turbulence and viscous damping forces finally dissipate their energy.

At low altitudes, near the mountains, the flow is turbulent and the simplifying assumptions in the present wave drag treatment are not justified. At altitudes greater than some level indicated by the dashed line in Figure 5.26, however, the flow is smooth, and the present treatment is more applicable.

In the present treatment, the effects of the mountains are felt only through the vertically deflected air. This contribution enters through the term  $\overline{WD}$  in Eq. (5.59) and is the subject of this section.

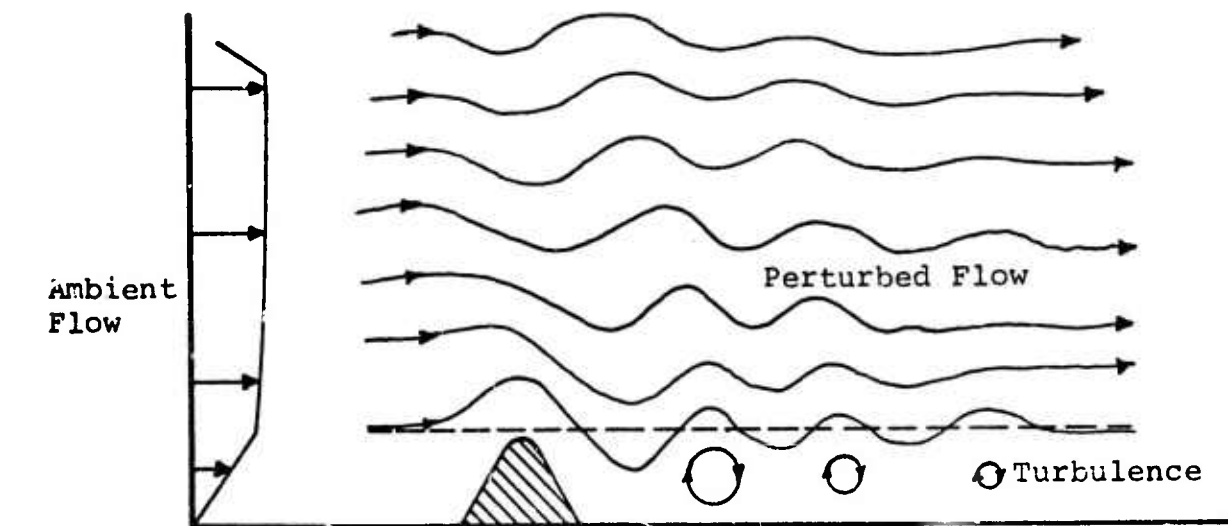


Figure 5.26 - Schematic diagram of mountain wave configuration.

The wave drag treatment described here is based on a linearized, steady-state, Boussinesq, adiabatic, frictionless non-rotating model derived by Eliassen and Palm,<sup>[29]</sup> and implemented by Bretherton<sup>[25]</sup> who also provides theoretical insight into some of the subtleties of the model.

### 5.3.2 Summary of the Bretherton Model

#### 5.3.2.1 Reduction to a Fourier Integral

The wave drag contributions to the horizontal momentum equations are

$$WD_x = - \frac{\partial}{\partial z} \rho u w \quad (5.60)$$

$$WD_y = - \frac{\partial}{\partial z} \rho v w , \quad (5.61)$$

where  $u$  ,  $v$  ,  $w$  are the  $x$  ,  $y$  and  $z$  components of the velocity perturbation due to the mountains. Integrating over the three-dimensional GCM grid cells as shown in Figure 5.27, the contribution to the momentum equations for the air in a particular cell is

$$WD_x = \int dx dy \rho u w \Big|_{z_1}^{z_2} \quad (5.62)$$

$$WD_y = \int dx dy \rho v w \Big|_{z_1}^{z_2} \quad (5.63)$$

These terms represent shear stresses integrated over the bottom and top faces of the cells. The Bretherton treatment calculates the perturbation velocities  $u$  ,  $v$  , and  $w$  appearing in Eqs. (5.62) and (5.63) from a steady state linearized theory.

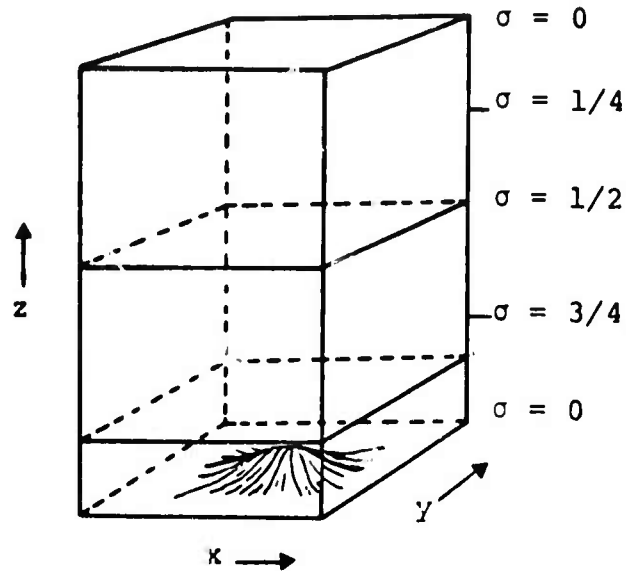


Figure 5.27 - Coordinate system in the 2-level General Circulation Model.

Whereas Bretherton merely states the formulas for  $\overline{wD}$  without derivation, a satisfactory derivation is presented in Section 5.1 of this report. We will not repeat the derivation here, but merely summarize the results:

$$\int dx dy \rho w = \rho(0) \int_{-\infty}^{\infty} \int_{-\infty}^{\infty} U_n^2(0) A(k,l) F(k,l) k dk dl \quad (5.64)$$

$$\int dx dy \rho v w = \rho(0) \int_{-\infty}^{\infty} \int_{-\infty}^{\infty} U_n^2(0) A(k,l) F(k,l) l dk dl \quad (5.65)$$

In these formulas,  $k$  and  $l$  represent wave numbers corresponding to a Fourier decomposition of the topography with respect to surface coordinates  $x$  and  $y$ . The topographical information is wholly contained in the function  $A(k,l)$  and the effects of the atmosphere are contained both in the velocity  $U_n^2(0)$  and the atmospheric response function  $F(k,l)$ .

### Numerical Evaluation of the Integrals

The integrals in Eqs. (5.64) and (5.65) are approximated using the trapezoid rule. An initial simplification may be made by realizing that the integrands, denoted  $I_k$  and  $I_l$  respectively, obey the symmetry properties

$$I_k(k, l) = I_k(-k, -l) \quad (5.66)$$

and

$$I_l(k, l) = I_l(-k, -l) \quad (5.67)$$

Equations (5.64) and (5.65) thus reduce to

$$\int dx dy \rho_{uw} = 2\rho(0) \int_0^\infty dk \int_{-\infty}^\infty dl U_n^2(0) k A(k, l) F(k, l) \quad (5.68)$$

$$\int dx dy \rho_{vw} = 2\rho(0) \int_0^\infty dk \int_{-\infty}^\infty dl U_n^2(0) l A(k, l) F(k, l) \quad (5.69)$$

The trapezoid rule which is used to approximate these integrals makes use of nine points in  $l$ -space and five points in  $k$ -space:

$$WD_x = 2\rho(0) \sum_{i=1}^5 \sum_{j=-4}^4 \Delta k_i \Delta l_j U_n^2(0) A(k_i, l_j) F(k_i, l_j) k_i \Big|_{z_1}^{z_2} \quad (5.70)$$

$$WD_y = 2\rho(0) \sum_{i=1}^5 \sum_{j=-4}^4 \Delta k_i \Delta l_j U_n^2(0) A(k_i, l_j) F(k_i, l_j) l_j \Big|_{z_1}^{z_2} \quad (5.71)$$

where  $\Delta k_i$  and  $\Delta l_j$  are given below.

### 5.3.2.2 Topography Function, A(k,l)

As described above, all of the topography information is contained in the term  $A(k,l)$ .  $A(k,l)$  is defined in terms of the complex function  $h(k,l)$  as follows:

$$A(k,l) = \frac{4\pi^2}{XY} h^*(k,l) h(k,l) , \quad (5.72)$$

where  $h$  is the two-dimensional Fourier transform of the topographical features within the rectangular lower surface of the GCM cell with corners  $(0,Y)$ ,

$$h(k,l) = \frac{1}{4\pi^2} \int_0^X dx \int_0^Y dy h(x,y) e^{-i(kx + ly)} . \quad (5.73)$$

and  $h^*$  is the complex conjugate.  $h(x,y)$  is the altitude of the surface within the rectangle. If  $h(x,y)$  is known at  $N_x$  points in the interval  $[0,X]$  and  $N_y$  points in the interval  $[0,Y]$ , approximately  $N_x \cdot N_y$  cosine/sine amplitudes may be determined for

$$k_m = \frac{2\pi m}{X} , \quad -\frac{N_x}{2} + 1 \leq m \leq \frac{N_x}{2} \quad (5.74)$$

$$l_m = \frac{2\pi m}{Y} , \quad -\frac{N_y}{2} + 1 \leq m \leq \frac{N_y}{2}$$

### Numerical Calculation of the Topography Function A(k,l)

The topography function  $A(k,l)$  is evaluated at 32 points in the interval  $[0,X]$  and  $[0,Y]$  for each GCM grid cell, and from these values, a 32 by 32 array of Fourier amplitudes is calculated for wave numbers

$$k_m = \frac{2\pi m}{X} , \quad -15 \leq m \leq 16 \quad (5.76)$$

$$l_m = \frac{2\pi m}{Y} , \quad -15 \leq m \leq 16 . \quad (5.77)$$

Of these, only the 45 central values are used in the evaluation of the integral, i.e.,

$$k_m = \frac{2\pi m}{X} \quad m = 0, 1, 2, 3, 4 \quad (5.78)$$

$$l_m = \frac{2\pi m}{Y} \quad m = -4, -3, -2, -1, 0, 1, 2, 3, 4 \quad (5.79)$$

The topography data is taken from tapes provided by the Defense Mapping Service which provide the average surface elevation over a meridional square  $0.5^\circ \times 0.5^\circ$ . There are thus  $8 \times 10 = 80$  altitude data points in each  $4^\circ \times 5^\circ$  GCM grid cell. The 80 values are linearly extrapolated and interpolated to provide the  $32 \times 32$  table of  $h(x,y)$  which is then fast Fourier transformed to provide  $h(k,l)$  and subsequently,  $A(k,l)$ . These calculations are performed by an auxiliary code ATABLE which stores the 45 central Fourier components of the topography for each GCM grid cell. These data are then used to perform the drag integrals during the time dependent GCM calculations.

### 5.3.2.3 Atmospheric Response Function

The atmospheric properties are taken into account through two factors in Eqs. (5.64) and (5.65),  $U_n^2(0)$  and  $F(k,l)$ .  $U_n^2(0)$  is the wind at the surface of the earth in the direction determined by  $k$  and  $l$ ,

$$U_n = U \frac{k}{\kappa} + V \frac{l}{\kappa} \quad (5.80)$$

$$\kappa = \sqrt{k^2 + l^2} \quad (5.81)$$

where  $U$  is the easterly component and  $V$  is the northerly component of wind velocity.  $F(k,l)$  contains the atmospheric properties in a more complicated way:

$$F(k, l) = \frac{1}{2i} \left\{ \frac{d\hat{w}}{dz} \hat{w}^*(z) - \frac{d\hat{w}^*}{dz} \hat{w}(z) \right\} / \hat{w}^*(0)\hat{w}(0) . \quad (5.82)$$

$\hat{w}(z)$  in this equation is the x-y Fourier transform of the vertical velocity perturbation which depends on altitude through Scorer's equation:

$$\frac{d^2\hat{w}}{dz^2} + (\ell^2 - \kappa^2) \hat{w} = 0 \quad (5.83)$$

$w(0)$  refers to the solution to this equation at the surface.

Equation (5.83) may be derived from the linearized steady state equations assuming inviscid flow in the Boussinesq approximation. [9,25] The parameter  $\ell$  in this equation is given by

$$\ell^2(z) = \frac{N^2(z)}{U_n^2(z)} - \frac{1}{U_n} \frac{\partial^2 U_n}{\partial z^2} \quad (5.84)$$

where  $N$  is the Brunt-Vaisala frequency,

$$N^2 = - \frac{g}{\bar{\rho}} \frac{d\rho}{dz} = \left( \frac{g}{\bar{T}} \frac{\partial \bar{T}}{\partial z} + \Gamma \right) \quad (5.85)$$

where  $\bar{\rho}$  is the unperturbed density. In the present treatment, the second term in Eq. (5.84) is neglected since the RAND two level GCM code does not have sufficient resolution to evaluate it. If our model were to be used in a GCM calculation with more levels, the second term should be included. It appears to be roughly the same magnitude as the first term for representative wind profiles.

### Solution to Scorer's Equation

Two types of solutions may be obtained for Scorer's equation, Eq. (5.83), depending on the relative magnitude of  $\kappa^2$  and  $l^2$ . For  $\kappa^2 > l^2$ , a discrete spectrum is obtained, and for  $l^2 < \kappa^2$  a continuous spectrum is obtained. Theoretically, both will contribute to the wave drag, but the contribution from the discrete spectrum is usually much smaller (see Section 5.2.1), and in the present treatment has been neglected.

We now develop a general solution to the Scorer equation with which we can consider the boundary conditions. The real and imaginary parts of the vertical velocity,  $\hat{w}_R$  and  $\hat{w}_I$ , each obey the same linear second order equation,

$$\frac{d^2 u}{dz^2} + (l^2 - \kappa^2) u = 0 \quad (5.86)$$

A general solution of this equation contains two coefficients,

$$u = a_1 u_1 + a_2 u_2 \quad (5.87)$$

where  $u_1$  and  $u_2$  are linearly independent. We choose  $u_1$  and  $u_2$  to be solutions of Eq. (5.86) having the following boundary equations,

$$\begin{aligned} u_1(H) = 1 & \quad \left. \frac{du_1}{dz} \right|_{z=H} = 0 \\ u_2(H) = 0 & \quad \left. \frac{du_2}{dz} \right|_{z=H} = 1 \end{aligned} \quad (5.88)$$

Since the case  $\kappa^2 > \ell^2$  is neglected in the present treatment, we will consider only the case of the continuous spectrum,  $\ell^2 > \kappa^2$ . In this case we have the following boundary condition at the upper surface of the grid (Bretherton's<sup>[25]</sup> Eq. 50b),

$$\frac{d\hat{\omega}}{dz} = i \sqrt{\ell^2 - \kappa^2} \text{Sgn}(U_n) \hat{\omega} \quad (5.89)$$

where Sgn means (+1) corresponding to the numerical sign of  $U_n$ . This relation is derived to satisfy the requirement that wave energy can only be transported up out of the calculational grid. This is a reasonable assumption since the wave interaction is totally ignored above the grid. For the real and imaginary parts of the vertical velocity, we have

$$\frac{d\hat{\omega}_R}{dz} = -\sqrt{\ell^2 - \kappa^2} \text{Sgn}(U_n) v_0 \quad (5.90)$$

$$\frac{d\hat{\omega}_I}{dz} = \sqrt{\ell^2 - \kappa^2} \text{Sgn}(U_n) u_0 \quad (5.91)$$

where  $u_0$  and  $v_0$  are values of the vertical velocities at the upper boundary,  $z = H$ :

$$\hat{\omega}(H) = u_0 + iv_0$$

The general solutions satisfying these boundary conditions are

$$\hat{\omega}_R = u_1 u_0 - \sqrt{\ell^2 - \kappa^2} \text{Sgn}(U_n) u_2 v_2 \quad (5.92)$$

$$\hat{\omega}_I = u_1 v_0 + \sqrt{\ell^2 - \kappa^2} \text{Sgn}(U_n) u_2 u_0 \quad (5.93)$$

Returning to Eq. (5.82),

$$F(k, l) = \frac{1}{2i} \left\{ \frac{d\hat{\omega}}{dz} \hat{\omega}^* - \frac{d\hat{\omega}^*}{dz} \hat{\omega} \right\} / \hat{\omega}(0) \hat{\omega}^*(0)$$

we find that the numerator is independent of  $z$  and may be evaluated at  $z=H$ . The denominator is found by substituting from equations (5.92) and (5.93) evaluated at the earth's surface. Thus,

$$F(k, l) = \frac{\sqrt{l^2(H) - \kappa^2} \operatorname{Sgn}(U_n)}{[u_1^2(0) + (l^2(H) - \kappa^2) u_2^2(0)]} \quad (5.94)$$

This expression is independent of the assumed boundary values  $u_0$  and  $v_0$ . Consequently, we have shown that the Reynolds stress does not depend on the chosen values of vertical velocity at the top of the atmosphere. It also follows that for  $l^2 > \kappa^2$ ,

$$\frac{\partial}{\partial z} (\int dx dy \rho u w) = \frac{\partial}{\partial z} (\int dx dy \rho v w) = 0 \quad (5.95)$$

unless  $l^2 \rightarrow \infty$ .

#### Numerical Treatment of the Atmospheric Response Function

The numerical approximations of the atmospheric response function are probably the source of greatest inaccuracy in the present method. These approximations are necessitated by the extremely poor resolution of the GCM in the vertical direction with only two levels.

The problem arises in the integration of Scorer's equation when  $l(z)$  is a strongly varying function of  $z$  through the velocity (see Eq. (3.25)). The assumption is made in the

model that  $\ell(z)$  is constant over each of the two levels. The Scorer equation is then solved for constant  $\ell$  in each level, and the value and first derivative of  $\hat{w}$  is assumed constant across the interface between levels. This assumption is equivalent to assuming a continuous pressure gradient across the interface.

These assumptions lead to the relation

$$\hat{w}^*(0)w(0) = (v_0^2 + u_0^2) \left[ \frac{\Delta_1^2}{\Delta_3^2} + \left(1 - \frac{\Delta_1^2}{\Delta_3^2}\right) \cos^2(\Delta_3 z_{\text{Low}}) \right] \quad (5.96)$$

where

$$\Delta_i = \sqrt{\ell_i^2 - \kappa^2} \quad (5.97)$$

$z_{\text{Low}}$  = thickness of lower layer.

$i = 1, 3$  corresponds to the GCM altitude variable  $\sigma = 1/4, 3/4$ , respectively.

The form for  $F(k,1)$  then becomes

$$F(k,1) = \frac{\Delta_1 \text{Sgn}(U_n)}{\left[ \frac{\Delta_1^2}{\Delta_3^2} + \left(1 - \frac{\Delta_1^2}{\Delta_3^2}\right) \cos^2(\Delta_3 z_{\text{Low}}) \right]} \quad (5.98)$$

### Fast $\cos^2$ Routine

In order to reduce computation time, a subroutine was written to calculate the square of the cosine appearing in the denominator of Eq. (5.98). A method was used which made use of, at most, three terms in the Taylor series expansion of  $\cos^2 x$ , retaining accuracy of 0.7 percent. The program, which contains, at most, five floating point multiplications, is about

6-7 times faster than the conventional cosine routine on the UNIVAC 1108. This simple subroutine is included in the listing in Appendix B.

### Short Wavelength Limit

If  $\Delta_3 z_{\text{Low}}$  is large (many multiples of  $\pi/2$ ) and  $\Delta_1/\Delta_3$  is not close to one, the value of  $F(k,l)$  is very sensitive to  $\Delta_3 z_{\text{Low}}$ . On the other hand,  $z_{\text{Low}}$  is probably not known better than 20 percent, and due to the approximations of constant  $l$ ,  $\Delta_3$  is not known to be better than, say, 30 percent in the GCM. Therefore, if  $\Delta_3 z_{\text{Low}}$  is greater than  $\pi/[2(0.2 + 0.3)] = \pi$ , the correct value of  $\cos^2 \Delta_3 z_{\text{Low}}$  lies anywhere between 0 and 1. We then replace  $F(k,l)$  by its average over the uncertainty range,

$$F^{\text{lim}}(k,l) = \frac{1}{\pi/2} \int_{\Delta_3 z_{\text{Low}} - \pi/4}^{\Delta_3 z_{\text{Low}} + \pi/4} d\theta \frac{\Delta_1 \text{Sgn}(U_n)}{\frac{\Delta_1^2}{\Delta_3^2} + (1 - \frac{\Delta_1^2}{\Delta_3^2}) \cos^2 \theta} \quad (5.99)$$

$$= \Delta_3 \text{Sgn}(U_n)$$

#### 5.3.2.4 Effect of a Critical Level

If the profile of  $U_n$  for a pair of Fourier wave numbers,  $k$  and  $l$  includes a point at which  $U_n \rightarrow 0$ , this point defines a critical level. In the simple two level model used here, where the wind velocity is assumed to be linear with  $z$ , the second term of Eq. (5.84) vanishes and a critical level exists whenever  $U_n(z) \rightarrow 0$ .

Bretherton<sup>[25]</sup> and others offer the following interpretation of a critical level. Above the critical layer the Reynolds stress is extremely small for usual atmospheric conditions. The waves propagating upwards from below are completely absorbed, being neither reflected nor transmitted. On the other hand, if there is no critical level in a three-dimensional cell, the momentum flux entering the cell at the bottom is the same as the momentum flux leaving the top of the cell, so that there is no net momentum change in the cell. The momentum flux flows upward unimpeded until a critical level is reached for that wave component, and at that point the whole effect of the mountain for that wave component is felt. The altitude at which a critical level exists will, in general, be different for each wave number pair, and different components will be absorbed in different layers.

For the uppermost of the two layers shown in Figure 5.27, Eqs. (5.70) and (5.71) give the contribution to each level which does not contain a critical layer for any pair of wave numbers,  $k$  and  $l$ . But, since in this model the stress is independent of altitude, the stress at the top boundary equals the stress at the bottom, and

$$WD_x = WD_y = 0 .$$

If, however, a critical layer occurs anywhere within the upper cell for wave numbers  $k_c, l_c$ , the Reynolds stress for those wave numbers on the top cell boundary is zero, i.e., the effects of the mountains for those wavenumbers are all absorbed at the critical layer. Thus,

$$WD_x(k_c, l_c) = -WD_x(k_c, l_c) \Big|_{z_1} \quad (5.100)$$

$$WD_y(k_c, l_c) = -WD_y(k_c, l_c) \Big|_{z_2} \quad (5.101)$$

Furthermore, for the layer nearest the ground, the lower boundary momentum flux is zero, and the model gives the stress within the lowest layer above the mountain, i.e., across the dotted line in Figure 5.26. The net results of these considerations are the following:

- (a) For  $k, l, U_n$  such that there is no critical layer in either level, the momentum is removed from the lower level, passes through the upper level without interaction, and escapes from the top of the grid.
- (b) For  $k, l, U_n$  such that a critical level appears in the upper level, momentum is removed from the lower level, and deposited in the upper level.
- (c) For  $k, l, U_n$  such that a critical level appears in the lower level, there is no momentum change in either upper or lower levels.

### 5.3.3 The DRAG Subroutines

There are actually two subroutines used in the RAND GCM to compute the drag contributions. The first subroutine, DRGSET is called only once in each GCM run to calculate and store certain time independent parameters. These variables include various

trigonometric functions utilized in the Fourier space integration, and transfers the topography information from a permanent memory file to core for access during the time dependent calculation.

The second subroutine, WDRAG, is called either every cycle or every  $n^{\text{th}}$  cycle of the time dependent calculation since the atmospheric response function and wind velocity are time dependent. Currently, the wave drag terms are calculated explicitly using "old" values of the atmospheric parameters, although with little modification they could be calculated implicitly in order to avoid numerical instabilities.

The subroutines are listed in Appendix B.

#### 5.3.4 Representative Calculations

Several calculations were performed using the model for various geographic locations and several wind conditions, and the results compared with other models when possible. We present here results from four calculations of wind drag for flow over the Sierra Nevada and Himalayan mountains. (See Table 5.8.)

In these calculations the temperature was given at two altitudes (pressures) and interpolated or extrapolated adiabatically for other altitudes. Results are shown in Table 5.7.

TABLE 5.7  
TEMPERATURE DEPENDENCE ON PRESSURE FOR THE TEST PROBLEMS

$p = 400\text{mb}$	$\sigma = 1/4$	$T = 231^\circ\text{k}$
$p = 800\text{mb}$	$\sigma = 3/4$	$T = 263^\circ\text{k}$

The calculated quantities are the easterly and northerly momentum flux removed from the lower GCM level. In the particular

TABLE 5.8

CALCULATED WAVEDRAG FOR FOUR WIND CONDITIONS OVER THE SIERRA NEVADA AND HIMALAYAN MOUNTAINS USING THE DRAG SUBROUTINES

	Ambient Pressure (mb)	Easterly Wind Velocity (m/sec)	Northerly Wind Velocity (m/sec)	Easterly Flux Removed from Lower Level (dynes/cm <sup>2</sup> )	Northerly Flux Removed from Lower Level (dynes/cm <sup>2</sup> )
Case 1 Sierra Nevada	400*	33.6	- .97 } .82 } 1.71 }	1.07	.460
	800*	14.8			
	surface *	5.4			
Case 2 Sierra Nevada	400	29.3	- .97 } .82 } 1.71 }	2.37	.880
	800	15.0			
	surface	7.8			
Case 3 Himalayans	400	29.3	- .97 } .82 } 1.71 }	1.38	2.02
	800	15.0			
	surface	7.8			
Case 4 Himalayans	400	10.0	30.0 } 16.0 } 9.0 }	.298	12.1
	800	5.2			
	surface	2.5			

SSS-R-75-2556

\* These pressures correspond to altitudes at  $\sigma = 1/4, 3/4,$  and  $1$  respectively.

test calculations presented here, a critical layer did not appear in the upper level, and, therefore, the net flux loss from the top level is zero.

Cases 1 and 2 were problems run on the Sierra Nevada topography, the  $4^\circ \times 5^\circ$  rectangle, with the northwest corner at  $38^\circ$  latitude and  $240^\circ$  longitude. It includes the highest peak in the Sierra Nevadas, as well as Owens Valley, so that it may be compared with the results presented in Section 5.2. There the drag was calculated to be  $15 \text{ dynes/cm}^2$  for a surface velocity of  $\approx 20 \text{ m/sec}$ . Comparing results for Cases 1 and 2, it is evident that the magnitude of the drag is approximately proportional to the square of the surface wind velocity. (This is not surprising given the dependence of  $U_n^2(0)$  in the integrands of equations (3.64) and (3.65).) Scaling the Case 1 or Case 2 results by the square of the surface velocity, we obtain  $\approx 18 \text{ dynes/cm}^2$  to be compared with the value of  $15 \text{ dynes/cm}^2$  calculated by the more accurate LSS program.

The Sierra Nevada mountains are essentially north-south, while the Himalayas (Case 3 and Case 4) are essentially east-west. The difference in drag calculated in Cases 3 and 4, with different direction of wind flow, indicate the strong dependence on the topographical anisotropy.

Timing runs were also made to determine the speed of the subroutine package. The time (on the UCLA IBM 360/91) was 40 ms for 500 spatial cells, or 80  $\mu\text{s}$  for each spatial cell.

## 6. A THREE-DIMENSIONAL BOUSSINESQ CODE 'STUFF'

During this project, a three-dimensional Boussinesq code to treat the low-speed laminar and turbulent motion of stratified fluids has been developed. The numerical technique used is unique and was developed using funds from this contract as well as independent research and development funds provided by S<sup>3</sup>. The code was initially written in two dimensions since several new concepts were involved and has since been extended to three dimensions. The code's name, STUFF, is an acronym for Stratified Turbulent Unsteady Fluid Flow.

The principal difficulty involved in treating flows of this sort in the past has been that purely Eulerian finite difference procedures are diffusive in character. That is, diffusion-like errors in the finite-difference representation of the advection terms of the fundamental field equations will artificially "smear" the distribution of the field variables (i.e., density). Lagrangian procedures, on the other hand, avoid this difficulty but cannot treat flows in which high-amplitude waves or vortices occur such as those present in mountain lee wave phenomena since a Lagrangian grid will become so distorted that the finite difference approximations referred to such a grid will become meaningless.

The S<sup>3</sup> procedure avoids these difficulties by using both an Eulerian grid and an array of Lagrangian particles superimposed upon that grid which moves along with the fluid

as the calculation proceeds. All scalar field variables (density, turbulent energy, thermal energy) are carried by the Lagrangian marker particles as well as by the Eulerian grid. At late times, the Lagrangian net will become distorted just as in the purely Lagrangian case. Such distortion does not adversely affect the calculation, however, since all space derivatives of scalar field variables are determined using the Eulerian grid; the Eulerian values are determined by a "census" procedure which essentially sets the value of each scalar field variable within a Eulerian zone to the average of the values carried by the Lagrangian particles within the zone. On the other hand, the "artificial diffusion" which is characteristic of pure Eulerian schemes is absent, since advection effects are treated by moving the particles in a Lagrangian fashion.

In this chapter, the STUFF computer model, as presently developed at S<sup>3</sup>, is outlined in detail. The equations, boundary and initial conditions, and results of sample calculations are presented.

Also included are two calculations of a viscous internal wave decay problem which demonstrates the numerical diffusion associated with one Eulerian treatment of scalar advection transport (relative to the Eulerian/Lagrangian method in STUFF).

## 6.1 DERIVATION OF EQUATIONS

The equations in the Boussinesq approximation which express the conservation of mass, momentum and energy within the fluid system in the STUFF code are:

Mass

$$\frac{\partial}{\partial x_j} (U'_j) = 0 \quad (6.1)$$

Momentum

$$\begin{aligned} \frac{\partial}{\partial t} (U'_i) + \frac{\partial}{\partial x_j} (U'_i U'_j) &= \frac{\partial}{\partial x_j} \left[ \nu \frac{\partial}{\partial x_j} (U'_i) \right] - \frac{\partial \phi'}{\partial x_i} \\ &+ Qg_i + S \end{aligned} \quad (6.2)$$

Energy

$$\frac{\partial Q}{\partial t} + \frac{\partial}{\partial x_j} (U'_j Q) = \frac{\partial}{\partial x_j} \left[ D \frac{\partial}{\partial x_j} (Q) \right] + \pi_Q \quad (6.3)$$

where

$U'_1, U'_2, U'_3$  = components of velocity in  $x_1, x_2, x_3$  directions,

$S$  = momentum source ,

$Q$  = Boussinesq parameter =  $(\rho/\rho_0 - 1) = -\beta(T - T_0)$  ,

$\beta$  = volumetric expansion coefficient ,

$\rho$  = density ,

$g_i$  = gravity acceleration component in  $x_i$  direction

$\pi_Q$  = energy source term ,

$\nu$  = molecular kinematical viscosity ,

$D$  = molecular diffusion coefficient ,

and

$\phi'$  = the departure of the atmospheric pressure from the hydrostatic pressure divided by the reference density.

The turbulence scheme of Gawain and Pritchett<sup>[19]</sup> used previously in the HAIFA code, is an integral part of the computer model and will be reiterated here in some detail for completeness. However, it should be noted that alternative schemes based on a mixing length theory could be used. Additionally, the present model allows a prescribed set of diffusion coefficients at any space points in the numerical grid.

The derivation of the equations including the turbulence scheme is shown below. Only the momentum and mass equations are discussed in detail; the energy equation follows directly with  $D$  being redefined to include both the molecular and turbulent diffusion coefficient. As previously noted (see Section 3.5), the development of the turbulent energy equation as described by Gawain and Pritchett neglects the temperature stratification term  $-\overline{\rho' u_i'} \frac{g}{\rho_0}$  which can have a significant effect on the results of the problems associated with our studies. The investigation of a heuristic model for this term has not yet been carried out at  $S^3$  and a formulation must be developed to describe its relation to the mean flow and temperature fields. This term has been included in the final equations, however, by assuming that the thermal eddy diffusivity  $E'$  can be used to relate this buoyancy term to the mean temperature field and that  $\epsilon'$  is equal to  $\epsilon$ , the momentum eddy diffusivity.

Using a standard procedure, we define the  $U'$ ,  $\phi'$ , and  $\rho'$  fields as the sums of mean and fluctuating components

$$U'_i = U_i + u_i \quad ,$$

$$\phi' = \Phi + \phi$$

and

$$\rho' = \rho_0 + \rho \quad .$$

Now performing ensemble averaging, we obtain the conservation equations for the mean flow:

Mean Flow Continuity

$$\frac{\partial}{\partial x_j} (U_j) = 0$$

and

Mean Flow Momentum

$$\frac{\partial}{\partial t} (U_i) + \frac{\partial}{\partial x_j} (U_i U_j) = \frac{\partial}{\partial x_j} \left\{ \nu \left( \frac{\partial U_i}{\partial x_j} + \frac{\partial U_j}{\partial x_i} \right) - \overline{u_i u_j} \right\} - \frac{\partial \phi}{\partial x_i} + Qg_i + S \quad .$$

If it were not for the Reynolds stress term appearing in the momentum equation, the solution would be straightforward. The stress term can, however, be related heuristically to the strain rates of the mean flow through an eddy viscosity  $\epsilon$  via the relation:

$$\overline{u_i u_j} = -\frac{1}{3} \overline{u_k u_k} \delta_{ij} + \epsilon \left( \frac{\partial U_i}{\partial x_j} + \frac{\partial U_j}{\partial x_i} \right) \quad (6.4)$$

or more simply

$$-\overline{u_i u_j} = -\frac{1}{3} \overline{u_k u_k} \delta_{ij} + \epsilon \Gamma_{ij} \quad (6.5)$$

where

$$\Gamma_{ij} = \frac{\partial U_i}{\partial x_j} + \frac{\partial U_j}{\partial x_i}$$

is the strain rate tensor. With this relation we may now rewrite the mean flow momentum equation as:

$$\frac{\partial}{\partial t} (U_i) + \frac{\partial}{\partial x_j} (U_i U_j) = \frac{\partial}{\partial x_j} \left[ (\nu + \epsilon) \Gamma_{ij} \right] - \frac{\partial P}{\partial x_i} + Qg_i + S \quad (6.6)$$

where

$$P = \phi + \frac{2}{3} \frac{\overline{u_j u_j}}{2} .$$

It now remains to determine the functional form of  $\epsilon$ . Since we are about to postulate a functional dependence of  $\epsilon$  on the local turbulent kinetic energy, we will now include the turbulent energy equation in our equation set.

We return to the conservation equations and obtain an expression of the following form:

$$\begin{aligned}
\frac{\partial}{\partial t} (E) + \frac{\partial}{\partial x_k} (U_k E) &= - \frac{\overline{u_j u_k}}{2} \left( \frac{\partial U_j}{\partial x_k} + \frac{\partial U_k}{\partial x_j} \right) \\
&\quad - \frac{\nu}{2} \overline{\left( \frac{\partial u_j}{\partial x_k} + \frac{\partial u_k}{\partial x_j} \right) \left( \frac{\partial u_j}{\partial x_k} + \frac{\partial u_k}{\partial x_j} \right)} \\
&\quad - \frac{\partial}{\partial x_k} \left[ \overline{u_k (E + \phi)} \right] + \overline{\rho u_j} \frac{g_j}{\rho_0} \\
&\quad + \nu \frac{\partial}{\partial x_k} \left[ \frac{\partial}{\partial x_k} (E) + \frac{\partial}{\partial x_j} (\overline{u_j u_k}) \right] \quad (6.7)
\end{aligned}$$

where

$$E = \frac{\overline{u_j u_j}}{2} .$$

The terms on the right represent work done by the mean flow against the Reynold's stresses, dissipation as heat, ( $\dot{E}_H$ ), the effects of fluid stratification on turbulent energy dissipation, turbulent diffusion ( $\dot{E}_D$ ), and molecular diffusion. Henceforth, the molecular diffusion term will be assumed negligible as compared to the other terms. Using the relation coupling strain rates to stress we have:

$$\begin{aligned}
\frac{\partial}{\partial t} (E) + \frac{\partial}{\partial x_k} (U_k E) &= \frac{\epsilon}{2} \Gamma_{jk} \Gamma_{jk} \\
&\quad - \frac{\nu}{2} \overline{\left( \frac{\partial u_j}{\partial x_k} + \frac{\partial u_k}{\partial x_j} \right) \left( \frac{\partial u_j}{\partial x_k} + \frac{\partial u_k}{\partial x_j} \right)} + \overline{\rho u_j} \frac{g_j}{\rho_0} \\
&\quad - \frac{\partial}{\partial x_k} \left[ \overline{u_k (E + \phi)} \right] \quad (6.8)
\end{aligned}$$

At this point in time it is appropriate to examine the approach to be taken in solving the equation set. The attempt will be made to derive empirical expressions for the dissipative and remaining diffusive term in the turbulent energy equation. Once this has been accomplished, the local eddy viscosity will then be postulated as functionally dependent at the least on the local turbulent energy.

The diffusive term is relatively simple to approximate with a heuristic substitute. Gawain and Pritchett, basing their arguments on dimensional and physical grounds, derive the following expression:

$$u_k \frac{\overline{u_j u_j}}{2} + \phi = -\gamma \epsilon \frac{\partial E}{\partial x_k} \quad (6.9)$$

so that the diffusion term in the turbulent energy equation becomes

$$E_D = \frac{\partial}{\partial x_k} \left( \gamma E \frac{\partial E}{\partial x_k} \right)$$

where  $\gamma$  in this case is a slowly varying function whose form is empirically derived from past experiments. An explicit expression of  $\gamma$  will be given later. In a similar manner, the buoyancy term  $\overline{\rho u_j} \frac{g_i}{\rho_0}$  is set equal to  $-\gamma E' \frac{\partial Q}{\partial x_j}$ .

In order to develop expressions for turbulent Reynolds stresses, eddy viscosities, and dissipation rates, it is necessary to establish a "macro-scale" associated with the motion. Utilizing the fact that the flow characteristics at a point are influenced principally by the field immediately surrounding the point, Gawain and Pritchett have derived a heuristic formulation for the macro-scale of the following form:

$$\lambda^2(\vec{x}) = I^2(\vec{x})/J^2(\vec{x})$$

$$I^2(\vec{x}) = \int_{\text{All Space}} w(\vec{x}, \vec{x}') \Omega^4(\vec{x}') dv'$$

$$J^2(\vec{x}) = \int_{\text{All Space}} w(\vec{x}, \vec{x}') \left[ \Omega \Omega'(\vec{x}') \right]^2 dv'$$

$$w(\vec{x}, \vec{x}') = \frac{\exp \left[ - \frac{(\vec{x} - \vec{x}') \cdot (\vec{x} - \vec{x}')}{\lambda^2(\vec{x})} \right]}{\int_{\text{All Space}} \exp \left[ - \frac{(\vec{x} - \vec{x}') \cdot (\vec{x} - \vec{x}')}{\lambda^2(\vec{x})} \right] dv'}$$

$$\Omega^2 = \frac{1}{2} \Gamma_{ij} \Gamma_{ij}$$

$$(\Omega')^2 = (\partial \Omega / \partial x_i) (\partial \Omega / \partial x_i) \quad . \quad (6.10)$$

Note that  $\lambda$  must be solved for in an iterative fashion, since it appears on both sides of the equation. The Gawain Pritchett scheme models turbulent energy dissipation to heat by:

$$\dot{E}_H = \beta (2E)^{7/6} J^{1/3} \quad ; \quad (6.11)$$

$\beta$  is similar to  $\gamma$ , and will be defined later.

We now need only to obtain an expression for  $\epsilon$  and we will achieve a practical closure. One would expect that the eddy viscosity at a space time point would be somehow related to the local turbulent energy density. Also, it should depend on the macroscale at that point. An appropriate dimensional combination of these quantities is

$$\epsilon = \alpha \lambda (2E)^{1/2} \quad . \quad (6.12)$$

This is the final relation needed to effect closure.  $\alpha$ ,  $\beta$ , and  $\gamma$  are now defined as slowly varying functions which have been determined from experiments and are expressed as follows:

$$\begin{aligned} \alpha &= 0.065 \left\{ 1 + \exp \left[ - \left( \frac{y}{\lambda} - 1 \right)^2 \right] \right\} \\ \frac{1}{\beta} &= 3.7 \left\{ 1 + \exp \left[ - \left( \frac{y}{\lambda} - 1 \right)^2 \right] \right\} \\ \gamma &= 1.4 - 0.4 \exp \left[ - \left( \frac{y}{\lambda} - 1 \right)^2 \right] \end{aligned} \quad (6.13)$$

where  $y$  is the distance to the nearest physical boundary from the space grid point and where  $y/\lambda$  is never permitted to exceed unity.

The final hydrodynamic equations including the assumption that the thermal eddy diffusivities are equal to the momentum eddy diffusivities are:

$$\frac{\partial}{\partial x_i} (U_i) = 0 \quad (6.14)$$

$$\begin{aligned} \frac{\partial}{\partial t} (U_i) + \frac{\partial}{\partial x_j} (U_i U_j) &= \frac{\partial}{\partial x_j} \left[ (v + \alpha \lambda \sqrt{2E}) \left( \frac{\partial U_i}{\partial x_j} + \frac{\partial U_j}{\partial x_i} \right) \right] - \frac{\partial P}{\partial x_i} \\ &+ Qg_i + S \end{aligned} \quad (6.15)$$

$$\frac{\partial}{\partial t} (Q) + \frac{\partial}{\partial x_j} (U_j Q) = \frac{\partial}{\partial x_j} \left[ (\alpha \lambda \gamma \sqrt{2E} + D) \frac{\partial Q}{\partial x_j} \right] + \pi_Q \quad (6.16)$$

$$\begin{aligned} \frac{\partial}{\partial t} (E) + \frac{\partial}{\partial x_j} (U_j E) &= \alpha \lambda \sqrt{2E} \Omega^{2-\beta} (2E)^{7/6} J^{1/3} \\ &+ \frac{\partial}{\partial x_j} \left( \alpha \gamma \lambda \sqrt{2E} \frac{\partial E}{\partial x_j} \right) \\ &- \alpha \gamma \lambda \sqrt{2E} g_j \frac{\partial Q}{\partial x_j} \end{aligned} \quad (6.17)$$

In effect, Gawain and Pritchett's equations have been modified to include a buoyancy term in the momentum equation in the vertical direction, and the effects of fluid stratification on turbulent energy dissipation.

Note that the total energy equation carried through the derivation results in a final equation which is identical to Equation (6.3) with  $D$  being redefined to include both the molecular and turbulent diffusion coefficient.

The source/sink terms in the equations may be used to include the effects of radiation losses, and surface friction losses. In each case, the terms would be included using a prescription obtained from the literature.

### 6.1.1 The Numerical Scheme

In this section, the 2-D procedure used will be discussed; the 3-D extension is straightforward. The treatment of the momentum Equation (6.2) is explicit and second-order in space. Time derivatives may be specified as either first or second order by the user. The direct calculation of the pressure is avoided by the method of Chorin.<sup>[34]</sup> In this

method, "tentative" new velocities  $(\tilde{u}^{n+1}, \tilde{w}^{n+1})$  after a short time interval  $(\tau)$  are computed based upon the "old" velocities  $(u^n, w^n)$  using finite-difference versions of the momentum equations, but neglecting the pressure gradient terms. Next, since a pressure field alone cannot impart rotation to the fluid, the true new velocities cannot differ from the "tentative" values by more than a vector field which is the gradient of a scalar "velocity corrector potential"  $\psi$  :

$$u^{n+1} = \tilde{u}^{n+1} + \frac{\partial \psi}{\partial x} \quad , \quad w^{n+1} = \tilde{w}^{n+1} + \frac{\partial \psi}{\partial z} \quad . \quad (6.18)$$

Furthermore, the final new velocities must satisfy the continuity condition:

$$\frac{\partial u^{n+1}}{\partial x} + \frac{\partial w^{n+1}}{\partial z} = 0 \quad (6.19)$$

which, when combined with Equations (6.17) and (6.18), provides a Poisson equation for the  $\psi$  field:

$$\frac{\partial^2 \psi}{\partial x^2} + \frac{\partial^2 \psi}{\partial z^2} = - \frac{\partial \tilde{u}^{n+1}}{\partial x} - \frac{\partial \tilde{w}^{n+1}}{\partial z} \quad (6.20)$$

This equation is solved by an over-relaxed Gauss Seidel iteration procedure for  $\psi$ , and then the final new velocities are determined using Equation (6.18). The above procedure is first-order in time. The code also allows a second-order time approximation by iterating twice on the above procedure. Upon completion of the solution for the new (updated) velocities, the solution of the turbulent energy equation and thus the eddy diffusion coefficient may be obtained. The energy is then updated based upon the new velocities.

An important property of this code is the treatment of the scalar fields. An array of tracer particles is introduced which move with the mean flow, each particle has associated with it values of each field  $Q$ . To find values for these variables for a given computational cell, a "census" is taken of those particles within the cell at the time and the mean particle-based value is used for the cell as a whole. Given the cell-centered values for  $Q$ , a time rate of change of  $Q$  due to diffusion and source terms (the right-hand side of Equation (6.16)) may be computed for each cell. Next, the particle-based values of  $Q$  for those particles within the cell are changed at that rate for a short time interval  $\Delta t$ . Then, new velocities ( $u$  and  $w$ ) are calculated using the momentum equations, and finally the particles are moved to their new positions.

The advantage of this procedure over more conventional techniques is that no "numerical diffusion" of the scalar fields can occur. In ordinary Eulerian finite-difference schemes, it may be shown that high-order truncation errors in the finite-difference treatment of the advection terms of the scalar transport equation will inevitably produce fictitious diffusion-like effects.<sup>[35]</sup> In some procedures, this diffusion is always positive and smears the  $Q$  distribution; in others, it may be negative and cause computational instability. The present procedure circumvents these difficulties by simply not calculating the advection terms explicitly, but instead treating advection implicitly (that is, by moving the marker particles).

#### 6.1.2 Boundary Conditions

Both STUFF2 (2-D) and STUFF3 (3-D) allow several possible boundary structures. Any or all of the outer walls of

the grid may be set to simulate rigid, impermeable "free slip" walls, or one may choose to make the x-direction periodic. The latter case will allow comparison with HAIFA calculations. Internal boundaries are managed by the introduction of obstacle cells with impenetrable walls. The obstacle cells may be placed in any number and arrangement throughout the grid. One sees then that topography is easily handled through judicious arrangement of these cells. The last major feature presently incorporated is the provision for specifying any physically meaningful combination of outer walls as "planes of symmetry." Many problems encountered express some symmetry properties. Taking advantage of this feature of the code will allow considerable saving in computer cost since only a fraction of the physical problem need be modeled.

### 6.1.3 Initial Conditions

The initial flow field and scalar fields must be specified in STUFF. All scalar fields may be initialized in the following ways: (1) one may construct a field by specifying a series of rectangular cell blocks at a given temperature or density, (2) one may construct the field via specification of a vertical profile of essentially arbitrary functional form, and (3) one may initialize via a series of Gaussian distributions throughout the grid. With the attendant "flags" in the code, one may choose any possible combination of the above techniques to achieve the desired scalar field structure.

The initial flow field also can be specified in several ways. The prime requirement, however, is that no matter how pathological one wishes to be, the resulting field must be non-divergent. The simplest method of flow specification is that of a uniform flow in the x-direction. If this is specified,

then the field will be derived from potential flow and the given boundary flow. One may, as in the case of scalar fields, specify cell blocks as having given flow characteristics. The option is available for combinations of these blocks with the flow derived from the potential function to obtain a resultant field.

In addition to the above options in specifying flow, STUFF contains an elaborate intake/exhaust system. This system consists of groups of intake and/or exhaust cells which may be arbitrarily positioned throughout the grid. They are true sources/sinks of mass, momentum, and energy; hence, one must be careful in constructing the system to insure conservation of these quantities. Through judicious positioning of an intake system at the right edge of the grid and an exhaust system at the left edge of the grid, an upstream flow profile of essentially arbitrary structure may be maintained. This feature is extremely useful in constructing velocity profiles which are  $z$  dependent.

#### 6.1.4 The Buffering Scheme

STUFF3 utilizes a particle buffering scheme such that only a small fraction of the Lagrangian particle properties occupy core storage at any one time. The rest reside on mass storage devices in distinct batches. They are retrieved, when required, recalculated, and subsequently returned, to mass storage. This method allows a certain degree of machine independence, since the core requirements of the code are reduced drastically. Currently, STUFF3 has been utilizing a particle density of eight particles per Eulerian cell. This results in a requirement of 64,000 particles in a  $20 \times 20 \times 20$  cell grid. Since each particle requires six storage locations for position, density, contaminant and turbulent energy concentration, one sees that this

amounts to 384,000 required storage locations. To keep such a large amount of information in core would be prohibitively expensive.

With the advent of mass storage devices with high rates of information transfer, buffering schemes have become practical, both from an economical and run time standpoint. STUFF3 stores the particle variables, associated with 500 particles, in core at one time. As a result only 3000 core locations are required to handle the particle-based information. Since most accounting systems utilized by computer installations heavily weight core utilization, this technique results in marked economies. The penalty one pays is in the resultant increased run times and a high use of the I/O channels to the peripheral devices. Both of these factors increase the cost of a calculation.

Timing runs were made which indicated that the buffering scheme was, indeed, adding substantially to run costs. As a result, an examination of the code was made to determine if the particles contained in core were being utilized to their maximum efficiency. By alteration of the order of the particle calculation routines, it was found that the number of exchanges of particles between core and mass storage per time step could be reduced from 9.5 to 3.5. The effect of this reduction has been to render run costs considerably less dependent on the buffering feature; the contribution currently is approximately 15 percent. The reason for this small value is that arithmetic calculations now dominate the time required to execute a time step. Actual run time and cost have been reduced by more than 30 percent on an average basis. Larger grids yield larger relative saving.

### 6.1.5 The Macro-Scale Calculation

Further optimization was centered around the calculation of the local turbulent macro-scale length. Since this requires three-dimensional integrations over all space and calculation of the components of the strain-rate tensor for every cell, a large fraction of the total run time can be attributed to it. Two optimizing mechanisms were employed. The first was a rather straightforward implementation of a suggestion presented in Section 3.5, namely, that the characteristics of the local mean flow are influenced primarily by the quantities in the neighborhood of the point in question, and less by quantities further away. This scheme was incorporated into the optimization program as a limitation on the number of surrounding cells to be included in the spatial integration. This limit is established by the user, as an input number.

The second scheme is suggested by the fact that the code is used to study the evolution of fluid flow from a non-steady to steady-state configuration. As the fluid progresses through the evolutionary sequence, one would expect that the local macro-scale also reach a steady-state since they are, in effect, dependent on the mean flow. Also, we would not expect large changes in the eddy viscosity distribution unless the macro-scales have changed significantly. The user specifies a value which he considers to represent a significant change from one time step to the next in the macro-scale distribution. If this value is exceeded on any time step, then a complete re-integration occurs. If not, then the eddy viscosities are boosted at a rate which corresponds to the rate of change of the average macro-scale. This procedure has the advantage of entirely eliminating the integration at late times resulting in correspondingly more rapid executions of each time step.

#### 6.1.6 Numerical Method

STUFF3 is a mixed-mode hydrodynamics code in which both an Eulerian and Lagrangian matrix representation exist concurrently. In general, mixed-mode codes attempt to minimize the inadequacies of one representation by combining the best features of both. This usually results in some or all of the field variables being carried in both representations (i.e., available in either particle or cell based quantities), with one or the other being utilized as the solution progresses, to evaluate the various terms appearing in the differential equations. At some point there must exist an exchange of data between the two such that each may be able to exert a "corrective" function upon the other. It is through this mechanism that distortions in the Lagrangian net, such as those due to high amplitude waves, can be minimized and that artificial diffusion in the Eulerian sense is greatly reduced.

Before examining the data exchange routines of the STUFF code, a discussion of the allocation of the dynamic variables between the two representations is in order.

All of the scalar fields (density, contaminant concentration, and turbulent energy) are assigned to both representations, while the vector fields (in our case this is just the velocity field) are associated with the Eulerian grid alone. All changes in the distribution of a scalar dynamic variable are reflected in changes in the particle based values during a time step. At the completion of the evaluation of all differential terms, the Eulerian quantities are assigned the "average" of the values associated with particles contained within the cell. This censusing of the particles is one of two exchanges of data in the STUFF code. The purpose is primarily to replace the explicit Eulerian evaluation of the scalar advection terms with a more accurate Lagrangian one. In this

manner, the errors induced by artificial diffusion are avoided. This censusing procedure is defined more explicitly below.

The second exchange of data takes place in the calculation of the scalar diffusion terms. These terms use both particle and cell based values.

Perhaps the best method to describe the numerical techniques of STUFF3 is to detail the steps of a typical cycle of calculation.

Leaving the question of initialization to Section 6.1.6.1, we assume that sufficient data are available to begin a time step. The calculational sequence is as follows:

- STEP 1 Calculate the local eddy viscosity.
- STEP 2 Evaluate source and diffusion terms in the scalar equations.
- STEP 3 Partially update particle-based scalar variables by adding source and diffusion terms.
- STEP 4 Solve the momentum equations utilizing method of Chorin.
- STEP 5 Move the particles with the new velocity field and evaluate the scalar advection terms.
- STEP 6 Remove or add particles as needed to account for sources or sinks of momentum.
- STEP 7 Establish new cell-based values from a particle census.
- STEP 8 Advance the time.
- STEP 9 Honor output requests.

A basic flow diagram is shown in Figure 6.1.

#### STEP 1 - Calculation of the local eddy viscosity.

The local eddy viscosity is calculated in routine EVMAKE. Additionally, the turbulent energy source terms involving  $\Omega$  and  $J$  are calculated and stored in temporary storage. The diffusion-limited time step is also calculated. Finally, a "boosted" eddy viscosity is constructed for use in the momentum equations. This quantity is the larger of the

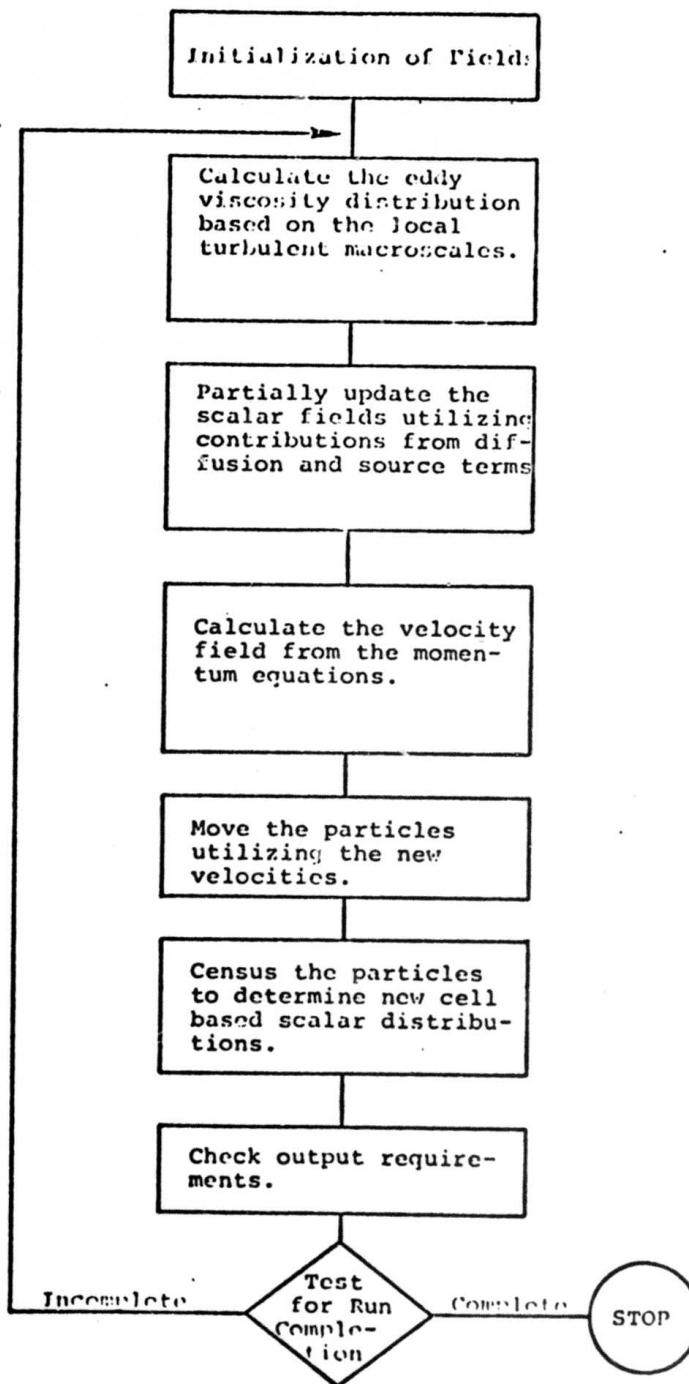


Figure 6.1 - General flow diagram for STUFF.

true eddy viscosity and a "stability" viscosity. The latter is the smallest viscosity needed to stabilize the weak instability arising from the finite difference operator used in the momentum equation. The sole purpose of this procedure is to insure computational stability.

The calculation of the eddy viscosity requires a knowledge of the local macro-scale distribution. Hence, EVMAKE calculates this as well. At this point a feature of the previously described code optimization is introduced. A value is assigned by the user which is a measure of the error that will be tolerated in the eddy viscosity calculation. The average macro-scale of the grid is calculated on each cycle. In order for the local macro-scale to be spatially integrated, the current average macro-scale must differ from the previous one by the given significance level. If the test fails, then the old local eddy viscosities are boosted by an amount corresponding to the rate of change in the average macro-scale. This procedure is found to give excellent results in practice, showing good agreement with the continuous integration procedure. The largest deviation appears in regions of abrupt changes in the boundary, as would be expected.

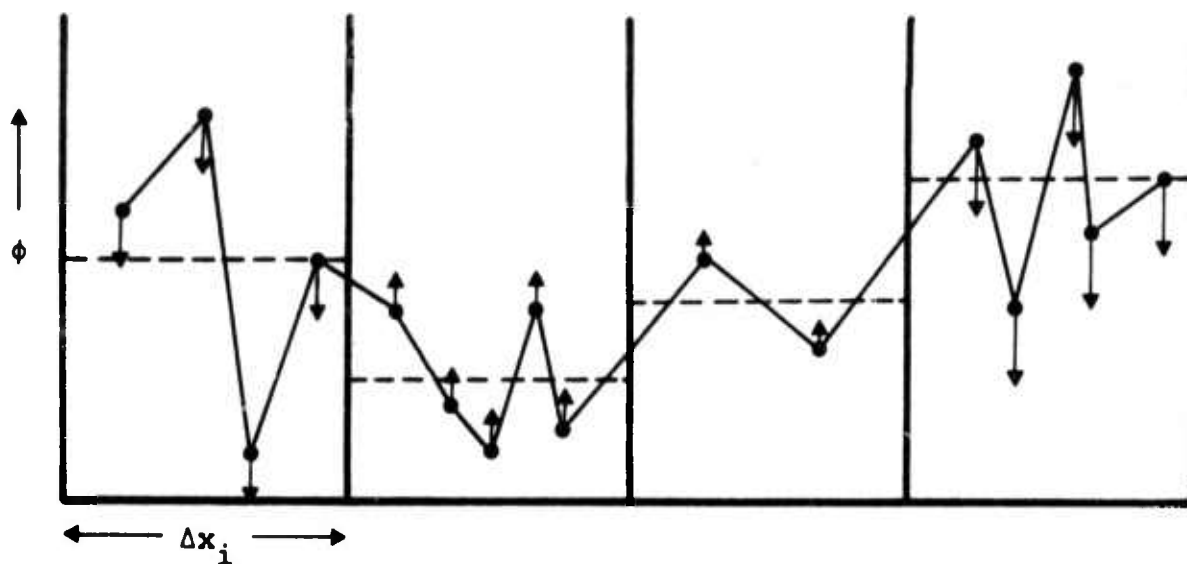
The user may also specify the maximum extent of the spatial integration of  $I^2$  and  $J^2$ . This allows substantial reduction in computing time with only a moderate loss in accuracy since the integrands fall off strongly at larger distances.

#### STEP 2 - Evaluation of scalar source and diffusion terms.

In this calculation, the cell-based scalar field values and eddy viscosity distribution are utilized to construct the diffusion term contributions to the scalar equations. To these terms are added any scalar source terms arising from sources or sinks. In the case of turbulent kinetic energy, the sources calculated in routine EVMAKE are included. The result is to create an effective "source" rate for each of the cells. This is stored temporarily for use in the next step.

STEP 3 - Partial update of particle scalar quantities.

Some difficulty is encountered in using the diffusion and source rates to update the particle scalar quantities for a time  $\Delta t$ . The diffusion and source rates are cell-centered quantities. A first approximation would be to apply a single rate to all particles falling within the confines of one cell. This procedure leads to computational difficulties as seen in the following figure.



The ordinate represents the local value of the scalar variable while the abscissa is marked off in cellular intervals. The dashed lines represent cell-based values of the scalar while the solid line traces through the particle-based distribution. The arrows represent the increase or decrease of particle-based values when the net "source" rates are applied to the particles falling within each of the cells. One sees that in many instances a universal application of cell-based rates to the internal particles could result in some particle-based values going negative. As a result of this, a weighting technique was developed which drives the average particle value to what would be the new Eulerian value but also drives the particles which deviate most from the norm at the fastest rate.

STEP 4 - Solution of the momentum equations.

Utilizing the boosted eddy viscosity calculated in Step 1 and the old velocity field, the subroutine MOMENT determines the resultant new field. The procedure is to first calculate the diffusion terms and store these in temporary storage. Next, the advection terms are calculated and temporarily stored. Finally, the buoyancy term is determined. A resultant tentative velocity field is then determined by applying the calculated rates for a time  $\Delta t$ . This velocity field is then utilized in the Poisson equation solution for the corrector potential. Finally, the resulting corrector potential is utilized to update the tentative velocities to the true new velocities as in Eq. (6.18). In order to achieve a second order accurate time differencing scheme in the momentum equation solution, a second iteration on the above procedure is carried out with the "old" velocity field being replaced by an average of the true old velocity field and the one just calculated. It is found that this second iteration is not very costly in terms of increasing total cycle execution times. This is not obvious since the Poisson equation solution requires an iterative procedure in its solution. It turns out that an over-relaxed Gauss-Seidel procedure produces quite rapid convergence. Additionally, a conservative value of the Courant number also aids in rapid convergence.

STEP 5 - Move the particles.

Once the new velocity field is determined, the evaluation of the scalar advection terms is carried out. This is done by moving the particles at their local velocity for a time  $\Delta t$ . The local velocity is determined from two considerations: first, the time centered velocity field is used, and second, an interpolation scheme is used to determine the velocity appropriate to the position of the particle.

STEP 6 - Add or delete particles to account for sources of momentum.

Lagrangian marker particles must be added or removed as necessary from the calculation as the fluid element in which they reside is swept into or out of the computational mesh. Additionally, the discrete representation of the velocity field will sometimes result in particles being moved into internal obstacle cells accidentally. These conditions are handled in two ways depending on the boundary conditions.

If the cyclic boundary option is specified, then particles swept out of the downstream side are reinserted at the upstream side and complete their movement for that time step. Any particle accidentally being moved into an obstacle region is placed at the position it occupied before the movement. This insures a constant number of particles within the fluid.

If an a priori boundary condition is specified, then particles which are swept out of the downstream side are flagged as deleted in their respective batches. The vacant space then becomes available for the insertion of new particles generated by fluid entering on the upstream side, or from interior sources of momentum. New particles are given scalar values characteristic of the source from which they emerged. Presently, the code deletes all particles which are accidentally moved into an interior obstacle when the a priori boundary condition is specified. This tends to reduce the number of active particles slightly but produces little alteration of results when compared to the repositioning method.

All of these calculations occur in routine PMOVE which also performs the search of the particle batches for particles flagged as deleted. It then packs the batches eliminating the deleted particles and inserting any newly generated ones into the vacancies.

STEP 7 - Establish new cell-based values.

With the completion of the movement of the particles, the equations effectively have been solved at the new time. The task remains, however, to generate the new cell-based quantities. These quantities are required in the calculation of additional time steps and are desired in the editing of problem results.

The cell-based quantities are calculated in routine CENSUS which utilizes essentially the same procedure found in the MAC method.<sup>[36]</sup> Each particle is visualized to extend  $\Delta x_i/N$  in each of the cellular dimensions and to have a scalar value throughout this volume equal to the value attributed to the particle.  $N$  is the cube root of the particle density. The result is to smooth the distribution and to reduce the likelihood of large discontinuities arising from particle clumping. The CENSUS routine determines the fraction each particle donates to each cell. These contributions are summed and normalized to yield a resultant cell-based distribution. Finally, CENSUS checks to insure that no cell is empty of particles. If any are found in this condition, then the cell value is given the averaged value of all the adjacent cells. This rarely happens in runs where the particle density is eight per cell or greater.

STEP 8 - Advance the time.

The time is now advanced so that a new cycle can begin. Several stability criteria representing different terms in the equations limit the size of the time step.

In order to avoid the problems associated with having to introduce more than one set of source particles per time step across any boundary of the domain, the stability number is restricted to values of  $f < 1/N$ . This allows considerable coding economy and does not restrict the allowable time steps too severely.

The stability criterion in explicit schemes requires a restriction on  $\Delta t$  due to diffusion. This is calculated in routine EVMAKE and has the following form:

$$\Delta t < \frac{f}{4\varepsilon} \frac{1}{\frac{1}{\Delta x^2} + \frac{1}{\Delta y^2} + \frac{1}{\Delta z^2}}$$

where  $\Delta x$ ,  $\Delta y$ ,  $\Delta z$  represent cellular dimensions,  $\varepsilon$  is the local eddy viscosity, and  $f$  is a stability number such that  $0 \leq f \leq 2$ .

Another stability criterion incorporated into STUFF reflects the stability associated with the propagation of internal waves. In order to ensure stability in this case, we require

$$\Delta t < f\Delta x/c$$

where  $\Delta x$  is the smallest dimension of the cell,  $f$  a stability number, and  $c$  the internal wave phase velocity given by

$$c^2 = g \frac{\lambda}{2\pi} \Delta\xi$$

where  $\lambda$  is the largest wavelength of the generated internal waves,  $g$  the gravitational acceleration and  $\Delta\xi$  the maximum fractional variation in density across the cell interfaces.  $\lambda$ , in effect, is a free parameter to be chosen a priori from past experience with waves arising in fluid flow problems. Its value is not critical for most cases.

Finally, the stability condition for the advection scheme can be expressed as follows:

$$\Delta t < \frac{-|U^{n+1}| + \sqrt{(U^{n+1})^2 + 2f\Delta x \left| \frac{\partial U^n}{\partial t} \right|}}{\left| \frac{\partial U^n}{\partial t} \right|}$$

Account has been taken above of the possible increase in velocity during the anticipated time step.

The final resultant time step to be used in the next increment is chosen to be the most restrictive of the four inequalities presented above.

#### STEP 9 - Honor output requests.

Requests for edits of output data can assume three forms: (1) requests for a printer dump of all variables of interest including vector and scalar arrays, (2) requests for printer plots of the velocity and scalar fields; an option is to be specified by the user of which particular variables are desired. The plots are depicted as if one were looking down from the top onto the model and successively removing layers of cells. Finally, (3) a tape dump may be made for the purposes of saving the variables for later use, such as a restart.

This completes a calculational cycle in STUFF3. We next discuss the initialization of a problem. The options available for starting a calculation are outlined below.

##### 6.1.6.1 Initialization

The Velocity Field --- Three methods are available to the user in specifying an initial configuration. The first, which is of limited use, involves the determination of the internal momentum distribution from potential flow and specified

boundary flow. This method requires the assumption that the boundary flow must be irrotational. This corresponds to an input flow uniform in  $z$  with no differential cross flow, a condition not likely to be found in atmospheric studies.

A second technique is to specify the velocity in the  $x$ -direction to be periodic and proceed as above. This has the advantage of uniquely determining the flow. A proper boundary condition is also imposed at the downstream grid face which does not introduce flow disturbances. However, this technique is of doubtful usefulness in 3-D codes since large numbers of downwind cells are required so that wrap around effects do not become significant. This approach becomes prohibitively expensive in realistic situations.

The third method appears to be the most useful for mountain wave problems. This involves the usage of the corrector potential-velocity relations expressed by Eqs. (6.19) and (6.20). The procedure is to use the best guess of the ambient field available. This will be in considerable error near highly convoluted regions and the divergence will probably be non-zero. This field is then utilized as a source term of the Poisson equation to derive a corrector potential which, when combined as in Eq. (6.20) with the guessed ambient field, will result in a field which is non-divergent and preserves the vorticity distribution of the original guess. This procedure gives realistic ambient fields, and although they are not unique, they have represented excellent starting fields for several test cases. This method will allow the specification of essentially arbitrary  $z$ -dependent  $u$ -velocity profiles. Cross winds are also allowed.

#### 6.1.6.2 The Grid

The grid utilized by STUFF 3 is pictured in Figure 6.2. For computational efficiency and boundary condition

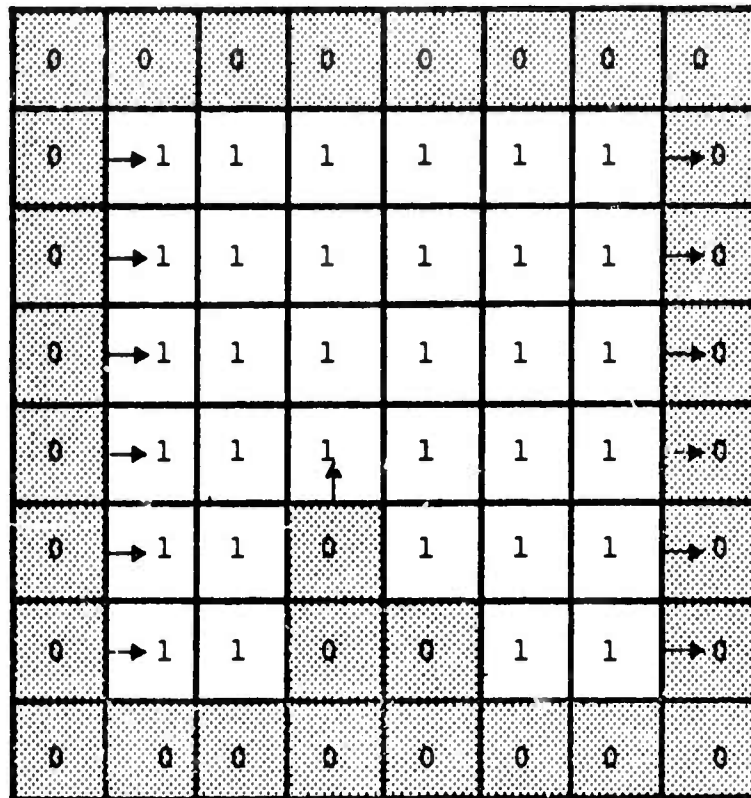


Figure 6.2 - Cross-section of STUFF3 grid with interior and boundary obstacle cells. One interior cell represents a source of momentum. Flow has been specified to the right via the a priori imposed boundary flow.

application, the true grid is surrounded on all sides by a layer of border cells. The velocities at the interior faces of these cells can be assigned to apply various boundary conditions on the flow. Work has been completed to incorporate outflow boundary conditions utilizing extrapolated internal values. This procedure is equivalent to the setting of the second derivative of the normal component to zero, thereby minimizing the disturbing effect of the boundary on the internal flow.

Boundary cells and interior obstacle cells are flagged with a value of zero in the grid-defining array, FULL(I,J,K). Any cell characterized by zero (meaning zero fluid) is assigned velocities associated with its interfaces at problem generation time. This allows interior obstacle cells to act as ducts through which fluid can be removed from or injected into the system, i.e., these become sources or sinks of momentum.

The particles are initially distributed within the grid at a specified density (in terms of number of particles (N) per cellular dimension). Hence, a three-dimensional problem will have  $N^3$  particles per cell. The initial spatial distribution within the fluid filled cells is seen in Figure 6.3.

The indexing notation used to access the various scalar and vector quantities is shown for an arbitrary  $i,j,k$  cell in Figure 6.4. All scalar quantities are cell-centered with  $i,j,k$  referring to the cell center coordinates. Velocities are interface quantities with the  $u,v,w$  components of a cell being defined on the  $i+\frac{1}{2}$ ,  $j+\frac{1}{2}$ , and  $k+\frac{1}{2}$  faces, respectively.

#### 6.1.6.3 Procedure in Updating Particle Arrays Due to Source and Diffusion Terms

In a purely Eulerian scheme the updating of the field variables due to diffusive contributions is straightforward.

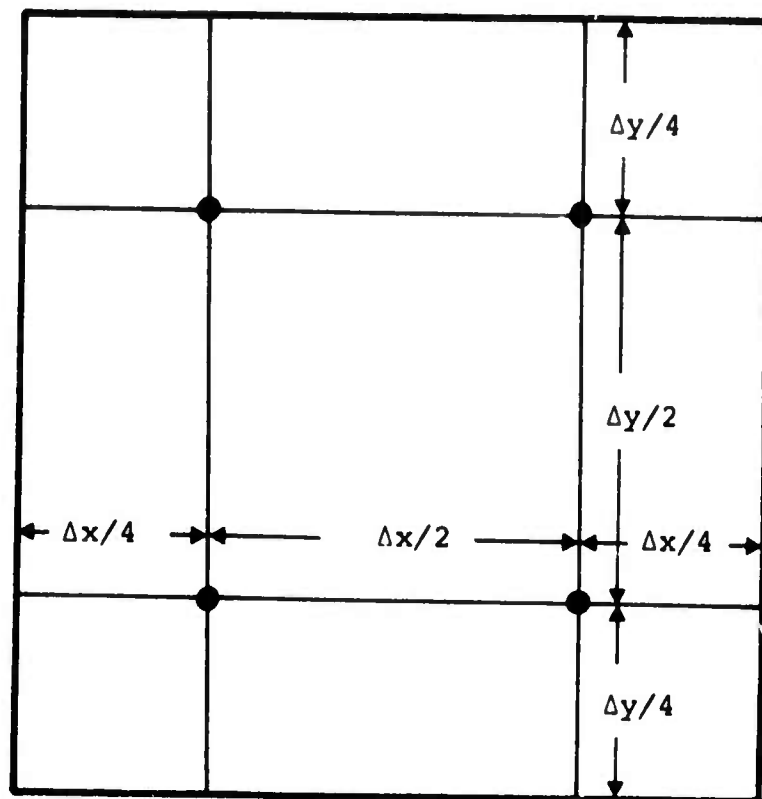


Figure 6.3 - The distribution of particles within a given cell. The third dimension is not shown but exhibits the same symmetry.  $N$  is 2.

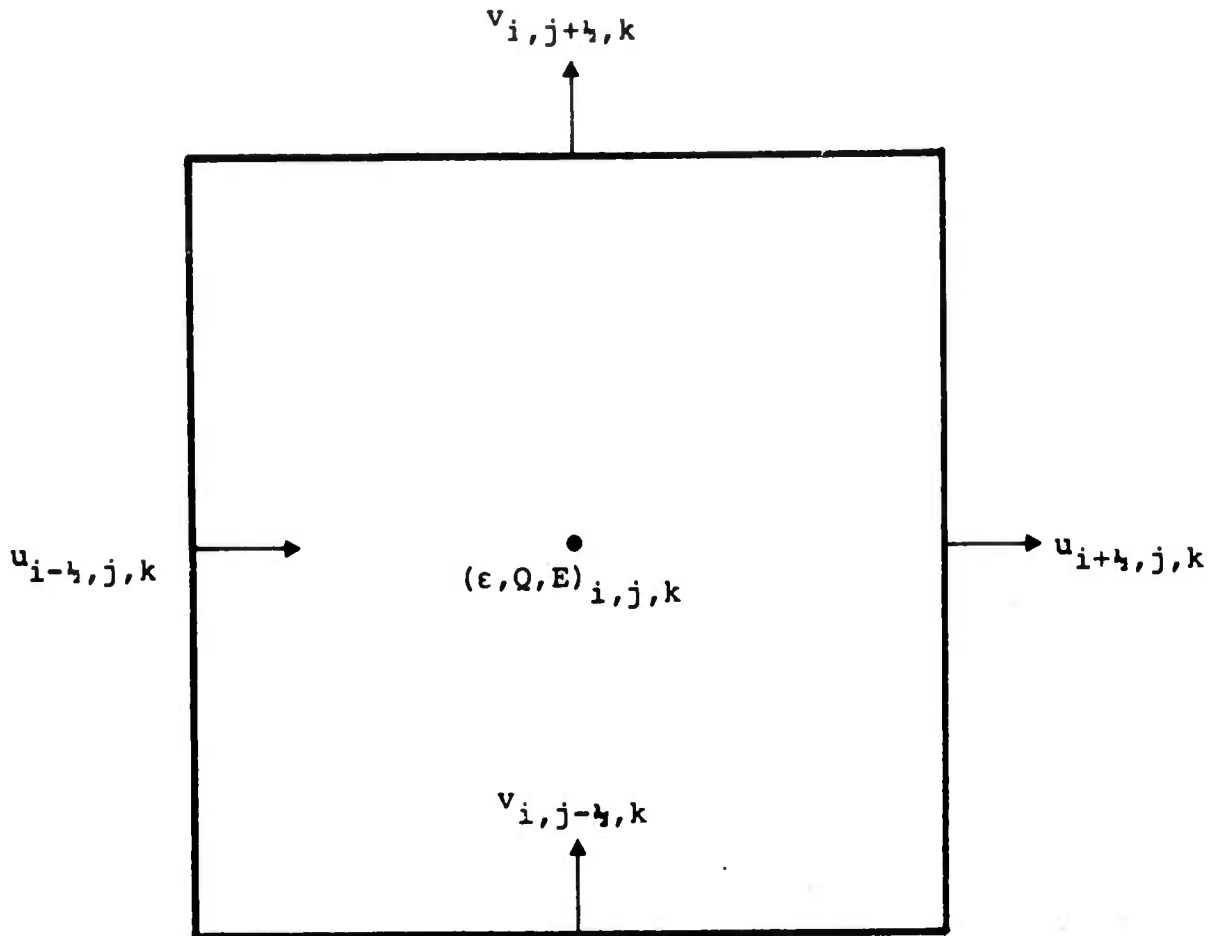


Figure 6.4 - Notation utilized by STUFF. An xy cross-section is shown taken through the cell center. Scalars are cell-centered quantities. Vector components are interface quantities.

Utilizing the standard centered difference operator, the cell-based quantity tends with time to a value more in equilibrium with its neighbors. Since STUFF utilizes the Eulerian-based diffusion rates to modify the particle-based values in the cell, it is possible, using an average rate, to force values associated with some of the particles, negative. While a subsequent census would yield a cell-based value in agreement with the purely Eulerian method, discontinuities may develop when these particles undergo subsequent advection. For example, some of the negative particles might be moved into cells in which they are the sole contributors. A subsequent census would then yield negative cell-based quantities. In order to avoid this problem a smoothing function was developed which preferentially modifies particle values and reduces the variation from the expected Eulerian value.

This function should be related to the local curvature in the field. Also, it should be functionally dependent on the strength of the diffusive coefficient and the time interval over which it can act. After much experimentation, the following form was selected:

$$Q_{\text{PART}}^{n+1} = Q_{\text{CELL}}^n + \left( Q_{\text{PART}}^n - Q_{\text{CELL}}^n \right) e^{-\Delta t S \epsilon} + \Delta t \frac{\partial Q}{\partial t}$$

where  $Q$  represents the field variable, PART and CELL refer to particle and cell-based values, respectively.  $\epsilon$  represents the sum of the turbulent eddy viscosity and molecular diffusion coefficients, and  $S$  is related to the field shape by:

$$S = \frac{\sum \left( \frac{\partial Q}{\partial x_i} \right)^2}{\sum \left( \frac{\partial^2 Q}{\partial x_i^2} \right)^2}$$

where the summation range over all cells, and the derivatives are approximated by standard cell centered finite difference operators. The last term involving  $\frac{\partial Q}{\partial t}$  represents the rate of change due to diffusion and sources and is determined from all based quantities at  $t = t^n$  as is the S factor.

Once the particles have been moved to their final positions for the current time step, a census is carried out to determine the resultant cell-based values so that a new time step may commence. For the purposes of the census, each particle is considered to fill a finite volume, whose dimensions are given by  $\Delta x_i = \Delta X_i / N$ .  $\Delta x_i$  is the particle dimension in the  $i$ th direction,  $\Delta X_i$  is the cell-dimension in the  $i$ th direction, and  $N$  is the cube root of the particle density per cell. This description is defined graphically in Figure 6.5.

The calculation of the cell-based quantities now becomes a series of summations, whereby the value for a particular cell is given by:

$$\phi_{\text{CELL}} = \frac{\sum_i \phi_{\text{PART}_i} \cdot dv_i}{\sum_i dv_i}$$

where  $\phi$  is the scalar variable with PART and CELL referring to particle and cell-based values, respectively.  $dv_i$  is the part of the volume of particle  $i$  falling within the boundaries of the given cell.

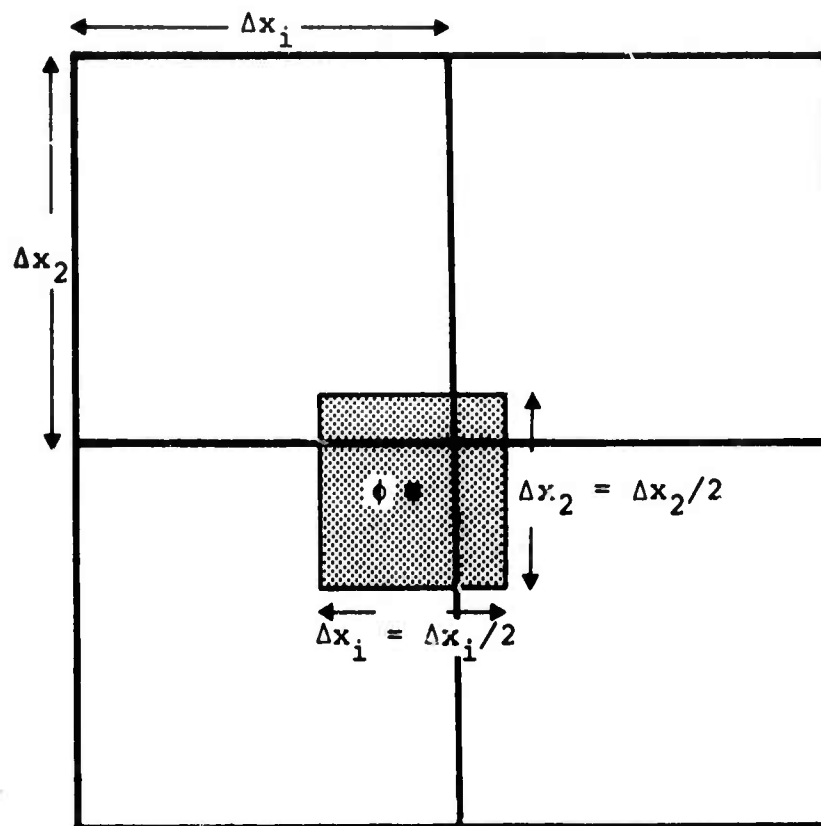


Figure 6.5 - A cross-section of Eulerian cells containing a particle "cube". In this example, particle density is 8/cell, hence  $\Delta x_i = \Delta x_i/2$ .

The scalar advection terms are calculated through the actual moving of the particles. After the completion of this procedure a census is taken to establish the new cell-based values. This results in an evaluation of the advection terms which is free of artificial diffusion.

Some errors are introduced by this scheme, however. While they are much less significant than those found in the method they replace, they should be noted.

Each particle in the fluid should be advected by the fluid. In order for this to be the case, the instantaneous velocity of the particle must be the local velocity of the fluid. A finite difference scheme can only approximate the velocity field at each space-time point. As a result, the velocity which they experience is some interpolated value between locally defined values. Once this value has been determined the particle is moved at this velocity for the time  $\Delta t$ .

Two types of errors are introduced. The first results from the fact that the calculated instantaneous velocity of the particle is an interpolated one. The resulting error will be small if the Eulerian grid is of the proper resolution to adequately resolve the problem. A second error is introduced when the particle is moved at the constant velocity for a time  $\Delta t$ . Actually, the local velocity is a function of  $t$ . The magnitude of this error is still significantly less than the scheme being replaced, however.

In order to insure that the scheme is second order accurate in time, the time centered velocity field is utilized for the particle movement.

### 6.1.7 Sample Calculations

Test problems have been completed using the STUFF code in both a two-dimensional and three-dimensional configuration. The problems give an indication of the code's capabilities to treat flows over mountains. Two-dimensional problems were calculated for flow over a rectangular obstacle, and the results were compared with HAIFA. The agreement was good with no significant differences showing up in the results.

A typical three-dimensional test problem was constructed for the STUFF code. The problem was also configured so as to simulate flow over a rectangular obstacle in a vertically stratified atmosphere. The stratification was represented via a Boussinesq parameter distribution corresponding to a temperature lapse rate of one-half the dry adiabatic lapse rate. An input flow profile corresponding to

$$U(y) = (10 + 0.02y) \text{ m/s}$$

was included. No cross-winds were specified in this problem but the option has been checked out in a separate calculation. The obstacle consisted of a rectangular block one cell high, two cells wide and one cell long, where each cell in the grid represents a cubical volume 1 km on a side. The grid extends eight cells in the horizontal direction and five in the vertical. Since the input flow is uni-directional, problem symmetry exists about a plane which bisects the obstacle in the direction of flow. For this reason, the symmetry handling capabilities of STUFF were utilized. The obstacle was placed against the near side of the grid in the bottom cell layer close to the left edge. The obstacle reduces to one cell in the symmetric case. The results of this problem, after 50 iterative cycles, are given in Figures 6.6 through 6.8. These results present the velocity flow field over and around the obstacle. As noted in the figures, acceleration of the flow

20	21	23	25	27	29	28	24
20	21	24	26	28	29	29	24
20	21	24	27	28	29	28	23
20	20	22	24	25	24	24	22
18	13	4	0	4	11	17	19

x-direction

y-direction

Figure 6.6 - Lateral (x-direction) velocities (cell centered in m/s) for lowest horizontal layer of cells (K > 5 not represented).

100	100	99	98	97	96	96	98
80	81	81	81	80	79	79	80
60	60	60	60	60	59	59	60
39	38	39	40	39	37	36	38
19	13		0	4	11	17	19

x-direction

Figure 6.7 - Lateral (x-direction) velocities (cell centered in m/s) in a vertical slice taken through the obstacle centerline.

y-direction

0	0	0	0	0	0	0	0	0	0
0	0	0	0	0	0	0	0	0	0
0	1	1	1	1	1	0	0	0	-2
1	1	1	1	0	0	0	0	-1	-2
1	2	4	0	-3	-2	-2	-3	-2	-3

x-direction

Figure 6.8 - Axial (y-direction) velocities (cell centered in m/s) in a vertical slice taken through the obstacle centerline.

around the obstacle is much more evident than the acceleration over it. It is necessary to point out that these results are only a summarization of the flow field lifted from the computer printout after 50 calculational cycles.

#### 6.1.7.1 Treatment of Advection - Viscous Wave Calculations

Numerical diffusion errors can have profound effects upon the solutions obtained using hydrodynamic codes. As an illustration, a laminar internal wave problem was solved twice; once using the STUFF 2-D code and once using a conventional Eulerian finite-difference scheme. The case considered was that of the oscillation of a viscous-damped internal wave in a channel of unit height acted upon by a unit downward gravity acceleration (see Figure 6.9). The wavelength was equal to two, and the fluid's molecular kinematic viscosity ( $\nu$ ) was  $5 \times 10^{-4}$ , yielding a Reynolds number of about 50 ( $N_R = A^2/T\nu$ , where  $A$  = amplitude,  $T$  = period,  $\nu$  = kinematic viscosity). In the upper portion of the fluid, the density was 0.95 and in the lower portion 1.05, as shown; initially, the fluid was motionless. To isolate the effects of numerical diffusion, the thermal diffusivity (i.e., "density diffusivity") of the fluid was set to zero. Thus, in principle, the density of a particular fluid element should never change through the calculation, and the interface between the two regions should remain sharply defined. For both calculations, a 20x20 computational mesh was used, and the time step was fixed at 0.05. The same finite-difference procedure was used for both calculations, except that the density transport equation in one case was treated using the STUFF Eulerian-Lagrangian particle technique. In the other calculation, a conventional pure Eulerian "donor-cell" first order scheme was applied. This latter procedure is in common use in many operational codes (see, for example, Hirt and Cook<sup>[37]</sup>).

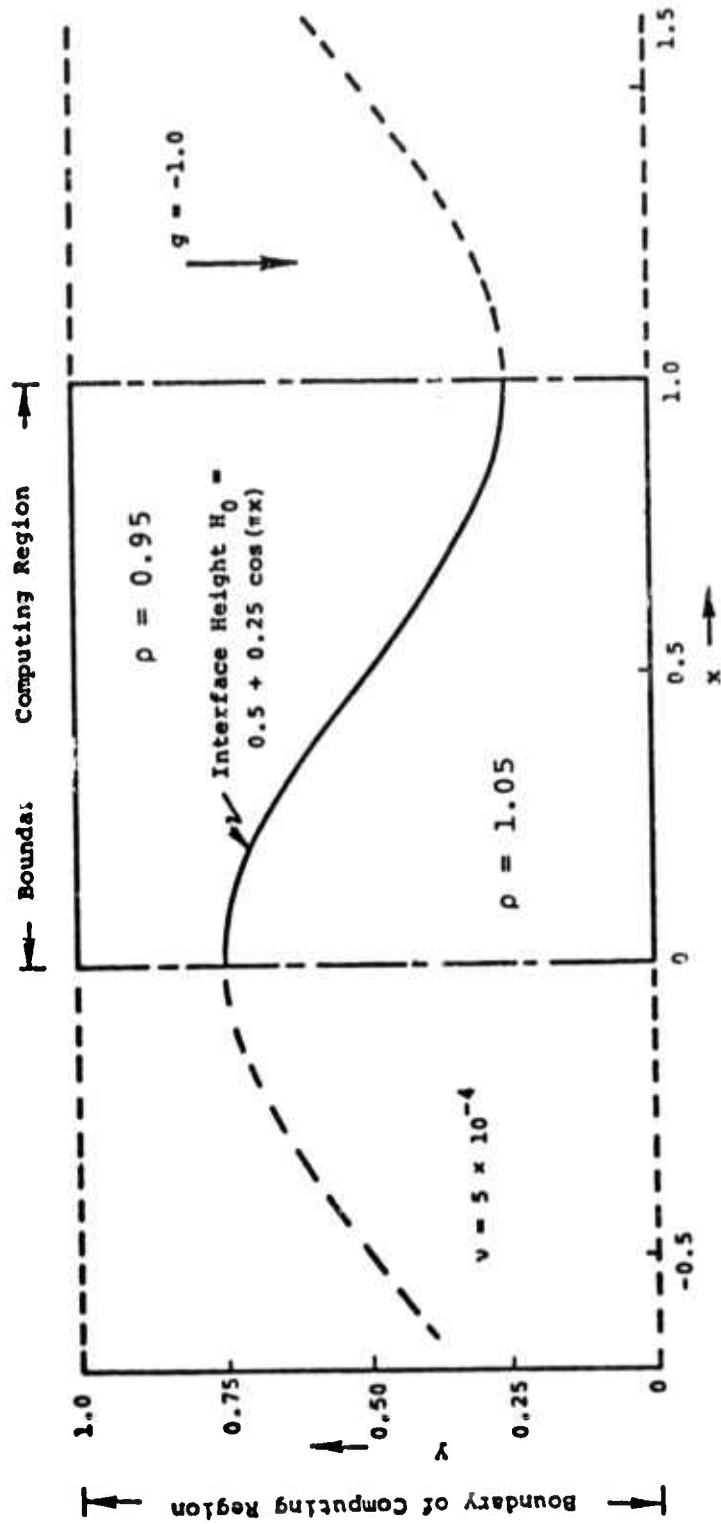
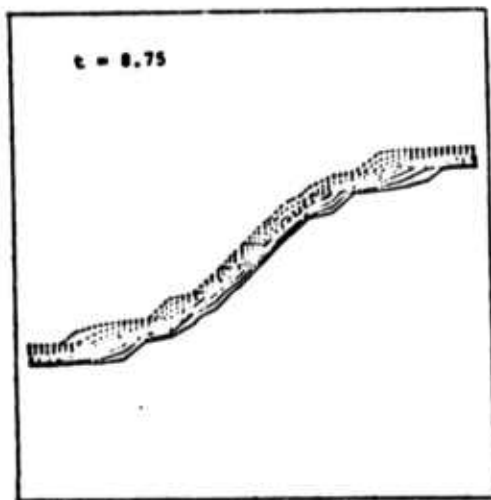
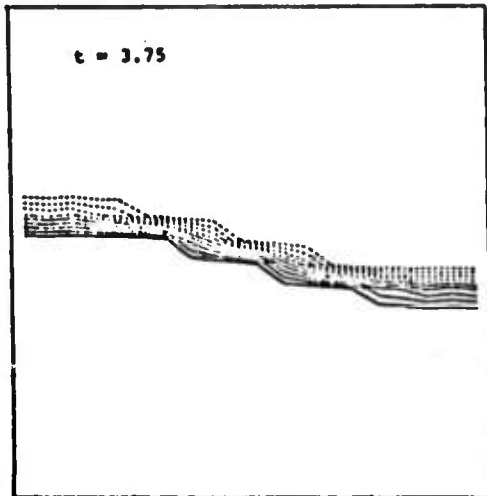
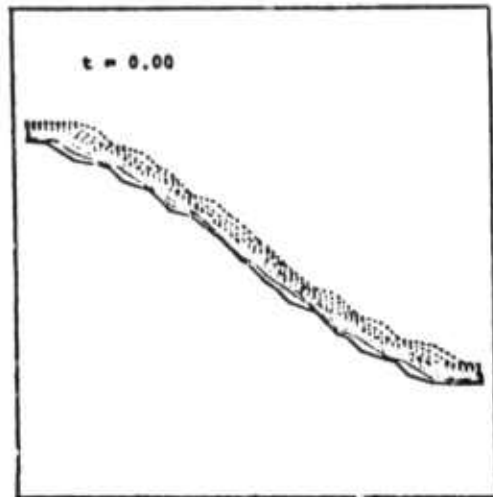


Figure 6.9 - Initial conditions for laminar internal wave test problem.

Figure 6.10 shows the evolution with time of the density field. As can be seen, in the STUFF calculation the density interface remains sharp (i.e., one computational cell thick) whereas in the purely Eulerian calculation the interface diffuses more and more widely as time goes on. Figure 6.11 shows the density distribution along the left-hand edge of the grid ( $x = 0$ ) at  $t = 25$  for both cases; by this time, the Eulerian procedure has "smeared" the interface over a vertical region comparable to the wave height itself. This "smearing" of the density field, in turn, affects the overall fluid flow pattern.

Figure 6.12 shows, as a function of time, the height of the interface along the left-hand edge of the grid. In the Eulerian case, the interface height was taken as the height where  $\rho = 1.0$ . Agreement is fairly good out to  $t = 7$  or so, but, thereafter, the "natural period" of the oscillation in the pure Eulerian calculation begins to increase with time. If the Eulerian calculation were carried further, the "numerical diffusion" effect would eventually homogenize the density field completely; thus the buoyant restoring force would be lost and the natural oscillation period would become infinite. In the STUFF calculation, the period remains essentially constant since the numerical procedure automatically precludes "numerical diffusion."

## EULERIAN/LAGRANGIAN



## PURE EULERIAN

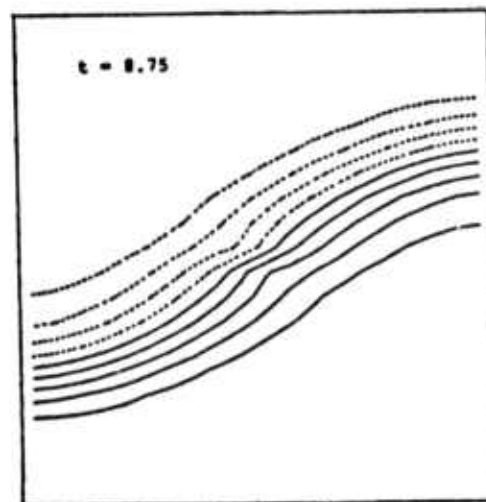
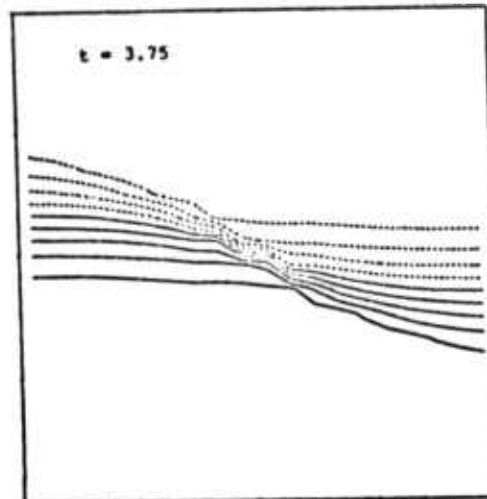
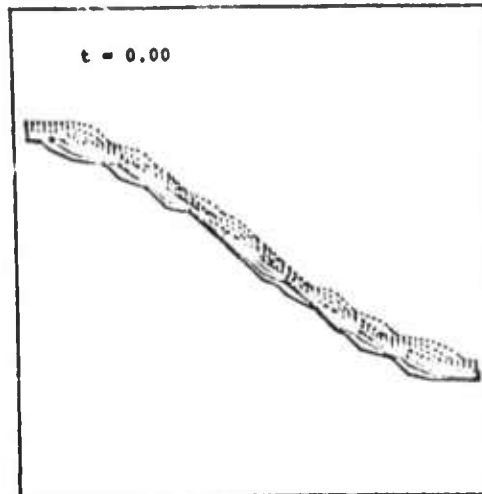
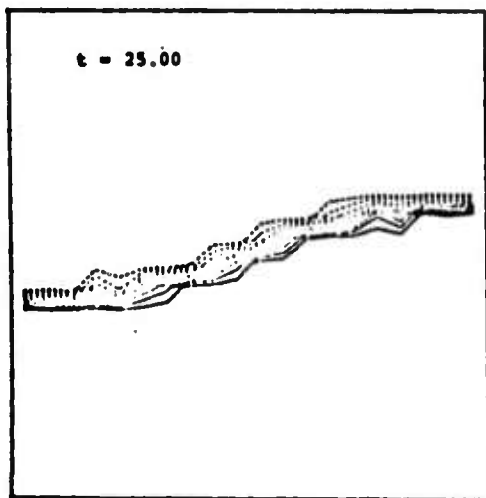
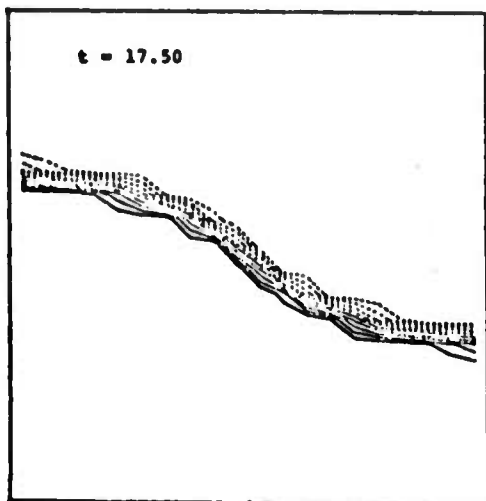
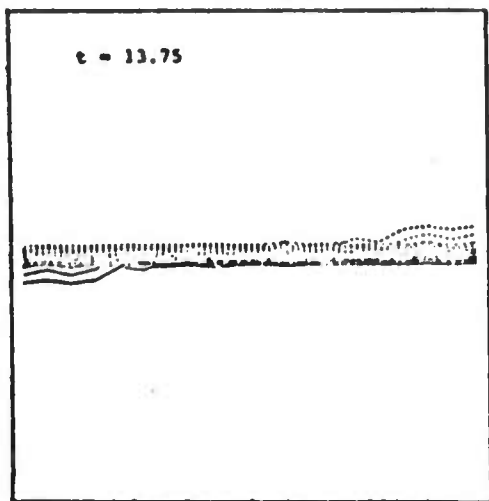


Figure 6.10 - Evolution of the density field with time - laminar internal wave test problem (contour levels:  $\rho = 0.96, 0.97, 0.98, 0.99, 1.00, 1.01, 1.02, 1.03, 1.04$ ).

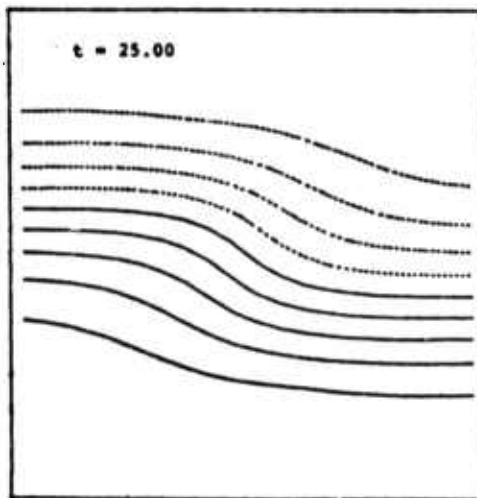
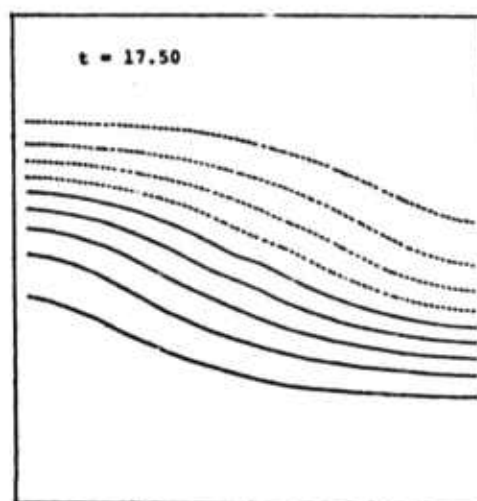
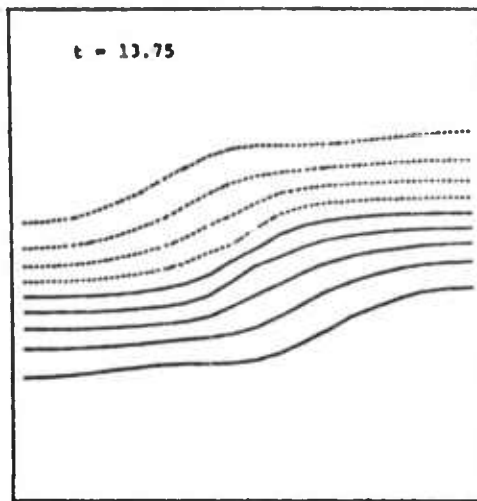
Figure 6.10 - Contd.

SSS-R-75-2556

EULERIAN/LAGRANGIAN



PURE EULERIAN



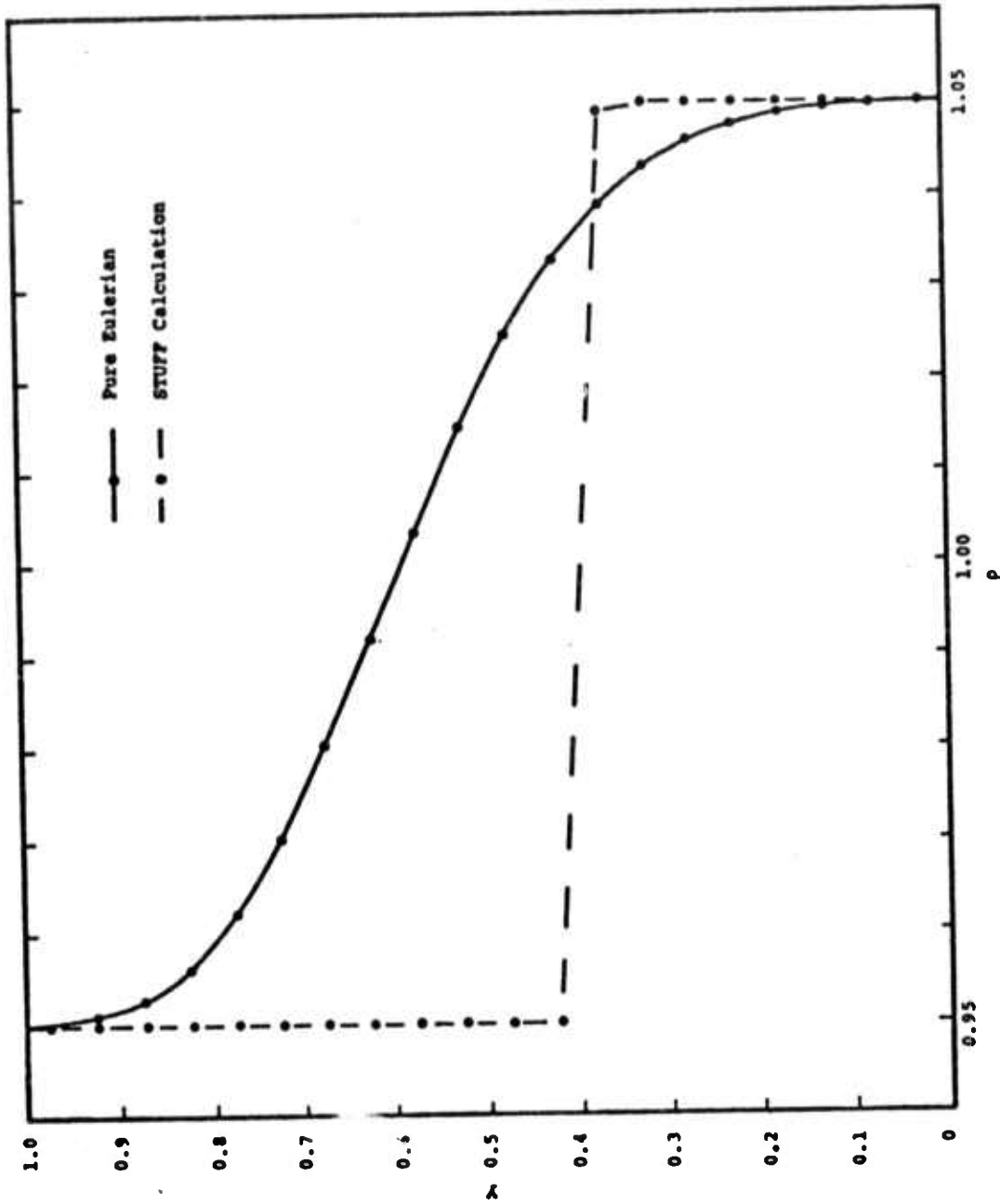


Figure 6.11 - Vertical distribution of density at  $t=25$ .  $x=0$  for internal wave problem.

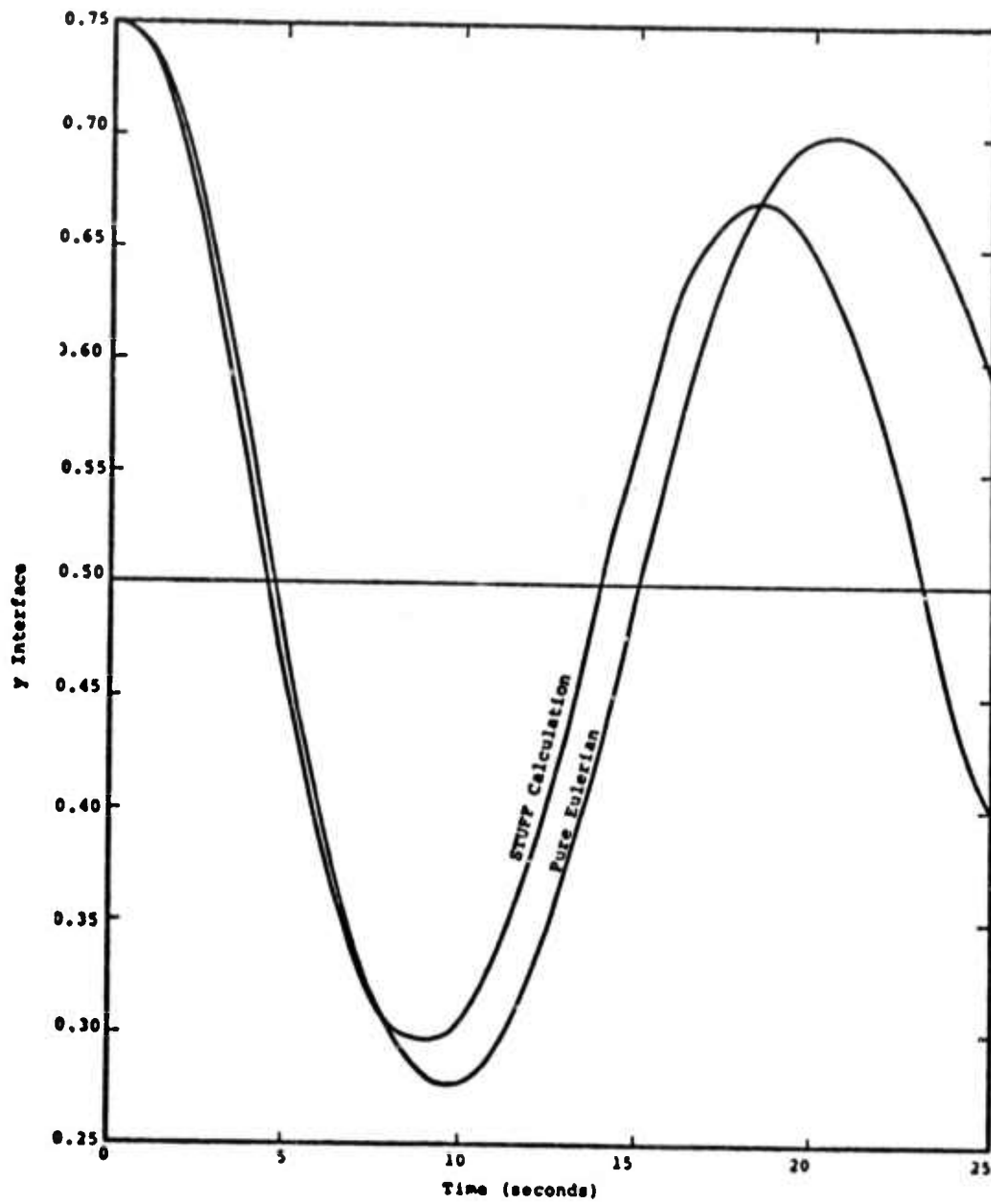


Figure 6.12 - Internal wave problem - height vs time of interface at  $x=0$ .

## REFERENCES

1. Crowley, W. P., "Numerical Advection Experiments," Monthly Weather Review 1, pp. 1-11, January 1968.
2. Buzbee, B. L., F. W. Door, J. A. George, and G. H. Golub, "The Direct Solution of the Discrete Poisson Equation on Irregular Regions," STAN-CS-71-195, December 1970.
3. Cooley, J. W. and J. W. Tukey, "An Algorithm for the Machine Calculation of Complex Fourier Series," Mathematics of Computation 19, pp. 297-301 (1965).
4. Crowley, W. P., "A Global Numerical Ocean Model; Part 1," J. Comp. Phys. 3, pp. 111-147 (1968).
5. Ogura, Y. and N. A. Phillips, "Scale Analysis of Deep and Shallow Convection in the Atmosphere," J. Atmos. Sci. 19, pp. 173-179 (1962).
6. "The Effects of Meso-Scale and Small-Scale Interactions on Global Climate," Systems, Science and Software, 3SR-795, (30 September 1971).
7. "The Effects of Meso-Scale and Small-Scale Interactions on Global Climate," Systems, Science and Software, 3SR-1034, (31 March 1972).
8. Palm, E. and A. Foldvik, "Contribution to the Theory of Two-Dimensional Mountain Waves," Geof. Publ. 6 (1959).
9. Hesstvedt, E., Geof. Publ. 20, No. 10 (1959), Oslo.
10. Liu, J. Y. and H. D. Orville, "Numerical Modeling of Precipitation and Cloud Shadow Effects on Mountain-Induced Cumuli," J. Atmos. Sci. 6, pp. 1283-1298 (November 1969).
11. Arnason, G., R. S. Greenfield, and E. A. Newburg, "A Numerical Experiment in Dry and Moist Convection Including the Rain Stage," J. Atmos. Sci. 25, pp. 404-415 (1968).

12. List, R. J., "Smithsonian Meteorological Tables," (1958), Smithsonian Institute.
13. Srivastava, R. C., "A Study of the Effects of Precipitation on Cumulus Dynamics," J. Atmos. Sci. 24 (1967).
14. Orville, H. D., "Ambient Wind Effects on the Initiation and Development of Cumulus Clouds Over Mountains," J. Atmos. Sci. (May 1968).
15. Ogura, Y., "The Evolution of a Moist Convection Element in A Shallow, Conditionally Unstable Atmosphere: A Numerical Calculation," J. Atmos. Sci. 20 (1963).
16. Kessler, E., "On the Distribution and Continuity of Water Substance in Atmospheric Circulation," Meteor. Monographs 32 (November 1969).
17. Brundidge, K. C., et. al., "Project Themis Prediction of Environmental Parameters," Technical Report ECOM-0073-5 (March 1971), United States Army Electronics Command, Fort Monmouth, New Jersey.
18. Thompson, P. D. Numerical Weather Analysis and Prediction, The MacMillan Co., New York (1961).
19. Gawain, T. H. and J. W. Pritchett, "A Unified Heuristic Model of Fluid Turbulence," J. Computational Phys. 5 (June 1970).
20. Lilly, D. K., private communication with M. G. Wurtele (1971).
21. Vergeiner, I., "An Operational Linear Lee Wave Model for Arbitrary Basic Flow and Two-Dimensional Topography," Qtrly. J. R. Met. Soc. 97 (1971).
22. Foldvik, A. and M. G. Wurtele, "The Computation of the Transient Gravity Wave," Geophys. J. R. Astr. Soc. 13, pp. 167-185 (1967).
23. Lyra, G., "Theory der Stationäre Leewellen-strömung in freier Atmosphäre," Z. Angew. Math. Mech. 23, pp. 1-28 (1943).
24. "Investigations of Mountain Lee Waves and the Air Flow Over the Sierra Nevada," (March 1957), Dept. of Meteorology, University of California at Los Angeles.
25. Bretherton, F. P., "Momentum Transport by Gravity Waves," Qtrly. J. R. Met. Soc. 95 (April 1969).

26. Danielsen, E. F. and R. Bleck, "Tropospheric and Stratospheric Ducting of Stationary Mountain Lee Waves," J. Atmos. Sci. 27 (August 1970).
27. "The Effects of Meso-Scale and Small-Scale Interactions on Global Climate," Systems, Science and Software, SSS-R-72-1255, (15 September 1972).
28. Sawyer, J. S., "The Introduction of the Effects of Topography into Methods of Numerical Forecasting," Qtrly. J. R. Met. Soc. (1969).
29. Eliassen, A. and E. Palm, "On the Transfer of Energy in Stationary Mountain Waves," Geofysiske Publikasjoner Geophysica Norvegica 22, No. 3, pp. 1-23 (1960).
30. Phillips, O. M., The Dynamics of the Upper Ocean, Cambridge University Press, pp. 178-185 (1966).
31. Weather Tapes Obtained from the National Weather Service, Asheville, N. C.
32. Crutcher, H. L., "Meridional Cross Sections - Upper Winds Over the Northern Hemisphere," U.S. Dept. of Commerce Tech. Paper No. 41 (June 1961).
33. Klemp, J. B. and D. K. Lilly, Submitted to J. Atm. Sci. (May 1974).
34. Chorin, A. J., "Numerical Solution of the Navier-Stokes Equations," Mathematics of Computation (October 1968).
35. Richtmeyer, R. D. and K. W. Morton, Difference Methods for Initial Value Problems, Interscience Publications, New York (1967).
36. Welch, E. J., et. al., "The MAC Method: A Computing Technique for Solving Viscous Incompressible Transient Fluid Flow Problems Involving Free Surfaces," Los Alamos Scientific Laboratory, LA 3425, November 1965.
37. Hirt, C. W. and J. L. Cook, "Calculating 3-D Flows Around Structures and Over Rough Terrain," J. Comp. Physics 10, No. 2, pp. 324-340 (October 1972).

APPENDIX A  
DERIVATION OF BOUSSINESQ EQUATIONS

The conservation equations governing macroscopic fluid motion are frequently simplified for problems of thermal convection by introducing certain approximations which are attributed to Boussinesq. These approximations can best be summarized by

- (1) fluctuations in density which appear with the advent of motion result principally from thermal (as opposed to pressure) effects, and
- (2) in the conservation equations of mass and momentum, density variations may be neglected except when they are coupled to the gravitational acceleration in the buoyancy force.

These approximations are examined in the derivation of equations presented below.

The general equations of mass and momentum conservation are

$$\frac{d\rho}{dt} = -\rho\nabla\cdot\bar{V} \quad (\text{A.1})$$

$$\rho \frac{d\bar{V}}{dt} = -\nabla p + \nabla \cdot \bar{P} - \rho g \hat{k} \quad . \quad (A.2)$$

For purposes of this derivation the viscous stress tensor  $\bar{P}$  will be dropped from the equations. The equation of state will be assumed to be of the form

$$\rho = \rho(p, T) \quad . \quad (A.3)$$

The basic approximation to be made may be examined by the following procedure:

(1) Let  $f$  represent any one of the state variables. It will be expressed in the following form

$$f = f_m + f_o(Z) + f'(x, z, t) \quad (A.4)$$

where

- $f_m$  = space average of  $f$
- $f_o(Z)$  = variation of  $f$  in the absence of motion
- $f'(x, z, t)$  = fluctuations in  $f$  resulting from fluid motions.

(2) If a scale height is introduced as

$$H(f) = \left| \frac{1}{f_m} \frac{df_o}{dz} \right|^{-1} \quad (A.5)$$

the basic approximation is that the fluid be confined to a layer whose thickness,  $d$ , is much less than that of the scale height ( $d \ll H$ ).

In particular, Eq. (A.5) implies that  $d/H(\rho) \ll 1$ . On integrating this latter condition over the layer, one concludes that

$$\frac{\Delta\rho_0}{\rho_m} \equiv \epsilon \ll 1, \quad (\text{A.6})$$

where  $\Delta\rho_0$  is the maximum variation of  $\rho_0$  across the layer.

It is also required in non-linear investigations to make the additional restriction that the motion induced fluctuations do not exceed, in order of magnitude, the static variation, i.e.,

$$\left| \frac{\rho'}{\rho_m} \right| \leq 0(\epsilon). \quad (\text{A.7})$$

Condition A.7 must be verified a posteriori from solutions of the problem. In the absence of motion and introducing Eq. (A.4), the vertical component of Eq. (A.2) is

$$\frac{\partial p_0}{\partial z} = -g\rho_m - g\rho_0. \quad (\text{A.8})$$

Introducing the hydrostatic relation into Eq. (A.2), we have

$$\rho \left( \frac{\partial \bar{v}}{\partial t} + \bar{v} \cdot \nabla \bar{v} \right) = -\nabla p' - g\rho' \hat{k}. \quad (\text{A.9})$$

We may introduce Eqs. (A.4) and (A.6) into the continuity Eq. (A.1) to obtain

$$\nabla \cdot \bar{v} = - \left( \frac{\partial}{\partial t} + \bar{v} \cdot \nabla \right) \left( \epsilon \frac{\rho_0}{\Delta\rho_0} + \frac{\rho'}{\Delta\rho_0} \right) + 0(\epsilon^2). \quad (\text{A.10})$$

Hence to order  $\epsilon$ , Eqs. (A.9) and (A.10) may be written

$$\frac{\partial \bar{v}}{\partial t} + \bar{v} \cdot \nabla \bar{v} = - \frac{1}{\rho_m} \nabla p' - g \epsilon \frac{\rho'}{\Delta \rho_0} \hat{k} \quad (\text{A.11})$$

$$\nabla \cdot \bar{v} = 0 \quad (\text{A.12})$$

In Eq. (A.11) we have retained the term  $g \epsilon (\rho' / \Delta \rho_0) \hat{k}$  even though it contains  $\epsilon$  as a factor. This procedure is necessary if we are to study convection problems in the Boussinesq approximation, and the following justification may be made: The quantity  $\frac{\partial \bar{v}}{\partial t}$  measures the characteristic acceleration of the fluid. Now the system is driven by fluctuations of the density field, and hence we must insist that the characteristic acceleration be of order  $(g \epsilon \rho' / \Delta \rho_0)$ . This, in turn, forces the conclusion that the acceleration of gravity is always much greater than the characteristic acceleration, i.e.,

$$\frac{g \rho'}{\Delta \rho_0} \sim 0 \left( \frac{1}{\epsilon} \frac{\partial \bar{v}}{\partial t} \right) .$$

APPENDIX B  
LISTING OF THE DRAG PROGRAM

Two subroutines have been developed for the RAND Mintz-Arakawa two-level GCM, and they are presented in this Appendix. Subroutine DRGSET is called once for each calculation and need not be repeated every GCM cycle. The second subroutine, WVDRAG, is called every cycle (or every  $n^{\text{th}}$  cycle) and performs the calculation of the net stress gain in each level in  $\text{nt}/\text{met}^2$ . The variable names were chosen to be as consistent with the GCM as possible.

```

00010      SUBROUTINE DRGSET
00020      COMMON /DRAG/ MTN(46,72),DK(46),DL(46),A(5,10,409),
00030      1      SINPHI(5,10,46),COSPHI(5,10,46),GAMMA
00040      COMMON /GCM / P(46,72),T(46,72,2),KAPA,RGAS,GRAV,IM,JM,I,J,P
T,
00050      1      U1,U3,V1,V3,V4,U4,Z0,Z1,Z2,Z3,Z4,FX1,FX3,FY1,F
Y3
00060      REAL KAPA /
00070
00080 C-----DEFINE CONSTANTS
00090 C-----JM=46
00100 C-----IM=72
00110 C-----KAPA=0.286
00120 C-----RGAS=287.0
00130 C-----GRAV=9.8
00140 C-----GAMMA = G / C-SUB-P
00150      GAMMA=0.01
00160      PT=200.0
00170      DO 100 J=1,JM
00180      DK(J)=0
00190      DL(J)=0
00200      DO 100 I=1,IM
00210      MTN(J,I)=0
00220      100 CONTINUE
00230 C-----READ SPECTRUM FUNCTION VALUES INTO COPE FOR WAVE DRAG CALCUL
ATION
00240 C-----NGRIDS IS THE NUMBER OF GCM GRIDS FOR WHICH DRAG IS CALCULAT
ED
00250      NGRIDS = 409
00260      DO 200 N=1,NGRIDS
00270      READ(14) LATD,LATM,LOND,LONM,DK1,DL1,((A(K,L,N),K=1,5),L=1,1
0)
00280 C-----ZERO WAVL=WAVK=0 A VALUE
00290      A(1,5,N) = 0.0
00300 C-----DEFINE MTN FIELD
00310      WRITE(6,750) LATD,LATM,LOND,LONM,DK1,DL1
00320      750 FORMAT(' LATD',15,8X,'LATM',15,4X,'LOND',15,8X,
00330      '$LONM',15,/,', DK1',1PE13.5,8X,'DL1',1PE13.5)
00340      JJ=(90+LATD)/4+1
00350      II=LOND/5+37
00360      IF(II.GT.IM) II=II-IM
00370      MTN(JJ,II)=N
00380      DK(JJ)=DK1
00390      DL(JJ)=DL1
00400      200 CONTINUE
00410
00420 C-----SET UP TRIG TABLE FOR UN CALCULATION
00430      DO 300 J=1,JM
00440      DO 300 L=1,10
00450      DO 300 K=1,5
00460      MWL=(L-5)*DL(J)
00470      MWK=(K-1)*DK(J)
00480      PAD=SQRT(MWK*MWK+MWL*MWL)
00490      IF(PAD.LE.0.0) PAD=1.0
00500      SINPHI(K,L,J)=MWL/PAD
00510      COSPHI(K,L,J)=MWK/PAD
00520      300 CONTINUE
00530
00540
00550
00560      RETURN
00570      END
00580

```

```

00590
00600
00610
00620      SUBROUTINE MVDPRG
00630      COMMON /DRAG/ MTN(46,72),DK(46),DL(46),A(5,10,409),
00640      1      SINPHI(5,10,46),COSPHI(5,10,46),GAMMA
00650      COMMON /GCM / P(46,72),T(46,72,2),KAPA,RGAS,GRAV,IN,JM,I,J,PT
00660      1      U1,U3,V1,V3,V4,U4,Z0,Z1,Z2,Z3,Z4,FX1,FX3,FY1,F
Y3
00670      REAL KAPA
00680
00690 C-----IS THIS A MOUNTAINOUS GRID
00700      IF(MTN(J,I).LE.0) GO TO 500
00710      N=MTN(J,I)
00720
00730 C-----IN THIS SUBROUTINE, PGASS=RGAS*10.0
00740 C-----RGASS=P(MB) / ( RHO(G/CM**3) * T(DEG-K) )
00750
00760      RGASS=RGAS*10.0
00770
00780 C-----OBTAIN T1,T3,PS CENTERED AT U,V POINT
00790      IF(J.EQ.1) GO TO 500
00800      IF(I.LT.IM) GO TO 115
00810      T1=0.25*(T(J,I,1)+T(J,1,1)+T(J-1,I,1)+T(J-1,1,1))
00820      T3=0.25*(T(J,I,2)+T(J,1,2)+T(J-1,I,2)+T(J-1,1,2))
00830      PS=0.25*(P(J,I)+P(J,1)+P(J-1,I)+P(J-1,1))
00840      GO TO 120
00850      115 T1=0.25*(T(J,I,1)+T(J,I+1,1)+T(J-1,I,1)+T(J-1,I+1,1))
00860      T3=0.25*(T(J,I,2)+T(J,I+1,2)+T(J-1,I,2)+T(J-1,I+1,2))
00870      PS=0.25*(P(J,I)+P(J,I+1)+P(J-1,I)+P(J-1,I+1))
00880
00890      A(1,1,3)=A(1,1,3) + 1.0
00900 C-----CALCULATE THE GEOPOTENTIAL PARAMETERS
00910      120 P1=0.25*PS+PT
00920      P2=0.50*PS+PT
00930      P3=0.75*PS+PT
00940      PS=PS+PT
00950      PSK=PS**KAPA
00960      PTK=PT**KAPA
00970      P1K=P1**KAPA
00980      P2K=P2**KAPA
00990      P3K=P3**KAPA
01000      PSK2=PSK*PSK
01010      P1K2=P1K*P1K
01020      P2K2=P2K*P2K
01030      PTK2=PTK*PTK
01040      P3K2=P3K*P3K
01050      DDD=2.0*KAPA*(P3K-P1K)
01060      TD1=T1/(DDD*P1K)
01070      TD3=T3/(DDD*P3K)
01080      CCC=RGAS*(TD1-TD3)
01090      BBB=2.0*RGAS*(TD3*P1K-TD1*P3K)
01100      AAA=0.5*RGAS*(T1*(P1-PT)/P1+TD1*(P3K2-P1K2+2.0*P1K*P3K)
01110      1      +T3*(P3-PT)/P3+TD3*(P3K2-P1K2-2.0*P1K*P3K))
01120
01130 C-----CALCULATE THE TEMPERATURE GRADIENT PARAMETERS
01140      A1=1.0/(P3K-P1K)
01150      A2=A1*(T1*P3K/P1K-T3*P1K/P3K)
01160      B2=A1*(T3/P3K-T1/P1K)
01170      C2=-KAPA*GRAV/PGAS
01180      A4=A2*C2
01190      B4=2.0*B2*C2

```

```

01200
01210 C-----CALCULATE THE GEOPOTENTIAL HEIGHT AT 0,2,4 LEVELS
01220      Z4=AAA+BBB*PSK+CCC*PSK2
01230      Z2=AAA+BBB*P2K+CCC*P2K2
01240      Z0=AAA+BBB*PTK+CCC*PTK2
01250      Z0=(Z0+Z4)/GRAV
01260      Z2=(Z2+Z4)/GRAV
01270      Z4=Z4/GRAV
01280      PSNK=PS**KAPA
01290      PSNK2=PSNK*PSNK
01300      TS=A2*PSNK+B2*PSNK2
01310      PD4=1000.0*PS/(PGASS+TS)
01320      PD1=1000.0*P1/(PGASS+T1)
01330      PD3=1000.0*P3/(PGASS+T3)
01340
01350 C-----CALCULATE THE TEMPERATURE GRADIENT AT 1,3 LEVELS
01360      DTDZ1=(A4+P1K+B4*P1K2)/T1
01370      DTDZ3=(A4+P3K+B4*P3K2)/T3
01380
01390 C-----CALCULATE THE U,V VELOCITY AT 0,2,4 LEVELS
01400 C-----LINEAR IN SIGMA SPACE
01410      U0=1.5*U1-0.5*U3
01420      V0=1.5*V1-0.5*V3
01430      U2=0.5*(U1+U3)
01440      V2=0.5*(V1+V3)
01450      U4=1.5*U3-0.5*U1
01460      V4=1.5*V3-0.5*V1
01470
01480 C-----CALCULATE THE BRUNT-VAISALA FREQUENCY AT 1,3 LEVELS
01490      XNSQ1=GRAV*(DTDZ1+GAMMA)/T1
01500      XNSQ3=GRAV*(DTDZ3+GAMMA)/T3
01510 C-----XNSQ .LE. 0.0 IMPLIES INSTABILITY . SKIP DRAG CALCULATIONS
01520      IF(XNSQ1.LE.0.0 .OR. XNSQ3.LE.0.0) GO TO 500
01530
01540 C-----SET UP VARIOUS COMBINATIONS OF PI
01550      PI=3.1415926
01560      PII=1.0/PI
01570      PI4=0.25*PI
01580      PI2=0.50*PI
01590
01600 C-----SET UP INTEGRATION VARIABLES
01610      PKAF1=0.0
01620      PKAF3=0.0
01630      PLAF1=0.0
01640      PLAF3=0.0
01650
01660 C*****
*****
01670 C*          BEGIN K,L INTEGRATION LOOP
      *
01680 C*****
*****
01690      DO 450 L=1,9
01700      DO 450 K=1,5
01710      IF(L.EQ.5 .AND. K.EQ.1) GO TO 400
01720
01730 C-----FORM WAVENUMBERS
01740      MWL=(L-5)*DL(J)
01750      MWK=(K-1)*DK(J)
01760      CAP2=MWL*MWL+MWK*MWK
01770
01780 C-----CALCULATE UN AT 0,1,2,3,4 AND UN**2 AT 1,3 LEVELS
01790      UN0=U0*COSPHI(K,L,J)+V0*SINPHI(K,L,J)
01800      UN1=U1*COSPHI(K,L,J)+V1*SINPHI(K,L,J)
01810      UN2=U2*COSPHI(K,L,J)+V2*SINPHI(K,L,J)
01820      UN3=U3*COSPHI(K,L,J)+V3*SINPHI(K,L,J)
01830      UN4=U4*COSPHI(K,L,J)+V4*SINPHI(K,L,J)
01840      UN12=UN1*UN1
01850      UN32=UN3*UN3

```

```

01860
01870 C-----TEST FOR CRITICAL LEVELS
01880     IF (UN0*UN4.GE.0.0) GO TO 300
01890     IF (UN0*UN2.GE.0.0) GO TO 200
01900
01910 C-----CRITICAL LAYER IN TOP LEVEL
01920     SIG=0.5*UN0/(UN0-UN2)
01930     SIGH=0.5*(SIG+0.5)
01940     PCEN=SIGH*(PS-PT)+PT
01950     PCENK=PCEN**KAPA
01960     PCENK2=PCENK*PCENK
01970     TCEN=A2*PCENK+B2*PCENK2
01980     TGRAD=(A4*PCENK+B4*PCENK2)/TCEN
01990     UNCEN=0.5*UN2
02000     XNS1=GRAV*(TGRAD+GAMMA)/TCEN
02010     XLS1=XNS1/(UNCEN+UNCEN)
02020     XLS3=XNS3/UN32
02030     IF (XLS1.LE.CAP2) GO TO 400
02040     IF (XLS3.LE.CAP2) GO TO 400
02050     F1=XLS1-CAP2
02060     FREQ1=SQRT(F1)
02070     F3=XLS3-CAP2
02080     FREQ3=SQRT(F3)
02090     RAT=F1/F3
02100     X=FREQ3*(Z2-Z4)
02110     IF (X.GE.PI) GO TO 156
02120 C-----EVALUATE SCORER SOLUTION USING FAST TRIG SOLVER
02130     NN=X*PI
02140     Y=X-NN*PI
02150     Y=AMIN1(Y,PI-Y)
02160     IF (Y.GT.PI/4) GO TO 150
02170     YS=Y*Y
02180 C-----C32=COS(X)*COS(X)
02190     C32=1.0-YS*(1.0-0.3333333*YS)
02200     GO TO 155
02210 150 Y=PI/2-Y
02220     YS=Y*Y
02230     C32=YS*(1.0-0.3333333*YS)
02240 155 DEN=RAT+C32*(1.0-RAT)
02250     GO TO 157
02260 156 DEN = FREQ1/FREQ3
02270 157 CONTINUE
02280     F=FREQ1*SIGN(1.0,UN4)/DEN
02290 C-----UPDATE THE STRESS INTEGRALS
02300     X=UN4*UN4*A(K,L,N)*F*DK(J)*DL(J)
02310     IF (Y.EQ.1.DP,K.EQ.5) X=0.5*X
02320     IF (L.EQ.1.DP,L.EQ.9) X=0.5*X
02330     PKAF1=PKAF1+X*MVK
02340     PLAF1=PLAF1+X*MVL
02350     PKAF3=PKAF3-X*MVK
02360     PLAF3=PLAF3-X*MVL
02370     GO TO 400
02380
02390 C-----CRITICAL LAYER IN BOTTOM LEVEL
02400     200 CONTINUE
02410 C-----FLUX IS GENERATED AND ABSORBED IN BOTTOM LEVEL . NO NET IFAG
02420     GO TO 400
02430
02440 C-----NO CRITICAL LAYER
02450     300 CONTINUE
02460     XLS1=XNS01/(UN1*UN1)
02470     XLS3=XNS03/(UN3*UN3)
02480     IF (XLS1.LE.CAP2) GO TO 400
02490     IF (XLS3.LE.CAP2) GO TO 400

```

```

02500      F1=XLS1-CAP2
02510      F3=XLS3-CAP2
02520      FRE01=SQRT(F1)
02530      FRE03=SQRT(F3)
02540      RAT=F1/F3
02550      X=FRE03*(Z2-Z4)
02560      IF(X.GE.PI) GO TO 321
02570 C-----EVALUATE SCORER EQUATION USING FAST TRIG SOLVER
02580      NN=X*PII
02590      Y=X-NN*PI
02600      Y=AMIN1(Y,PI-Y)
02610      IF(Y.GT.PI4) GO TO 310
02620      YS=Y*Y
02630 C-----C32=COS(X)+COS(X)
02640      C32=1.0-YS*(1.0-0.3333333*YS)
02650      GO TO 320
02660 310 Y=PI2-Y
02670      YS=Y*Y
02680      Y32=YS*(1.0-0.3333333*YS)
02690 320 DEN=RAT+C32*(1.0-RAT)
02700      GO TO 322
02710 321 DEN = FRE01/FRE03
02720 322 CONTINUE
02730      F=FRE01*SIGN(1.0,UN4)/DEN
02740 C-----UPDATE THE STRESS INTEGRALS
02750 350 X=UN4+UN4*A(K,L,N)+F*DK(J)+DL(J)
02760      IF(K.EQ.1.DR.L.EQ.9) X=0.5*X
02770      IF(K.EQ.1.DR.K.EQ.5) X=0.5*X
02780      PKAF3=PKAF3-X*MVK
02790      PLAF3=PLAF3-X*MVL
02800
02810      400 CONTINUE
02820      450 CONTINUE
02830 C.....
02840 C*          END OF K,L LOOP,  CONSTRUCT MOMENTUM EQUATION TERMS
02850 C.....
02860
02870 C-----PD4*PKAF1 HAS UNITS OF NEWTONS/METER**2
02880 C-----F CONTAINS SURFACE VELOCITY**2. TO BE CONSISTENT
02890 C-----WITH GCM, MULTIPLY BY 0.49=0.7**2
02900 C-----PD1 THROUGH PD4 ARE DENSITIES. DIVIDE BY PD1*DELTA21
02910 C-----TO GET NT/KG. FACTOR OF 2 COMES FROM SYMMETRY IN K SPACE
02920
02930      FX1=2.0*PD4*PKAF1*0.49
02940      FY1=2.0*PD4*PLAF1*0.49
02950      FX3=2.0*PD4*PKAF3*0.49
02960      FY3=2.0*PD4*PLAF3*0.49
02970      RETURN
02980
02990 500 FX1=0.0
03000      FX3=0.0
03010      FY1=0.0
03020      FY3=0.0
03030
03040      RETURN
03PVH      END

```